EAST EUROPEAN JOURNAL OF PHYSICS. 3. 309-313 (2025)
DOI:10.26565/2312-4334-2025-3-28 ISSN 2312-4334

STATICAL CURRENTS OF p-Si–n-$Si_{1-\delta}Sn_\delta$–n^+-$Si_{1-\delta}Sn_\delta$ ($0 \le \delta \le 0.04$)-STRUCTURES WITH TIN QUANTUM DOTS

Avazbek Sh. Ikromov[a], Azizbek A. Abdurakhmonov[b], Khurshidjon M. Madaminov[a]*
[a]*Andijan State University, 129 Universitet st., Andijan, Uzbekistan*
[b]*Ferghana State University, 19 Murabbiylar st., Ferghana, Uzbekistan*
**Corresponding Author E-mail: khurmad@mail.ru*

Received May 25, 2025; revised July 13, 2025; accepted July 21, 2025

In this work, the current-voltage characteristics of p-Si-n-$Si_{1-\delta}Sn_\delta$ structures at room temperature were investigated to clarify the role of injection effects in the formation of electrical properties of heterostructures obtained based on the $Si_{1-\delta}Sn_\delta$ ($0 \le \delta \le 0.04$) solid solution. It is shown that the sub linear sections observed on the current-voltage characteristics are well described within the framework of the theory of the injection depletion effect. The value of the parameter "a" was determined directly from the sub linear section of the current-voltage characteristic, which in the following allowed determining the concentration of deep impurities responsible for the appearance of the sub linear section. With this it was proved that the investigated structure can be considered as p-Si-n-$Si_{1-\delta}Sn_\delta$–n^+-$Si_{1-\delta}Sn_\delta$ ($0 \le \delta \le 0.04$) - a junction with a high-resistance n-$Si_{1-\delta}Sn_\delta$ layer. An analysis of the results obtained allowed us to conclude that in this $Si_{1-\delta}Sn_\delta$ ($0 \le \delta \le 0.04$) solid solution, scattering of charge carriers not only on complex complexes, but also on nanoformations plays a significant role in the formation of electro physical properties. Based on the results of the studies, it was concluded that the use of epitaxial films of $Si_{1-\delta}Sn_\delta$ ($0 \le \delta \le 0.04$) solid solutions, obtained on silicon substrates, as promising materials, when developing diodes based on them, operating in the double injection mode.

Key words: *Liquid-phase epitaxy; Solid solution; Current-voltage characteristic; Sub linear region; Effect of injection depletion*
PACS: 73.40.Lq, 77.55.df, 61.82.Fk

INTRODUCTION

In connection with the development of nanotechnology and the relevance of research into nano-objects, in particular, the production of semiconductor quantum dots is of interest both for fundamental physics and for potential applications in micro- and nanoelectronics devices [1-3]. This situation has led to intensive research into growing, for example, crystalline perfect solid solutions (SS) of "silicon + tin" with quantum dots (QDs) [4].

Semiconductor p-n-n^+ structures based on the "silicon+tin" solid-state transistor are of significant interest for solid-state electronics and it is very important to have a clear understanding of the current-voltage characteristic (CVC) of these structures [5-6]. Interest in these objects is due to their unique physical properties associated with the atomic-like energy spectrum of QDs and the possibility of producing various semiconductor devices based on them [7-8].

Based on this, the goal of this work was set to study the features of the room CVC of p-n-n^+ structures based on the solid solution "silicon+tin".

The studied p-n-n^+ structures were produced by liquid-phase epitaxy from a tin melt solution [9]. To improve structural perfection, growth was carried out at temperatures below 1100^0 C. The solution-melt composition for low-temperature epitaxy was determined from phase diagrams, which showed that the most suitable component was antimony. In addition, the addition of antimony to the melt solution ensures reliable pouring of the melt solution into the gap between the silicon substrates and the necessary wet ability. The substrates were KDB washers, 40 mm in diameter, oriented in the (111) direction. The growth was carried out from a solution-melt confined between two horizontally located substrates. The grown layers had n-type conductivity with a specific resistance of 0.8 Ohm·cm and a current carrier concentration of 10^{17} cm^{-3}, at room temperature.

MATERIALS AND METHODS

Formation of solid solutions of "silicon – tin". It is appropriate to add here that before this work we did not find any data in the literature on the synthesis of a substitution solid solution based on silicon (Si) and tin (Sn) [9].

Taking into account the charge state and geometric factors of the components, we discuss the possibilities of forming a solid solution based on $Si_{1-\delta}Sn_\delta$. To do this, we will first consider the possibilities of forming solid substitution solutions based on Si and Sn, associated with the conditions for the formation of continuous solid substitution solutions based on molecular-statistical and crystallochemical concepts. These conditions are given in the work [9] in the form

$$\Delta z = \sum_{i=1} z_i^m - \sum_{i=1} z_i^n = 0 \tag{1}$$

$$\Delta r = \left|\sum_{i=1} r_i^m - \sum_{i=1} r_i^n\right| \le 0.1 \sum_{i=1} r_i^m = 0 \tag{2}$$

where z_i^m, z_i^n - valency, r_i^m, r_i^n covalent radius of the atoms of the solvent m and dissolved n chemical element or elements that form the molecules of the solvent and dissolved compounds, respectively, *i=1, 2, 3, 4.*

Cite as: A.Sh. Ikromov, A.A. Abdurakhmonov, Kh.M. Madaminov, East Eur. J. Phys. 3, 309 (2025), https://doi.org/10.26565/2312-4334-2025-3-28
© A.Sh. Ikromov, A.A. Abdurakhmonov, Kh.M. Madaminov, 2025; CC BY 4.0 license

Condition (1) presupposes the electrical neutrality of the dissolved chemical elements or compounds in the solvent semiconductor material. It is satisfied when the dissolved elements are isovalent with respect to the solvent semiconductor.

Condition (2) provides for the proximity of the geometric parameters of the solvent m and soluble n compounds, which excludes the occurrence of significant distortions of the crystal lattice in solid solutions. The smaller, the smaller the energy of elastic distortions of the crystal lattice and, consequently, the greater the crystalline perfection of the solid solution and the solubility n in m. When the difference in the sum of the covalent radii of the atoms of the molecules forming the solution is greater than 10%, the formation of a solid substitution solution of these components is insignificant. Based on the equality of the sum of the valences of the atoms of the Si_2 and SiSn molecules, it is easy to verify that the conditions of electroneutrality (1) are met for them:

$$\Delta z = (z_{Si} + z_{Si}) - (z_{Si} + z_{Sn}) = 0, \tag{3}$$

where z_{Si} and z_{Sn} - valences of silicon and tin atoms, respectively. The sums of the covalent radius of the atoms of the Si_2 and Sn molecules have close values, then from condition (2) we can obtain:

$$\Delta r = \left|(r_{Si} + r_{Si}) - (r_{Si} + r_{Sn)}\right| = \left|2.34\text{Å} - 2.51\text{Å}\right| = 0.17\text{Å} \approx 0.073 \cdot (r_{Si} + r_{Si}) < 0.1(r_{Si} + r_{Si}), \tag{4}$$

where r_{Si} and r_{Sn}covalent radius of silicon and tin atoms according to Pauling, respectively.

From (4) it is evident that the difference in the sum of the covalent radii of the atoms of the Si_2 and SiSn molecules is about 7.3%, therefore, these components satisfy the condition for the formation of a continuous substitution solid solution presented in [10]. Thus, the substitution of Si_2 by a SiSn molecule does not greatly deform the crystal lattice, while the energy of elastic distortions of the crystal lattice will be insignificant and the substitution solid solution in the form of $Si_{1-\delta}Sn_{\delta}$ is a stable solid phase.

A model explaining the formation of tin quantum dots. It is in this process that the driving force of synthesis is the gradient of chemical potentials of the atoms of the crystallized substance in two phases: liquid (μ_L) and solid (μ_S).

Since the lattice constant of the quantum dot material a_2 (a_{Sn}) differs significantly from the lattice constant of the base semiconductor a_1 (a_{Si}), shear mechanical stresses arise at the boundary of subcrystallites (blocks) and epitaxial layers during the formation of QDs [1]. These mechanical stresses can be expressed through the elastic energy *U(x)* per one QD atom with coordinate x, where $0 \leq x \leq R$, *R*– is the radius of the QD base [3]. Then the difference in chemical potentials will be determined by the expression [11]:

$$\Delta\mu_{ST} = \mu_L - \mu_S - U(x) = \Delta\mu - U(x)$$

Under condition $\Delta\mu < U(x)$, the crystallization process is replaced by a dissolution process, since $\Delta\mu_{ST}$ becomes a negative value.

The equality $\Delta\mu = U(x)$ defines the maximum allowable mechanical stresses in a quantum dot. Under these growth conditions, the lattice parameter of the base semiconductor a_{Si} and the quantum dot material a_{Sn} do not depend on temperature. It is in this situation, when calculating the maximum value of the radius of the base (R) of the nascent quantum dot, that we use the expression determined from the condition $\Delta\mu = U(R)$, given in the literature [3]:

$$R = \sqrt{\frac{N_S \Delta\mu (a_1 + a_2) a_1 a_2}{G (a_1 - a_2)^2}}, \tag{6}$$

here N_S is the number of atoms per unit surface area; *G* is the shear modulus.

Since the nuclei formed at the boundary of subcrystallites (blocks) of epitaxial layers are spherical segments whose radius of curvature corresponds to the radius of a homogeneous critical nucleus formed in the liquid phase under the same crystallization conditions, the calculation of the radius of curvature of the nucleus is calculated using the formula:

$$r = \frac{2\sigma M}{\rho R_C T} ln \frac{C_0}{C}, \tag{7}$$

where σ is the interfacial surface energy in the liquid phase; ρ, M are the density and molar mass of the nucleus substance, respectively; R_C is the universal gas constant; C, C_0 are the concentrations of the base semiconductor (Si) and QD (Sn) in supersaturated and equilibrium solutions, respectively. Then the height h of the heterogeneous CT nucleus will be determined by the expression:

$$h = r\left[1 - \left(1 - \frac{R^2}{r^2}\right)\right]. \tag{8}$$

During the growth of the QD nucleus, the mechanical stresses in the QD material layer (Sn) adjacent to the heterointerface increase to values corresponding to the elastic constants of the bulk Si layer [11].

Due to the fact that the stresses in the QD have a gradient directed along the normal to the plane of the base semiconductor, a curvilinear etching front of the lateral surface of the QD is formed at the base of the QD at $\mu_{ST} < 0$. This in turn changes the condition of local phase equilibrium near the heterointerface compared to a flat etching front [12].

Thus, when a mechanically stressed wetting layer is formed, arrays of QDs of the surface regions of the base semiconductor are formed.To confirm the above-described model, an analysis of surface images obtained using AFM was carried out [13].

To confirm the above, the surface properties of these films were investigated using an industrial atomic force microscope (AFM) “Solver-NEXT”, which allows studying the surface relief.

Figure 1 shows a two-dimensional image (a) and a surface profilogram (b) of an epitaxial film of substitution solid solutions $Si_{1-\delta}Sn_\delta$. It is evident (Fig. 1a) that individual nanoislands of different sizes are formed on the surface of the films. Analysis (Fig. 1b) showed that the diameter of the base of the nanoislands varies in the range from 50 to 70 nm, and the height from 3 to 15 nm.

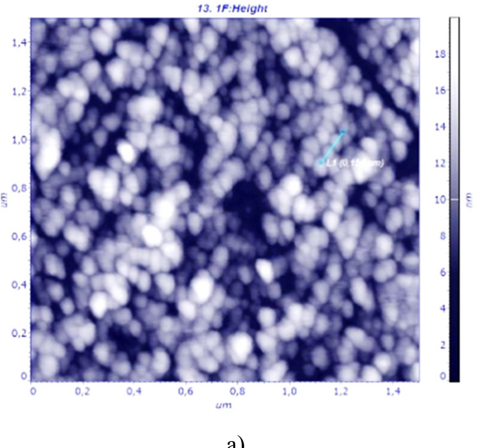

a)

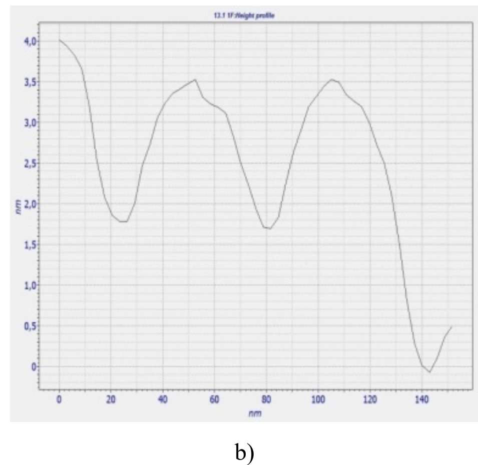

b)

Figure 1. Two-dimensional image (a) and surface profilogram (b) of an epitaxial film of $Si_{1-\delta}Sn_\delta$ solid solutions

The data obtained by the atomic force microscope show that at the growth stage, the Sn nanoislands in the $Si_{1-\delta}Sn_\delta$ solid solution have a geometric shape of a dome, the so-called dome islands with a characteristic lateral size of 50-70 nm with a round base. The appearance of such forms of tin nanoislands is usually explained by strong relaxation of elastic stresses in the dome- phase configuration. According to the data presented in [13], these nanoclusters are called hut-clusters with lateral dimensions of 15 ... 25 nm, they are absorbed by dome-clusters. Such a process is often accompanied by a bimodal distribution of islands by size, corresponding to the coexistence of hut- and dome-phases [14]. Based on these data, it can be concluded that the observed nanoislands on the surface of epitaxial layers are caused by Sn quantum dots with dimensions R = 25 ÷ 35 nm and height h = 3 ÷ 15 nm.

Sample preparation and research methods. As is known, a very important indicator of a p-n junction is its current-voltage characteristic. The appearance of the current-voltage characteristic curves allows us to reason about certain properties of the p-n junction. Since usually, the creation of p-n junctions is complicated by the formation of various types of surface states, which sharply reduce the electrical parameters of devices manufactured on their basis. The resulting p-n junction in a single technological cycle causes a decrease in the density of surface defects. Taking this circumstance into account, the studied pSi-n$Si_{1-\delta}Sn_\delta$ structures were obtained in a single technological cycle using the liquid-phase epitaxy method [9-10].

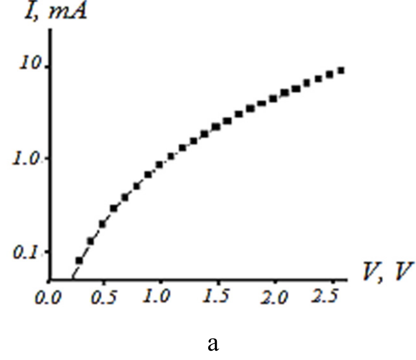

a

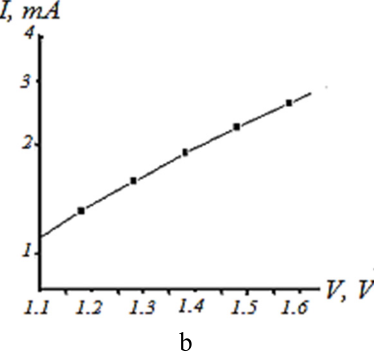

b

Figure 2. Straight branches of the VAX of pSi–n$Si_{1-\delta}Sn_\delta$ heterostructures (a) and their sublinear sections (b) at room temperature

Therefore, to determine some electrophysical characteristics of pSi-$Si_{1-\delta}Sn_\delta$ structures, experiments were conducted to measure the I–V characteristics. For this purpose, pSi-n$Si_{1-\delta}Sn_\delta$ ($0 \le \delta \le 0.04$) structures with a base n-layer thickness of $d \approx 20\ \mu m$ were fabricated. During the study, ohmic contacts were created to the structure using the vacuum deposition method of silver - solid on the back side and quadrangular with an area of 12 mm^2 on the side of the epitaxial layer. During the experiments, dark CVC were measured (Fig. 2). The I–V measurements were carried out at room temperature

T = 293 *K* in the forward current mode (Fig. 2a). The direct direction of current in the structure was considered to be when a positive potential was applied to the contact from the rear side.

RESULTS AND DISCUSSION

According to the obtained experimental results, CVC of the studied samples contains a sublinear region. Figure 2b shows the sublinear region CVC reconstructed on a semi-logarithmic scale. It is easy to see that in these coordinates the sublinear section straightens out. This indicates that it is satisfactorily described by an exponential dependence of the type

$$V \approx V_0 \cdot \exp\,(JA). \tag{9}$$

Theoretical studies of the processes of ambipolar transport of nonequilibrium carriers in p-n-n$^+$ structures show that VAX, described by expression (9), can arise under the conditions of the injection depletion effect, first predicted by Leiderman, Karageorgiy-Alkalaev [15].

This effect occurs under conditions of developed carrier accumulation at the n-n$^+$- junction of the n-base, causing opposite directions of diffusion and drift. In this case, due to the injection modulation of the charge of deep impurities, there is a decrease in the concentration of nonequilibrium current carriers n, a linear increase in the ambipolar drift velocity v_a with an increase in current in the form

$$v_a = a \cdot D_p \cdot J, \tag{10}$$

$$a = (2qN_tD_n)^{-1}, \tag{11}$$

where q is the electron charge, D_n, D_p are the diffusion coefficients of electrons and holes, respectively; N_t is the concentration of deep impurities.

As shown in [16, 17], the coefficient A in (9) is determined by the formula

$$A = a \cdot d, \tag{12}$$

where W is the length of the n-base.

The I(V) graph in Fig. 2b allows us to estimate the parameter “a” using the formula

$$a = \frac{\ln\,(^{V_2}/_{V_1})}{(I_1 - I_2)\cdot d} \tag{13}$$

where S is the cross-sectional area of the sample. Calculation using formula (11) shows that the values of the parameter $a = 6.58\cdot10^3$ cm/A and the concentration of deep impurities responsible for the appearance of the sublinear section in the form (9), at room temperature, the value of which was $N_t = 5.3\cdot10^{12}$ cm^{-3}.

It is appropriate to add here that the specific resistance of the epitaxial layer, determined by the Hall method, is 0.8 Ohm·cm, but all the characteristics obtained indicate that a layer with other characteristics is formed between the epitaxial film and the substrate, otherwise such VAX are not observed, and, therefore, the exponential dependence (9) cannot be observed.

This allows us to reason that the studied structure can be considered as a p-Si–n-$Si_{1-\delta}Sn_\delta$-n$^+$-$Si_{1-\delta}Sn_\delta$ ($0\le\delta\le0.04$) junction with a high-resistance n-$Si_{1-\delta}Sn_\delta$ layer (Fig. 3).

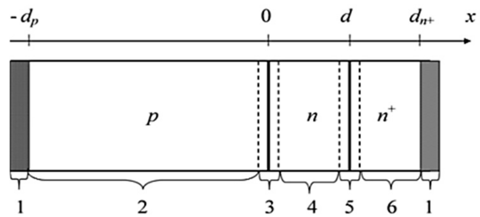

Figure 3. Scheme of pSi-n$Si_{1-\delta}Sn_\delta$-n$^+$$Si_{1-\delta}Sn_\delta$– structures
1 – ohmic current collector contacts; 2 – pSi layer (substrate); 3 – pSi-n$Si_{1-\delta}Sn_\delta$ junction volume charge region; 4 – high-resistance epitaxial layer of pSi - n$Si_{1-\delta}Sn_\delta$ solid solution; 5 – n$Si_{1-\delta}Sn_\delta$- n+$Si_{1-\delta}Sn_\delta$ junction volume charge region; 6 – low-resistance epitaxial layer of pSi - n$Si_{1-\delta}Sn_\delta$ solid solution

CONCLUSIONS

The obtained results allow us to conclude that the presence of a sublinear region in VAX p-n-n$^+$ structures based on silicon-tin solid solutions is associated with the effect of injection depletion [18].

Thus, the epitaxial films of $Si_{1-\delta}Sn_\delta$, solid solutions obtained on silicon substrates that we studied, can be used as an active element for developing injection diodes. The structures obtained on this basis and the description of the mechanisms of physical processes occurring in them are of both theoretical and practical interest for semiconductor materials science [19].

As a result, it can be assumed that the epitaxial films of $Si_{1-\delta}Sn_\delta$ solid solutions studied in the work may be promising materials for the manufacture of diodes operating in the double injection [4, 20].

ORCID
A.Sh. Ikromov, https://orcid.org/0009-0009-3145-1326; **A.A. Abdurakhmoov**, https://orcid.org/0009-0007-6758-2585
Kh.M. Madamiov, https://orcid.org/0000-0003-0117-9316

REFERENCES

[1] A.P. Kokhanenko, A.V. Voitsekhovskii, K.A. Lozovoy, R. Douhan, V.V. Dirko, and N.Yu. Akimenko, "Dark current of photodetectors based on multilayer structures with quantum dots," Applied Physics, **5**, 42 (2022). https://doi.org/10.51368/1996-0948-2022-5-42-48. (in Russian).
[2] I.I. Izhnin, K.A. Lozovoy, A.P. Kokhanenko, K.I. Khomyakova, R.M.H. Douhan, V.V. Dirko, A.V. Voitsekhovskii, *et al.*, "Single-photon avalanche diode detectors based on group IV materials," Applied Nanoscience **12**, 253 (2022), https://doi.org/10.1007/s13204-021-01667-0
[3] K.A. Lozovoy, Kinetics of nanoheterostructures formation with quantum dots of germanium on silicon for optoelectronics devices. Ph.D. thesis, Tomsk State University, 2016. (in Russian).
[4] Kh.M. Madaminov, "Temperature dependences of the electrophysical properties of the solid solution $Si_{1-x}Sn_x$ (0 ≤x≤ 0.04)," Applied Physics, **1**, 63-68 (2021), https://doi.org/10.51368/1996-0948-2021-1-63-68. (in Russian).
[5] A.S. Saidov, S.N. Usmonov, M.U. Kalanov, *et al.*, "Structural and some electrophysical properties of the solid solutions $Si_{1-x}Sn_x$ (0 ≤ x ≤ 0.04)," Phys. Solid State, **1**(55), 45–53 (2013). https://doi.org/10.1134/S1063783413010290
[6] A.S. Saidov, Sh.N. Usmonov, M.U. Kalanov, Kh.M. Madaminov, and D.A. Nishanova, "Effect of Gamma Irradiation on Photoconductivity and Photosensitivity of $Si_{1-x}Sn_x$ Solid Solutions," Applied Solar Energy, **47**(1), 48-51 (2010). https://doi.org/10.3103/S0003701X11010142
[7] Z. Li, H.-Z. Gao, W.-R. Xu, J.-M. Wang, W. Li, and X.-D. Jiang, "Optoelectronic artificial synapse based on $Si_{1-x}Sn_x$ alloyed film," Vacuum, **6**(212), 112002 (2023). https://doi.org/10.1016/j.vacuum.2023.112002
[8] A.M. Hussain, N. Wehbe, and M.M. Hussain, "SiSn diodes: theoretical analysis and experimental verification," Appl. Phys. Lett. **107**, (2015). https://doi.org/10.1063/1.4929801
[9] A.S. Saidov, D.V. Saparov, Sh.N. Usmonov, A.Sh. Razzakov, and M. Kalanov, "Features of liquid-phase epitaxy of new solid solutions of $(GaAs)_{1-y-z}(Ge_2)_y(ZnSe)_z$ and their photoelectric properties," International Journal of Modern Physics B, **14**(37), 2350132 (2023). https://doi.org/10.1142/S0217979223501321
[10] Sh.K. Ismailov, A.S. Saidov, Sh.N. Usmonov, D.V. Saparov, D.O. Eshonkhojaev, U.P. Asatova, and S.G. Bobojanov, "Investigation of the Spectral Photosensitivity of nGaAs-$n^+(GaAs)_{1-x-y}(Ge_2)_x(ZnSe)_y$ Heterostructure Obtained from Bi Solution-Melt," The Transactions of the Korean Institute of Electrical Engineers, **6**(73), 980-986 (2024). https://doi.org/10.5370/KIEE.2024.73.6.980
[11] A. Medvid, P. Onufrijevs, R. Jarimaviciute-Gudaitiene, *et al.*, "Formation mechanisms of nano and microcones by laser radiation on surfaces of Si, Ge, and SiGe crystals," Nanoscale Res. Lett. (1)8, 264 (2013). https://doi.org/10.1186/1556-276X-8-264
[12] V.G. Dubrovskiy, *Theory of formation of epitaxial nanostructures*, (Fizmatlit, Moskow, 2009). (in Russian).
[13] Y. Seo, and W. Jhe, "Atomic force microscopy and spectroscopy," Reports on Progress in Physics, **71**(1), 016101 (2008). https://doi.org/10.1088/0034-4885/71/1/016101
[14] S.Z. Zaynabidinov, and A.O. Kurbanov, "Nickel-dopant atom clusters and their effect on the recombination properties of silicon," Herald of the Bauman Moscow State Technical University, Series Natural Sciences, **2**(93), 81–93 (2019). https://doi.org/10.18698/1812-3368-2019-2-81-93 (in Russian).
[15] A.Yu. Leiderman, and P.M. Karageorgy-Alkalaev, "On the theory of sublinear current-voltage characteristics of semiconductor structures," Solid State Communications, **10**(25), 781-783 (1978). https://doi.org/10.1016/0038-1098(78)90529-X
[16] Kh.M. Madaminov, "Effect of injection phenomena on electrical properties of pSi-n$Si_{1-x}Sn_x$ heterojunctions," Herald of the Bauman Moscow State Technical University, Series Natural Sciences, **2**(95), 71-84 (2021). https://doi.org/10.18698/1812-3368-2021-2-71-84. (in Russian).
[17] A.S. Saidov, A.Yu. Leyderman, Sh.N. Usmonov, and K.A. Amonov, "Effect of injection depletion in p-Si-n-$(Si_2)_{1-x}(ZnSe)_x$ (0≤x≤0.01) heterostructure," Semiconductors, **9**(52), 1188-1192 (2018). https://doi.org/10.1134/S1063782618090142
[18] A.Yu. Leiderman, R.A. Ayukhanov, R.M. Turmanova, A.K. Uteniyazov, and E.S. Esenbaeva, "Non-recombination injection mode," SPQEO, **3**(24), 248-254 (2021). https://doi.org/10.15407/spqeo24.03.248
[19] P. Harrison, and Alex Valavanis, *Quantum wells, wires and dots: theoretical and computational physics of semiconductor nanostructures,* 4th edition (West Sussex, United Kingdom; Hoboken, NJ: John Wiley & Sons, Inc., 2016), pp. 16.
[20] H. El Ghonimy, M.R. Abdel-Rahman, M. Hezam, M.A. Alduraibi, N.F. Al-Khalli, and B. Ilahi, "Amorphous SiSn alloy: another candidate material for temperature sensing layers in uncooled microbolometers," Phys. Status Solidi (b), **258**, (2021). http://dx.doi.org/10.1002/pssb.202100103

СТАТИЧНІ СТРУМИ p-Si–n-$Si_{1-\delta}Sn_\delta$–n^+-$Si_{1-\delta}Sn_\delta$ (0≤δ≤0.04)-СТРУКТУР З КВАНТОВИМИ ТОЧКАМИ ОЛОВА

Авазбек Ш. Ікромов[a], Азізбек А. Абдурахмонов[b], Хуршиджон М. Мадамінов[a]
[a]*Андижанський державний університет, вул. Університетська, 129, Андижан, Узбекистан*
[b]*Ферганський державний університет, вул. Мураббійлар, 19, Фергана, Узбекистан*

У цій роботі досліджено вольт-амперні характеристики структур p-Si-n-$Si_{1-\delta}Sn_\delta$ за кімнатної температури з метою з'ясування ролі ефектів інжекції у формуванні електричних властивостей гетероструктур, отриманих на основі твердого розчину $Si_{1-\delta}Sn_\delta$ (0≤δ≤0,04). Показано, що сублінійні ділянки, що спостерігаються на вольт-амперних характеристиках, добре описуються в рамках теорії ефекту виснаження інжекції. Показано, що сублінійні ділянки, що спостерігаються на вольт-амперних характеристиках, добре описуються в рамках теорії ефекту виснаження інжекції. Значення параметра «а» визначалося безпосередньо з сублінійної ділянки вольт-амперної характеристики, що надалі дозволило визначити концентрацію глибоких домішок, що відповідають за появу сублінійної ділянки. Цим було доведено, що досліджувану структуру можна розглядати як p-Si-n-$Si_{1-\delta}Sn_\delta$–n^+-$Si_{1-\delta}Sn_\delta$ (0≤δ≤0,04) – перехід з високоомним шаром n-$Si_{1-\delta}Sn_\delta$. Аналіз отриманих результатів дозволив зробити висновок, що в цьому твердому розчині $Si_{1-\delta}Sn_\delta$ (0≤δ≤0,04) розсіювання носіїв заряду не лише на складних комплексах, але й на наноутвореннях відіграє значну роль у формуванні електрофізичних властивостей. На основі результатів досліджень було зроблено висновок про використання епітаксійних плівок твердих розчинів $Si_{1-\delta}Sn_\delta$ (0≤δ≤0,04), отриманих на кремнієвих підкладках, як перспективних матеріалів при розробці діодів на їх основі, що працюють у режимі подвійної інжекції.

Ключові слова: *рідкофазна епітаксія; твердий розчин; вольт-амперна характеристика; сублінійна область; вплив виснаження інжекції*

East European Journal of Physics. **3.** 314-318 (2025)
DOI:10.26565/2312-4334-2025-3-29 ISSN 2312-4334

THE PHOTOELECTRIC PROPERTIES OF *n*-Si–*p*-$(Ge_2)_{1-x-y}(ZnSe)_x(GaAs_{1-\delta}Bi_\delta)_y$ HETEROSTRUCTURES

Akramjon Y. Boboev, Ulugbek R. Karimberdiev, Nuritdin Y. Yunusaliyev, Jamshidbek S. Madaminov
Andijan State University, named after Z.M. Babur, Andijan, Uzbekistan
**Corresponding Author E-mail: aboboevscp@gmail.com*
Received March 28, 2025; revised June 28, 2025; accepted July 9, 2025

In this paper, the photovoltaic properties of $(Ge_2)_{1-x-y}(ZnSe)_x(GaAs_{1-\delta}Bi_\delta)_y$ solid solutions grown on silicon substrates are investigated. It is found that the solid solutions $(Ge_2)_{1-x-y}(ZnSe)_x(GaAs_{1-\delta}Bi_\delta)_y$ possess selective photosensitivity due to the presence of ZnSe, Ge_2, and $GaAs_{1-\delta}Bi_\delta$ components, as well as the difference in the ionisation energy of their covalent bonds. The photoconductivity mechanisms in n-Si-p-$(Ge_2)_{1-x-y}(ZnSe)_x(GaAs_{1-\delta}Bi_\delta)_y$ heterostructures were analysed based on the E_i values that provided the best fit to the experimental spectrum and Gaussian approximation curves. Photopeaks corresponding to Gaussian curves at the energy levels 1.23 eV, 1.45 eV, 1.64 eV, 1.91 eV, 2.21 eV, and 2.45 eV were observed in the photon energy range: $E_{ph,1}$ - 0.98÷1.75 eV, $E_{ph,2}$ - 1.01÷2.03 eV, $E_{ph,3}$ - 1.15÷2.28 eV, $E_{ph,4}$ - 1.34÷2.52 eV, $E_{ph,5}$ - 1.75÷2.71 eV and $E_{ph,6}$ - 2.1÷2.77 eV. The observation of intermediate states in the photosensitivity spectrum of this solid solution confirmed the presence of nano-objects formed based on ZnSe and Ge_2 molecules, as well as $GaAs_{1-\delta}Bi_\delta$ compounds in these films. It was found that solid solutions $(Ge_2)_{1-x-y}(ZnSe)_x(GaAs_{1-\delta}Bi_\delta)_y$ have the potential to be used as selective photoactive materials operating in the ranges of infrared and visible radiation.
Keywords*: Silicon; Solid solution; $GaAs_{1-\delta}Bi_\delta$ compound; Covalent bonding; Photosensitivity*
PACS: 78.30.Am

INTRODUCTION

High-performance photovoltaic and optoelectronic devices are largely controlled by the capability of semiconductor materials to react to a wide spectral range effectively. Winding of the photosensitivity range of photoactive elements is one of the major functional parameters of a device. Extending this range not only enhances the efficiency of energy conversion but also widens the use of such devices in various technological applications, including solar energy harvesting, photodetection, and optical communications. Among the most commonly utilized techniques of broadening the spectral response is introducing specific impurities into semiconductor material, especially within the active parts of p-n junctions [1]. This method enables the creation of other energy levels within the bandgap and thus enhances the interaction between incoming photons and charge carriers [2].

There has also recently been a developing interest in adding isovalent impurities into epitaxial semiconductor films. When carefully chosen and controlled, these impurities have been shown to add localized energy levels inside the valence or conduction bands of the host semiconductor material. These newly added levels are of great importance for optical absorption, carrier recombination rates, and transport characteristics, and, in turn, bring about enhancements of photoelectric responses. Such effects need to be investigated for the development of future semiconductor heterostructures optimized for operation under high efficiency in various irradiation conditions [3,4].

This study focuses on a novel class of solid-solution heterostructures based on the $(Ge_2)_{1-x-y}(ZnSe)_x(GaAs_{1-\delta}Bi_\delta)_y$ composition, epitaxially grown on silicon substrates. Such multi-component alloys comprise several semiconductor elements of different bandgaps and ionization strengths that may be engineered to blend together in an array of permutations to yield a required set of electronic and optical properties. Insertion of $GaAs_{1-\delta}Bi_\delta$, for instance, provides deep-level isovalent dopants that serve essentially to redefine the valence band edge along with augmenting infrared absorption. Wide-bandgap response is brought into the matrix with ZnSe and Ge_2 atoms provide long-wavelength sensitivity in virtue of lower bandgap response.

Among the distinctive features of the solid solutions of this kind is the occurrence of nano-objects based on $GaAs_{1-\delta}Bi_\delta$ components incorporated into films, as inferred from the occurrence of intermediate states in the photosensitivity spectrum. Nanoscale structures are responsible for creating localized energy states, which alter the energy band diagram of the heterostructure and develop new channels of photon absorption. These features lead to increased selective photosensitivity, especially in the visible and infrared regions of the spectrum. Such selectivity also arises due to variations in ionization energy of covalent bonds of the element constituting it, producing uneven energy levels as well as specific optical transitions.

Through detailed experimental analysis, this research demonstrates the potential of $(Ge_2)_{1-x-y}(ZnSe)_x(GaAs_{1-\delta}Bi_\delta)_y$ heterostructures as high-performance photoactive materials. Their ability to operate efficiently across a wide spectral range, including both infrared and visible regions, highlights their suitability for next-generation optoelectronic applications [5]. Additionally, the use of silicon substrates ensures compatibility with existing semiconductor processing technologies, further enhancing the practical relevance of the findings.

Cite as: A.Y. Boboev, U.R. Karimberdiev, N.Y. Yunusaliyev, J.S. Madaminov, East Eur. J. Phys. 3, 314 (2025), https://doi.org/10.26565/2312-4334-2025-3-29
© A.Y. Boboev, U.R. Karimberdiev, N.Y. Yunusaliyev, J.S. Madaminov, 2025; CC BY 4.0 license

We believe that the understanding gained in this work provides new insights to the mechanistics of impurity induced spectral tuning and nanostructure enhanced photoresponse. This work is part of the larger field of semiconductor device engineering, enabling the design of bespoke materials with controlled band structures and localized optoelectronic properties. The findings highlight the potential of such heterostructures in high-performance photovoltaic devices, infrared sensors and phase-locked photonic integrated circuits, where it is crucial to independently control the charge carrier properties and spectral sensitivity.

MATERIALS AND METHODS

Silicon wafers with a radius of 10 mm and an approximate thickness of 350 µm were used as substrates. These wafers had a specific resistivity of 10 Ω·cm, a charge carrier concentration of $4.4\cdot10^{14}$ cm^{-3}, and carrier mobility of 1439 $cm^2/(V\cdot s)$. The possibility of obtaining high-quality solid solutions was established by controlling the thickness of the epitaxial films, the initial and final crystallization temperatures, as well as the cooling rate. Based on preliminary electron microscopic investigations, optimal technological conditions were determined: the initial crystallization temperature of the layers was set at 750°C, the crystallization rate of the epitaxial layers was υ_k = 0.15 µm/min, and the forced cooling rate was 1°C/min.

The initial electrophysical properties of $(Ge_2)_{1-x-y}(ZnSe)_x(GaAs_{1-\delta}Bi_\delta)_y$ epitaxial films were measured at room temperature using the Van der Pauw method. The type of electrical conductivity was identified using a thermal zone and the Hall constant. It was established that undoped films exhibited predominantly p-type (hole) conductivity. Measurements revealed that at room temperature, the specific resistivity, charge carrier concentration, and mobility of the epitaxially grown films were approximately 10 Ω·cm, $1.8\cdot10^{15}$ cm^{-3}, and 368 $cm^2/V\cdot s$, respectively. Furthermore, based on the preliminary electrophysical parameters, the mobility of minority carriers was estimated to be 4673 $cm^2/V\cdot s$.

Ohmic contacts for the $(Ge_2)_{1-x-y}(ZnSe)_x(GaAs_{1-\delta}Bi_\delta)_y$ heterostructures were formed using gold (Au) and silver (Ag). The ohmic nature of these contacts was initially confirmed using a characterograph, followed by voltage drop and resistance measurements. Taking into account the p-type conductivity of the $(Ge_2)_{1-x-y}(ZnSe)_x(GaAs_{1-\delta}Bi_\delta)_y$ solid solutions, optimal ohmic contacts with low resistance and linear I–V characteristics were obtained by thermally evaporating Au and Ag onto the epitaxial surface at 150°C under vacuum conditions.

The spectral dependence of the photosensitivity of the resulting n-Si–p $(Ge_2)_{1-x-y}(ZnSe)_x(GaAs_{1-\delta}Bi_\delta)_y$ heterostructures was investigated using an optical spectrometer equipped with a CARL ZEISS JENA monochromator and quartz optics. This setup allowed for the study of the samples within the photon energy range of 1 to 3 eV.

RESULTS AND DISCUSSION

Figure 1 presents the photosensitivity spectrum of n-Si–p $(Ge_2)_{1-x-y}(ZnSe)_x(GaAs_{1-\delta}Bi_\delta)_y$ heterostructures based on epitaxial layers with a thickness of approximately 10 µm. For comparative analysis, the spectrum of a reference n-Si–p-Si structure is also shown (Figure 1, Spectrum 2). The comparison reveals that the presence of ZnSe and $GaAs_{1-\delta}Bi_\delta$ compounds within the epitaxial layers shifts the sensitivity spectrum toward shorter wavelengths (higher photon energies, $E_{ph} \geq 1.45$ eV), while the incorporation of Ge atoms causes a redshift toward longer wavelengths.

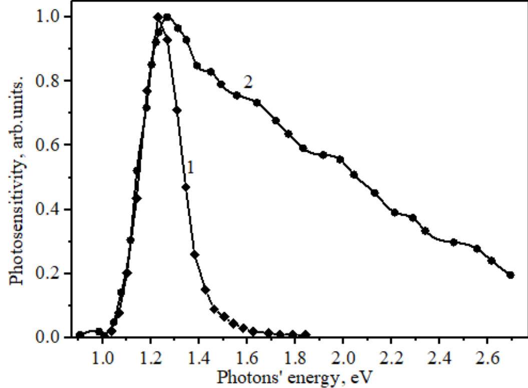

Figure 1. Photosensitivity spectra of the n-Si–p-($(Ge_2)_{1-x-y}(ZnSe)_x(GaAs_{1-\delta}Bi_\delta)_y$ (1) and n-Si-p-Si (2) structures

The maximum photosensitivity peak is observed at a photon energy of 1.26 eV (Figure 1, Spectrum 1), which suggests that the heterostructure includes a thin Ge buffer layer on the silicon surface. Subsequent formation of the $(Ge_2)_{1-x-y}(ZnSe)_x(GaAs_{1-\delta}Bi_\delta)_y$ epitaxial layers involve partial atomic substitution between ZnSe molecules and Ge_2 atom pairs, resulting in a solid solution with a bandgap of approximately 1.26 eV. This bandgap value was experimentally determined using the following equation [6]:

$$E_{g,s.s.}=(1-x-y)E_{g,Ge}+(x)E_{g,ZnSe}+(y)E_{g,GaAs/Bi}-\xi_1(x)(1-x-y)-\xi_2(y)(1-x-y). \quad (1)$$

Here, x=0.31 and y=0.12 are the molar fractions of ZnSe and $GaAs_{1-\delta}Bi_\delta$, determined from X-ray microanalysis. The micmatch parameters between the lattice constants of Ge, ZnSe, and $GaAs_{1-\delta}Bi_\delta$ are given by

$\xi_1 = 2|a_{Ge}-a_{GaAs}| / (a_{Ge} + a_{ZnSe}) = 0.0017$ and $\xi_2 = 2|a_{Ge}-a_{GaAs/Bi}| / (a_{Ge}+a_{GaAs/Bi}) = 0.037$. For the given composition, the calculated bandgap of the $(Ge_2)_{1-x-y}(ZnSe)_x(GaAs_{1-\delta}Bi_\delta)_y$ epitaxial layers is 1.248 eV, which is in excellent agreement with the experimentally observed values.

In addition, the photosensitivity spectrum of the n-Si–p$(Ge_2)_{1-x-y}(ZnSe)_x(GaAs_{1-\delta}Bi_\delta)_y$ heterostructures exhibited several weak sensitivity peaks at photon energies of 1.45, 1.64, 1.91, 2.21, and 2.45 eV. During the spectral analysis, significant overlapping of multiple photoresponse peaks of varying intensities was observed, which is likely associated with the close proximity of the absorption energies of the film constituents.

To further explore the photoconductivity mechanicms in the n-Si–p-$(Ge_2)_{1-x-y}(ZnSe)_x(GaAs_{1-\delta}Bi_\delta)_y$ heterostructures, the photosensitivity spectrum was reanalyzed using the Gaussian approximation method implemented in Wolfram Mathematica 7. The resulting spectrum was deconvoluted into Gaussian components. The initial energy values (E_e) of each individual photopeak were selected based on the experimentally observed maximum sensitivity points on the original curve. As a result, the photosensitivity spectrum was successfully modeled using six Gaussian components with optimal fitting to the experimental and total Gaussian curves. The deviations between the calculated peak energies and the tabulated values did not exceed 0.01 eV, confirming high accuracy.

All six photopeaks corresponding to the Gaussian fits were observed in the following photon energy ranges: $E_{ph,1}$ – 0,98-1,75 eV, $E_{ph,2}$ – 1,01-2,03 eV, $E_{ph,3}$ – 1,15-2,28 eV, $E_{ph,4}$ – 1,34-2,52 eV, $E_{ph,5}$ – 1.75-2.71 and $E_{ph,6}$ – 2.1-2,77 eV

The corresponding maximum sensitivity peaks were identified at 1.23, 1.45, 1.64, 1.91, 2.21, and 2.45 eV, respectively (Figure 2).

As seen in Figure 2, the primary Gaussian curve's (dashed line 1) onset at 0.98 eV suggests a shallow level, which can be explained by covalent bonding resulting from a partial substitution of ZnSe molecules and Ge_2 atomic pairs during the early stage of the Ge buffer layer crystallization and the latter epitaxy portion [7]. Also, research works [8] has pointed out that atoms of Zn, in particular, which are constituent of the germanium layer, as well as the other Zinc along with Molecule of Selenium, are able to act as recombination centers bearing acceptor type features, which corresponds with a very large increase of sensitivity to the spectrum starting at approximately 1.0 eV. Also, in another study [9], it was noted that minor atomic substitution between the molecules of ZnSe and pairs of Ge_2 causes the spontaneous formation at nanocrystals with variable dimension and shape positioned in regions of the crystal lattice with a high density of defects. Related study [10] reported an energy level in the 1.23 eV region in the bandwidth of absence of $(GaAs)_{1-x-y}(ZnSe)_x$ structures. This energy matches with what has been identified as the first maximum of the first Gaussian component in our work. In addition, other literature [11] has also indicated that nanocrystals of ZnSe implanted in monocrystals of germanium produce levels of energy which are similar to acceptor.

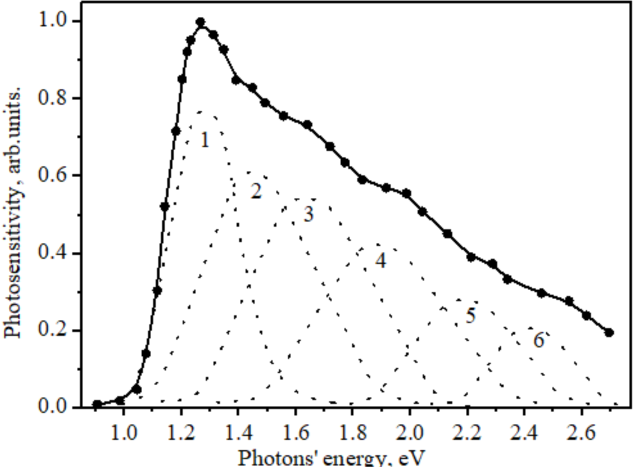

Figure 2. Photosensitivity spectrum of n-Si–p-$(Ge_2)_{1-x-y}(ZnSe)_x(GaAs_{1-\delta}Bi_\delta)_y$ heterostructures in Gaussian approximation; - experimental points – solid line – general Gaussian approximation line; continuous (dotted) lines – general Gaussian approximation line organizers

The maximum of the second Gaussian component (Figure 5.4.2, dashed line 2) was observed at a photon energy of 1.53 eV. This corresponds to the known photoluminescence range of p-GaAs crystals, typically within 1.35–1.65 eV, and confirms their spectral contribution to the heterostructure's response [12]

The third Gaussian component showed its peak sensitivity at 1.64 eV (Figure 2, dashed line 3), which can be attributed to the formation of isovalent Ge–Se valence-band-related impurity states in the GaAs layers. The study [13] reported three distinct photoresponse peaks in GeSe-doped GaAs layers at 1.43, 1.63, and 2.25 eV, all of which were also observed in the current study. Among these, the first peak in our sample shifted toward longer wavelengths, while the second peak matched the third Gaussian component at 1.64 eV.

Two additional Gaussian components were identified in the photosensitivity spectrum of the n-Si-p-$(Ge_2)_{1-x-y}(ZnSe)_x(GaAs_{1-\delta}Bi_\delta)_y$ heterostructure within the 1.34–3.71 eV photon energy range, showing maximum

photoresponse at 1.91 eV and 2.21 eV (Figure 2, dashed lines 4 and 5). According to [14] the photoluminescence spectrum of $(GaAs)_{1-x}(ZnSe)_x$ solid solutions grown by liquid-phase epitaxy spans almost the entire visible spectrum (400–760 nm). Moreover, [15] identified deep energy levels associated with GaSe ($h\nu_{max}$ = 1.88 eV), ZnAs ($h\nu_{max}$ = 2.15 eV), and ZnSe ($h\nu_{max}$ = 2.69 eV). In the present study, three photoresponse peaks were detected at 1.91 eV and 2.21 eV, suggesting that atomic-scale modifications of GaSe and ZnAs within the crystal lattice may be responsible for the observed spectral shifts toward shorter wavelengths.

Furthermore, a sixth Gaussian peak was observed at 2.45 eV. Although the bandgap energy of pure ZnSe is $E_{g,ZnSe}$ = 2.70 eV, in these solid solutions, covalent bonds within ZnSe molecules are weakened due to interaction with Ge_2 and $GaAs_{1-\delta}Bi_\delta$ components. This interpretation is consistent with findings by Zainabidinov et al. [16], who reported that in such solid solutions, tetrahedral ZnSe crystal structures undergo partial substitution with GaAs or Ge_2, thereby weakening Zn–Se bonds due to interactions with Ga, As, and Ge atoms. Additional support comes from Saidov et al. [17], who observed that continuous substitution in $(GaAs)_{1-x}(ZnSe)_x(Ge_2)_y$ leads to the emergence of impurity states below the valence band edge ($\Delta E_i = E_{ph} - Eg_{,t-r}$) of ZnSe. Given ZnSe's direct bandgap nature and its molar concentration in the present material (~10^{20} cm^{-3}), these structures exhibit photosensitivity at photon energies above 2.4 eV.

CONCLUSIONS

The n-Si–p-$(Ge_2)_{1-x-y}(ZnSe)_x(GaAs_{1-\delta}Bi_\delta)_y$ heterostructures showed results of spectral photosensitivity analyses which suggest that the $(Ge_2)_{1-x-y}(ZnSe)_x(GaAs_{1-\delta}Bi_\delta)_y$ solid solutions have selective photosensitivity because of integrated ZnSe and Ge constituents and the ionic bond covalent energies' differences in their ionization. The energy band diagram reveals the presence of impurity-related states that indicate the existence of nano-objects based on on $GaAs_{1-\delta}Bi_\delta$ compounds within the films. In conclusion, these results prove that the obtained solid solutions are likely barrier-layer structures and can also be utilized as selective photoactive materials for hyper/MW and visible optoelectronic devices in the infrared radiation spectrum.

Conflict of Interests

The authors declare that they have no conflict of interests.

Funding

The present research work was financed under the project FZ-292154210 granted by the Ministry of Innovative Development of the Republic of Uzbekistan.

ORCID

Akramjon Y. Boboev, https://orcid.org/0000-0002-3963-708X; **Nuritdin Y. Yunusaliyev**, https://orcid.org/0000-0003-3766-5420 **Ulugbek R. Kariberdiev**, https://orcid.org/0009-0002-9421-938X; **Jamshidbek S. Madaminov**, https://orcid.org/0009-0001-3786-4457

REFERENCES

[1] S.Z. Zainabidinov, A.S. Saidov, M.U. Kalanov, and A.Y. Boboev, "Synthesis, Structure and Electro-Physical Properties of n-GaAs-p-$(Ge_2)_{1-x-y}(ZnSe)_x(GaAs_{1-\delta}Bi_\delta)_y$ Heterostructures," Applied Solar Energy, **55**(5), 291–308 (2019). https://doi.org/10.3103/S0003701X1905013X

[2] L. Yu. *et al.*, "First Principles Study on Electronic Structure and Optical Properties of Ternary GaAs:Bi Alloy," Materials, **5**(12), 2486–2497 (2012). https://doi.org/10.3390/ma5122486

[3] D.C. Li, M. Yang, S.Z. Zhao, Y.Q. Cai and Y.P. Feng, "First Principles Study of Bicmuth Alloying Effects in GaAs Saturable Absorber," Optics Express, **20**, 11574–11580 (2012). https://doi.org/10.1364/oe.20.011574

[4] A.Y. Boboev, "Photoelectric Characteristics of the Heterojunction n-GaAs-p-$(Ge_2)_{1-x-y}(ZnSe)_x(GaAs_{1-\delta}Bi_\delta)_y$," East European Journal of Physics, (3), 298–302 (2024). https://doi.org/10.26565/2312-4334-2024-3-31

[5] A.S. Saidov, S.Z. Zainabidinov, M.U. Kalanov, A.Y. Boboev and B.R. Kutlimurotov, "Peculiarities of Photosensitivity of n-(GaAs)-p-($(Ge_2)_{1-x-y}(ZnSe)_x(GaAs_{1-\delta}Bi_\delta)_y$ Structures with Quantum Dots," Applied Solar Energy, **51**(3), 206–208 (2015). https://doi.org/10.3103/S0003701X15030111

[6] S. Zainabidinov, A.Y. Boboev and N.Y. Yunusaliyev, "Effect of γ-Irradiation on Structure and Electrophysical Properties of S-Doped ZnO Films," East European Journal of Physics, (2), 321–326 (2024). https://doi.org/10.26565/2312-4334-2024-2-37

[7] D. Stark, *et al.*, "THz Intersubband Electroluminescence from n-Type Ge/SiGe Quantum Cascade Structures," Applied Physics Letters, **118**, 101101 (2021). https://doi.org/10.1063/5.0041327

[8] H. Tang-Wang, *et al.*, "Study of the Type-I to Type-II Band Alignment Transition in InAs(Sb)/GaAs Quantum Dot Nanostructures," Optical Materials, **134**, 113156 (2022). https://doi.org/10.1016/j.optmat.2022.113156

[9] S. Zainabidinov, Sh. Utamuradova and A. Boboev, "Structural Peculiarities of the $(ZnSe)_{1-x-y}(Ge_2)_x(GaAs_{1}–\delta Bi\delta)_\gamma$ Solid Solution with Various Nanoinclusions," Journal of Surface Investigation: X-ray, Synchrotron and Neutron Technique*s*, **16**, 1130–1134 (2022). https://doi.org/10.1134/S1027451022060593

[10] A.A. Reznitsky, A. Klochikhina, and M. Eremenko, "Thermally Activated Resonance Tunneling in Asymmetric Systems of CdSe/ZnSe Double Quantum Wells with Self Assembled Quantum Dots," Semiconductors, **48**(3), 345 (2014). https://doi.org/10.1134/S1063782614030221

[11] S. Suprun, V. Sherstyakova and E. Fedosenko, "Epitaxial Growth of ZnSe on GaAs with the Use of the ZnSe Compound as the Source," Semiconductors, **43**(11), 1526–1531 (2009). https://doi.org/10.1134/S1063782609110220

[12] N. Papez, R. Dallaev, S. Talu and J. Kastyl, "Overview of the Current State of Gallium Arsenide-Based Solar Cells (Review)," Materials, **14**, 3075 (2021). https://doi.org/10.3390/ma14113075

[13] S. Zainabidinov, A. Saidov, A. Boboev and D. Abdurahimov, “Structure, Morphology and Photoelectric Properties of n-GaAs-p-$(GaAs)_{1-x}(Ge_2)_x$ Heterostructure,” Herald of the Bauman Moscow State Technical University, Series Natural Sciences, **100**(1), 72–87 (2022). https://doi.org/10.18698/1812-3368-2022-1-72-87

[14] V.Ya. Aleshkin, *et al*., “1.3 µm Photoluminescence of Ge/GaAs Multi-Quantum-Well Structure,” Journal of Applied Physics, **115**, 043512 (2014). https://doi.org/10.1063/1.4863121

[15] S. Suprun, V. Sherstyakova and E. Fedosenko, “Epitaxial Growth of ZnSe on GaAs with the Use of the ZnSe Compound as the Source,” Semiconductors, **43**(11), 1526–1531 (2009). https://doi.org/10.1134/S1063782609110220

[16] S. Zainabidinov, A. Saidov, M. Kalanov and A. Boboev, “Synthesis, Structure and Electro-Physical Properties of n-GaAs–p-$(Ge_2)_{1-x-y}(ZnSe)_x(GaAs_{1-\delta}Bi_\delta)_y$ Heterostructures (Review),” Applied Solar Energy, **55**, 291–308 (2019). https://doi.org/10.3103/S0003701X1905013X

[17] S. Saidov, A.Yu. Leiderman, Sh.N. Ucmonova and U.P. Asatova, “Peculiarities of the Current–Voltage Characteristic of n-GaP-p-$(InSb)_{1-x}(Sn_2)_x$ Heterostructures,” Technical Physics Letters, **46**(11), 1124–1127 (2020). https://doi.org/10.1134/S1063785020110279

ФОТОЕЛЕКТРИЧНІ ВЛАСТИВОСТІ ГЕТЕРОСТРУКТУР *n*-Si–*p*-$(Ge_2)_{1-x-y}(ZnSe)_x(GaAs_{1-\delta}Bi_\delta)_y$

Акрамджон Й. Бобоєв, Улугбек Р. Карімбердієв, Нурітдін Й. Юнусалієв, Джамшидбек С. Мадамінов
Андижанський державний університет імені З.М. Бабура, Андижан, Узбекистан

У цій статті досліджуються фотоелектричні властивості твердих розчинів $(Ge_2)_{1-x-y}(ZnSe)_x(GaAs_{1-\delta}Bi_\delta)_y$, вирощених на кремнієвих підкладках. Встановлено, що тверді розчини $(Ge_2)_{1-x-y}(ZnSe)_x(GaAs_{1-\delta}Bi_\delta)_y$ мають селективну фоточутливість завдяки наявності компонентів ZnSe, Ge_2 та $GaAs_{1-\delta}Bi_\delta$, а також різниці в енергії іонізації їх ковалентних зв'язків. Механізми фотопровідності в гетероструктурах n-Si-p-$(Ge_2)_{1-x-y}(ZnSe)_x(GaAs_{1-\delta}Bi_\delta)_y$ були проаналізовані на основі значень Ei, які забезпечили найкраще наближення до експериментального спектру та кривих гауссового наближення. Фотопіки, що відповідають гауссовим кривим на рівнях енергії 1,23 еВ, 1,45 еВ, 1,64 еВ, 1,91 еВ, 2,21 еВ та 2,45 еВ, спостерігалися в діапазоні енергій фотонів: $E_{ph,1}$ - 0,98÷1,75 еВ, $E_{ph,2}$ - 1,01÷2,03 еВ, $E_{ph,3}$ - 1,15÷2,28 еВ, $E_{ph,4}$ - 1,34÷2,52 еВ, $E_{ph,5}$ - 1,75÷2,71 еВ та $E_{ph,6}$ - 2,1÷2,77 еВ. Спостереження проміжних станів у спектрі фоточутливості цього твердого розчину підтвердило наявність нанооб'єктів, сформованих на основі молекул ZnSe та Ge_2, а також сполук $GaAs_{1-\delta}Bi_\delta$ у цих плівках. Було виявлено, що тверді розчини $(Ge_2)_{1-x-y}(ZnSe)_x(GaAs_{1-\delta}Bi_\delta)_y$ мають потенціал для використання як селективні фотоактивні матеріали, що працюють у діапазонах інфрачервоного та видимого випромінювання.

Ключові слова: *кремній; твердий розчин; сполука $GaAs_{1-\delta}Bi_\delta$; ковалентний зв'язок; фоточутливість*

EAST EUROPEAN JOURNAL OF PHYSICS. 3. 319-324 (2025)
DOI:10.26565/2312-4334-2025-3-30 ISSN 2312-4334

SURFACE MORPHOLOGY AND ROUGHNESS OF SULFUR-DOPED ZnO THIN FILMS: ANALYSIS BASED ON ATOMIC FORCE MICROSCOPY

Akramjon Y. Boboev[a], Nuritdin Y. Yunusaliyev[a], Khushroy A. Makhmudov[b], Fayzuloh A. Abdulkhaev[a], Gaybullo G. Tojiboyev[a], Mohlaroyim O. G‘ofurjonova[a]
[a]*Andijan state university named after Z.M. Babur, Andijan, Uzbekistan*
[b]*Kokand University Andijan branch, Andijan, Uzbekistan*
**Corresponding Author E-mail: aboboevscp@gmail.com*
Received March 30, 2025; revised July 9, 2025; accepted July 20, 2025

The surface morphology of undoped ZnO as well as 3 at. % sulfur-doped ZnO (ZnO:S) thin films were examined utilizing atomic force microscopy (AFM). Surface characteristics evaluations and comparisons were made based on 2D and 3D AFM images, line profile analyses, and roughness parameters; R_a, R_q, R_z, R_t R_{sk}, and R_{ku}. The undoped ZnO medium showed a smooth surface, with moderate height fluctuations and a comparatively narrow Gaussian-like height. On the other hand, ZnO:S film showed much higher surface roughness and topographical alternation with larger and more symmetrical height histograms. Both the R_q/R_a ratios for both started at around the theoretical Gaussian value (~1.25) with the skewness and kurtosis parameters showing distinctly different degrees of surface symmetry and texture. Sulfur incorporation was shown to change the grain morphology, to introduce peak-to-valley contrast and to increase the overall surface area. The morphological improvements further show that ZnO:S thin films could be more adequate for applications where high surface activity is essential, provided by gas sensing and catalysis. This study presents a quantitative and qualitative evaluation of the influence of sulfur doping on the surface morphology of ZnO at the nanoscale level.
Keywords*: Morphology; Histogram; Atomic force microscopy; Roughness; Doping; Sulfur*
PACS: 78.30.Am

INTRODUCTION

Thin films of zinc oxide (ZnO) have been extensively studied for their diverse applications in optoelectronics, gas sensors, catalysts, and so on, because of their excellent optical, electrical, and catalytic properties [1–3]. The surfaces have a key influence on their performance as they affect surface area, grain boundaries, and active sites for surface reactions [4,5]. Atomic force microscopy (AFM) is a proven dominant tool for the morphological characterization of surfaces that offers the images of surface textures in nanoscale and also allows a quantitative determination of surface roughness parameters [6,7]. Dopants like Al, S, and N into ZnO thin films were also studied which had considerable implications on the structural, electrical, and optical properties [8–11]. Especially, the sulfur doping can increase the surface area and modify the grain boundaries of ZnO, which can improve the gas-sensing property and catalytic activity [12,13]. Zainabidinov et al. investigated the influence of gamma radiation on the electrophysical characteristics of sulfur-doped ZnO films, noting that irradiation caused structural changes [14]. Likewise, structural and morphological properties of Al-doped ZnO films have been studied and it has been exhibited that the doping in ZnO causes a change in the grain size and its distribution [15]. Additional studies performed in our laboratory focused on elucidating structural properties by means of X-ray diffraction and electron microscopy, demonstrating significant morphological changes produced by sulfur doping in ZnO films synthesized by ultrasonic spray pyrolysis [16]. Moreover, Zainabidinov et al. have tuned an ultrasonic spray pyrolysis system for the deposition of metal oxide films with improved uniformity and structure [17]. Other investigations have elucidated defect formation in metal-insulator-semiconductor (MIS) structures based on silicon doped with rare-earth elements, potentially up to moderate concentrations, opening the pathway for understanding how doping modifies morphological and electrophysical properties. However, notwithstanding a number of studies, a broad statistical description of the morphological differences amongst undoped and sulfur-doped ZnO thin films at the nanoscale is undocumented. More advanced characterizations employing amplitude parameters like average roughness (Ra), root mean square roughness (Rq), skewness (Rsk), kurtosis (Rku), and peak-to-valley height (Rt) are required to provide a complete understanding of surface structure–function relationships. This paper studies the influence of sulfur doping on those surfaces using atomic force microscopy (AFM), in an effort to fill this gap in the literature. In summary, by carefully analyzing statistical parameters of surface roughness and relating them with probable functional dynamism, this work sheds valuable light in pathways for future exploration and evolution of ZnO materials for emerging technological domains.

MATERIALS AND METHODS

As the base material, monocrystalline n-type silicon (Si) wafers with a (100) crystallographic orientation were selected due to their high purity and compatibility with thin film deposition. The wafers were cut into rectangular pieces measuring

Cite as: A.Y. Boboev, N.Y. Yunusaliyev, Kh.A. Makhmudov, F.A. Abdulkhaev, G.G. Tojiboyev, M.O. G‘ofurjonova, East Eur. J. Phys. 3, 319 (2025), https://doi.org/10.26565/2312-4334-2025-3-30
© A.Y. Boboev, N.Y. Yunusaliyev, Kh.A. Makhmudov, F.A. Abdulkhaev, G.G. Tojiboyev, M.O. G‘ofurjonova, 2025; CC BY 4.0 license

approximately 2 mm × 2 mm × 5 μm for experimental use. To improve surface smoothness and cleanliness, a multi-step treatment was performed. Initially, the substrate surface was mechanically polished using abrasive papers with 3 μm and 0.5 μm grit sizes, sequentially. This process significantly reduced the surface roughness. After polishing, substrates were rinsed with deionized (DI) water. To remove organic, inorganic, and metallic contaminants, the wafers were subjected to standard RCA cleaning. In the RCA-1 step, substrates were immersed in an $NH_4OH:H_2O_2:H_2O$ (1:1:5) solution at ~75 °C for 15 minutes, followed by thorough DI water rinsing. The RCA-2 step involved immersion in $HCl:H_2O_2:H_2O$ (1:1:6) at the same temperature and duration to eliminate metal ions. Finally, the native SiO_2 oxide layer on the wafer surface was etched in a 5% HF solution for 1 minute, and the cleaned substrate was immediately rinsed and dried to prevent reoxidation. Zinc acetate dihydrate ($Zn(CH_3COO)_2{\cdot}2H_2O$, >99%, Sigma-Aldrich) was used as the zinc source. For the undoped ZnO films, precursor solutions of 0.5 M and 1 M concentrations were prepared by dissolving the appropriate amount of zinc acetate in deionized water and stirring until complete dissolution. Specifically, 10.97 g of $Zn(CH_3COO)_2{\cdot}2H_2O$ was dissolved in 100 mL of DI water to obtain a 0.5 M solution. For sulfur doping, thiourea (CH_4N_2S, >99%, Sigma-Aldrich) was used as the sulfur source. A doping concentration of 3 atomic percent (at%) was targeted by calculating the required thiourea amount relative to the total anion content in the solution. Based on a 1:1 molar ratio of Zn to O in ZnO, 0.0015 mol of sulfur atoms were needed for 3 at% doping, which corresponds to approximately 0.114 g of thiourea for 0.05 mol of Zn precursor. Thiourea was added to the prepared zinc acetate solution and stirred thoroughly to ensure homogeneity. Thin films of ZnO and sulfur-doped ZnO (ZnO:S) were deposited on the prepared Si substrates using the ultrasonic spray pyrolysis technique [17]. The deposition was performed under controlled conditions, with optimized parameters for spray rate, substrate temperature, and carrier gas flow (not detailed here). Immediately after the HF etching step, substrates were transferred for coating to minimize surface reoxidation and maintain chemical reactivity.

Atomic Force Microscopy (AFM) was used to analyze the surface morphology and topography of the deposited films. 2D and 3D AFM images were acquired over a 500 × 500 nm scan area. Roughness parameters such as R_a, R_q, R_t, and R_z were calculated, along with statistical descriptors like skewness (R_{sk}) and kurtosis (R_{ku}). Additionally, line profiles and histogram analyses were used to assess height distribution symmetry and uniformity across the samples.

RESULTS AND DISCUSSION

2D AFM Images of Surface Morphology for Undoped ZnO and 3 at. Topography images of ZnO:S thin films with a concentration of 3 at.% sulfur, obtained on an area of 500 nm × 500 nm scale (Figure 3 but with two samples showed in comparison), show fundamental differences in surface structure. The surface of undoped ZnO film is smoother and more uniform, with larger grains available, lacking noticeable grain boundaries. This means that the crystallites merged into a surface with a much lower height difference during the film growth. This sample shows low surface roughness, suggesting that the height across the scanned point is not fluctuating heavily. In sharp contrast to this, the ZnO:S sample shows a highly textured surface and well separated fine nanograins that are very densely packed. You have multi-grain with smaller size, which can lead to a surface structure that is more heterogeneous and complex. The improved nanostructuring is probably a result of the effects of sulfur doping on the nucleation kinetics during the formation of the film, leading to a higher amount of nucleation centers. The distinct morphologies suggest that the sulfur doping has a strong influence on the surface growth of the ZnO films, which results in denser coalescence of the grains, sharper grain boundaries, and higher surface area. In-contrast to pure ZnO, where the surface activity is depicted by a relatively low rate of charge reaction, several such modifications have been reported introducing higher surface-related functionalities, making ZnO:S more favorable in the context of high surface activity applications.

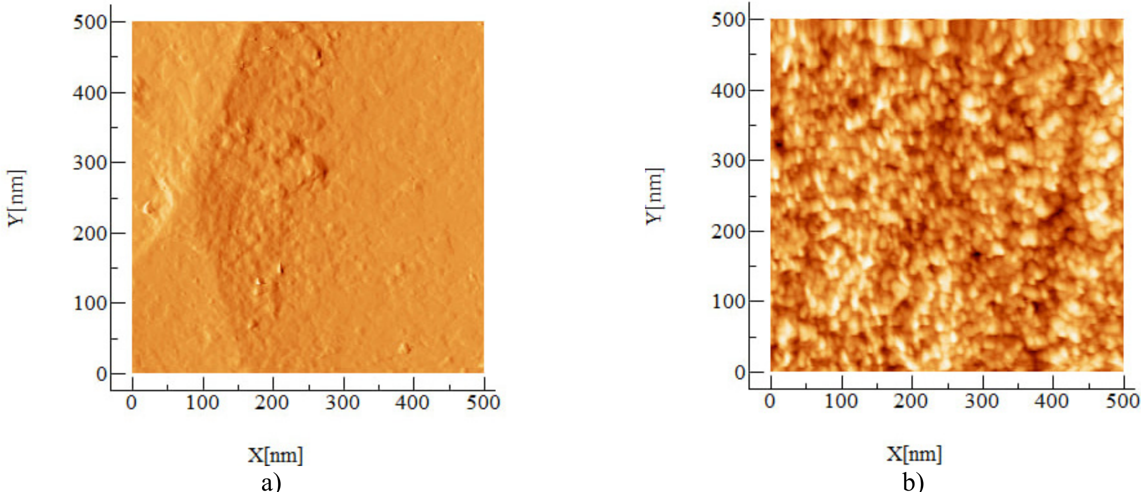

Figure 3. 2D AFM surface morphology images of thin films scanned over a 500 nm × 500 nm area. a) ZnO; b) S doped ZnO

Figure 4 shows 3D AFM topography images will reveal even more details of the surface features for each sample. The 3D perspectives give a better sense of peak-to-valley height differences as well as surface texture roughness.

A typical moderately textured surface can be seen in the undoped ZnO film featuring a clear grain elevation although the features seem less defined and broader. There are fewer grain peaks which are also more widely separated from each other, which is consistent with the earlier identification of a relatively smooth, low-roughness morphology. Contrasting with it, the rough surface of ZnO:S film, with an arrangement of sharp peaks and valleys uniformly in the scanned area, is very noticeable. The nanograins are smaller, denser, and well separated which assists in better vertical variation in the Z-axis. Higher density of nucleation sites during film growth arising from incorporation of sulfur leads to again higher surface roughness as indicated here. ZnO:S provides a highly complex surface with an increased surface area which should have functional benefits. The enhanced light scattering, increased surface reactivity and better sensitivity of the rougher and rougher morphology in optoelectronic and sensing applications [18].

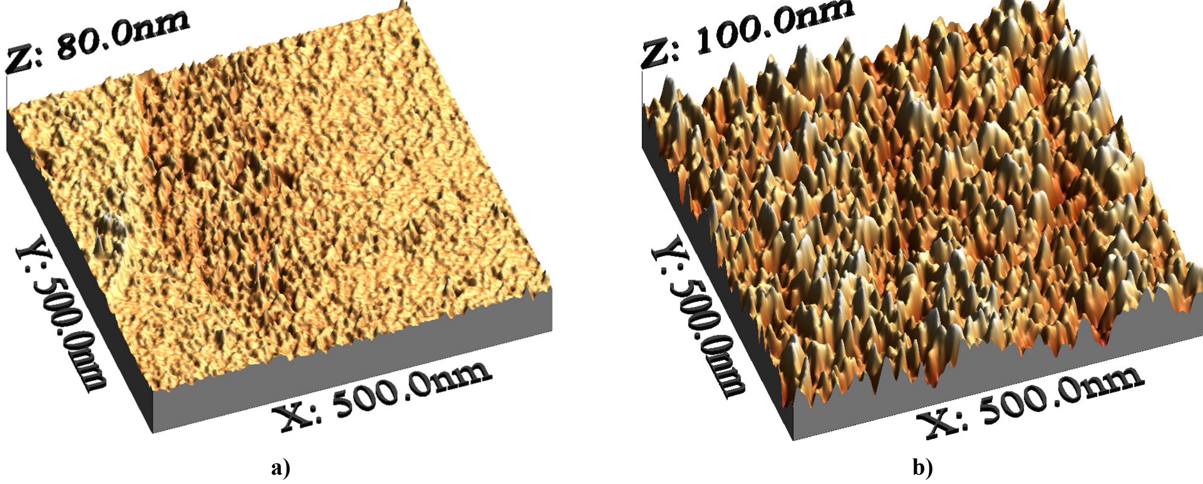

Figure 4. 3D AFM topography of ZnO and ZnO:S thin films over a 500 nm × 500 nm area, revealing differences in vertical surface features and roughness. a) ZnO; b) S doped ZnO

Before delving into the quantitative surface profile results, it is essential to understand the key amplitude parameters used in AFM surface topography analysis. These parameters provide critical insights into the statistical features of a surface, including average height levels, asymmetry, and extreme height variations. One of the most widely used metrics is the average roughness (R_a), which quantifies the mean deviation from the central line and serves as a general indicator of surface uniformity and quality. The root mean square roughness (R_q) provides a more sensitive measure by considering the squared deviations from the mean line and is particularly important in high-precision optical surface evaluation. The maximum peak-to-valley height (R_t) defines the total relief of the surface and indicates the full vertical range of topographic variation. In contrast, the ten-point height roughness (R_z) calculates the average difference between the five highest peaks and the five deepest xvalleys, making it suitable for assessing local irregularities. To evaluate the shape and symmetry of the height distribution, skewness (R_{sk}) and kurtosis (R_{ku}) are employed. A negative R_{sk} implies a surface dominated by valleys, while a positive Rsk suggests dominant peaks. The kurtosis R_{ku} indicates whether the surface texture is spiky ($R_{ku} > 3$), flat and bumpy ($R_{ku} < 3$), or normally distributed ($R_{ku} \approx 3$). Together, these parameters form a comprehensive statistical framework to evaluate and compare surface characteristics across thin film samples.

Table 1 demonstrates that the changes in average roughness (R_a) and ten-point mean height (R_z) correspond closely with the variations observed in RMS roughness (R_q) across all examined samples. The maximum peak-to-valley height (R_t) remains a key indicator of surface topography, as it effectively captures the overall vertical relief of the surface. Furthermore, it is evident from Table 1 that higher R_t values are typically associated with increased R_z values, indicating a strong relationship between R_z and the extreme height differences in the surface profile. The mathematical expression for R_z is given below:

$$R_z = \frac{1}{n}\left(\sum_{i=1}^{n} P_i - \sum_{i=1}^{n} V_i\right) \tag{1}$$

where n is the number of sampling points along the assessment length, which is 5 in this study, P_i is the height of the ith peak and V_i is the depth of the ith valley with respect to the line profile. In addition, R_q values for all the samples are higher than Ra values, which can be mathematically explained according to the following equation:

$$R_z = \frac{1}{L}\int_0^L |y(x)|\, dx \tag{2}$$

$$R_q = \sqrt{\frac{1}{L}\int_0^L |(y(x))^2|\, dx} \tag{3}$$

where L is the length of the profile on the x-axis used for measurement and y(x) is the variation of the height from the profile line for each data point.

For surfaces exhibiting Gaussian height distributions, theoretical models suggest that the ratio of root mean square roughness (R_q) to average roughness (R_a) approaches a value of 1.25. According to Ward [19], many engineering surfaces can be reasonably approximated by a Gaussian distribution, with typical R_q/R_a ratios extending up to around 1.31. In our study, as shown in Table 1, the calculated R_q/R_a values for all three materials—Si, ZnO, and ZnO:S—are in close agreement with the theoretical prediction, indicating that the surface profiles follow an approximately Gaussian distribution at the nanometer scale. his finding validates the use of standard statistical surface roughness descriptors in characterizing the samples. Additionally, the skewness values provide insight into the asymmetry of the height distribution. Negative skewness reflects a surface dominated by valleys, while positive skewness indicates a prevalence of elevated features. In our results, skewness variations between the samples suggest different degrees of surface uniformity and grain structure. Furthermore, the kurtosis (R_{ku}) parameter reveals the nature of surface texture—whether it is spiky or bumpy. A value of R_{ku} less than 3 corresponds to a bumpy surface with fewer extreme features, while R_{ku} greater than 3 indicates a spikier texture with pronounced peaks and valleys. For instance, the ZnO:S sample demonstrated a R_{ku} value close to 3, suggesting a balanced distribution of surface features, whereas undoped ZnO exhibited a higher R_{ku}, indicative of a more irregular and spiky morphology. These trends are consistent with the R_t and R_z values, as kurtosis is strongly influenced by the amplitude of surface extremes.

$$R_{ku} = \frac{1}{NR_q^4}\left(\sum_{i=1}^{N} Y_i^4\right) \quad (4)$$

Where R_{ku} is the RMS roughness parameter and Y is the height of the profile at point number i

Table 1. Roughness parameters.

Materials	R_a nm	R_q nm	R_t nm	R_z nm	R_q/R_a	R_{sk}	R_{ku}
ZnO	2.5976	3.7144	79.9983	43.6536	1.4299	-0.6842	8.2098
S doped ZnO	8.4809	10.8674	100.0075	49.9415	1.2814	-0.005	3.3892

Such observation is confirmed by the computed roughness parameters presented in Table 1. The S-doped ZnO sample has much larger average roughness (R_a) and root mean square roughness (R_q) values than undoped ZnO as the incorporation of sulfur clearly increases the complexity of the surface (no flake-like structure). For both samples, the R_q/R_a ratio approaches the theoretical limit of the nominal Gaussian distribution (~1.25), as evident by the ratios of 1.4299 for ZnO and 1.2814 for ZnO:S, confirming that both surfaces yield approximately the same Gaussian distribution. Values for skewness (R_{sk}) also indicate asymmetry of surface features. The ZnO film shows a negative skewness value of -0.6842, indicating a surface with deep valleys predominating. On the other hand, the near zero skewness (-0.005) of the ZnO:S film reflects an approximately even topographical structure without a strong dominance of peaks or valleys. Another parameter is kurtosis (R_{ku}), which enhances the interpretation. The high value of R_{ku} = 8.21 of ZnO sample indicates that this surface is also spiky and irregular with very extreme value of height variation. In contrast, the ZnO:S display a kurtosis value of 3.39, which is significantly closer to the Gaussian ideal ($R_{ku} \approx 3$) indicating a distribution that has more uniformity, morphology-wise, which is bumpier. This, in addition to the maximum peak-to-valley height (R_t) and ten-point roughness (R_z), confirms the topographically balanced and statistically homogeneous surface resulting from sulfur doped Si core. Such surface features can improve selected functions, like an increased surface area for sensing or catalytic interactions.

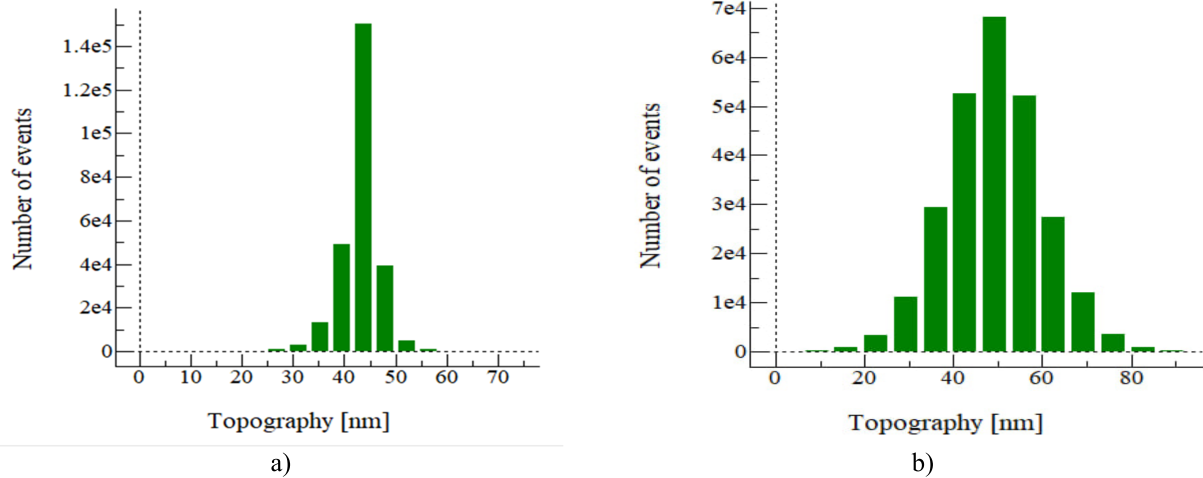

Figure 5. Height distribution histograms. a) ZnO; b) S doped ZnO

In an effort to gain insight into the statistical behavior of the surface morphology, we analyzed the height distribution histograms and numerical roughness parameters of both the ZnO and S-doped ZnO thin films. The histogram (Figure 5) provides a visual clear depiction of the distribution of topographical features on the scanned surface.

The crystalline particle size distribution of the ZnO gives a very narrow and sharply peaked distribution centered around 55 nm which means a relatively less rough surface with a relatively more even distribution. In comparison, the histogram of the S-doped ZnO sample displays a wider, more symmetrical distribution centered around 50 nm, implying a surface with more topographical deviation and a greater diversity of nanostructures.

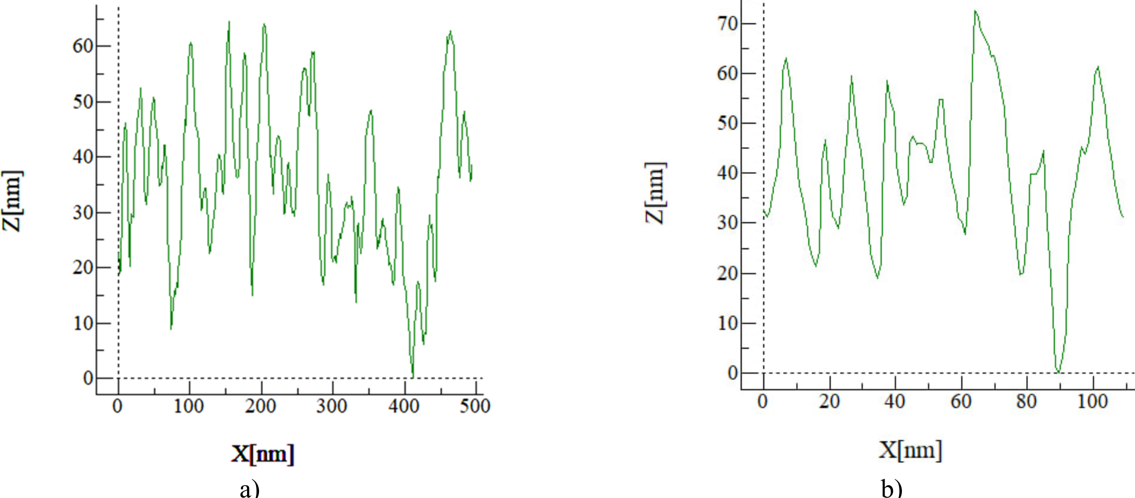

Figure 6. Line profile analysis showing the surface height fluctuations. a) ZnO; b) S doped ZnO

The line profile analysis for the as-deposited ZnO and S-doped ZnO thin films are depicted in Figure 6 and is useful to evaluate the vertical surface height variations within a span of 100 nm. Moderate variations in height (4 nm to 10 nm) can be seen in the ZnO film (Figure 6a), indicating a relatively smooth and uniform surface with minor topographical irregularities. This was also observed in the histogram data, as we saw a narrow and symmetric height distribution centered at 50 nm, indicating an overall less complex surface morphology. Compared to the ZnO:S film (Fig. 6b), which exhibits obviously bigger vertical fluctuations with a thickness of 5 nm to 25 nm. It implies that the water bodies could adjust to an increase in surface roughness indicating a surface with a more intricate structure featuring peaks and valleys. These results help confirm the above observations, as also evidenced by the broader and more symmetrical histogram distribution of the S-doped sample, indicating the more complex feature of the surface brought by the nitrogen doping. The increased height fluctuations of the ZnO:S film are due to sulfur incorporation and modification of the grain structure, increasing the surface roughness. In summary, analysis of the line profiles supports the histogram results and confirms the higher surface complexity of the ZnO:S thin films. The enhanced roughness values indicate that sulfide doping increases the surface area, potentially useful for applications such as gas sensors or catalysis, where high surface reactivity is favorable.

CONCLUSIONS

In this study, the surface morphology of ZnO and S-doped ZnO thin films was analyzed using atomic force microscopy (AFM) and key statistical parameters such as average roughness (R_a), root mean square roughness (R_q), peak-to-valley height (R_t), and skewness (R_{sk}). The results indicate a clear contrast in the surface characteristics between undoped ZnO and S-doped ZnO films. ZnO films exhibited a relatively smooth and uniform surface with moderate height variations ranging from 4 nm to 10 nm. These results were supported by the narrow height distribution observed in the histograms, indicating a less complex surface morphology. On the other hand, the ZnO:S films demonstrated significantly higher surface roughness, with height variations reaching up to 25 nm. The broader and more symmetrical histogram distribution confirmed the increased surface complexity brought about by sulfur doping. The analysis of the line profiles and histograms indicated that sulfur incorporation into ZnO modifies the grain structure and increases surface roughness. The R_q/R_a ratio for both films approached the theoretical Gaussian value, confirming the Gaussian distribution of surface height. The skewness and kurtosis values further highlighted the differences in surface symmetry and texture. ZnO:S films exhibited more pronounced surface features with balanced peaks and valleys, while ZnO films showed a dominance of valleys.

These results suggest that sulfur doping enhances the surface area and complexity of ZnO films, making them potentially more suitable for applications that require high surface reactivity, such as in gas sensing or catalytic processes. The findings provide a comprehensive understanding of how surface morphology can be tailored through doping and offer valuable insights for optimizing functional thin film applications.

Conflict of Interests

The authors declare that they have no conflict of interests

Funding

The present research work was financed under the project FZ-292154210 granted by the Ministry of Innovative Development of the Republic of Uzbekistan

ORCID
A.Y. Boboev, https://orcid.org/0000-0002-3963-708X; **N.Y. Yunusaliyev**, https://orcid.org/0000-0003-3766-5420
Kh.A. Makhmudov, https://orcid.org/0009-0004-8845-8741; **F.A. Abdulkhaev**, https://orcid.org/0009-0004-3933-5171
G.G. Tojiboyev, https://orcid.org/0009-0000-5022-8108; **M.O. G'ufurjonova**, https://orcid.org/0009-0009-8830-9371

REFERENCES

[1] Z. Zhang, Y. Chen, H. Liu, *et al*., Sens. Actuators B Chem. **344**, 130218 (2021). https://doi.org/10.1016/j.snb.2021.130218
[2] R. Kumar, and O. Al-Dossary, J. Mater. Sci. Mater. Electron. **33**, 927 (2022). https://doi.org/10.1007/s10854-021-07491-8
[3] X. Chen, H. Yu, J. Sun, *et al*., Catal. Sci. Technol. **13**, 734 (2023). https://doi.org/10.1039/D2CY01807D
[4] M. Hasanpour, S. Hatamie, and H. Zare, Appl. Surf. Sci. Adv. **2**, 100025 (2020). https://doi.org/10.1016/j.apsadv.2020.100025
[5] D. Sharma, K.M. Batoo, and S. Singh, Mater. Sci. Semicond. Process. **151**, 106986 (2022). https://doi.org/10.1016/j.mssp.2022.106986
[6] P. Eaton, and P. West, *Atomic Force Microscopy*, (Oxford University Press, 2020).
[7] S. Moreno-Flores, Prog. Mater. Sci. **120**, 100816 (2021). https://doi.org/10.1016/j.pmatsci.2021.100816
[8] A. Wei, Y. Huang, Y. Wang, *et al*., Thin Solid Films **713**, 138341 (2020). https://doi.org/10.1016/j.tsf.2020.138341
[9] H. Hamrouni, H. Saidi, and A. Bouzidi, Mater. Today Commun. **26**, 102019 (2021). https://doi.org/10.1016/j.mtcomm.2020.102019
[10] R. Mohan, and V. Krishnakumar, J. Mater. Sci. Mater. Electron. **32**, 14053 (2021). https://doi.org/10.1007/s10854-021-06044-9
[11] C. Jayachandraiah, V. Sreenivasulu, and M. Sundararajan, Optik **219**, 165051 (2020). https://doi.org/10.1016/j.ijleo.2020.165051
[12] H. J. Kim, S. Y. Kim, and J. H. Lee, Sens. Actuators B Chem. **307**, 127675 (2020). https://doi.org/10.1016/j.snb.2019.127675
[13] Y. Liu, X. Wang, and M. Zhang, J. Alloys Compd. **867**, 158986 (2021). https://doi.org/10.1016/j.jallcom.2021.158986
[14] S. Zainabidinov, A.Y. Boboev, and N.Y. Yunusaliyev, East Eur. J. Phys. (2), 321 (2024). https://doi.org/10.26565/2312-4334-2024-2-37
[15] S. Zainabidinov, Sh.Kh. Yulchiev, A.Y. Boboev, *et al*., East Eur. J. Phys. (3), 282 (2024). https://doi.org/10.26565/2312-4334-2024-3-28
[16] S. Z. Zaynabidinov, ShU Yuldashev, A. Y. Boboev, and N. Y. Yunusaliyev, Her. Bauman Moscow State Tech. Univ. Ser. Nat. Sci. **1**, 78 (2024).
[17] S.Z. Zainabidinov, A.Y. Boboev, N.Y. Yunusaliyev, and J.N. Usmonov, East Eur. J. Phys. (3), 293 (2024). https://doi.org/10.26565/2312-4334-2024-3-30
[18] M.K. Karimov, U.O. Kutliev, S.B. Bobojonova, and K.U. Otabaeva. Physics and Chemistry of Solid State, **22**(4), 742 (2021). https://doi.org/10.15330/pcss.22.4.742-745
[19] M. Nosonovsky, and B. Bhushan, J. Appl. Phys. **105**, 104303 (2009). https://doi.org/10.1063/1.3130404

МОРФОЛОГІЯ ПОВЕРХНІ ТА ШОРСТКІСТЬ ТОНКИХ ПЛІВОК ZnO, ЛЕГОВАНИХ СІРКОЮ: АНАЛІЗ НА ОСНОВІ АТОМНО-СИЛОВОЇ МІКРОСКОПІЇ

Акрамджон Й. Бобоєв[a], Нурітдін Й. Юнусалієв[a], Хушрой А. Махмудов[b], Файзулох А. Абдулхаєв[a], Гайбулло Г. Тоджибоєв[a], Мохлароїм О. Гофурджонова[a]
[a]*Андижанський державний університет імені З.М. Бабура, Андижан, Узбекистан*
[b]*Андижанська філія Кокандського університету, Андижан, Узбекистан*

Морфологію поверхні нелегованого ZnO, а також тонких плівок ZnO (ZnO:S), легованого 3 ат.% сіркою, досліджували за допомогою атомно-силової мікроскопії (АСМ). Оцінку та порівняння характеристик поверхні проводили на основі 2D та 3D АСМ-зображень, аналізу профілю ліній та параметрів шорсткості; Ra, Rq, Rz, Rt Rsk та Rku. Нелеговане середовище ZnO мало гладку поверхню з помірними коливаннями висоти та порівняно вузькою гаусівською висотою. З іншого боку, плівка ZnO:S показала значно вищу шорсткість поверхні та топографічне чергування з більшими та симетричнішими гістограмами висоти. Обидва співвідношення Rq/Ra починалися приблизно з теоретичного гаусівського значення (~1,25), причому параметри асиметрії та ексцесу демонстрували чітко різні ступені симетрії поверхні та текстури. Було показано, що введення сірки змінює морфологію зерен, вводить контраст між піками та западинами та збільшує загальну площу поверхні. Морфологічні покращення також показують, що тонкі плівки ZnO:S можуть бути більш адекватними для застосувань, де важлива висока поверхнева активність, що забезпечується газовим зондуванням та каталізом. Це дослідження дає кількісну та якісну оцінку впливу легування сіркою на морфологію поверхні ZnO на нанорівні.

Ключові слова: *морфологія; гістограма; атомно-силова мікроскопія; шорсткість; легування; сірка*

EAST EUROPEAN JOURNAL OF PHYSICS. 3. 325-335 (2025)
DOI:10.26565/2312-4334-2025-3-31 ISSN 2312-4334

CURRENT TRANSFER MECHANISM IN A THIN-BASED HETEROSYSTEM BASED ON A^2B^6 COMPOUNDS

Sharifa B. Utamuradova[a], **Feruza A. Giyasova**[b], **Khayot N. Bakhronov**[c], **Murodjon A. Yuldoshev**[d]*, **Mira R. Bekchanova**[f], **Bakhtiyor Ismatov**[e]

[a]*Institute of Semiconductor Physics and Microelectronics, National University of Uzbekistan, Tashkent, Uzbekistan*
[b]*Kimyo International University in Tashkent, Uzbekistan*
[c]*Tashkent University of Information Technologies named after Muhammad al-Khwarizmi, Uzbekistan*
[d]*Turan International University, Namangan, Uzbekistan*
[e]*Tashkent Institute of Irrigation and Agricultural Mechanization Engineers National Research University*
[f]*University of Public Security of the Republic of Uzbekistan*
**Corresponding Author e-mail: murod.yuldoshev1993@gmail.com*
Received June 4, 2025; revised July 28, 2025; accepted July 31, 2025

The possibility of fabricating a heterosystem based on A^2B^6 compounds with potential barriers (Au)CdS/Si/CdTe(Au) with a minimum density of surface states is presented, confirmed by measurements of the potential barrier height based on capacitance-voltage methods. Various exponential dependences of the current on the voltage at forward biases associated with a change in the kinetic parameters of the CdS/Si/CdTe structure base are determined, and it is revealed that at current densities of $2.1\times10^{-7} \div 0.35\times10^{-6}$ A/cm^{-2} in the studied CdS/Si/CdTe structure, the current is limited by recombination in the space charge layer. It is shown that when a reverse bias is applied to the structure, the structure base is completely covered by the space charge accompanied by electron injection from the rear contact, which in turn determines the mechanism of current transfer of the structure.
Keywords: *Heterosystem; Deposition; Base; Layer; Barrier; Photodiode; Current density; Capacity; SEM, Band diagram*
PACS: 64.70.kg, 73.40.Kp, 68.37.Hk

INTRODUCTION

The prospect of using phenomena occurring in the volume of a semiconductor to increase the functional capabilities, improve the reliability of semiconductor and microelectronic devices and expand the ranges of their operating frequencies and powers allows for a significant simplification of the technology of semiconductor instrument making [1]. In recent years, there has been particular research interest in the creation of heterojunctions based on A^2B^6 compounds, in particular based on cadmium sulfide and telluride. Heterostructures based on these materials are proposed as photoelectric converters of solar energy [2-4], photodetectors [5-7], and detectors [8-11, 28].

However, for high-quality optoelectronic devices (photodetectors), such heterojunctions are combined with silicon in the CdTe-Si and CdS-Si systems. These heterojunctions are difficult to manufacture, since the crystal lattice parameters of CdS, CdTe and Si differ by 15%, which leads to the formation of a high density of surface defects at the Si-CdTe, Si-CdS interfaces. Nevertheless, the possibility of obtaining high-quality Si-CdTe-CdS heterojunctions with low surface density by forming an intermediate transition layer that acts as a buffer in the nSi-pCdTe, pCdTe-nCdS, CdTe-Si structure has been demonstrated in [12, 13].

For A^2B^6 semiconductors, including CdS and CdTe, it is technologically difficult to obtain a p-i-n structure on its basis due to the self-compensation effect. As is known, when manufacturing heterojunctions, a high-resistance i-layer is often formed at the heterointerface due to mutual diffusion of atoms of one semiconductor into another [14, 32]. To avoid this problem, we created a two-side sensitive thin-base structure (Au)CdS/Si/CdTe(Au) with heterojunctions grown by compositionally differentiated layers of CdTe and CdS on n-type Si substrates, with certain layer compositions depending on their thickness. It is well known that thin films of CdTe and CdS can be grown on various substrates using different methods [15,16]. Basically, such films are obtained by thermal deposition in vacuum, that is, by growing from the vapor phase [17].

In this work, CdTe and CdS layers were grown using this method because it allows obtaining various photosensitive structures with fast response.

There is no information in the sources about the creation of two-way sensitive photodiodes with CdS/Si/CdTe with a heterosystem with internal amplification, which are tuned to the required wavelengths of optical radiation by external action, i.e. with different supply of bias voltage. Their production is a topical task, since such a photodiode replaces several photodetectors that are sensitive in different regions of the wavelength of optical radiation and are rigidly connected with the width of the forbidden zone. In the CdS/Si/CdTe semiconductor system, the counter currents of nonequilibrium carriers are regulated, due to which the inversion of the sign of photosensitivity occurs at different base thicknesses [18, 19]. This paper presents the results of studies to identify the role of high-resistance and low-resistance heterolayers in the current transfer mechanism in the CdS/Si/CdTe heterosystem by studying the electrophysical characteristics of heterosystems.

Cite as: Sh.B. Utamuradova, F.A. Giyasova, K.N. Bakhronov, M.A. Yuldoshev, M.R. Bekchanova, B. Ismatov, East Eur. J. Phys. 3, 325 (2025), https://doi.org/10.26565/2312-4334-2025-3-31
© Sh.B. Utamuradova, F.A. Giyasova, K.N. Bakhronov, M.A. Yuldoshev, M.R. Bekchanova, B. Ismatov, 2025; CC BY 4.0 license

EXPERIMENTAL PART

The investigated heterosystem CdS/Si/CdTe photodiode structure [20, 28] was fabricated by successive vacuum thermal evaporation [21] of CdS and CdTe powders onto a substrate - the surface of a wafer of single-crystal n-type silicon. During deposition of the CdS film onto the surface of the silicon substrate, the evaporator temperature was 850÷950°C, which is necessary for congruent evaporation of CdS particles, and a CdTe film was deposited on the back side of the substrate at an evaporator temperature of 580 °C. During film deposition, the substrate temperature was 270÷290°C, the film growth time was 5 min. at a rate of 16.7 Å/s, at which the thickness of each film was 0.55 µm. To obtain a rectifying contact on the surface of the film layers of the heterosystem, metal-semiconductor junctions made of Au with a thickness of 70 Å were formed in the vacuum post VUP-4 at a temperature of 435°C. The contact area of Au on the surface is 0.29 cm^2. The technological route for manufacturing the heterosystem is given in [22, 23]. The manufactured structure of a photodiode based on the CdS/Si/CdTe heterosystem with contacts made of Au is shown in Fig. 1.

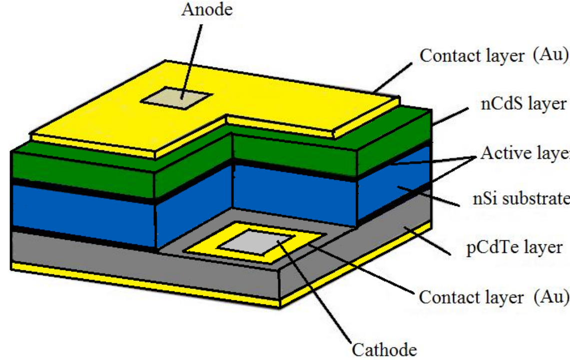

Figure 1. Design of a lateral bidirectional photodiode based on (Au)CdS/Si/CdTe(Au)

ELEMENTAL ANALYSIS OF SAMPLES

The morphology of the CdS/Si/CdTe heterostructure samples based on silicon substrates was studied using a scanning electron microscope SEM EVO MA 10 (Carl Zeiss, Germany). The elemental composition was studied using an energy-dispersive analyzer EDX (Oxford Instruments) - Aztec Energy Advanced X-act SDD. During the measurements, an accelerating voltage of 15 kV was applied to the filament of the device, while the working distance from the structure was 8.5 mm.

Fig. 2-4 show the surface morphology of a sample of a two-side sensitive CdS/Si/CdTe heterosystem. Measurements were carried out on both sides of the heterostructure.

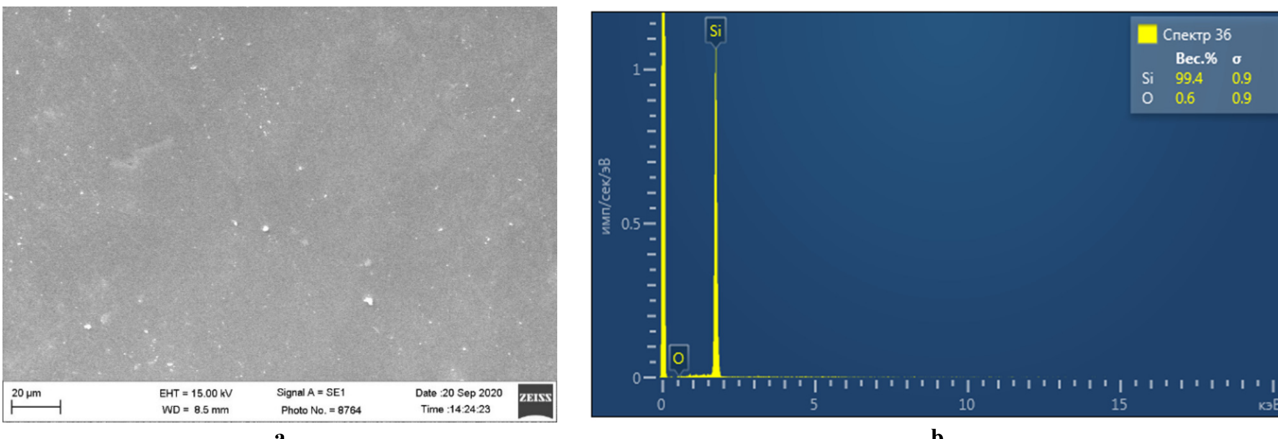

Figure 2. SEM images of the surface (a) and elemental analysis (b) of single-crystal n-type silicon heterostructure CdS/Si/CdTe

The results of the scanning electron microscope (SEM) analysis, presented in Figure 2, confirm that silicon is the predominant element in the sample composition, as evidenced by the intensity of its main peak. The presence of low-intensity oxygen peak (O) indicates the formation of oxide compounds or surface contamination, which may have occurred during sample growth or storage. Quantitative analysis shows that the mass fraction of silicon is 99.4%, oxygen – 0.6%.

Fig. 3 shows an image of a thin-base CdS film grown on a silicon substrate of an n-type heterostructure. According to the quantitative analysis, it is clear that the mass fraction of cadmium (Cd) is 52.9%, sulfur (S) is 15.1%, silicon (Si) is 32.1% and, accordingly, the amount of Cd significantly exceeds the amount of S. However, point defects can form near the boundary of Si and CdS [24,25].

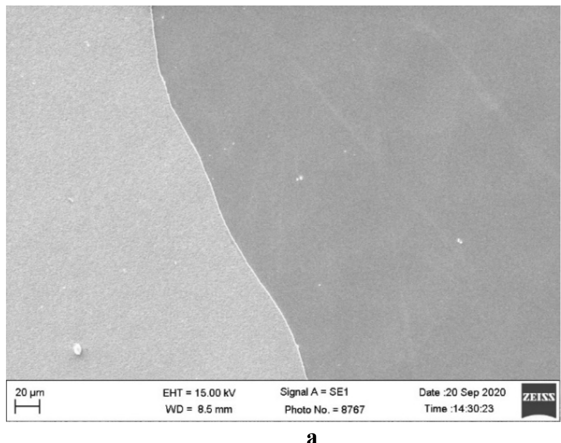

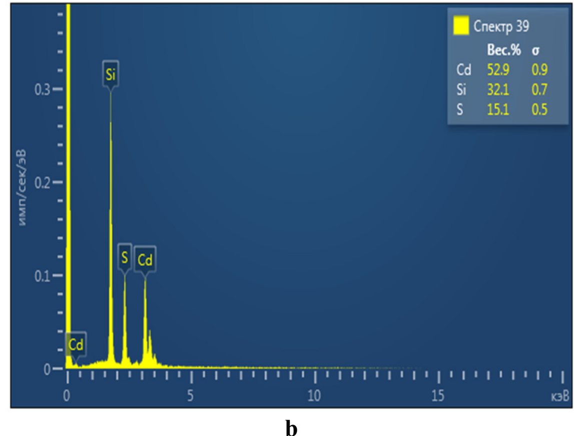

a **b**

Figure 3. SEM images of the surface (a) and elemental analysis (b) of a thin base layer based on CdS of the n-type CdS/Si/CdTe heterostructure

Fig. 4 shows an image of a thin-based CdTe film grown on a silicon substrate of an n-type heterostructure. The mass fractions of cadmium (Cd) and tellurium (Te) are 47.8% and 52.2%, respectively, the amounts of these elements are almost identical. It can also be seen that the back side of the sample, consisting of silicon, is completely covered with a thin CdTe film, as evidenced by the absence of Si in the spectra.

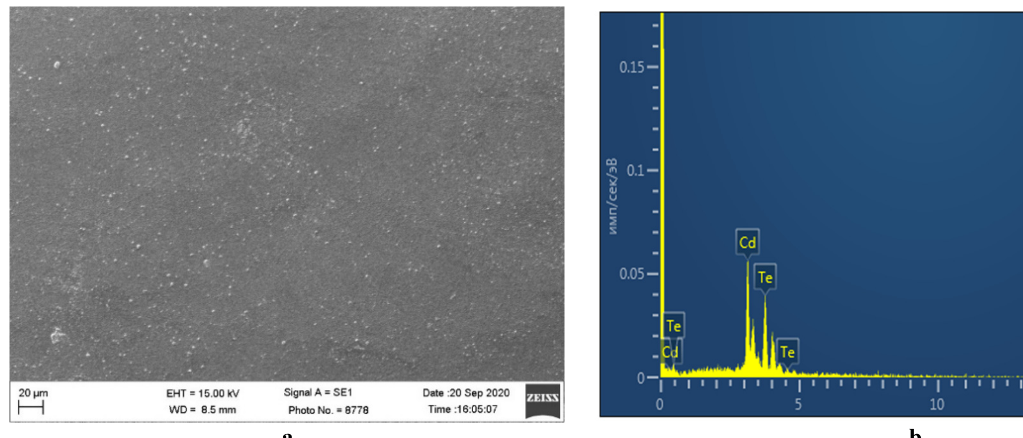

a **b**

Figure 4. SEM images of the surface (a) and elemental analysis (b) of a thin base layer based on CdTe p-type heterostructure CdS/Si/CdTe

The CdS/Si/CdTe heterosystem structures obtained by vacuum thermal evaporation in a quasi-closed volume are a simple, effective and inexpensive method for microelectronic devices. However, intensive research is required to fully reveal its potential. The presented results demonstrate compactness, the ability to grow in one direction and obtain rod- or columnar-type grains with normal properties for growing substrates [26,27].

The current-voltage characteristics (CVC) of the manufactured CdS/Si/CdTe photodiode heterosystem were measured with forward and reverse current directions in the dark and in the light at room temperature. The operating voltage was supplied from a B5-48 and B5-50 power supply with a step of 0.05 volts. The voltage and current were recorded with a B7-21A and B7-35 universal voltmeter. The minimum current was 2 nA, the relative measurement error was 0.2÷0.4%. The structures were illuminated with a JDSU850 laser with a radiation power of 2.3 W and a wavelength of 850 µm, as well as with a SIRSh 6-100 incandescent lamp with a power of N=100 W, which in its parameters is identical to the reference white light lamp [23]. In such a lamp, the power of electromagnetic radiation in the visible spectrum in one lumen is 9.1×10^{-3} W [28].

The capacitance-voltage characteristics of the studied CdS/Si/CdTe heterosystems were measured with a capacitance value within the range of (0.1÷50 nF) at a room temperature of 300 K in the forward and reverse switching modes in the frequency range f=0.4÷50 kHz, since in this frequency range they are identical in shape. A detailed description of the CVC measurement technique for the studied structure is given in [23].

RESULTS AND DISCUSSION

Establishing the patterns and processes of current flow through homo- and heterojunction structures is the initial stage of studying semiconductor devices based on them. Under the condition of electrical activity of defects, the analysis of the current-voltage characteristics allows us to draw conclusions about the defectiveness of the heterostructures formed [29].

Fig. 5 shows the forward and reverse branches of the CVC of the CdS/Si/CdTe heterosystem with potential barriers. The dependence is plotted on a semi-logarithmic scale. The conducted analysis of the CVC indicates that the structure has pronounced rectifying properties. At a voltage of 18 V, the rectification coefficient is ~ 10, which confirms the presence of diode-like behavior of the structure [30, 31].

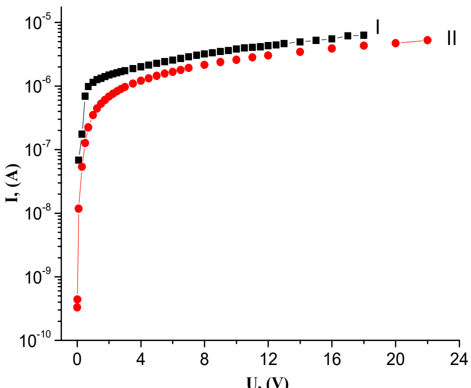

Figure 5. Forward (I) and reverse (II) branches of the CVC of the CdS/Si/CdTe heterosystem with potential barriers at t=20 °C

Analysis of the direct branch of the CdS/Si/CdTe heterosystem current-voltage characteristic shows that the curve consists of four characteristic sections (Fig. 6). Each of the sections: the first, second, third and fourth – is described by an exponential dependence of the current on the applied voltage and is represented by an analytical equation [32]:

$$I = I_0[\exp(qV/ckT)-1] \tag{1}$$

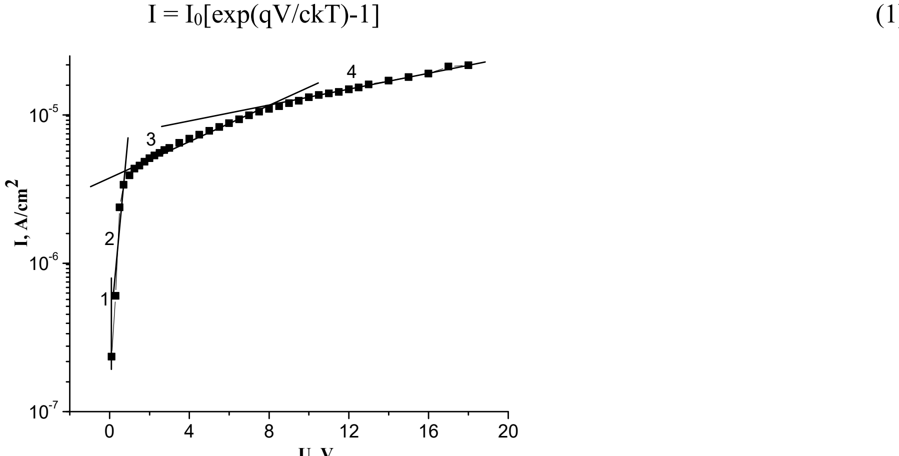

Figure 6. Direct branch of the CdS/Si/CdTe heterosystem with potential barriers on a semi-logarithmic scale in the dark

As can be seen in Fig. 6, in the first section of the direct branch of the I-V characteristic at a current density within the range of $I \approx 2.02\times10^{-8} \div 0.52\times10^{-7}$ A/cm², an exponential dependence is observed with the exponent c_1= 1.028 and the pre-exponential factor $I_{01}=2.2\times10^{-7}$ A/cm². The current flowing in this section of the structure is caused by thermionic emission [32]. Such a current transfer mechanism is typical for structures with a Schottky barrier and metal-insulator junctions. The thermionic current is described by the following equation [33, 39]:

$$I_{01} = AT^2\exp(-V_D/kT) \tag{2}$$

Using the experimentally determined value of the pre-exponential factor $I_{01}=2.2\times10^{-7}$ A/cm², obtained from the analysis of the first section of the I-V characteristic based on expression (2), the value of the potential barrier height was calculated: $V_D=0.843 \pm 0.02$ eV. The obtained value is in good agreement with the barrier value determined from the results of the I-V characteristic given below. From the given data, it can be said that in the first section of the direct branch of the I-V characteristic, the main current mechanism is thermionic emission, which is caused by the emission of electrons from the gold contact Au into the CdTe (or CdS) layers.

In the second section of the current-voltage characteristic, at current densities $I=2.1\times10^{-7} \div 0.35\times10^{-6}$ A/cm² for the Si/CdTe heterojunction, the dependence of the current on the voltage is also exponential. In this case, the exponent is c_2=1.98, and the pre-exponential factor is $I_{02}=6.1\times10^{-7}$ A/cm² (Fig. 6, straight line 2).

The value $c_2 \approx 2$ indicates that the current in this mode is limited by carrier recombination in the space charge layer [34]. In wide-gap semiconductors, especially at low temperatures, recombination processes have a significant effect on the shape of the current-voltage characteristic even at forward voltage.

The carrier concentration, including nonequilibrium, in the space charge layer changes by a factor of e over a characteristic distance l, at which the potential changes by kT/q. At a low injection level, the recombination rate is determined by the product of the electron and hole concentrations, and maximum recombination occurs at the boundary of the p- and n-regions.

Calculations show that the bulk of carriers in the space charge layer recombine into a layer less than 0.55 μm thick, located near the geometric boundary of the CdTe (Au) potential barrier. The expression $l=kT/qE_{max}$ is used to determine the diffusion displacement length in neutral regions. For the structure under study, the maximum electric field strength is 5.23×10^2 V/cm [32]. Recombination processes are especially noticeable in semiconductors containing metastable complexes [35]. Similar patterns are observed in A^2B^6 compounds, where excitation causes chemical reactions that lead to the disintegration of complex complexes, such as a shallow donor – vacancy [36]. Despite the differences in the mechanisms, the following remains common to all cases: the recombination of nonequilibrium carriers occurs with a delay, and the inertia of the electron exchange within the recombination complex leads to the appearance of an additional term in the denominator of formula (3), which, at a high level of excitation, can become the dominant factor [37, 38].

$$U = N_R \frac{c_n c_p (pn - n_i{}^2)}{c_n(n+n_1) + c_p(p+p_1) + a\tau_i pn}\,. \quad (3)$$

Since at sufficiently high values of forward voltage the recombination current increases with increasing bias more slowly than the diffusion current, the main contribution to the current begins to be made by carrier diffusion in the quasi-neutral regions of the base. In such a situation, the applied voltage is redistributed between the potential barrier and the quasi-neutral part of the base, which is reflected in the value of the exponent c in the I-V equation. The value of the exponential factor depends on the ratio of the base thickness to the diffusion length of minority carriers. For different ratios of these parameters, the exponent can take different values, which allows us to judge the dominant mechanism of current transfer in the heterosystem.

In Fig. 6, sections 3 and 4 of the I-V characteristics are described by the dependence: I=exp(qV/ckT), where the values of the exponent c significantly exceed 2 and are 12.7 for section 3, and 48.3 for section 4, and the pre-exponential factors are 4.4×10^{-6} A/cm² and 1.1×10^{-5} A/cm², respectively. Such high values of c indicate the presence of complex recombination processes occurring through several channels. This indicates that at a given injection level, certain types of recombination centers participate in recombination, probably representing complex formations in which carriers are retained for a certain time. Such a model is valid for a high-resistance compensated base of the Si/CdTe heterosystem. Electrons are injected into the quasi-neutral part of the CdS/Si base from the metal contact (Au)CdS, and the resistance of this contact makes a significant contribution to the shape of the I–V characteristic [39].

It is worth noting that no holes are injected from the CdS/Si heterojunction into the base, as shown in [34], since this effect is characteristic only of ideal heterojunctions. In real conditions, surface states at the interface of semiconductors can act as recombination or tunneling centers for holes.

Based on the above, the main contribution to the structure current is made by the flow of electrons injected from the (Au)CdS contact. At the same time, as the analysis of the second section of the I-V characteristic shows, diffusion currents flow in the base, caused by non-main nonequilibrium holes coming from the Si/CdTe heterojunction to compensate for the charge and ensure the electrical neutrality of the injected electrons.

According to literature data [40], with an insignificant accumulation effect, in the diffusion mode only two characteristic types of current-voltage dependences can be realized: I∼exp(qV/kT) and I∼exp(qV/ckT).

Under forward bias near the CdTe(Au) contact, electrons and holes accumulate to maintain electroneutrality. This is due to the presence of a high potential barrier of 0.843 eV, which promotes the accumulation of nonequilibrium charge carriers and the formation of a positive concentration gradient: dn/dx>0. As a result, diffusion and drift carrier flows directed in opposite directions arise in this region. Upon reaching a certain bias level (about 1.5 V), these flows mutually compensate, which leads to an increase in the base resistance and the appearance of a sublinear dependence of current on voltage [28, 41].

The CdS/Si/CdTe heterosystem may contain point defects, such as cadmium (Cd), sulfur (S) or tellurium (Te) atom vacancies. Despite the difference in composition and type, the recombination of nonequilibrium electrons and holes in the structure occurs with a delay. This behavior is due to the inertia of the electron exchange inside the recombination complex, which manifests itself at a sufficiently high excitation level. This inertia leads to a recombination delay, which must be taken into account when analyzing the dynamic characteristics of the structure.

As is known, in CdTe and CdS compounds, cadmium atoms are volatile components, as a result of which cadmium atom vacancies are easily formed in their crystal lattice: both singly charged V_{Cd}^{-} and doubly charged V_{Cd}^{2-}, and the appearance of interstitial cadmium atoms (Cd_i) is also possible. [41-43]. These complexes represent deep acceptor levels, similar to gold atoms, and probably play an important role in recombination processes. There is a high probability that such defect-impurity formations form recombination complexes of the type: negatively charged acceptor - positively charged interstitial ion, positively charged donor - negatively charged vacancy [44, 45]. Recombination of nonequilibrium charge carriers through such complexes occurs with a characteristic delay due to the inertia of the electron exchange inside the complex. At high current densities, it is these processes that become dominant in recombination, especially in Si/CdTe base layers.

As a rule, the height of the potential barrier at the metal-semiconductor interface is determined by the difference in the work function between the metal and the semiconductor. According to [29], the work function of gold (Au) is in the range of 4.0÷5.2 eV, and its exact value largely depends on the state of the metal surface.

Next, we will analyze the behavior of the reverse branch of the CdS/Si/CdTe heterosystem's I–V characteristic (Fig. 7).

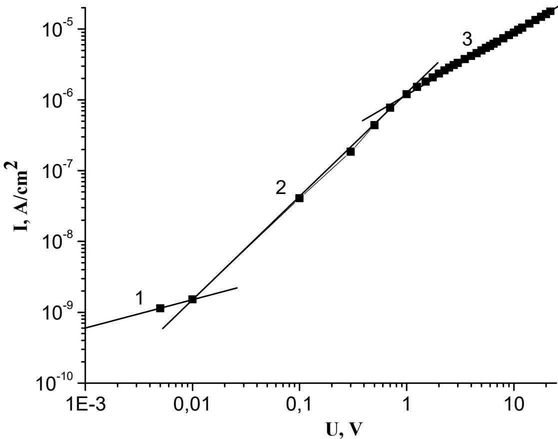

Figure 7. I-V characteristics of the reverse-biased CdS/Si/CdTe heterosystem in double logarithmic scale

The geometric parameters of the space charge region, in particular its thickness, as well as leakage currents through the rectifying contact and the characteristics of the ohmic contact, have a significant effect on the formation of the spectrometric parameters of the photodiode [46]. In this regard, it is of interest to study the electronic processes occurring in the space charge layers formed in the base layers of the CdS/Si/CdTe heterosystem with potential barriers. An important task of the study is to study the influence of the properties of the rear ohmic contacts on the nature and intensity of these processes, since they also significantly affect the overall efficiency and stability of the photodiode structures [47].

Analyzing the reverse branch of the current-voltage characteristic (Fig. 7) by power dependences of the type - $I=AV^{\alpha}$ with different values of the exponent α, at room temperature, we have three clearly defined sections: in the voltage range from 0 to 0.01 V – $J\propto V^{0.78}$ (recombination process) in section 1, in the range from 0.02 V to 3 V – $J\propto V^{2.44}$ (injection depletion effect) in section 2, in the range from 4 to 13 V – $J\propto V^{5.55}$ (pre-breakdown) in section 3.

According to the theory [48], diode structures have a power-law dependence of current on voltage of the type $J\propto V^{\alpha}$, ($\alpha\geq2$), including a section of sharp current growth when, in addition to point defects, complex defect-impurity complexes participate in recombination processes, within which electron exchange occurs, determined by formula (3).

According to the theory presented in [41], in structures with developed accumulation, the sublinear section of the I–V characteristic appears when the conditions Jad≥2 is met. This shows that for samples of structures based on CdS/Si/CdTe, the value of Jad=3 at T=300 K.

This section of the I–V characteristic can be well described within the framework of the above-described theory of the injection depletion effect [40]:

$$V = V_0\, exp(\, aJd) \tag{4}$$

where, $a = \frac{1}{2kT\mu_n N_t}$ is a parameter that depends only on the mobility of the majority carriers – electrons (μ_n) and the concentration of deep impurities – N_t. Using expression (4), the value of the parameter "a" can be determined directly from the sublinear section of the current-voltage characteristic, as shown in Fig. 5. With forward and reverse bias on a logarithmic scale:

$$a = \frac{S\cdot ln(V_2/V_1)}{(I_2-I_1)\cdot d}, \tag{5}$$

The value of the parameter "a" in expression (5), determined on the basis of the experimental data of the CdS/Si/CdTe structure I–V characteristics, was at room temperature $a=5.22\times10^4$ cm/A, then, accordingly, $\mu_n\times N_t=2.31\times10^{15}$ $V^{-1}\cdot cm^{-1}\cdot s^{-1}$. The mobility of the majority carriers was $\mu_n\approx500$ $cm^2/V\cdot s$, and that of the minority carriers $\mu_p\approx60$ $cm^2/V\cdot s$, therefore, the concentration of deep impurities leading to the appearance of the injection depletion effect was $N_t\approx4.62\times10^{12}$ cm^{-3} [30,31].

In section 1 of the current-voltage characteristic, the dependence of the current on the voltage is close to $I \sim V^{1/2}$. Such a dependence is typical for cases when, with an increase in the reverse bias, the expansion of the volume charge region occurs [36]. When the diode operates with potential barriers in the reverse direction, the reverse current density can be described by the following expression [34]:

$$I_0 = qL_n(n_p/\tau_n) + qd(n_i/2\tau_0), \tag{6}$$

The first term of expression (6) describes the current resulting from thermal generation of charge carriers at a rate n_p/τ_n in a base layer of width L_n behind the space charge region, and the second part of formula (6) represents the current resulting from generation of charge carriers in the space charge region. Since the space charge region is depleted of carriers, $p_n \le n^2_i$ and the Shockley-Read statistics [49] are written as $r\text{-}g\!=\!-n_i/2\tau_0$, i.e., under reverse bias, carrier generation in the space charge region predominates over recombination. In semiconductors with a large band gap, such as silicon, gallium arsenide, and cadmium telluride, n_i is small, and therefore the generation current clearly predominates.

In section (1) of the reverse I–V characteristic (Fig. 7), the current is indeed limited by the generation of carriers in the space charge layer, and the contribution to it of the current of the space charge region is insignificant. Further on the I–V characteristic, there is section (2), where the dependence of the current on the voltage has the form $I=AV^{\alpha}$, $\alpha=2.44$. Such a section of the I–V characteristic can take place in long diodes at low and high levels of injection of minority carriers. Consequently, electrical neutrality is ensured at each point in the base of such diodes. However, the studied diodes with a Schottky barrier are connected in the reverse direction, and the space charges in them are quite thick. Therefore, it is assumed that there is an injection of nonequilibrium electrons into the space charge layer. The injection of electrons into the space charge layer can occur from the interlayers of the grain boundary, as in [50], or from the rear contact made of Au, when a negative bias is applied to this contact. The appearance of the linear section of the current-voltage characteristic is because the thickness of the volume charge is filled with injected nonequilibrium electrons. As a result, the resistance of the entire part of the base is equalized. However, the concentration of nonequilibrium electrons injected from the rear contact (Au) is still less than the concentration of equilibrium carriers in the quasi-neutral part of the base layer of the structure.

After the section $I \sim V^{2.44}$ on the I-V characteristic (Fig. 7) there is a section $I \sim V^{5.55}$. With further increase in voltage, as can be seen from Fig. 7, a sharp increase in current is observed, and the exponent $\alpha \approx 5.55$. Such a section is called pre-breakdown. The section of sharp current growth appears with monopolar injection [51], when the sticking levels intersect with the Fermi quasi-level, or are at a very close distance. Electrons injected from the rear contact will affect the leakage currents and the noise characteristics of semiconductor devices.

One of the methods for obtaining information on the substantiated electrophysical parameters of semiconductors (the concentration of charge carriers and its distribution across the thickness of the sample; the concentration of impurities and defects; the density of surface states; the surface potential; the interface) is the frequency voltage-capacitance characteristic (VCC) method [52]. In the manufacture of electronic devices, the above-mentioned parameters of semiconductors are essential.

The capacitance-voltage characteristics of the structure under study show the presence of a metal-insulator-semiconductor structure (MIS structure) (Fig. 8).

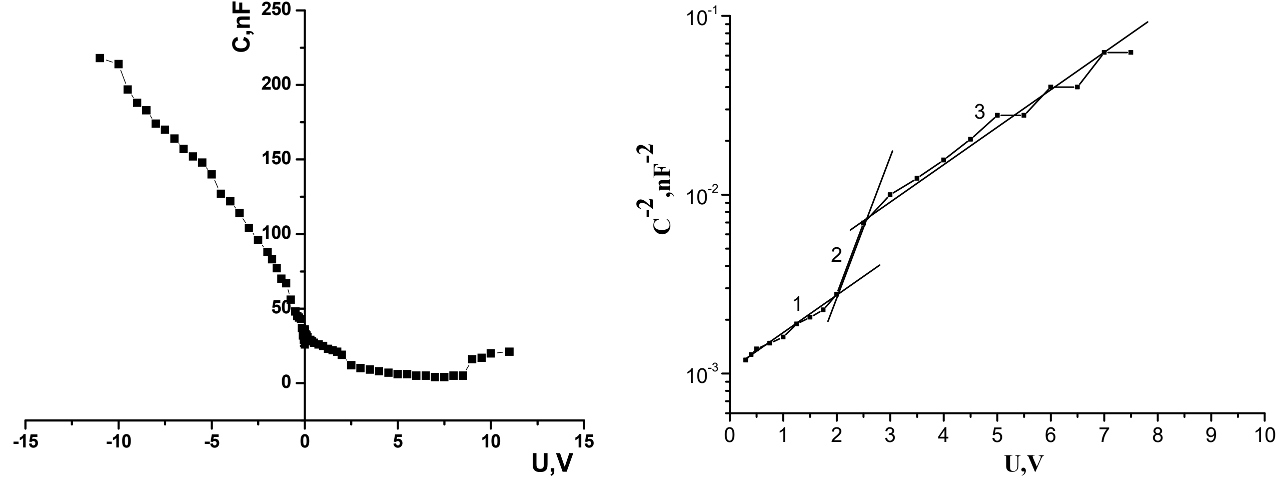

C(U) dependence of the heterosystem under forward and reverse bias voltage (a)

$C^{-2}(U)$ dependence of reverse-biased heterosystem (b)

Figure 8. Volt-capacitive characteristics of the CdS/Si/CdTe heterosystem at a frequency of f=50 kHz and t = 20°C

In the CdS/Si/CdTe heterosystem, the CdS layer is a high-resistance and compensated material, therefore this layer and the oxide layers formed during the deposition of CdS on the surface of the silicon wafer in vacuum behave as a dielectric, and the surface state densities N_{SS} in the heterojunction are slow surface states. The surface state density of the MIS structure is determined by the shift of the experimental VCC relative to the calculated curve at the same capacitance value [32]. It follows that $N_{ss}=\Delta VC/q$. The structure has a high surface state density at positive values of the surface potential, and the value of $N_{ss} \sim 9.2\times10^{10}$cm^{-2}.

When CdS type films are deposited on the silicon surface and manifest themselves as a high-resistance i-layer, it makes it possible to form transition i-layers of the CdS/Si and Si/CdTe interfaces on the boundary layer.

In Fig. 8.a it is seen how the thickness d_i=0.011 μm was determined from the capacitance C_i=217 nF using the formula for a flat capacitor $C=\varepsilon\varepsilon_0 S/d$. The thickness of the space charge W≈0.103 μm was determined from the minimum capacitance of the structure C_{min}≈23.3 nF. At thermodynamic equilibrium, its thickness, which was calculated from the capacitance of 31.7 nF in the absence of bias voltage, is equal to ~ 0.073 μm.

As is known, the thickness of the space charge narrows in the forward direction of the current. In the reverse direction, on the contrary, it expands with an increase in the bias voltage. From these experimental data, it also follows that the resistance of the space charge is the determining resistance of the entire structure, as evidenced by the coincidence of the value of its capacitance with the value of the dielectric capacitance in the C(U) characteristic.

The concentration of equilibrium electrons n_0 is determined by the capacity of flat bands and the steep section of the VCC characteristic (Fig. 8, b). To determine n_0 by the VCC characteristic, a steep section with two slopes is constructed in the C^{-2}(U) coordinates: section 1 and section 2 (Fig. 8, b). According to the well-known formula (7) [51]:

$$n_0 = \frac{2}{q\varepsilon_0\varepsilon_S S^2}\frac{dV_D}{d(C^{-2})}, \tag{7}$$

The concentration of equilibrium electron carriers was determined. The concentrations of equilibrium electron carriers are $N_c \approx 3.3\times10^{15}$ cm^{-3} and $N_v \approx 4.1\times10^{14}$ cm^{-3}. By extrapolating the C^{-2}(U) dependence onto the voltage axis U (Fig. 8, b) with the value of the structure capacitance C = 24 nF, V_D = (0.843 ± 0.02) eV was determined for n_0 in nSi. In addition, the value of the equilibrium electron concentration was estimated from the capacitance of flat bands [32]. The value of n_0 determined by VCC is consistent with the value of the equilibrium electron concentration of $3.6\cdot10^{12}$ cm^{-3} for nSi.

The effective concentration of charged acceptor centers is determined from the smoothly decreasing section of the volt-capacitance dependence C^{-2}(U) of the heterostructure under study (Fig. 8, b), which has kinks and consists of three straight lines. This indicates the non-uniformity of the surface layer of the CdTe thin-base layer. The values of the lifetime τ_{01} and τ_{02} of nonequilibrium charge carriers are in agreement with the data given in the literature [36] for the lifetimes of carriers in CdTe with intrinsic conductivity.

The value of the lifetime of nonequilibrium carriers is determined by formula (8) [32]:

$$\tau_0 = \frac{n_i(2q\varepsilon\varepsilon_0)^{1/2}\,(V_2^{1/2}-V_1^{1/2})}{2N_{A,eff}^{1/2}\,(I_{r2}-I_{r1})} \tag{8}$$

and is $\tau_{01}\approx3.13\times10^{-7}$ s, $\tau_{02}\approx0.52\times10^{-7}$ s. The appearance of two values of τ_0 is due to two concentrations of charged local immobile centers. These centers were determined from the rapidly decreasing section of the dependence C^{-2}(U), consisting of two straight lines 2 and 3 (Fig. 8, b), which indicates the inhomogeneity of the base layer of the CdTe film structure. The obtained results show that with an increase in the specific resistance of the base of the structure, the lifetime of equilibrium current carriers increases, therefore, the concentration of unfilled recombination centers decreases.

For the calculated C(U) characteristic, the concentration of equilibrium holes p_0 was determined by the capacitance of flat bands and by the steep section of the C^{-2}(U) characteristic (Fig. 8, b), using the well-known formula (9) [53].

$$P_0 = \frac{2}{q\varepsilon_0\varepsilon_s S^2}\frac{dV}{d(C^{-2})} \tag{9}$$

and it is 8.3×10^{10} cm^{-3} and 2.6×10^{12} cm^{-3}. The capacity decreases with increasing reverse voltage (Fig. 8, b), which confirms the expansion of the space charge layer. This C^{-2}(U) characteristic reaches a plateau at voltages of ∼ 2÷2.5 V. This means that the space charge already at these voltages completely covers the entire thickness of the base (Si/CdTe) of the structure. When applying reverse bias to the thin-base CdS/Si heterojunction, the process of space charge expansion is compensated by the process of electron injection from the heterojunctions.

The experimental results confirm the formation of a CdS/Si heterojunction with a comparatively low density of surface states, despite the fact that the lattice constants of cadmium sulfide and silicon differ by more than 7%. The experimental results obtained become explainable if we take into account that an intermediate layer is formed in the heterojunction, which smooths out the difference in the lattice constants of cadmium sulfide and silicon [54]. Such intermediate layers can be solid solutions of these semiconductors or thin oxide layers that are present on the silicon surface during the formation of the CdS/Si heteropair.

Based on these data, a band diagram of the structure of (Au)CdS/Si/CdTe(Au) was constructed, shown in Fig. 9 (a complete description and calculated data of the band diagram of the structure are given in [28,31]).

The calculations of the electronic band structure performed are based on the density functional theory [29,55]. It is evident from the diagram that the reverse and forward currents at the interface of the CdS/Si and Si/CdTe heterojunction are limited by the resistance of the space charge layer. The space charge contains negatively charged mobile and immobile donor centers located at the interface between the layer and silicon due to the donor concentration in nSi, which is ten orders of magnitude greater than the carrier concentration in the chalcogenide layers. The isotypic CdS/Si junction has a contact potential difference with a value of Δφ=0.204 eV. Consequently, an enriched space charge layer appears at the interface of the CdS and Si junction, since the value of the metal work function $A_{(Au)}$=4.9 eV located in the CdS layer is less than the work function $A_{(Si)}$=5.01 eV.

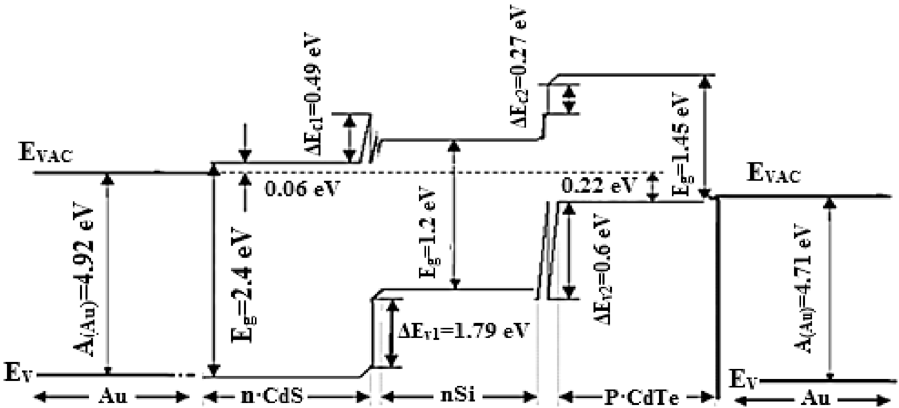

Figure 9. Energy band diagram of the heterosystem (Au)CdS/Si/CdTe(Au) [22,23]

From the band diagram of the structure (Au)CdS/Si/CdTe (Au) it is seen that the forward and reverse currents are limited by the resistance of the space charge layer at the interface of the heterojunction CdS/Si and Si/CdTe. This space charge consists of positively and negatively charged fixed donor (acceptor) centers, mobile holes and electrons, which are located in the surface layer of CdS and CdT. Since the concentration of electrons in nSi is ten orders of magnitude greater than the concentration of holes in the layer of CdS and CdT. Therefore, the external potential applied to the structure, including the contact potential difference, mainly falls on the space charge layer formed between Si and CdTe, and the surface states of Nss at the interface of the contacting semiconductors cadmium telluride and silicon can affect the height of the potential barrier, the nature of which is due to the difference in the constants of the crystal lattices of the heteropair and the technological conditions during the creation of heterojunctions [39,55-57]. The results of the VCC show that the structure under study behaves as an MIS structure and in it the main potential barrier is created in the near-surface layer of CdS at the interface of the CdS/Si heterojunction. These data also show that one of the reasons for the high concentration of nonequilibrium electrons in the high-resistance base (CdS) in the forward direction of the current is the relatively low density of surface states in the lower half of the silicon band gap, which is explained by the fact that in the forward direction of the current, nonequilibrium charge carriers interact with N_{ss} located in the lower half of the band gap, and in the reverse direction - with surface states located in the upper half of the silicon band gap.

CONCLUSIONS

Thus, the possibility of obtaining a heterosystem based on A^2B^6 compounds with potential barriers – (Au)CdS/Si/CdTe(Au) with a minimum density of surface states is shown, which is confirmed by measuring the height of the potential barrier, volt-capacitance methods. It is established that at current densities of $2.1\times10^{-7}\div0.35\times10^{-6}$ A/cm^{-2} in the studied CdS/Si/CdTe structure, the current is limited by recombination in the space charge layer. In this case, the difference of almost an order of magnitude between the calculated value of the lifetime of nonequilibrium carriers and its experimental value is explained by the participation of complex centers in the recombination processes, inside which the carriers are retained. Using the study of the current-voltage characteristics, it was determined that the CdS/Si/CdTe heterosystem has three sections at a constant temperature caused by the recombination process: a power-law section - $I\propto V^{2.44}$ (the effect of injection depletion), a sublinear section - $I\propto V^{0.78}$ (the recombination process), and a pre-breakdown section - $I\propto V^{5.55}$, which are explained by the fact that at low current densities the recombination of nonequilibrium carriers occurs through local centers, while complexes with internal electron exchange are responsible for recombination processes at high current densities. It was established that the CdS/Si heterojunction has a low density of surface states at the interface, which is evidenced by the high value of the rectification coefficient of the CdS/Si/CdTe structure and the appearance of a sublinear section in the reverse current-voltage characteristic in a wide range of bias voltages.

By studying the VC characteristics of the structure when turned on in the reverse direction, it was shown that after the complete coverage of the structure base by the space charge, electrons are injected from the rear contact, which determine the mechanism of charge transfer of the structure. In the compounds, Si is the source of electron injection. The results of VCC measurements of CdS/Si/CdTe heterostructures showed that the thickness of the space charge narrows in the forward bias, and in the reverse bias, it expands with increasing bias voltage. In addition, the resistance of the space charge is the determining resistance of the entire structure, since the CdS layer in the heterosystem is a high-resistance and strongly compensated material, which is evidenced by the fact that the structures belong to semiconductor MIS structures.

ORCID

Sharifa B. Utamuradova, https://orcid.org/0000-0002-1718-1122; **Feruza A. Giyasova,** https://orcid.org/0000-0003-0746-4986
Khayot N. Bakhronov, https://orcid.org/0009-0000-4138-3149; **Murodjon A. Yuldoshev,** https://orcid.org/0000-0002-9722-9439

REFERENCES

[1] M.A. Scarpulla, *et al.,* "CdTe-based thin film photovoltaics: Recent advances, current challenges and future prospects," Solar Energy Materials and Solar Cells, **255**, 112289 (2023). https://doi.org/10.1016/j.solmat.2023.112289
[2] R.R. Kabulov, F.A. Akbarov, and A.A. Alimov, "Time of transition processes in a CdS-CIGS structural solar cells in the short-wave part of the absorption spectrum at different loading resistances," Nanosystems: Physics, Chemistry, Mathematics, **14**(1), 127-131 (2023).
[3] I.M. Dharmadasa, P.A. Bingham, O.K. Echendu, H.I. Salim, T. Druffel, R. Dharmadasa, G.U. Sumanasekera, *et al*., "Fabrication of CdS/CdTe-Based Thin Film Solar Cells Using an Electrochemical Technique," Coatings, **4**, 380-415 (2014). https://doi.org/10.3390/coatings4030380
[4] T.M. Mazur, V.V. Prokopiv, M.P. Mazur, and U.M. Pysklynets, "Solar cells based on CdTe thin films," Physics and Chemistry of Solid State, **22**(4), 817-827 (2021). https://doi.org/10.15330/pcss.22.4.817-827
[5] Sh.A. Mirsagatov, I.B. Sapaev, Sh.R. Valieva, and D. Babajanov, "Electrophysical and Photoelectric Properties of Injection Photodiode Based on pSi-nCdS-In Structure and Influence of Ultrasonic Irradiation on them," Journal of Nanoelectronics and Optoelectronics, **9**, 1-10 (2014). https://doi.org/10.1166/jno.2014.1685
[6] J. Wang, Y. Chang, L. Huang, K. Jin, and W. Tian, "Designing CdS/Se heterojunction as high-performance self-powered UV-visible broadband photodetector," APL materials **6**, 076106 (2018). https://doi.org/10.1063/1.5042549
[7] H.R. Shakir, O.A. Chichan, M.S. Sada, S.A. Hussein, S.S. Chiad, N.F. Habubi, Y.H. Kadhim, *et al*., "The effect of aluminum doping on nanostructured CdS optical, structural and sensing characterization" Chalcogenide Letters, **22**(1), 77–89 (2025). https://doi.org/10.15251/CL.2025.221.77
[8] S. Abbaspour, B. Mahmoudian, and J.P. Islamian, "Cadmium Telluride Semiconductor Detector for Improved Spatial and Energy Resolution Radioisotopic Imaging," World J. Nucl. Med. **16**(2), 101-107 (2017). https://doi.org/10.4103/1450-1147.203079
[9] V. Gnatyuk, V. Sklyarchuk, T. Aoki, A. Koike, and W. Pecharapa, "Development of CdTe-based nuclear radiation sensors and related devices," AIP Conference Proceedings, 020012 (2018). https://doi.org/10.1063/1.5053188
[10] M.A. Yuldoshev, "Investigation of optical heterogeneity of lithium niobate crystal under radiation exposure," Physics AUC, **34**, 192-197 (2024). http://cis01.central.ucv.ro/pauc/vol/2024_34/15_PAUC_2024_192_197.pdf
[11] M.A. Yuldoshev, Z.T. Azamatov, A.B. Bakhromov, and M.R. Bekchanova, East Eur. J. Phys. (4), 250-255 (2024), https://doi.org/10.26565/2312-4334-2024-4-25
[12] I.B. Sapaev, Sh.A. Mirsagatov, B. Sapaev, and M.B. Sapaev, "Fabrication and Properties of nSi–pCdTe Heterojunctions," Inorganic Materials, **56**(1), 7–9 (2020). https://doi.org/10.1134/S002016852001015X
[13] F.Kh. Khasanov, I.B. Sapaev, B.S. Mirzaev, Q.A. Shakarov, U.T. Davlatov, and N.N. Abdusattorov, "Si-CdTe-CdS Structures of Electronic Processes," AIP Conference Proceedings **2432**, 050017 (2022). https://doi.org/10.1063/5.0089974
[14] G.H. Mavlonov, Kh.Kh. Uralbaev, B.O. Isakov, Z.N. Umarkhodjaev, and Sh.I. Hamrokulov, East Eur. J. Phys. (2), 237-241 (2025), https://doi.org/10.26565/2312-4334-2025-2-27
[15] J.R. Winger, M.A. Scarpulla, "Grain growth in CdTe films during $CdCl_2$ treatment: TeCl4 theory," in: *IEEE 46th Photovolt. Special. Conf. (PVSC)*, (IEEE, Chicago, IL, USA, 2019), pp. 1834–1838. https://doi.org/10.1109/PVSC40753.2019.8980923
[16] Sh.A. Mirsagatov, and A.K. Uteniyazov, "Injection photodiode based on p-CdTe film," Tech. Phys. Lett. **38**, 34–37 (2012). https://doi.org/10.1134/S1063785012010099
[17] S.A. Mirsagatov, R.R. Kabulov, and M.A Makhmudov, "Injection photodiode based on an n-CdS/p-CdTe heterostructure," Physics of Semiconductor Devices, **47**, 815 (2013). https://doi.org/10.1134/S106378261306016X
[18] I.M. Karageorgiy-Alkalaev, and A.Yu. Leiderman, *Photosensitivity of semiconductor structures with deep impurities*, (Tashkent, FAN, 1981). (in Russian)
[19] M. Akramov, B. Eshchanov, S. Usanov, Sh. Norbekov, and D. Matrasulov, "Second-harmonic generation in branched optical waveguides: Metric graphs-based approach," Physics Letters A, **524**, 129827 (2024). https://doi.org/10.1016/j.physleta.2024.129827
[20] F.A. Giyasova, and M.A. Yuldoshev, "Investigation of temporal characteristics of photosensitive heterostructures based on gallium arsenide and silicon," Chalcogenide Letters, **22**(2), 123–129 (2025). https://doi.org/10.15251/CL.2025.222.123
[21] A.M. Bothwell, J.A. Drayton, P.M. Jundt, and J.R. Sites, "Characterization of thin CdTe solar cells with a CdSeTe front layer," MRS Adv. **4**(37) 2053–2062 (2019). https://doi.org/10.1557/adv.2019.332
[22] F.A. Giyasova, "Development of Multilayer Photosensitive Structures Based on GaAs and Si for Optoelectronic Devices," D.Sci. thesis, Institute of Semiconductor Physics and Microelectronics, 2024. (in Uzbek)
[23] Sh. Utamuradova, Kh. Daliev, Sh. Daliev, S. Muzafarova, K. Fayzullaev, and G. Muzafarova, "Study of a solar cell with a silicon-based photodiode structure," E3S Web of Conferences, **583**, 04006 (2024). https://doi.org/10.1051/e3sconf/202458304006
[24] F. Saker, L. Remache, D. Belfennache, K.R. Chebouki, and R. Yekhlef, "Effect of porosity of mesoporous silicon substrates on CdS thin films deposited by chemical bath deposition," Chalcogenide Letters, **22**(2), 151–166 (2025). https://doi.org/10.15251/CL.2025.222.151
[25] R.I. Jasim, E.H. Hadi, A.A. Mansour, S.A. Hussein, S.S. Chiad, N.F. Habubi, Y.H. Kadhim, *et al*., "Sensing of nanostructured CdS thin films via several solution concentrations," Chalcogenide Letters, **22**(1), 43–55 (2025). https://doi.org/10.15251/CL.2025.221.43
[26] M.E. Akramov, J.R. Yusupov, M. Ehrhardt, H. Susanto, and D.U. Matrasulov, "Transparent PT-symmetric nonlinear networks" Phys. Scr. **100**, 045209 (2025). https://doi.org/10.1088/1402-4896/adb914
[27] H.A. Ahmed, M.Y. Ali, S.S. Hamood, and A.N. Abd, "The importance of CdS and ZnO-NPs in study anti-microbial activity prepared by laser ablation and simple chemical method," Chalcogenide Letters, **22**(1), 11–22 (2025). https://doi.org/10.15251/CL.2025.221.11
[28] S.M. Sze, *Semiconductor Devices Physics and Technology*, 2nd ed. (John Wiley & Sons, Inc. 2002).
[29] A. Milnes, and D. Feucht, "Heterojunctions and metal-semiconductor transitions", (Academic Press Inc. 1972).
[30] Sh.B. Utamuradova, Z.T. Azamatov, A.I. Popov, M.R. Bekchanova, M.A. Yuldoshev, and A.B. Bakhromov, East Eur. J. Phys. (3), 278-281 (2024), https://doi.org/10.26565/2312-4334-2024-3-27
[31] Sh.B. Utamuradova, Kh.S. Daliev, Sh.Kh. Daliev, S.A. Muzafarova, K.M. Fayzullaev, and G.A. Muzafarova, "Volt-ampere Characteristics of Hetero Film Photosensitive Structure Au-CdS-nSi-CdTe-Au," East Eur. J. Phys. (4), 256-261 (2024). https://doi.org/10.26565/2312-4334-2024-4-26

[32] S.M. Sze, and M.-K. Lee, *Semiconductor Devices: Physics and Technology*, 3rd ed. (Wiley, 2012).
[33] Sh.A. Mirsagatov, A.S. Achilov, and B.N. Zaveryukhin, "Thin-film detector CdTe structures with a Schottky barrier," Journal of Surface Physics and Engineering, **11**(2), 216-222 (2013). https://periodicals.karazin.ua/pse/article/view/8775/8297 (in Ukrainian)
[34] J.Sh. Abdullayev, I.B. Sapaev, N.Sh. Esanmuradova, S.R. Kadirov, Sh.M. Kuliyev, East Eur. J. Phys. 2, 220 (2025). https://doi.org/10.26565/2312-4334-2025-2-24
[35] M.O. Tursunov, Kh.M. Iliev, and B.K. Ismaylov, "High-temperature analysis of silicon properties with manganese-oxygen binary complexes," Physical Sciences and Technology, 11(1-2), 4-12 (2024). https://doi.org/10.26577/phst2024v11i1a1
[36] K. Zanio, *Semiconductors and semimals*, (Acad. Press, 1978).
[37] A.Yu. Leiderman, M.K. Minbaeva, FTP, 30 (11) 1729 (1996).
[38] Sh.A. Mirsagatov, A.Yu. Leiderman, B.U. Aitbaev, and M.A. Makhmudov, "Investigation of current-voltage characteristics of the n-CdS-p-CdTe structure with an extended layer of the intermediate solid solution," Phys. Solid State, **51**, 2032–2039 (2009). https://doi.org/10.1134/S1063783409100072
[39] Sh.A. Mirsagatov, A.K. Uteniyazov, and A.S. Achilov, "Mechanism of current transport in Schottky barrier diodes based on coarse-grained CdTe films," Phys. Solid State, **54**, 1751–1763 (2012). https://doi.org/10.1134/S1063783412090193
[40] R. Triboulet, P. Siffert, CdTe and Related Compounds; Physics, Defects, Heteroand Nano-Structures, Crystal Growth, Surfaces and Applications, Elsevier, (2010). https://doi.org/10.1016/C2009-0-61369-6
[41] S. Saidov, A.Yu. Leyderman, Sh.N. Usmonov, and K.A. Amonov, "Effect of injection depletion in p-Si–n-$(Si_2)_{1-x}(ZnSe)_x$ $(0 \le x \le 0.01)$ heterostructure," Semiconductors, **52**(9), 1188-1192 (2018). https://doi.org/10.1134/S1063782618090142
[42] A.H. Munshi, et al., "Polycrystalline CdSeTe/CdTe absorber cells with 28 mA/cm^2 short-circuit current," IEEE J. Photovoltaics 8 (1) (2018). https://doi.org/10.1109/JPHOTOV.2017.2775139
[43] K. Zanio, *Cadmium telluride. Semiconductors and semimetals*, edited by R.K. Willardson, and C. Beer, (NY, 1978).
[44] S.H. Wei, S.B. Zhang, and A. Zunger, "First-principles calculation of band offsets, optical bowings, and defects in CdS, CdSe, CdTe, and their alloys," J. Appl. Phys, **87**(3), 1304-1311 (2000). https://doi.org/10.1063/1.372014
[45] A.S. Saidov, K.A. Amonov, and A.Yu. Leiderman, "Study of the dependence of the current-voltage characteristic of p-Si–n-(Si2)1-x-y(Ge2)x(ZnSe)y structures on temperature," Computational nanotechnology, **6**(3), 16-20 (2019). (in Russian)
[46] S. Rakhmanov, K. Matchonov, H. Yusupov, K. Nasriddinov, and D. Matrasulov, "Optical high harmonic generation in Dirac materials," **98**, 35 (2025). https://doi.org/10.1140/epjb/s10051-025-00885-7
[47] G. Ghibaudo, and Q. Rafhay, "Electron and Hole Mobility in Semiconductor Devices," in: Wiley Encyclopedia of Electrical and Electronics Engineering, (France, 2014), pp 1-13. https://doi.org/10.1002/047134608X.W3148.pub2
[48] A.Yu. Leiderman, and M.K. Minbaeva, "Mechanism of rapid growth of forward current in semiconductor diode structures," FTP, **30**(11), 1729-1738 (1996). (in Russian)
[49] W. Shockley, W. Read, jr, "Statistics of the Recombinations of Holes and Electrons," Phys. Rev. **87**, 835 (1952). https://doi.org/10.1103/PhysRev.87.835
[50] Sh.A. Mirsagatov, and B.U. Aitbaev, V. Rubinov, FTP, 30, 550 (1996). (in Russian)
[51] M. Lampert, and P. Mark, *Currents Injection in solids*, (Academic Press, New York, 1973).
[52] J.B. Garcia, Indium Gallium Nitride Multijunction Solar Cell Simulation Using Silvaco Atlas, Security, 110, (2007)
[53] J.L. Gray, Handbook of Photovoltaic Science and Engineering, Chapter 3, (John Wiley & Sons, Ltd, 2003), pp. 61–112.
[54] Sh.A. Mirsagatov, and I.B. Sapaev, "Mechanism of charge transfer in injection photodetectors based on the M(In)-*n*-CdS-*p*-Si-M(In) structure," Phys. Solid State, **57**, 659–674 (2015). https://doi.org/10.1134/S1063783415040162
[55] I. Zidani, Z. Bensaad, L. Hafaifa, H. Abid, A. Hafaifa, East Eur. J. Phys. 1, 141 (2025), https://doi.org/10.26565/2312-4334-2025-1-13
[56] Z.T. Azamatov, Sh.B. Utamuradova, M.A. Yuldoshev, and N.N. Bazarbaev. "Some properties of semiconductor-ferroelectric structures," East Eur. J. Phys. (2), 187-190. (2023), https://doi.org/10.26565/2312-4334-2023-2-19
[57] J.P. Ponpon, "A review of ohmic and rectifying contacts on cadmium telluride," Solid State Electron. 28 (7) 1985). https://doi.org/10.1016/0038-1101(85)90019-X

МЕХАНІЗМ ПЕРЕНОСУ СТРУМУ В ТОНКОСНОВНІЙ ГЕТЕРОСИСТЕМІ НА ОСНОВІ СПОЛУК A^2B^6

Ш.Б. Утамурадова[a], Ф.А. Гіясова[b], Х.Н. Бахронов[c], М.А. Юлдошев[d], М.Р. Бекчанова[f], Б. Ісматов[e]
[a]*Інститут фізики напівпровідників та мікроелектроніки Національного університету Узбекистану. Ташкент, Узбекистан*
[b]*Міжнародний університет Кімьо в Ташкенті, Узбекистан*
[c]*Ташкентський університет інформаційних технологій імені Мухаммада аль-Хорезмі, Узбекистан*
[d]*Міжнародний університет Туран, Наманган, Узбекистан*
[e]*Ташкентський інститут інженерів іригації та механізації сільського господарства Національний дослідницький університет, Узбекистан*
[f]*Університет громадської безпеки Республіки Узбекистан*

Представлено можливість створення гетеросистеми на основі сполук A^2B^6 з потенційними бар'єрами (Au)CdS/Si/CdTe(Au) з мінімальною густиною поверхневих станів, що підтверджено вимірюваннями висоти потенційного бар'єру на основі вольтажних методів. Визначено різні експоненціальні залежності струму від напруги при прямих зміщеннях, пов'язані зі зміною кінетичних параметрів бази структури CdS/Si/CdTe, і виявлено, що при густинах струму $2{,}1\times10^{-7} \div 0{,}35\times10^{-6}$ А/см$^{-2}$ у досліджуваній структурі CdS/Si/CdTe струм обмежується рекомбінацією в шарі просторового заряду. Показано, що при прикладенні до структури зворотного зміщення база структури повністю покривається просторовим зарядом, що супроводжується інжекцією електронів з тильного контакту, що, у свою чергу, визначає механізм передачі струму структури.
Ключові слова: *гетеросистема; осадження; база; шар; бар'єр; фотодіод; густина струму; ємність; SEM; зонна діаграма*

DOI:10.26565/2312-4334-2025-3-32 ISSN 2312-4334

ELECTRICAL, OPTICAL, AND STRUCTURAL PROPERTIES OF SILICON n^+-p STRUCTURES

Mykola S. Kukurudziak[a,b]*, Dmytro P. Koziarskyi[a], Ivan P. Koziarskyi[a], Eduard V. Maistruk[a], Maria I. Ilashchuck[a], Dmytro V. Kysil[c]

[a]Yuriy Fedkovych Chernivtsi National University, Kotsyubyns'kogo str. 2, 58012, Chernivtsi, Ukraine
[b]Rhythm Optoelectronics Shareholding Company, Holovna str. 244, 58032, Chernivtsi, Ukraine
[c]V.E. Lashkaryov Institute of Semiconductor Physics, NAS of Ukraine, Pr. Nauky 41, 03028, Kyiv, Ukraine
**Corresponding Author E-mail: mykola.kukurudzyak@gmail.com*
Received April 14, 2025; revised May 7, 2025; accepted August 2, 2025

The article investigates the structural, optical, and electrical properties of silicon n^+-p structures. The experimental samples were made from high-resistance single-crystal silicon using two-stage phosphorus diffusion from solid-state planar sources. It was found that the introduction of phosphorus impurities with a concentration of $1.2\cdot10^{20}$ cm^{-3} provokes the formation of dislocations with a surface density of $2\cdot10^3$-$3\cdot10^3$ cm^{-2} due to the formation and relaxation of mechanical stresses. The formation of a lightening oxide film on the silicon surface reduces the reflection coefficient by 25%. However, the formation of an n^+-layer reduces the transmittance coefficient of the structure. It was established from the voltage-current characteristics of the n^+-p structure under forward and reverse voltage bias, that in the temperature range T = 295–346 K, these structures have rectifying properties. At room temperature, the height of the potential barrier is 0.6 eV and decreases with temperature and its height at 0 K is 1.32 eV. At low forward biases, the dominant mechanism of current transport in the structure is superbarrier emission. With an increase in forward voltage from 0.1 V to 0.6 V, the generation-recombination mechanism prevails, and with an increase in temperature, an increase in the contribution of tunnel current is observed. At low reverse voltages, the *I-V* characteristics of diodes are well described by the formula for the generation current. The depth of occurrence of donor energy levels, from which thermal generation of charge carriers occurs is 0.15 eV.
Keywords: *Semiconductors; Thin film; SEM; Electrical conductivity; Structural defects; Reflection; Electromagnetic field sensor; Sensors; Ion implantation; Doping*
PACS: 61.72. Ji, 61.72. Lk, 85.60. Dw

The functioning of virtually all semiconductor devices is based on the physical phenomenon of p-n junction – the boundary between two semiconductor regions with different types of conductivity. Silicon n^+-p junctions are one of the fundamental elements of modern electronics and photonics, due to the high technological capabilities and widespread availability of the base material [1, 2]. Thanks to the combination of a heavily doped n-region (n^+) with p-type silicon, this structure provides unique electrophysical properties that are widely used in power semiconductor devices such as rectifiers [3, 4], thyristors [5, 6], and Schottky diodes [7, 8]. At the same time, n^+-p structures are important for photovoltaic devices, particularly in solar cells [9, 10] electromagnetic field sensors, photodetectors or another sensors [11, 12]. This structure creates an electric field in the depletion region, which allows for effective control of charge carrier movement [13]. Special attention to n^+-p junctions is due to their important role in reducing energy losses, increasing device speed, and improving energy conversion efficiency.

With the growing demand for energy-efficient and compact electronic components, as well as the development of micro- and nanofabrication technologies, n^+-p junctions remain the focus of scientists and developers. Current research focuses on improving doping technologies [14], reducing surface defects [15], passivation [16], and integrating silicon structures with new materials – particularly in the context of creating high-efficiency solar cells and powerful new-generation electronics [17].

Silicon n^+-p junctions can be formed by various methods, including ion implantation and thermal diffusion doping. We have established that the method of doping silicon substrates to create n^+-p junctions and the concentration of the dopant significantly affect the photovoltaic properties of the final products [18]. In particular, phosphorus diffusion from solid-state planar sources [19] allows for low structural defects densities even at high impurity concentrations compared to doping from liquid-phase sources [20]. However, the kinetic and electrical properties of silicon n^+-p structures based on high-resistance base material have not been studied, since most of the work is devoted to low-resistance silicon, which is mainly used for solar cells [9,10, 14, 17]. Thus, the aim of this work is to study the electrical properties of planar n^+-p structures based on high-resistance silicon obtained by phosphorus diffusion from solid sources, and also to investigate the change in the optical and structural properties of silicon after doping.

EXPERIMENTAL

The base material was monocrystalline p-Si with a resistivity of ρ = 18-19 kΩ·cm and crystallographic orientation [111]. The experimental samples were silicon substrates with an n^+-p junction formed by two-stage phosphorus diffusion from solid planar sources using the modes given in [18]. The area of the substrates was 28.3 mm^2

Cite as: M.S. Kukurudziak, D.P. Koziarskyi, I.P. Koziarskyi, E.V. Maistruk, M.I. Ilashchuck, D.V. Kysil, East Eur. J. Phys. 3, 336 (2025), https://doi.org/10.26565/2312-4334-2025-3-32
© M.S. Kukurudziak, D.P. Koziarskyi, I.P. Koziarskyi, E.V. Maistruk, M.I. Ilashchuck, D.V. Kysil, 2025; CC BY 4.0 license

and 500 μm thick. Surface resistance (R_S) was measured using a four-probe method. The surface resistance after phosphorus pre-deposition reached $R_S \approx 4.1$-4.2 Ω/□, and after phosphorus driving-in reached $R_S \approx 2.7$-2.8 Ω/□. The antireflective SiO_2 on the surface of the experimental samples was formed by oxidation in a dry oxygen atmosphere during phosphorus driving-in and reached d_{SiO2} = 180-200 nm.

The depth of the diffusion layer (x_{n+-p}) was measured using scanning electron microscopy (SEM, Tescan Lyra 3). To investigate the defective structure of the silicon substrates chemical treatment was performed in selective Sirtle`s etchant [20] with the following composition: HF—100 cm^3, CrO_3 50 g, H_2O—120 cm^3. The density of dislocations was calculated by the metallographic method [21]. The transmission spectra were investigated using NIKOLET 6700 and SF-2000 spectrophotometer at room temperature. For measuring reflection (R) UV-Vis spectrophotometer Specord 210 plus was used. Reflection spectra were measured in total reflection geometry using additional equipment – an integrating sphere. The *I-V* characteristics (at T = 295-346 K) of the samples were measured using a hardware-software complex implemented on the basis of the Arduino platform, an Agilent 34410 A digital multimeter and a Siglent SPD3303X programmable power source, which were controlled by a personal computer using software created by the authors in the LabView environment. Experimental studies of kinetic phenomena in silicon n^+-layers were conducted in the temperature range T = 290-380 K based on measurements of the Hall effect in film structures [22], considers that the n^+-layer is a thin film.

RESULTS OF THE RESEARCH AND THEIR DISCUSSION

A) Structural and optical properties of silicon n^+-p structures

After phosphorus pre-deposition, the depth of the diffusion layer reached x_{n+-p} = 0.8–1 μm, and after driving-in, it reached x_{n+-p} = 4.2–4.4 μm (Fig. 1). The measurements correlate well with the values obtained by the layer-slab method.

The density of dislocations in the base silicon reached about N_{dis} = 10-20 cm^{-2} (Fig. 2a). After phosphorus diffusion, the density of structural defects increased to $N_{dis} = 2\cdot10^3$-$3\cdot10^3$ cm^{-2} (Fig. 2b). The increase in the density of structural defects is caused by the introduction of an impurity with a larger atomic radius than silicon, which leads to the emergence of mechanical stresses. Accordingly, their relaxation during heat treatment occurs with the formation of dislocations [23]. However, such an increase in defect density does not lead to a significant deterioration in the electrophysical characteristics of structures [24].

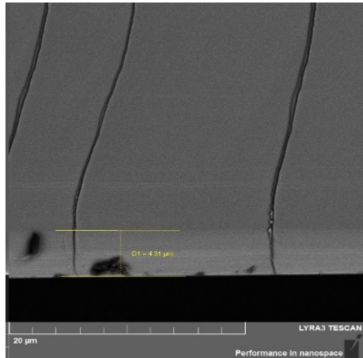

Figure 1. SEM photo of a silicon substrate chip with an n^+-layer

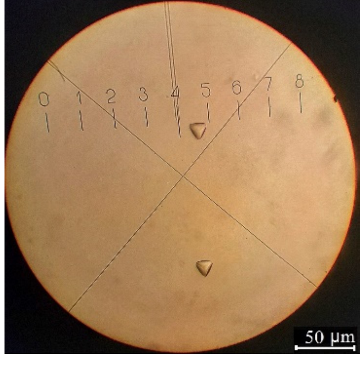

a

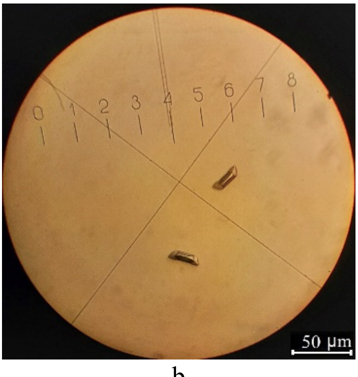

b

Figure 2. Images of dislocations on the surface of p-Si (a) and n^+-Si (b)

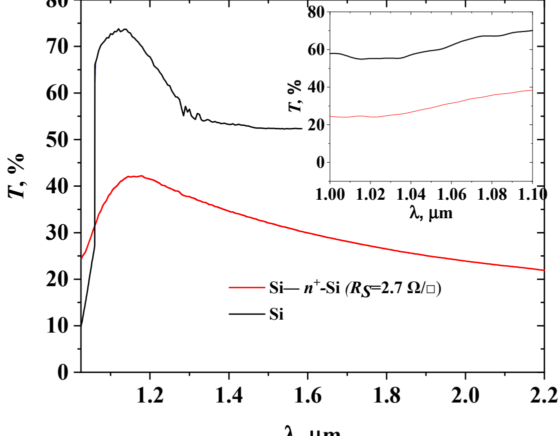

Figure 3. The transmission spectrum of silicon and its n^+-p structure (without SiO_2) (inset the range of λ = 1-1.1 μm)

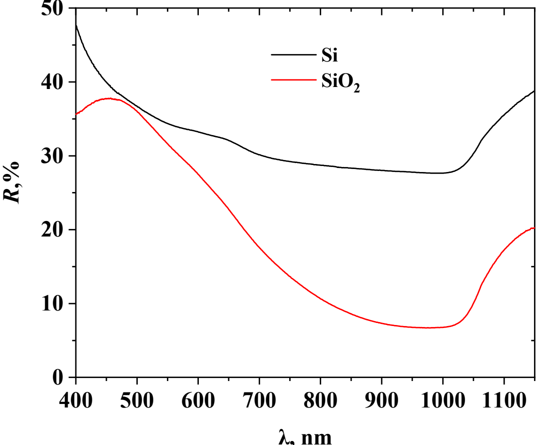

Figure 4. Reflection spectrum of Si and SiO_2

The formation of n^+-layers on the Si surface causes a significant decrease in the transmission coefficient of structures (Fig. 3), which is negative in the case of the need to ensure radiation absorption in the high-resistance region of the structure, for example, in the manufacture of *p-i-n* photodiodes [25]. Thus, in the range of λ = 1-1.1 µm (Fig. 3 inset), the difference in the transmittance coefficients of Si and silicon n^+-*p* structure reaches about 30%. This difference increases with increasing wavelengths.

However, the formation of SiO_2 on the surface of n^+-*p* structure significantly reduces the coefficient of radiation reflection compared to the case without thin film of oxide (Fig. 4). Thus, in the case under study, the difference in reflection coefficients in the range of 950-1050 nm reached about 25%, since the obtained thickness of SiO_2 corresponds to the condition of minimum reflection for these wavelengths [26].

B) Kinetic properties of silicon n^+-layers

Studies of silicon n^+-layers at T = 290-380 K showed that the Hall coefficient in this temperature range remains practically unchanged (Fig. 5). This indicates that at these temperatures, the concentration of charge carriers does not change (Fig. 5 inset), due to the depletion of impurity levels at these temperatures [22]. The electron concentration reached about $n \approx 1.2\cdot10^{20}$ cm^{-3}, which correlates well with the phosphorus concentrations determined in [19].

With increasing temperature, a decrease in electrical conductivity is observed (Fig. 6) due to a decrease in Hall mobility (Fig. 6 inset), since in this temperature range, charge carriers are scattered by thermal vibrations of the crystal lattice.

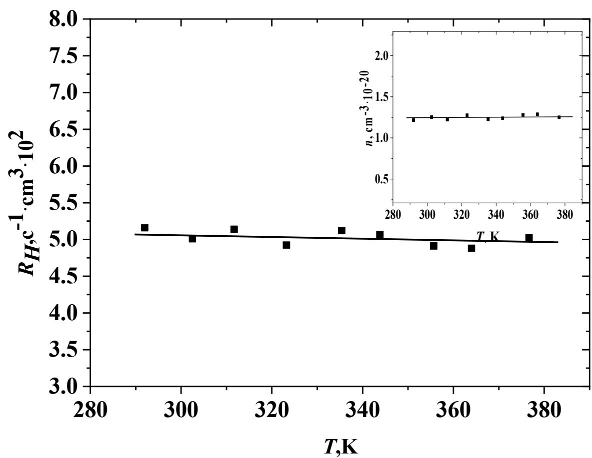

Figure 5. Temperature dependence of the Hall coefficient and electron concentration (inset) in a silicon n^+-layer

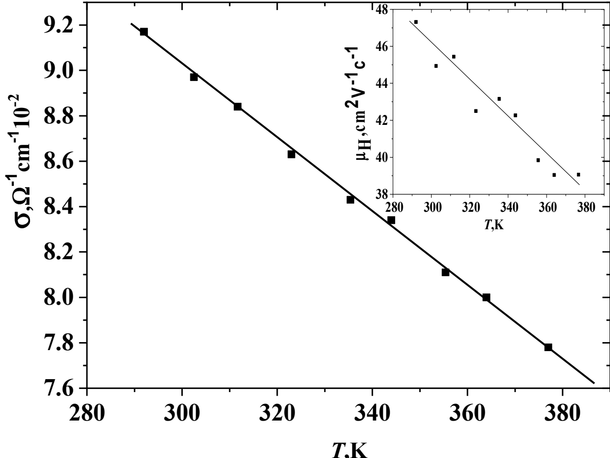

Figure 6. Temperature dependence of electrical conductivity and Hall mobility (inset) of a silicon n^+-layer

C) Electrical properties of silicon n^+-layers

From the voltage-current characteristics of the n^+-*p* structure at forward (Fig. 7) and reverse (Fig. 8) bias voltages, it can be seen that in the temperature range T = 295 – 346 K, these structures have rectifying properties. The rectification coefficient determined at T = 295 K and voltages $|V|$ = 0.6 V is equal to $RR \sim 10^5$.

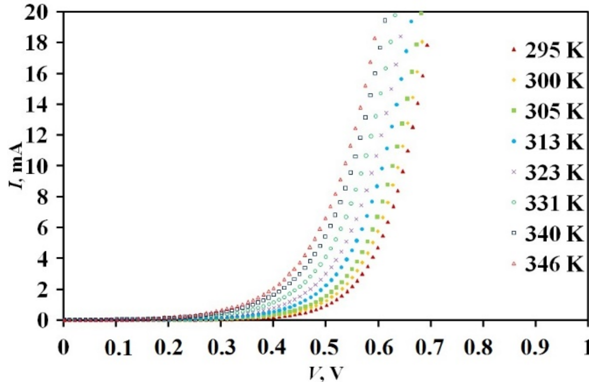

Figure 7. *I-V* characteristics of the n^+-*p* junction at forward biases in the temperature range from 297 K to 346 K

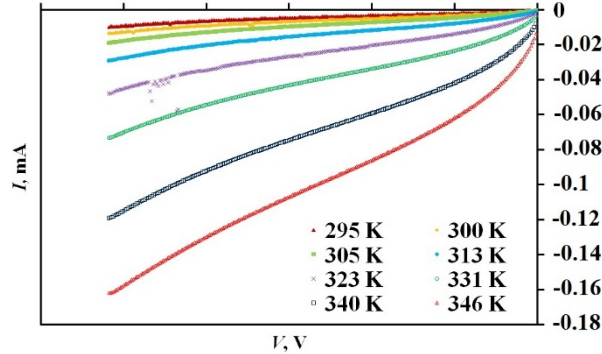

Figure 8. *I-V* characteristics of the n^+-*p* junction at reverse biases in the temperature range from 297 K to 346 K

The height of the potential barrier ($q\varphi_k$) was estimated by extrapolating the linear sections of the *I-V* characteristics in the forward voltage bias region. At room temperature, the height of the potential barrier is $q\varphi_k \sim 0.6$ eV and decreases with temperature (Fig. 9).

When the temperature is increased from $T = 295$ K to $T = 346$ K (Fig. 9), there is a linear decrease in the energy $q\varphi_k$ from 0.6 eV to 0.49 eV. This dynamic change occurs as a result of a decrease in the height of the potential barrier and is described by the equation [27]:

$$q\varphi_k(T) = q\varphi_k(0) - \beta_\varphi T \tag{1}$$

where β_φ is the temperature coefficient of the potential barrier height, and $q\varphi_k(0)$ is the value of the potential barrier height of the n^+-p structure at absolute zero temperature.

Using equation (1) and Fig. 9, we find the temperature coefficient of change in the height of the potential barrier and its height at 0 K, which are equal to $d(q\varphi_k)/dT = -2.45\cdot10^{-3}$ eV/K i $q\varphi_k(0\text{ K}) = 1.32$ eV, respectively.

Based on the values of the sequential resistance R_S of the structure determined at different temperatures along the linear sections of the direct branches of the *I-V* curve, the temperature dependence $lnR_S = f(10^3/T)$ was constructed (Fig. 10) and the activation energy $E_A = 0.25$ eV was determined, which characterizes the temperature dependence of the electrical conductivity of the structure components.

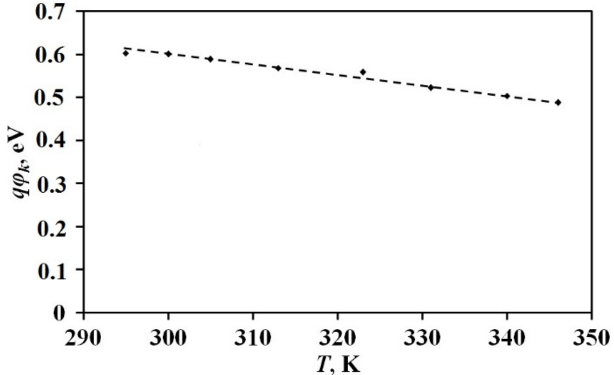

Figure 9. Temperature dependence of the height of the potential barrier

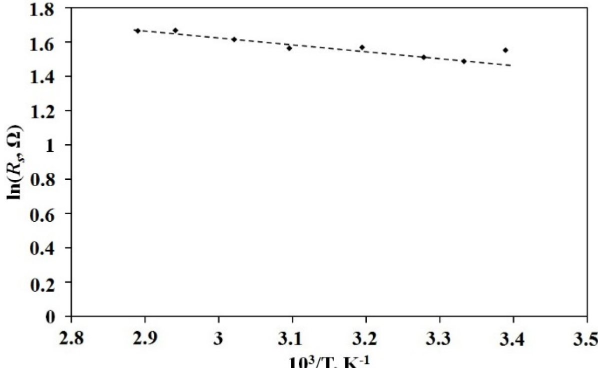

Figure 10. Temperature dependence of series resistance

To determine the mechanism of current flow through the junction at forward bias, the *I-V* characteristics are plotted in the coordinates $lnI = f(V)$ (Fig. 11). Fig. 11 shows two straight segments with different angles of inclination to the voltage axis. Based on the tangents of these angles, we determine the coefficient of n^+-p junction imperfection n (Fig. 12).

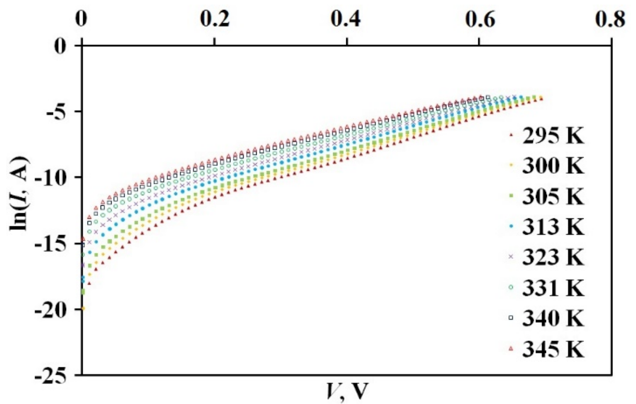

Figure 11. Temperature dependencies of $lnI = f(V)$ n^+-p junction at forward bias

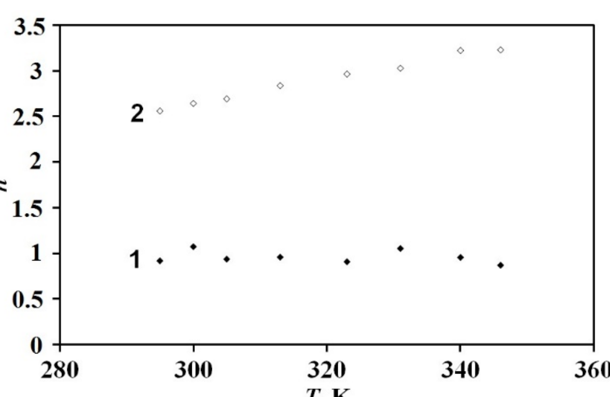

Figure 12. Temperature dependence of the imperfection coefficient at forward bias:
1 - $3kT/q < V < 0.1$ V; 2 – $0.1\text{ V} < V < 0.6$ V

At small forward biases $3kT/q < V < 0.1$ V, the slope to the voltage axis of linear dependencies $lnI = f(V)$ is characterized by the value of the imperfection coefficient $n \approx 1$ (Fig. 12-1), accordingly, the dominant mechanism of current transport is superbarrier emission. With an increase in direct voltage 0,1 V < V < 0.6 V, the imperfection coefficient is equal to $n \approx 2.5$ - 3 (Fig. 12-2), which indicates the predominance of the generation-recombination mechanism of current transport at room temperatures and an increase in the contribution of the tunnel current with increasing temperature.

It can be assumed that, in some approximation, the *I-V* characteristics of diodes are described by the equation for the recombination current density [23]:

$$j = \frac{qn_iW_i}{\tau}\left(e^{\frac{qV}{2kT}} - 1\right) = \frac{n_i}{\tau}\sqrt{\frac{2q}{N_A}(\phi_k - V)}\left(e^{\frac{qV}{2kT}} - 1\right), \tag{2}$$

where q is the charge of electron, n_i is the value of the intrinsic concentration of charge carriers, W_i is the thickness of the depleted region, τ is the lifetime of charge carriers in this region, and N_A is the concentration of acceptor impurities.

At low reverse voltages, the *I-V* characteristics of struscures are well described by the formula for the generation current (the multiplier before the brackets in expression 2), which is confirmed by the linear nature of the dependencies $I = f(\varphi_k - V)^{1/2}$ (Fig. 13).

Determined from the dependence $lnI_{rev} = f(10^3/T)$ (Fig. 14), obtained at a constant voltage value, the depth of the acceptor energy levels from which thermal generation of charge carriers occurs was $\Delta E \approx 0.15$ eV at -100 < V < 0 V.

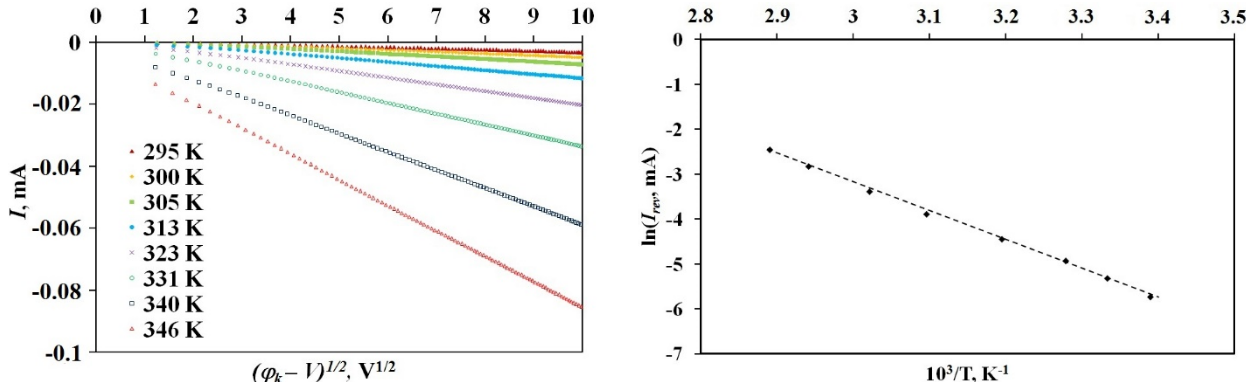

Figure 13. Reverse branches of *I-V* characteristics in coordinates $I = f(\varphi_k - V)^{1/2}$ at different temperatures

Figure 14. Dependence of $lnI_{rev} = f(10^3/T)$ at reverse bias

The reverse branches of the *I-V* characteristic at temperatures T = 295–346 K are described by the equation for tunnel current [27]:

$$I_t = a_0\, exp\left(-b_0(\phi_k - V)^{-1/2}\right), \tag{3}$$

where a_0 is a parameter, whose value is determined by the probability of filling the energy levels from which electron tunneling occurs, b_0 is determined by the rate of change of the current with voltage.

According to (2), the reverse *I-V* curves in the coordinates $ln(I_{rev}) = f(\varphi_k - qV)^{-1/2}$ will be linear, as observed in Fig. 15.

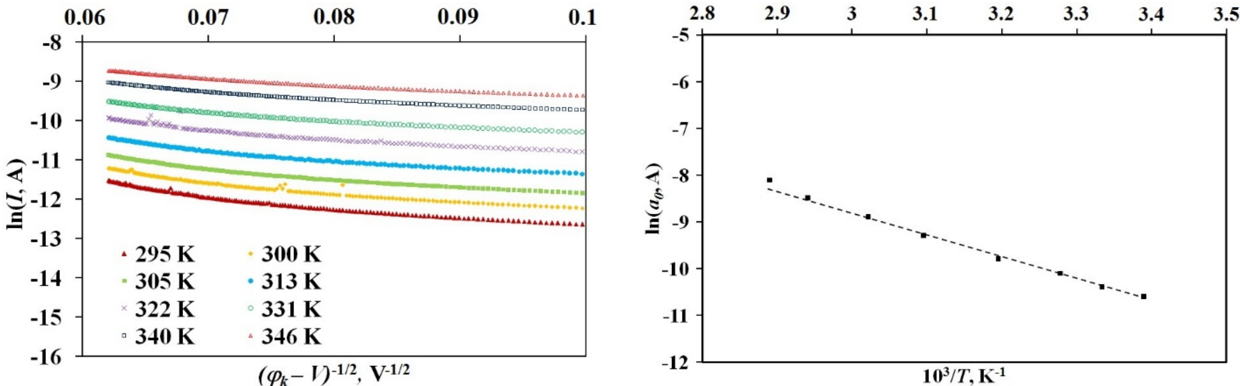

Figure 15. Dependence of tunnel current on reverse external displacement in the temperature range T = 295-346 K

Figure 16. Dependence $lga_0 = f(10^3/T)$ at reverse bias

The energy level value at large reverse biases (-100 < V), from which electron tunneling occurs, was calculated from the temperature dependence of the parameter a_0, which in the coordinates $lga_0 = f(10^3/T)$ is approximated by a straight line (Fig. 16). The parameter a_0 was determined by extrapolating the straight sections $ln(I_{rev}) = f(\varphi_k - qU_{зм})^{-1/2}$ to the current axis. The established depth of the energy level was 0.2 eV.

CONCLUSIONS

The structural, optical, and electrical properties of n^+-p structures of high-resistance silicon were investigated. The following conclusions were made during the research:

1. The introduction of phosphorus impurities with a concentration of $1.2 \cdot 10^{20}$ cm^{-3} provokes the formation of dislocations with a surface density of $2 \cdot 10^3$-$3 \cdot 10^3$ cm^{-2}
2. The formation of anti-reflective SiO_2 on the silicon surface reduces the reflection coefficient by 25%.
3. The formation of an n^+-layer reduces the transmittance coefficient of the structure relative to the transmittance coefficient of silicon.

4. At room temperature, the height of the potential barrier of the n^+-p structure is 0.6 eV and decreases with increasing temperature, and its height at 0 K is 1.32 eV.

5. At low forward voltages, the dominant mechanism of current flow in the structure is superbarrier emission. With an increase in forward voltage, the generation-recombination mechanism prevails, and with an increase in temperature, an increase in the contribution of tunnel current is observed.

6. At low reverse voltages, the generation mechanism of current transport prevails.

Acknowledgments

This work was partially supported by the Ministry of Education and Science of Ukraine (grant number 0125U000832, Rational design of quaternary detector materials for remote devices operating in conditions of significant radiation exposure, authors M.S. Kukurudziak).

ORCID

Mykola S. Kukurudziak, https://orcid.org/0000-0002-0059-1387; **Dmytro P. Koziarskyi,** https://orcid.org/0000-0002-9618-0418; **Ivan P. Koziarskyi,** https://orcid.org/0000-0002-4984-4349; **Eduard V. Maistruk**, https://orcid.org/0000-0002-9025-6485; **Maria I. Ilashchuck,** https://orcid.org/0000-0002-7618-0437; **Dmytro V. Kysil,** https://orcid.org/0000-0003-4637-9397

REFERENCES

[1] C. Ballif, F.J. Haug, M. Boccard, P.J. Verlinden, and G. Hahn, Nature Reviews Materials, **7**(8), 597 (2022). https://doi.org/10.1038/s41578-022-00423-2

[2] X. Pan, S. Li, Y. Li, P. Guo, X. Zhao, and Y. Cai, Minerals Engineering, **183**, 107600 (2022). https://doi.org/10.1016/j.mineng.2022.107600

[3] B.J. Baliga, IEEE Journal of Emerging and Selected Topics in Power Electronics, **11**(3), 2400-2411 (2023). https://doi.org/10.1109/JESTPE.2023.3258344

[4] R. Gupta, J.A. Fereiro, A. Bayat, A. Pritam, M. Zharnikov, and P.C. Mondal, Nature Reviews Chemistry, **7**(2), 106-122 (2023). https://doi.org/10.1038/s41570-022-00457-8

[5] C. Shen, S. Jahdi, O. Alatise, J. Ortiz-Gonzalez, A. Aithal, and P. Mellor, IEEE Open Journal of Power Electronics, **2**, 145-154 (2021). https://doi.org/10.1109/OJPEL.2021.3060942

[6] M. Faizan, X. Wang, and M. Z. Yousaf. Electronics, **12**(13), 2850 (2023). https://doi.org/10.3390/electronics12132850

[7] J.O. Bodunrin, D.A. Oeba, and S.J. Moloi, Sensors and Actuators A: Physical, **331**, 112957 (2021). https://doi.org/10.1016/j.sna.2021.112957

[8] Z. Berktaş, M. Yıldız, E. Seven, E.O. Orhan, and Ş. Altındal. Flat. Chem. **36**, 100436 (2022). https://doi.org/10.1016/j.flatc.2022.100436

[9] H. Zhang, X. Wang, X. Chen, and Y. Zhang, Nano Energy, 110715 (2025). https://doi.org/10.1016/j.nanoen.2025.110715

[10] M.A., Green, and Z. Zhou, Nature Communications, **16**(1), 251(2025). https://doi.org/10.1038/s41467-024-55681-1

[11] R.L. Politanskyi, P.M. Shpatar, M.V. Vistak, I.T. Kogut, I.S. Diskovskyi, and Y.A. Rudyak, Physics and Chemistry of Solid State, **24**(3), 433-440 (2023). https://doi.org/10.15330/pcss.24.3.433-440

[12] M.S. Kukurudziak, and E.V. Maistruk, in: *Fifteenth International Conference on Correlation Optics*, 121261V (SPIE, Chernivtsi, 2021). https://doi.org/10.1117/12.2616170

[13] I.P. Koziarskyi, E.V. Maistruk, I.G. Orletskyi, M.I. Ilashchuk, D.P. Koziarskyi, P.D. Maryanchuk, M.M. Solovan, and K.S. Ulyanytskiy, Semiconductor Science and Technology, **35**(2), 025018 (2020). https://doi.org/10.1088/1361-6641/ab6107

[14] I. García, in: *Fundamentals of Solar Cells and Photovoltaic Systems Engineering*, (Academic Press, 2025), pp. 129-171. https://doi.org/10.1016/B978-0-323-96105-9.00005-7

[15] F.L. Via, M. Zimbone, C. Bongiorno, A. La Magna, G. Fisicaro, I. Deretzis, and P. Wellmann, Materials, **14**(18), 5348 (2021). https://doi.org/10.3390/ma14185348

[16] J. Panigrahi, and V.K. Komarala, Journal of non-crystalline solids, **574**, 121166 (2021). https://doi.org/10.1016/j.jnoncrysol.2021.121166

[17] J. Pastuszak, and P. Węgierek, "Photovoltaic cell generations and current research directions for their development," Materials, **15**(16), 5542 (2022). https://doi.org/10.3390/ma15165542

[18] M.S. Kukurudziak, Semiconductor Physics, Quantum Electronics & Optoelectronics, **25**(4), 385 (2022). https://doi.org/10.15407/spqeo25.04.385

[19] M.S. Kukurudziak, Physics and Chemistry of Solid State, **23**(4), 756 (2022). https://doi.org/10.15330/pcss.23.4.756-763

[20] E. Sirtl, and A. Adler, International Journal of Materials Research, **52**(8), 529 (1961). https://doi.org/10.1515/ijmr-1961-520806 (in German)

[21] S.N. Knyazev, A.V. Kudrya, N.Y. Komarovsky, Y.N. Parkhomenko, E.V. Molodtsova, and V.V. Yushchuk, Electron. Eng. Mater. **25**, 323–36 (2023). https://doi.org/10.3897/j.moem.8.4.99385

[22] E.V. Maystruk, T.T. Kovalyuk, M.M. Solovan, and P.D. Maryanchuk. Journal of Nano- and Electronic Physics, **10**(5), 05028 (2018). https://10.21272/jnep.10(5).05028

[23] K.V. Ravi, *Imperfections and impurities in semiconductor silicon*, (Wiley, New York, 1981).

[24] M.S. Kukurudziak, East Eur. J. Phys. (2), 345 (2024). https://doi.org/10.26565/2312-4334-2024-0-41

[25] M.S. Kukurudziak, E.V. Maistruk, East Eur. J. Phys. (1), 386 (2024), https://doi.org/10.26565/2312-4334-2024-1-39

[26] S.B. Khan, S. Irfan, Z. Zhuanghao, and S.L. Lee, Materials, **12**(9), 1483 (2019). https://doi.org/10.3390/ma12091483

[27] H.P. Parkhomenko, M.M. Solovan, A.I. Mostovyi, I.G. Orletskyi, and V.V. Brus, East. Eur. J. Phys. (4), 43 (2021). https://doi.org/10.26565/2312-4334-2021-4-04

ЕЛЕКТРИЧНІ, ОПТИЧНІ ТА СТРУКТУРНІ ВЛАСТИВОСТІ КРЕМНІЄВИХ n^+-p СТРУКТУР

Микола С. Кукурудзяк[a,b], Дмитро П. Козярський[a], Іван П. Козярський[a], Едуард В. Майструк[a], Марія І. Ілащук[a], Дмитро В. Кисіль[c]
[a]*Чернівецький національний університет імені Юрія Федьковича, 58002, м. Чернівці, вул. Коцюбинського, 2, Україна*
[b]*АТ «Центральне конструкторське бюро Ритм», 58032, м. Чернівці, вул. Головна, 244, Україна*
[c]*Інститут фізики напівпровідників ім. В.Е. Лашкарьова, НАН України, 03028, м. Київ, пр. Науки, 41, Україна*

У статті досліджено структурні, оптичні та електричні властивості кремнієвих n^+-p структур. Експериментальні зразки були виготовлені з високоомного монокристалічного кремнію з використанням двостадійної дифузії фосфору з твердотільних планарних джерел. Було встановлено, що введення домішок фосфору з концентрацією $1{,}2\cdot10^{20}$ см$^{-3}$ провокує утворення дислокацій з поверхневою густиною $2\cdot10^3$-$3\cdot10^3$ см$^{-2}$ внаслідок утворення та релаксації механічних напружень. Утворення противідбиваючої оксидної плівки на поверхні кремнію зменшує коефіцієнт відбиття на 25 %. Однак утворення n^+-шару зменшує коефіцієнт пропускання структури. З вольт-амперних характеристик n^+-p структур при прямому та зворотному зміщенні напруги було встановлено, що в діапазоні температур T = 295–346 K ці структури мають випрямні властивості. При кімнатній температурі висота потенційного бар'єру становить 0,6 еВ і зменшується з підвищенням температури, а його висота при 0 K становить 1,32 еВ. При низьких прямих напругах домінуючим механізмом струмопереносу в структурі є надбар'єрна емісія. Зі збільшенням прямої напруги від 0,1 В до 0,6 В переважає механізм генерації-рекомбінації, а зі збільшенням температури спостерігається збільшення внеску тунельного струму. При низьких зворотних напругах вольт-амперні характеристики діодів добре описуються формулою для струму генерації. Глибина залягання енергетичного донорного рівня, з якого відбувається теплова генерація носіїв заряду, становить 0,15 еВ.

Ключові слова: *напівпровідники; тонкі плівки; SEM; електропровідність; структурні дефекти; відбиття; датчик електромагнітного поля; датчики; іонна імплантація; легування*

East European Journal of Physics. **3.** 343-347 (2025)
DOI:10.26565/2312-4334-2025-3-33 ISSN 2312-4334

EFFECT OF DYSPROSIUM ATOMS INTRODUCED DURING THE GROWTH PHASE ON THE FORMATION OF RADIATION DEFECTS IN SILICON CRYSTALS

Khodjakbar S. Daliev[a], **Sharifa B. Utamuradova**[b], **Shakhrukh Kh. Daliev**[b], **Jonibek J. Khamdamov**[b], **Shahriyor B. Norkulov**[b]*
[a]*Branch of the Federal State Budgetary Educational Institution of Higher Education "National Research University MPEI", 1 Yogdu st., Tashkent, Uzbekistan*
[b]*Institute of Semiconductor Physics and Microelectronics at the National University of Uzbekistan, 20 Yangi Almazar st., Tashkent, 100057, Uzbekistan*
**Corresponding Author e-mail: nshb19990@gmail.com*
Received May 24, 2025; revised July 15, 2025; accepted August 1, 2025

In this study, the formation and reduction mechanisms of radiation defects resulting from the incorporation of dysprosium (Dy) atoms during the growth process of silicon crystals (FZ) were investigated. Deep-level defects formed after doping n-type silicon with dysprosium and irradiating it with ^{60}Co γ-rays were analyzed using Deep Level Transient Spectroscopy (DLTS). The research revealed that in the presence of dysprosium, the concentration of defects such as A-center (vacancy-oxygen complex) and E-center (vacancy-phosphorus complex) decreased significantly - by 2-4 times - compared to control samples. EDS spectral analysis was conducted to determine the concentration of surface element atoms in the sample, which demonstrated that the Dy element was uniformly distributed on the silicon surface and present in sufficient concentration. These results substantiate that Dy atoms in silicon play a passivating role, inhibiting the kinetics of radiation defect formation, consequently increasing the radiation resistance of silicon-based structures.
Keywords: *Dysprosium-doped silicon; Radiation defects; Gamma radiation; DLTS (Deep-Level Transient Spectroscopy); Neutron activation analysis; EDS (Energy Dispersive Spectroscopy); A-center; E-center; Crystal growth; Oxygen-vacancy complex; Radiation stability*
PACS: 61.72.Cc, 61.80.Ed, 61.82.Fk, 68.37.Lp

INTRODUCTION

With the rapid advancement of modern electronics, particularly in the fields of micro- and nanoelectronics, there is a growing demand for materials with enhanced physicochemical, structural, and electrical properties. In this context, silicon (Si) holds a leading position as the most widely used primary semiconductor material. Silicon crystals are utilized to produce highly integrated circuits, high-speed photodiodes, radiation-resistant detectors, memory elements, as well as solar cells and numerous other electronic devices. One of the key factors determining the reliability and stability of such devices is the nature of internal and external defects in the material [1-3].

Defects that directly affect the performance of semiconductor materials, especially in silicon, are formed as a result of the interaction between vacancies (V) created by high-energy particles (such as γ-rays, protons, neutrons, and alpha particles), substitutional donors and acceptors (P, As, B), and oxygen atoms (O) present in the crystal lattice. Consequently, complex radiation defects with deep energy levels emerge. These defects lead to the recombination of electron-hole pairs and significantly impact the sensitivity, noise level, and operational lifespan of devices [4-5].

Modern scientific research is exploring numerous approaches to reduce the formation of radiation defects, decrease their stability, or neutralize them completely. One such approach is the method of doping silicon with rare earth elements (REE) [6-11]. This approach aims, in particular, to limit the activity of defects by gettering them, that is, removing them from the active parts of the crystal lattice and binding them in structural voids or peripheral regions. Due to their large ionic radius and chemical inertness, REE atoms do not actively bond with oxygen atoms or donor elements [7]. However, they strongly interact with existing defects, reducing their energetic activity. For example, scientific literature reports that it is possible to reduce the density of A- and E-centers formed in silicon by 2-4 times using elements such as Sm, Gd, Er, and Tm [12-14].

Among rare-earth elements, dysprosium (Dy) stands out with its unique physical properties. Primarily, Dy possesses a relatively large magnetic moment, which makes it a potential material for spintronic devices. Additionally, Dy atoms easily oxidize in the crystal lattice of silicon, forming oxide nanophases in the form of Dy_2O_3[2]. These phases bind oxygen atoms to themselves, preventing the formation of vacancy oxygen complexes. As a result, the crystalline structure of silicon becomes more stable, the occurrence of defects decreases, and its radiation resistance increases. However, the new defect states that arise during the Dy doping process and their kinetic behavior have not been thoroughly studied, necessitating further research in this direction [9].

The results of this study can be applied in the development of radiation-resistant electronic devices based on silicon, including optoelectronic detectors, photodiodes, and high-reliability integrated circuits [15-18]. Additionally, through in-depth analysis of the properties of defects arising from Dy doping, new possibilities for the application of rare-earth

Cite as: Kh.S. Daliev, Sh.B. Utamuradova, Sh.Kh. Daliev, J.J. Khamdamov, Sh.B. Norkulov, East Eur. J. Phys. 3, 343 (2025), https://doi.org/10.26565/2312-4334-2025-3-33
© Kh.S. Daliev, Sh.B. Utamuradova, Sh.Kh. Daliev, J.J. Khamdamov, Sh.B. Norkulov, 2025; CC BY 4.0 license

elements in silicon materials science are identified. This holds significant importance not only for fundamental science but also for applied device technologies.

MATERIALS AND METHODS

For the study, samples of ultra-pure n-type monocrystalline silicon were used. Their resistivity ranged from 10 to 65 Ω×cm, and the concentration of optically active interstitial oxygen atoms in the crystal lattice was in the range of (5×10^{16} - 7×10^{17}) cm^{-3}. The element dysprosium (Dy) was introduced into the silicon structure as a dopant during the growth process - at the stage of crystal growth from the solution. The samples were irradiated at room temperature (300 K) using γ-quanta emitted from the ^{60}Co isotope [16,19]. The radiation intensity was 3.1×10^{12} quanta/$cm^2\times s$. For comparison, silicon samples (control samples) with the same oxygen content, but without dysprosium introduction, were irradiated under the same conditions.

Deep-level capacitance spectroscopy (DLTS) was used to detect radiation defects [8,10,21]. Schottky barriers were formed by evaporating gold (Au) onto the silicon surface under high vacuum conditions. Chemically deposited nickel (Ni) was used as the ohmic contact, and in some cases, antimony (Sb) or aluminum (Al) was additionally evaporated [20]. DLTS measurements were conducted in constant capacitance and constant voltage modes.

In addition, energy-dispersive X-ray spectroscopy (EDS) techniques were employed to evaluate the surface morphology and elemental composition of silicon samples doped with dysprosium [22,24,25].

RESULTS AND DISCUSSION

The energy characteristics of deep levels in silicon samples doped with dysprosium and in undoped control samples, both obtained by growth from solution, were determined using the DLTS method before and after each irradiation stage. The analysis revealed that the oxygen concentration differs significantly depending on the silicon composition: in oxygen-free silicon samples, the amount of optically active oxygen (N_O^{OA}) was approximately 5×10^{16} cm^{-3}, while in oxygen-containing crystals, this amount reached up to 7×10^{17} cm^{-3}. This is considered an important factor directly influencing the formation of radiation defects and the emergence of deep levels.

Fig. 1 (curve 2) shows a newly identified deep-level defect revealed by DLTS spectra of γ-irradiated n-Si<Dy> samples. This level exhibits an ionization energy of $E_c - 0.17$ eV and an electron capture cross-section of approximately $\sigma_n \approx 1\times10^{-14}$ cm^2. Based on the extracted parameters, this defect is attributed to the well-known A-center, corresponding to a vacancy–oxygen (V–O) complex [15,23].

As shown in Fig. 1 (curve 1), the presence of A-centers was observed in oxygen-containing n-Si control samples after gamma irradiation. Notably, the concentration of these centers in undoped silicon changes linearly with increasing radiation dose, while doped samples do not exhibit this characteristic. Additionally, comparative analysis revealed that the quantity of A-centers in the control samples is significantly higher compared to samples doped with dysprosium.

DLTS analysis of oxygen-free control silicon samples revealed the formation of an additional radiation defect - an E-center - in these samples under the influence of γ-radiation. The ionization energy of this defect is E_c-0.43 eV, and its electron capture cross-section is 1.8×10^{-15} cm^2. Interestingly, in silicon doped with dysprosium, a significant decrease in the concentration of E-centers was observed compared to the control samples - almost tenfold (Fig. 2, curves 1 and 2).

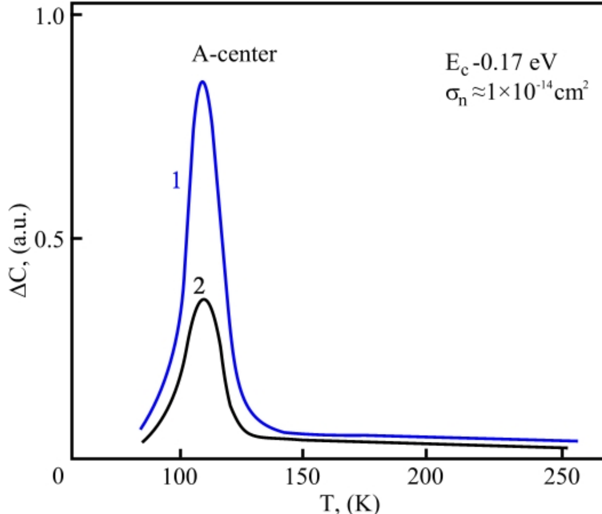

Figure 1. DLTS spectra of n-Si and n-Si<Dy> samples after γ-irradiation ($N_O^{OA}=7\times10^{17}$ cm^{-3}): 1 - control sample (n-Si); 2 - dysprosium-doped sample (n-Si<Dy>)

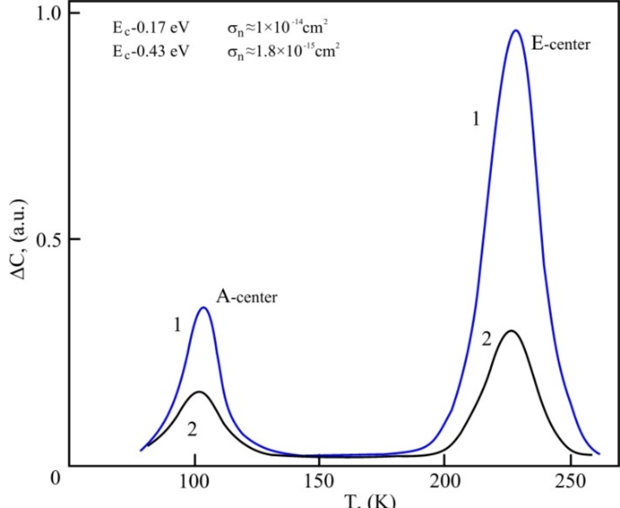

Figure 2. DLTS spectra of n-Si and n-Si<Dy> samples after γ-irradiation ($N_O^{OA}=7\times10^{17}$ cm^{-3}): 1 - control sample (n-Si); 2 - dysprosium-doped sample (n-Si<Dy>)

Based on the obtained samples, neutron activation analysis and EDS analysis were conducted to determine the concentration of Dy atoms on the surface and in the volume of the sample. The results of neutron activation analysis

indicate the presence of dysprosium atoms in the silicon sample at a high concentration - approximately $(3\times10^{16} – 4\times10^{18})$ cm^{-3}.

In Fig. 3, the concentration of elements on the surface of an oxygen-free silicon sample was studied using the energy-dispersive X-ray spectroscopy (EDS) method.

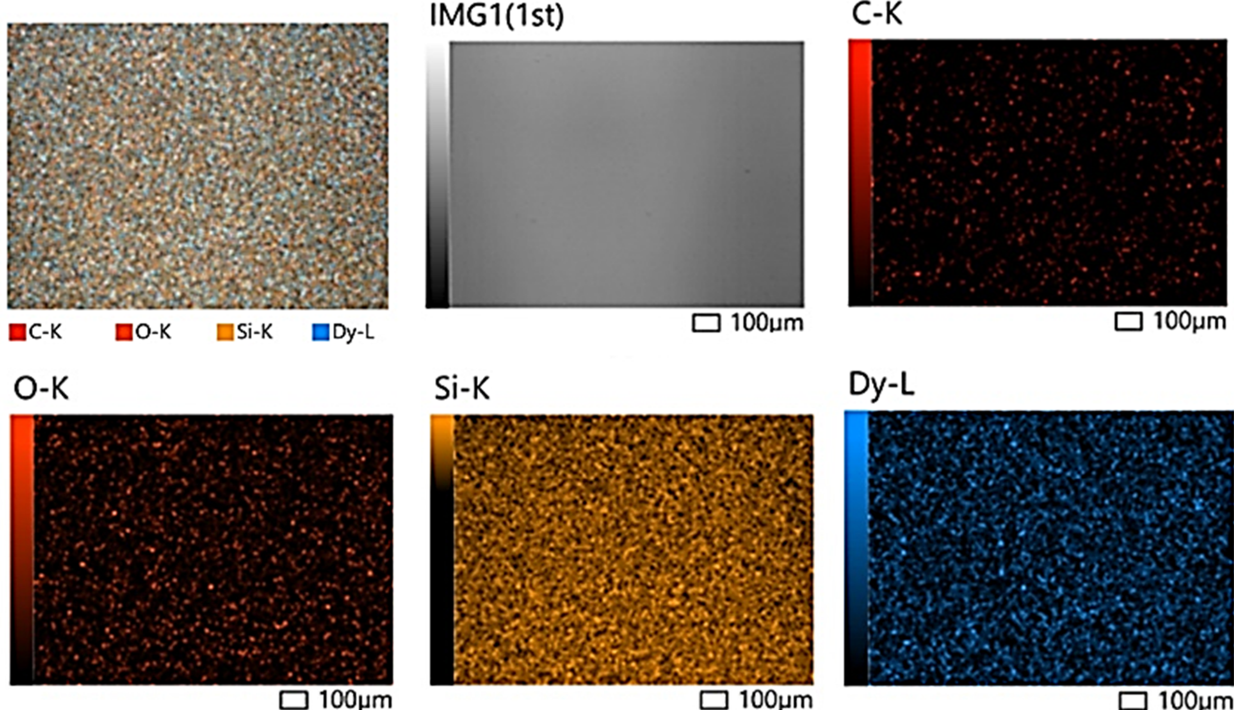

Figure 3. Image of the EDS spectral analysis for the n-Si sample.

Based on the analysis results, we can conclude that dysprosium atoms are evenly distributed on the surface of the silicon sample and in its adjacent regions. The mass fraction of dysprosium was found to be 0.16%, while its atomic fraction was 0.02%, which corresponds to the neutron activation analysis results (Table 1). These findings indicate the presence of Dy atoms both on the surface and within the volume of the silicon sample, demonstrating that their distribution is sufficiently homogeneous.

Table 1. Elemental composition of the surface of the n-Si<Dy> sample as determined by energy-dispersive X-ray spectroscopy (EDS).

Element	Line	Mass%	Atom%
C	K	10.27±0.10	21.09±0.20
O	K	0.37±0.01	0.57±0.02
Si	K	89.20±0.09	78.32±0.08
Dy	L	0.16±0.02	0.02±0.00
Total		100.00	100.00

CONCLUSIONS

In this work, a thorough analysis was conducted on the incorporation of dysprosium (Dy) as a dopant into ultra-pure n-type single-crystal silicon samples during the crystal growth stage (solution growth method) and its effect on radiation stability. The study utilized silicon samples with specific resistivity ranging from 10 to 65 Ω×cm and concentrations of optically active interstitial oxygen atoms between $(5\times10^{16} - 7\times10^{17})$ cm^{-3}.

Deep levels of samples exposed to gamma radiation (^{60}Co, 3.1×10^{12} quanta/cm^2×s) were studied using the DLTS method. The results showed that in silicon doped with Dy, after γ-radiation, A-centers with an ionization energy of E_c-0.17 eV were detected. These centers correspond to oxygen-vacancy (O-V) complexes. Additionally, the concentration of A-centers in silicon with Dy doping was significantly lower compared to the control samples, indicating a decreased formation rate of radiation defects.

In oxygen-free silicon, E-centers with an energy of E_c-0.43 eV were detected as a result of irradiation. The quantity of these centers was observed to be up to 10 times higher compared to samples doped with Dy. This clearly demonstrates the inhibitory effect of the Dy element on the mechanisms of defect formation.

EDS and neutron activation analyses confirmed the incorporation of the element dysprosium into the silicon structure. According to the EDS results, Dy atoms are uniformly distributed on the silicon surface with a mass fraction of 0.16% and an atomic fraction of 0.02%. Neutron activation analysis showed that the Dy concentration is in the range of $(3\times10^{16} - 4\times10^{18})$ cm^{-3}. Despite such high concentration, it was determined that Dy atoms are electrically passive and are positioned in the crystal lattice without forming deep energy levels.

In general, the conducted research indicates that doping silicon with a rare-earth element such as dysprosium during the growth stage from solution enhances its radiation stability and significantly reduces the probability of deep-level defect formation under the influence of γ-radiation.

ORCID
Khodjakbar S. Daliev, https://orcid.org/0000-0002-2164-6797; **Sharifa B. Utamuradova**, https://orcid.org/0000-0002-1718-1122
Shakhrukh Kh. Daliev, https://orcid.org/0000-0001-7853-2777, **Jonibek J. Khamdamov**, https://orcid.org/0000-0003-2728-3832
Shahriyor B. Norkulov, https://orcid.org/0000-0002-2171-4884

REFERENCES

[1] Kh.S. Daliev, Sh.B. Utamuradova, O.A. Bozorova, and Sh.Kh. Daliev, "Joint effect of Ni and Gf impurity atoms on the silicon solar cell photosensitivity," Applied Solar Energy (English translation of Geliotekhnika), **41**(1), 80–81 (2005). https://www.researchgate.net/publication/294234192_Joint_effect_of_Ni_and_Gf_impurity_atoms_on_the_silicon_solar_cell_photosensitivity
[2] K.S. Daliev, Sh.B. Utamuradova, A. Khaitbaev, J.J. Khamdamov, Sh.B. Norkulov, and M.B. Bekmuratov, "Defective Structure of Silicon Doped with Dysprosium," East Eur. J. Phys. (2), 283 (2024). https://doi.org/10.26565/2312-4334-2024-2-30
[3] X. Kong, Z. Xi, L. Wang, Y. Zhou, Y. Liu, *et al.*, "Recent Progress in Silicon−Based Materials for Performance Enhanced Lithium Ion Batteries," Molecules, **28**(5), 2079 (2023). https://doi.org/10.3390/molecules28052079
[4] V. Pelenitsyn, and P. Korotaev, "First-principles study of radiation defects in silicon," Computational Materials Science, **207**, 111273 (2022). https://doi.org/10.1016/j.commatsci.2022.111273
[5] I. Pintilie, G. Lindstroem, A. Junkes, and E. Fretwurst, "Radiation-induced point- and cluster-related defects with strong impact on damage properties of silicon detectors," Research Section A: Accelerators, Spectrometers, Detectors and Associated Equipment, **611**(1), 52-68 (2009). https://doi.org/10.1016/j.nima.2009.09.065
[6] K.P. Abdurakhmanov, Kh.S. Daliev, Sh.B. Utamuradova, and N.Kh. Ochilova, "On defect formation in silicon with impurities of manganese and zinc," Applied Solar Energy (English translation of Geliotekhnika), **34**(2), 73–75 (1998). https://api.semanticscholar.org/CorpusID:99796881
[7] S.B. Utamuradova, K.S. Daliev, A.I. Khaitbaev, J.J. Khamdamov, J.S. Zarifbayev, and B.S. Alikulov, "Defect Structure of Silicon Doped with Erbium," East European Journal of Physics, (2), 288-292 (2024). https://doi.org/10.26565/2312-4334-2024-2-31
[8] K.P. Abdurakhmanov, Sh.B. Utamuradova, Kh.S. Daliev, S.G. Tadjy-Aglaeva, and R.M. Érgashev, "Defect-formation processes in silicon doped with manganese and germanium," Semiconductors, **32**(6), 606–607 (1998). https://doi.org/10.1134/1.1187448
[9] K.S. Daliev, Sh.B. Utamuradova, J.J. Khamdamov, Sh.B. Norkulov, and M.B. Bekmuratov, "Study of Defect Structure of Silicon Doped with Dysprosium Using X-Ray Phase Analysis and Raman Spectroscopy," East Eur. J. Phys. (4), 311-321 (2024). https://doi.org/10.26565/2312-4334-2024-4-35
[10] K.S. Daliev, Sh.B. Utamuradova, J.J. Khamdamov, M.B. Bekmuratov, O.N. Yusupov, Sh.B. Norkulov, and Kh.J. Matchonov, "Defect Formation in MIS Structures Based on Silicon with an Impurity of Ytterbium," East Eur. J. Phys. (4), 301-304 (2024). https://doi.org/10.26565/2312-4334-2024-4-33
[11] K.S. Daliev, Sh.B. Utamuradova, J.J. Khamdamov, M.B. Bekmuratov, Sh.B. Norkulov, and U.M. Yuldoshev, "Changes in the Structure and Properties of Silicon During Ytterbium Doping: The Results of o Comprehensive Analysis," East Eur. J. Phys. (4), 240-249 (2024). https://doi.org/10.26565/2312-4334-2024-4-24
[12] L.S. Berman, "Depth distribution of deep-level centers in silicon dioxide near an interface with indium phosphide," Semiconductors, **31**, 67–68 (1997). https://doi.org/10.1134/1.1187040
[13] G.L. Miller, D.V. Lang, and L.C. Kimerling, "Capacitance Transient Spectroscopy," Annual review of materials research, **7**, 377-448 (1977). https://doi.org/10.1146/annurev.ms.07.080177.002113
[14] Sh.B. Utamuradova, Sh.Kh. Daliyev, J.J. Khamdamov, Kh.J. Matchonov, and Kh.Y. Utemuratova, East Eur. J. Phys. (2), 274-278 (2024). https://doi.org/10.26565/2312-4334-2024-2-28
[15] S.A. Smagulova, I.V. Antonova, E.P. Neustroev, *et al.*, "Relaxation of a defect subsystem in silicon irradiated with high-energy heavy ions," Semiconductors, **37**, 546–550 (2003). https://doi.org/10.1134/1.1575358
[16] J. Stahl, E. Fretwurst, G. Lindström, and I. Pintilie, "Deep defect levels in standard and oxygen enriched silicon detectors before and after ^{60}Co-γ-irradiation," Nuclear Instruments and Methods in Physics Research Section A: Accelerators, Spectrometers, Detectors and Associated Equipment, **512**(1-2), 111–116 (2003). https://doi.org/10.1016/S0168-9002(03)01884-9
[17] K.S. Daliev, S.B. Utamuradova, J.J. Khamdamov, and Z.E. Bahronkulov, "Morphology of the Surface of Silicon Doped with Lutetium," East European Journal of Physics, (2), 304-308 (2024). https://doi.org/10.26565/2312-4334-2024-2-34
[18] A.I. Prostomolotov, Yu.B. Vasiliev, and A.N. Petlitsky, "Mechanics of defect formation during growth and heat treatment of single-crystal silicon," (4), 1716–1718 (2011). http://www.unn.ru/pages/e-library/vestnik/19931778_2011_-_4-4_unicode/147.pdf
[19] J.R. Srour, and J.W. Palko, "Displacement Damage Effects in Irradiated Semiconductor Devices," IEEE Transactions on Nuclear Science, **60**(3), 1740–1766, (2013). https://doi.org/10.1109/tns.2013.2261316
[20] M.S. Kukurudziak, V.M. Lipka, and V.V. Ryukhtin, "Silicon p-i-n Mesa-Photodiode Technology," East Eur. J. Phys. (3), 385-389 (2024). https://doi.org/10.26565/2312-4334-2024-3-47
[21] D.V. Lang, "Deep-Level Transient Spectroscopy: A New Method to Characterize Traps in Semiconductors," Journal of Applied Physics, **45**(7), 3023–3032 (1974). https://doi.org/10.1063/1.1663716
[22] J. Goldstein, *et al.*, *Scanning Electron Microscopy and X-ray Microanalysis*, (Springer, 2017). https://doi.org/10.1007/978-1-4615-0215-9
[23] V.A. Kozlov, and V.V. Kozlovski, "Doping of semiconductors using radiation defects produced by irradiation with protons and alpha particles," Semiconductors, **35**, 735–761 (2001). https://doi.org/10.1134/1.1385708
[24] A.S. Zakirov, Sh.U. Yuldashev, H.J. Wang, H.D. Cho,T.W. Kang, J.J. Khamdamov, and A.T. Mamadalimov, Photoluminescence study of the surface modified and MEH-PPV coated cotton fibers, Journal of Luminescence, **131**(2), 2, 301-305 (2011). https://doi.org/10.1016/j.jlumin.2010.10.019
[25] A.S. Zakirov, S.U. Yuldashev, H.D. Cho, *et al.*, "Functional hybrid materials derived from natural cellulose," Journal of the Korean Physical Society, **60**, 1526–1530 (2012). https://doi.org/10.3938/jkps.60.1526

ВПЛИВ АТОМІВ ДИСПРОЗІЮ, ВВЕДЕНИХ НА ЕТАПІ ВИРОЩУВАННЯ, НА ФОРМУВАННЯ РАДІАЦІЙНИХ ДЕФЕКТІВ У КРИСТАЛАХ КРЕМНІЮ

Ходжакбар С. Далієв[a], Шарифа Б. Утамурадова[b], Шахрух Х. Далієв[b], Жонібек Ж. Хамдамов[b], Шахрійор Б. Норкулов[b]*

[a]Філія Федеральної державної бюджетної освітньої установи вищої освіти «Національний дослідницький університет MEI», вул. Йўгду, 1, Ташкент, Узбекистан

[b]Інститут фізики напівпровідників і мікроелектроніки Національного університету Узбекистану, вул. Янгі Алмазар, 20, Ташкент, 100057, Узбекистан

У цьому дослідженні проаналізовано механізми формування та зменшення радіаційних дефектів, що виникають у результаті впровадження атомів диспрозію (Dy) під час вирощування кристалів кремнію методом зонного плавлення (FZ). Глибокі рівні дефектів, що утворилися після легування n-типу кремнію диспрозієм і опромінення його γ-променями ізотопу ^{60}Co, були проаналізовані методом глибокорівневої ємнісної спектроскопії (DLTS). Встановлено, що у присутності диспрозію концентрація дефектів типу A-центр (вакансійно-кисневий комплекс) і E-центр (вакансійно-фосфорний комплекс) значно зменшується — у 2–4 рази у порівнянні з контрольними зразками. Спектральний аналіз методом EDS показав, що атоми Dy рівномірно розподілені по поверхні кремнію та присутні в достатній концентрації. Отримані результати підтверджують, що атоми Dy у кремнії відіграють пасивуючу роль, уповільнюючи кінетику формування радіаційних дефектів і підвищуючи радіаційну стійкість кремнієвих структур.

Ключові слова: *кремній, легований диспрозієм; радіаційні дефекти; гамма-випромінювання; DLTS (глибокорівнева ємнісна спектроскопія); нейтронно-активаційний аналіз; EDS (енергетично-дисперсійна рентгенівська спектроскопія); A-центр; E-центр; вирощування кристалів; киснево-вакансійний комплекс; радіаційна стійкість*

East European Journal of Physics. 3. 348-352 (2025)
DOI:10.26565/2312-4334-2025-3-34 ISSN 2312-4334

RESISTIVE SWITCHING BEHAVIOR OF SnO_2/ZnO HETEROJUNCTION THIN FILMS FOR NON-VOLATILE MEMORY APPLICATIONS

Jamoliddin X. Murodov[a,b]*, Shavkat U. Yuldashev[b], Azamat O. Arslanov[c], Noiba U. Botirova[b], Javohir Sh. Xudoyqulov[c,e], Ra'no Sh. Sharipova[b], Rafael A. Nusretov[a], Andrey A. Nebesniy[c], Mukhammad P. Pirimmatov[d]

[a]Tashkent State Technical University named after Islam Karimov, Tashkent, Uzbekistan
[b]Center of Nanotechnology Development, National University of Uzbekistan, Tashkent, Uzbekistan
[c]National University of Uzbekistan named after Mirzo Ulugbek, Tashkent, Uzbekistan
[d]Institute of Physics and Technology, Tashkent, Uzbekistan
[e]Central Asian University, Tashkent, Uzbekistan
**Corresponding Author E-mail: jamoliddinmilliy@gmail.com*
Received June 3, 2025, revised July 3, 2025; accepted August 8, 2025

This study presents the fabrication and resistive switching (RS) performance of bilayer SnO_2/ZnO thin films deposited via ultrasonic spray pyrolysis on p-type silicon substrates. The heterostructures were post-annealed at 450°C to enhance crystallinity and interfacial contact. Electrical characterization using I–V measurements revealed clear bipolar RS behavior without the need for an initial forming process. The devices exhibited a stable high resistance state (HRS) and low resistance state (LRS) across multiple cycles, with an ON/OFF ratio exceeding 10^2. The switching mechanism is attributed to the formation and rupture of conductive filaments likely induced by oxygen vacancies at the SnO_2/ZnO interface. Bandgap estimation using Tauc plots showed values of approximately 3.17 eV and 3.41 eV for ZnO and SnO_2, respectively. These findings confirm the potential of SnO_2/ZnO heterojunctions as efficient materials for next-generation non-volatile memory applications.
Keywords: *SnO_2; ZnO; Resistive switching; Memristor; Thin films; Heterojunction; Non-volatile memory; Oxygen vacancies*
PACS: 73.40.-c; 85.30 Tv; 73.6 Ga

INTRODUCTION

In recent years, memristors have become a highly relevant research topic due to their potential in neuromorphic computing, artificial intelligence hardware, and next-generation non-volatile memory systems. Memristors are considered the fourth fundamental passive circuit element—alongside resistors, capacitors, and inductors—and are capable of remembering their resistance state based on the history of electrical charge passed through them. This unique feature enables memristors to retain information even when the power is turned off, making them ideal candidates for low-power, high-density memory devices [1-3].

Metal oxide-based memristors, particularly those formed from binary oxides such as ZnO and SnO_2, have drawn substantial interest due to their low fabrication cost, ease of synthesis, and compatibility with flexible substrates. Both ZnO and SnO_2 are wide-bandgap n-type semiconductors, with bandgaps of approximately 3.4 eV and 3.6 eV, respectively. ZnO offers high electron mobility and good surface reactivity, while SnO_2 is chemically stable and exhibits strong electrical conductivity in its doped forms [4,5]. Combining these materials into a bilayer or heterojunction structure can enable new resistive switching mechanisms, such as interface-modulated filament formation and oxygen vacancy migration.

Prior investigations by Pant et al. [6] have revealed strong bipolar resistive switching and pronounced negative differential resistance (NDR) characteristics in SnO_2/ZnO heterojunctions synthesized via magnetron sputtering. These effects were attributed to enhanced grain boundary diffusion and the emergence of quantum confinement phenomena at the nanoscale interface. In a more recent study, Saha et al. [7] demonstrated reliable resistive switching in one-dimensional SnO_2 nanofiber-based memristors, where switching dynamics were effectively analyzed and predicted using artificial neural network (ANN)-based computational models, further supporting the applicability of data-driven approaches in oxide-based memory device engineering. Furthermore, Co-doped SnO_2 memristors fabricated on p-type silicon substrates have been shown to exhibit tunable negative differential resistance behavior, highlighting the role of doping in modulating the electronic properties of oxide-based heterostructures [8].

In this study, we investigate the resistive switching behavior of a p-Si/SnO_2/ZnO heterostructure fabricated using ultrasonic spray pyrolysis (USP), an accessible and scalable thin-film deposition technique. The SnO_2 and ZnO layers were sequentially deposited on both p-type silicon and quartz substrates, with post-annealing at 450°C. Current–voltage (I–V) measurements were performed using a Keithley 2460 SourceMeter. The results show a clear hysteresis loop, indicative of memristive switching. However, the relatively close bandgap values of ZnO and SnO_2 may limit the strength of the switching contrast, as both layers are n-type semiconductors. This study contributes to the ongoing effort to optimize binary oxide heterojunctions for low-power memory devices.

Cite as: J.X. Murodov, Sh.U. Yuldashev, A.O. Arslanov, N.U. Botirova, J.Sh. Xudoyqulov, R.Sh. Sharipova, R.A. Nusretova, A.A. Nebesniy, M.P. Pirimmatov, East Eur. J. Phys. 3, 348 (2025), https://doi.org/10.26565/2312-4334-2025-3-34
© J.X. Murodov, Sh.U. Yuldashev, A.O. Arslanov, N.U. Botirova, J.Sh. Xudoyqulov, R.Sh. Sharipova, R.A. Nusretova, A.A. Nebesniy, M.P. Pirimmatov, 2025; CC BY 4.0 license

METHODS

The p-Si/SnO_2/ZnO heterostructure thin films were fabricated using the ultrasonic spray pyrolysis (USP) technique due to its cost-effectiveness, simplicity, and suitability for oxide thin film deposition. In this study, p-type silicon substrates were used. Prior to deposition, the substrates were cleaned sequentially by rinsing in deionized (DI) water, followed by ethanol and then acetone, and finally rinsed again in DI water. This multi-step cleaning process was performed to remove organic and inorganic contaminants and to ensure uniform and adherent film growth. After cleaning, the substrates were dried naturally under ambient laboratory conditions.

The schematic structure of the fabricated memristor device is illustrated in Figure 1. The device consists of a bilayer SnO_2/ZnO heterostructure deposited on a p-type silicon substrate. Silver (Ag) top contacts were applied as electrodes. The ZnO layer serves as the intermediate interface layer, while SnO_2 is the top oxide layer. The bottom electrode is the p-Si substrate itself. This vertical "sandwich-like" configuration enables charge transport across the oxide layers under applied bias, which is essential for studying resistive switching behavior.

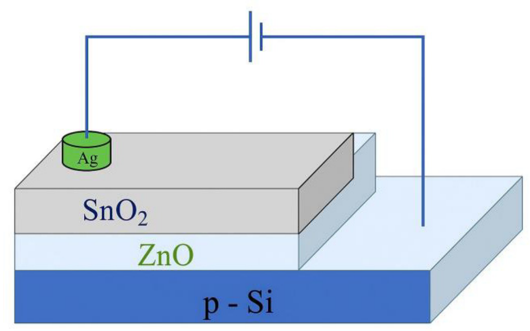

Figure 1. Schematic illustration of the Ag/SnO_2/ZnO/p-Si memristor device structure

After the chemical cleaning steps, the substrates were rinsed thoroughly with deionized (D.I.) water to remove any remaining traces of solvents and impurities. Finally, the cleaned substrates were dried using nitrogen gas. This multi-step cleaning process was crucial for achieving a uniform film morphology and ensuring reproducible electrical performance of the memristor devices. Compared to a simple rinse method, this procedure significantly reduced surface contamination, thereby improving the quality and reproducibility of the SnO_2 and ZnO films deposited via ultrasonic spray pyrolysis (USP) [9].

The SnO_2 precursor solution was prepared by dissolving 15 mL of stannous chloride dihydrate ($SnCl_2 \cdot 2H_2O$) in double-distilled water. For the ZnO layer, 15 mL of zinc acetate dihydrate [$Zn(C_2H_3O_2)_2 \cdot 2H_2O$] was similarly dissolved in double-distilled water. Each solution was atomized using a 2.5 MHz ultrasonic transducer and carried toward the heated substrates using oxygen gas as the carrier.

The deposition process was conducted at a substrate temperature of 450 °C, which was maintained using a controlled hotplate. The SnO_2 layer was deposited first, followed by the ZnO layer, forming a bilayer heterostructure. This sequence was designed to promote appropriate band alignment and interfacial contact between the n-type semiconductors. Following deposition, the films were annealed in ambient air at 450 °C to improve crystallinity and stabilize the interface. Silver (Ag) top contacts were applied using silver paste for electrical measurements, and the p-Si substrate served as the bottom electrode in the case of silicon-based structures.

Electrical characterization of the memristor devices was performed using a Keithley 2460 SourceMeter. A voltage sweep protocol of 0 → +5 V → 0 → –5 V → 0 was applied to examine the current–voltage (I–V) characteristics. The presence of a hysteresis loop in the I–V curve confirmed the resistive switching behavior of the fabricated structures.

RESULTS

A. Current–Voltage (I–V) Characteristics

The electrical response of the p-Si/SnO_2/ZnO heterostructure was evaluated through current–voltage (I–V) measurements using a Keithley 2460 SourceMeter. A voltage sweep in the range of 0 → +5 V → 0 → –5 V → 0 was applied. As shown in Figure 2, the device exhibits a pronounced hysteresis loop, which is characteristic of bipolar resistive switching behavior. Notably, the switching occurred without the requirement of an initial forming voltage, suggesting the presence of intrinsic defect states – most likely oxygen vacancies – within the oxide layers that facilitate the conductive filament formation.

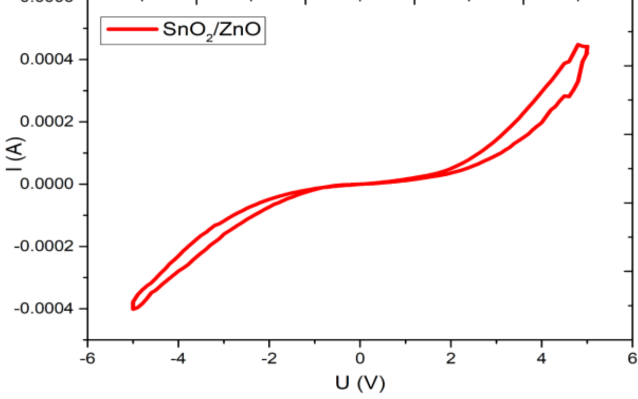

Figure 2. Linear-scale I–V characteristics of the SnO_2/ZnO heterostructure, showing memristive switching.

This behavior is consistent with the findings of Pant et al. [6], who observed similar bipolar switching in SnO_2/ZnO interfaces attributed to the diffusion of ZnO into SnO_2 at the grain boundaries, forming a resonant tunneling-like interface. The observed switching behavior here can be explained by the formation and rupture of conductive filaments in the oxide layers, likely modulated by the applied electric field and the associated drift of oxygen vacancies.

However, due to the small bandgap difference between ZnO (~3.4 eV) and SnO_2 (~3.6 eV), and the fact that both are n-type semiconductors, the overall barrier height at the interface may be low. As a result, the current contrast between the high resistance state (HRS) and the low resistance state (LRS) is moderate, though stable. The ON/OFF current ratio was estimated to be $>10^2$, which is suitable for low-power memory applications.

B. Optical Bandgap Estimation

The optical bandgaps of the individual ZnO and SnO_2 layers were estimated using Tauc plot analysis derived from UV–Vis absorbance spectra (see Figure 3). By plotting $(\alpha h\nu)^2$ versus photon energy ($h\nu$) and extrapolating the linear region to the energy axis, the direct bandgap values were determined. The estimated optical bandgaps were found to be approximately: ZnO layer (3.17 eV), SnO_2 layer (3.41 eV)

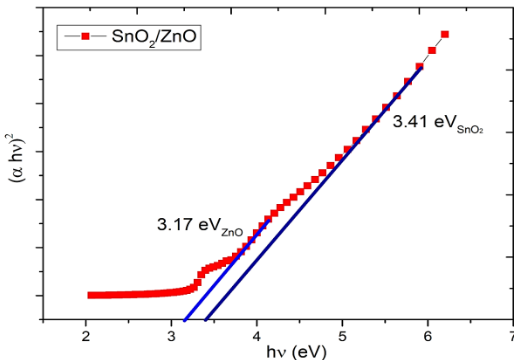

Figure 3. Tauc plot used for bandgap estimation of ZnO (3.17 eV) and SnO_2 (3.41 eV)

These values closely match literature-reported data [6,7], confirming the successful synthesis of phase-pure oxide layers. The slight narrowing of the SnO_2 bandgap compared to the nominal 3.6 eV may be attributed to oxygen vacancy-related subgap states, which can affect the switching performance by serving as electron trapping centers.

C. Structural Characterization (XRD Analysis)

The crystallographic properties of the synthesized SnO_2/ZnO bilayer thin films were investigated using X-ray diffraction (XRD). Figure 4 presents the XRD pattern of the heterostructure deposited on a p-type Si substrate. The diffraction peaks observed at $2\theta \approx 31.7°$, 34.4°, 36.2°, 47.5°, 56.6°, and 62.8° are assigned to the (100), (002), (101), (102), (110), and (103) planes of hexagonal wurtzite ZnO, respectively (JCPDS Card No. 36-1451). Additional peaks located at approximately 26.6°, 33.9°, 37.9°, 51.7°, and 54.8° correspond to the (110), (101), (200), (211), and (220) planes of the tetragonal rutile phase of SnO_2 (JCPDS Card No. 41-1445).

These results confirm the successful formation of a polycrystalline bilayer structure containing both ZnO and SnO_2 phases without detectable secondary impurities. The predominance of ZnO peaks is attributed to its top-layer placement in the heterostructure, which contributes to stronger X-ray signal intensity. The sharp and well-defined diffraction peaks indicate good crystallinity, while the absence of unidentified peaks affirms the high phase purity of the deposited films.

The confirmed crystallographic structure supports the electrical measurements, as high crystallinity and structural integrity at the interface are known to influence the stability and reproducibility of resistive switching behavior. The SnO_2/ZnO heterointerface, therefore, provides a favorable platform for the formation and rupture of conductive filaments, modulated by oxygen vacancy migration, as discussed in the preceding electrical characterization section.

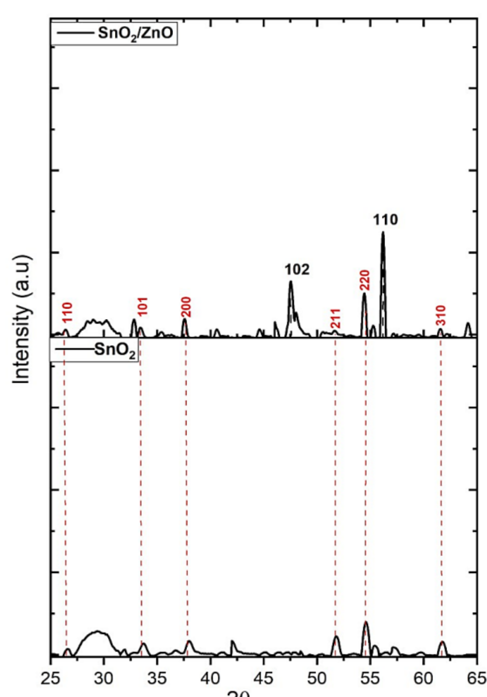

Figure 4. XRD pattern of the SnO_2/ZnO heterojunction thin film

D. Mechanism Interpretation

The resistive switching mechanism in this heterostructure is likely governed by oxygen vacancy migration and associated filament formation at the SnO_2/ZnO interface. When a positive bias is applied, oxygen ions drift away from the anode, leaving behind oxygen vacancies that accumulate to form conductive paths (filaments). The application of a reverse bias disrupts these paths, returning the device to the high-resistance state.

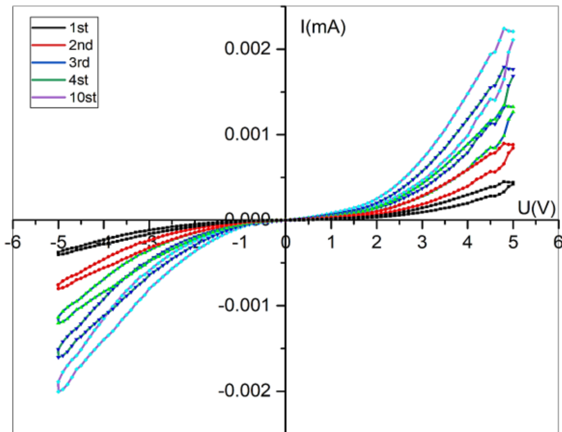

Figure 5. Multi-cycle I–V measurements demonstrating reproducibility and stability of resistive switching behavior

Figure 5 shows multi-cycle I–V measurements, clearly demonstrating the reproducibility and stability of the resistive switching behavior over several cycles. The overlapping hysteresis loops indicate consistent switching between high-resistance and low-resistance states, confirming the non-volatile nature and endurance of the memristor device.

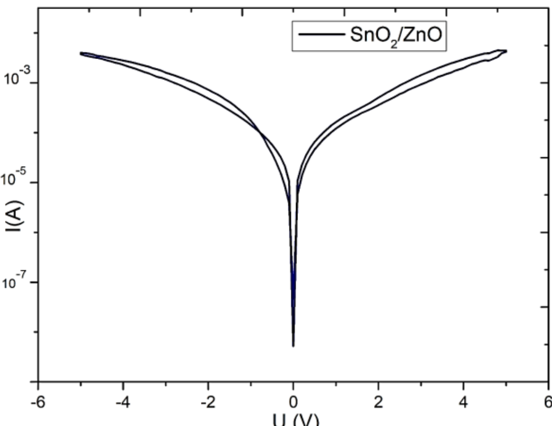

Figure 6. Log-scale I–V curve showing clear bipolar switching characteristics of the SnO_2/ZnO heterojunction

Figure 6 presents the log-scale I–V characteristics of the SnO_2/ZnO heterojunction device. The plot clearly illustrates the bipolar switching behavior, with distinct transitions between the high-resistance and low-resistance states under opposite bias polarities. This logarithmic representation helps to highlight the exponential nature of current conduction and the stability of the switching behavior across several orders of magnitude.

The heterointerface, supported by a p-type Si substrate, may also induce additional band bending or depletion effects, modulating the switching threshold. Although both oxide layers are n-type, their slightly different work functions and bandgaps still create an asymmetric potential barrier that contributes to the observed resistive switching (RS) behavior.

CONCLUSION

In this study, a p-Si/SnO_2/ZnO heterojunction thin film was successfully fabricated using the ultrasonic spray pyrolysis technique. The electrical analysis of the device revealed clear bipolar resistive switching behavior with a stable hysteresis loop observed in the I–V characteristics. The switching occurred without the requirement for a forming step, suggesting that oxygen vacancies and interface effects play a critical role in the RS mechanism.

Tauc plot analysis showed that the optical bandgaps of ZnO and SnO_2 were approximately 3.17 eV and 3.41 eV, respectively, consistent with reported values in the literature. Although the small band offset between the two n-type oxides may reduce the overall switching contrast, the device demonstrated repeatable ON/OFF cycles and reasonable resistance state separation.

These findings confirm that the p-Si/SnO_2/ZnO heterostructure is a viable platform for exploring low-cost, oxide-based memristors. Future studies may focus on interface engineering, doping, or inclusion of buffer layers to enhance RS characteristics and device scalability for neuromorphic and non-volatile memory applications.

ORCID
Jamoliddin X. Murodov, https://orcid.org/0009-0006-3088-4881; **Shavkat U. Yuldashev,** https://orcid.org/0000-0002-2187-5960; **Azamat O. Arslanov,** https://orcid.org/0009-0000-4817-8770; **Mukhammad P. Pirimmatov,** https://orcid.org/0009-0000-4829-7817; **Javohir Sh. Xudoyqulov,** https://orcid.org/0009-0005-4223-8863

REFERENCES

[1] D. Ielmini, "Resistive switching memories based on metal oxides: Mechanisms, reliability and scaling," Semiconductor Science and Technology, **31**(6), 063002 (2016). https://doi.org/10.1088/0268-1242/31/6/063002
[2] B. Cao, H. Liu, T. Li, J. Gong, S. Zhang, and M.T. Dove, "Synthesis of composite films for ZnO-based memristors with superior stability," Materials Research Express, **11**, 056302 (2024). https://doi.org/10.1088/2053-1591/ad4777
[3] P.D. Walke, *et al.*, "Memristive Devices from CuO Nanoparticles," Nanomaterials, **10**(9), 1677 (2020). https://doi.org/10.3390/nano10091677
[4] P.A. Hind, P. Kumar, U.K. Goutam, and B.V. Rajendra, "Impact of deposition temperature on persistent photoconductivity of SnO_2 thin films deposited using spray pyrolysis technique suitable in optoelectronic synaptic devices," Optical Materials, **146**, 115579 (2024). https://doi.org/10.1016/j.optmat.2024.115579
[5] N.U. Rehman, R. Khan, N. Rahman, I. Ahmad, A. Ullah, M. Sohail, S. Iqbal, *et al.*, "Dual-doped ZnO-based magnetic semiconductor resistive switching response for memristor-based technologies," Journal of Materials Science: Materials in Electronics, **35**, 1557 (2024). https://doi.org/10.1007/s10854-024-13318-5
[6] R. Pant, N. Patel, K.K. Nanda, and S.B. Krupanidhi, "Negative differential resistance and resistive switching in SnO_2/ZnO interface," Journal of Applied Physics, **122**(12), (2017). https://doi.org/10.1063/1.5004969
[7] S. Saha, *et al*. "Experimental demonstration of SnO_2 nanofiber-based memristors and their data-driven modeling for nanoelectronic applications," Chip, **2**, 100075 (2023). https://doi.org/10.1016/j.chip.2023.100075
[8] J.X. Murodov, Sh.U. Yuldashev, M.S. Mirkamilova, and U.E. Jurayev, "Tunable Negative Differential Resistance in SnO_2:Co Memristors on p-Si," East European Journal of Physics, (2), 211-214 (2025). https://doi.org/10.26565/2312-4334-2025-2-22
[9] A. Arslanov, Sh. Yuldashev, N. Botirova, R. Nusretov, J. Murodov, and J. Xudoyqulov, "Impact of precursor molar concentration on the structural and optical properties of ZnO thin films synthesized by ultrasonic spray pyrolysis," Physical Science International Journal, **29**(1), 29–35 (2025). https://doi.org/10.9734/psij/2025/v29i1871

РЕЗИСТИВНА ПЕРЕМИКАЛЬНА ПОВЕДІНКА ТОНКОПЛІВКОВОГО ГЕТЕРОПЕРЕХОДУ SnO_2/ZnO ДЛЯ ЗАСТОСУВАНЬ В ЕНЕРГОНЕЗАЛЕЖНІЙ ПАМ'ЯТІ

Джамоліддін Х. Муродов[a,b], Шавкат У. Юлдашев[b], Азамат О. Арсланов[c], Нойба У. Ботірова[b], Джавохір Ш. Худойкулов[c,e], Рано Ш. Шаріпова[b], Рафаель А. Нусретов[a], Андрій А. Небесний[c], Мухаммад П. Пірімматов[d]
[a]*Ташкентський державний технічний університет імені Іслама Карімова, Ташкент, Узбекистан*
[b]*Центр розвитку нанотехнологій, Національний університет Узбекистану, Ташкент, Узбекистан*
[c]*Національний університет Узбекистану імені Мірзо Улугбека, Ташкент, Узбекистан*
[d]*Інститут фізики та технологій, Ташкент, Узбекистан*
[e]*Центральноазіатський університет, Ташкент, Узбекистан*

У цьому дослідженні представлено виготовлення та властивості резистивного перемикання (РС) двошарових тонких плівок SnO_2/ZnO, нанесених за допомогою ультразвукового розпилювального піролізу на кремнієві підкладки p-типу. Гетероструктури були відпалені при 450°C для покращення кристалічності та міжфазного контакту. Електрична характеристика за допомогою вольт-амперних вимірювань виявила чітку біполярну РС-поведінку без необхідності початкового процесу формування. Пристрої демонстрували стабільний стан високого опору (HRS) та стан низького опору (LRS) протягом кількох циклів, зі співвідношенням увімкнення/вимкнення, що перевищує 10^2. Механізм перемикання пояснюється утворенням та розривом провідних ниток, ймовірно, викликаних вакансіями кисню на межі розділу SnO_2/ZnO. Оцінка ширини забороненої зони за допомогою графіків Таука показала значення приблизно 3,17 еВ та 3,41 еВ для ZnO та SnO_2 відповідно. Ці результати підтверджують потенціал гетеропереходів SnO_2/ZnO як ефективних матеріалів для застосування в енергонезалежній пам'яті наступного покоління.

Ключові слова: *SnO_2; ZnO; резистивне перемикання; мемристор; тонкі плівки; гетероперехід; енергонезалежна пам'ять; кисневі вакансії*

East European Journal of Physics. 3. 353-356 (2025)
DOI:10.26565/2312-4334-2025-3-35 ISSN 2312-4334

EFFECT OF GATE OXIDE AND BACK OXIDE MATERIALS ON SELF-HEATING EFFECT IN FinFET

M.M. Khalilloev[a]*, B.O. Jabbarova[a], F. Eshchanov[b], A.E. Atamuratov[a]
[a]*Urgench State University named after Abu Rayhan Biruni, Urgench, Uzbekistan*
[b]*Agency for Assessment of Knowledge and Skills, Khorezm Regional Department, Urgench, Uzbekistan*
**Corresponding Author e-mail: x-mahkam@urdu.uz; x-mahkam@mail.ru*
Revised May 23, 2025; revised July 8, 2025; accepted July 18, 2025

The self-heating effect on the fin field effect transistor (FinFET) is investigated. The dependence of the lattice temperature in the channel center of the transistor on the thickness of the gate oxide, as well as the back oxide, is simulated. Different types of the most used oxide materials (SiO_2, HfO_2, and Si_3N_4) and their combination, SiO_2+Si_3N_4, are considered for gate and back oxides. 3D simulation is performed using Sentaurus TCAD. It is shown that the lattice temperature slowly and monotonically decreases with increasing gate oxide thickness. However, the lattice temperature is monotonically increasing with the thickness of the back oxide. This behavior of the lattice temperature depends on the relation between heat generation and dissipation rates in the transistor channel. A difference in the heat conductivity of the oxide materials explains the obtained behavior of the lattice temperature. Also, the lattice temperature dependence on the gate oxide thickness is explained by the increase in the contact area between the gate oxide and the gate with increasing gate oxide thickness. Besides this, it is accounted that the Joule heat generation rate depends on the drain current, which also depends on the oxide materials.
Keywords: *3D simulation; FinFET; Self-heating effect; Gate oxide; Back oxide*
PACS: 85.30.Tv

INTRODUCTION

One of the main tasks of nanoelectronics is to reduce power consumption and increase the degree of integration of integrated circuits (ICs). This task is connected with the considerable reduction in size of the transistors that make up the integrated circuit. Along with other elements, metal-oxide-semiconductor field-effect transistors (MOSFETs) are one of the most important components of ICs. The reduction in the size of MOSFETs leads to the appearance of various degradation effects, including short-channel effects (SCE), self-heating effect (SHE), Negative Bias Temperature Instability (NBTI), etc.

SCEs are strongly manifested in MOSFETs based on planar technology, which is one of the initial technologies for manufacturing MOSFETs. To increase the resistance of MOSFETs to short-channel effects, a structure of a vertical (or Fin) MOSFET (FinFET) was proposed instead of planar MOSFETs, with gate lengths of the order of 20 nm and lower, which operate in the inversion mode [1]. FinFET has three gates and, as a consequence, has a high degree of electrostatic integrity that ensures high immunity against short-channel effects [2].

One of the features of the FinFETs is that they are based on silicon-on-insulator technology. This feature is characterized by the fact that the channel of the transistor borders an oxide layer, the so-called back oxide layer (BOX). This feature leads to the manifestation of a self-heating effect in FinFET due to the low thermal conductivity of the oxide layer, leading to a low dissipation rate of heat generated in the channel of the transistor [3], [4], [5]. As a result, increasing the temperature in the transistor channel leads to changing the drain current and, as a consequence, degradation of the I-V characteristics of the FinFET.

Therefore, finding the oxide materials that increase the immunity of the transistors against SHE and that are compatible with FinFET fabrication technology is a very important task. In this work, the impact of the BOX materials, as well as gate oxide materials, on the temperature in the transistor channel is investigated [6], [7]. SiO_2, HfO_2, Si_3N_4, and combination SiO_2+Si_3N_4 are mainly used in FinFET fabrication technology, and therefore, in this research, these materials are considered as BOX as well as gate oxide materials.

TRANSISTOR STRUCTURE PARAMETERS AND SIMULATION MODELS

The cross-section along the channel of the 3D structure simulated in this work, a silicon-based FinFET, is shown in Fig. 1. The silicon-based transistor's channel is n-type. TiN is used as a gate material. Geometrical sizes of the different parts of the transistor and channel doping level are presented in Table 1. In the simulation, the gate oxide thickness varies between 1 and 1.5 nm, while the back oxide thickness varies between 10 and 1000 nm.

In the simulation, Sentaurus TCAD software is used. For the estimation of the self-heating effect, the drift-diffusion transport model in conjunction with the thermodynamic transport model was used. To account for quantum effects, the quantum correction Density gradient was also used. The doping-dependent mobility model and velocity saturation in the high field are taken into account. Coulomb and phonon scatterings are included in the simulation model to consider the

Cite as: M.M. Khalilloev, B.O. Jabbarova, F. Eshchanov, A.E. Atamuratov, East Eur. J. Phys. 3, 353 (2025), https://doi.org/10.26565/2312-4334-2025-3-35
© M.M. Khalilloev, B.O. Jabbarova, F. Eshchanov, A.E. Atamuratov, 2025; CC BY 4.0 license

mobility degradation at the interface as the high-k material HfO_2 is used as the gated oxide. A simulation drift-diffusion transport model was calibrated by comparing the I-V characteristics of the simulated transistor with experimental results presented in [8], [9], [10]. The results of the comparison given in Fig. 2 show a good agreement.

Table 1. Geometrical and physical parameters of the considered transistor

Parameter	Designation	Value
Source and drain doping level	N_d	5×10^{18} cm^{-3} (n-type)
Channel doping level	N_a	1×10^{16} cm^{-3} (p-type)
Gate oxide (HfO_2, Si_3N_4) thickness	t_{ox}	t_{EOT} = 1.0-1.5 nm
Channel thickness	T_{si}	9 nm
Channel width	W_b	22 nm
Back oxide layer (SiO_2, HfO_2, SiO_2+Si_3N_4) thickness	T_{box}	10-1000 nm
Gate length	L_{gate}	10 nm

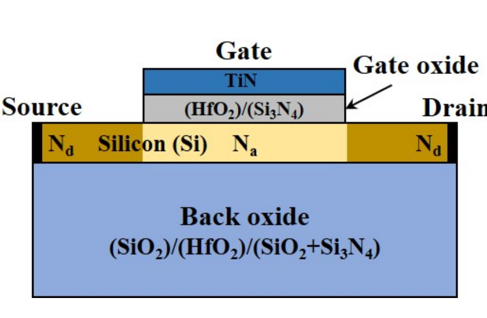

Figure 1. Simulated FinFET cross-section structure

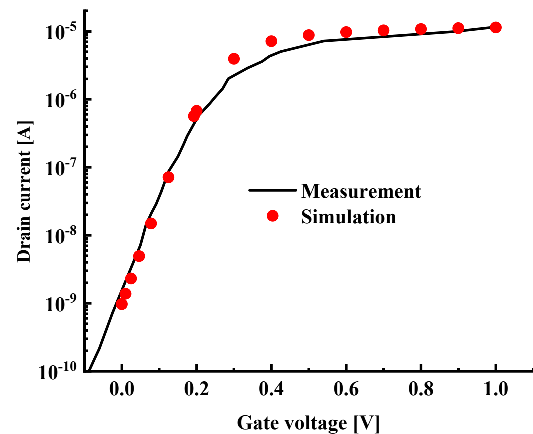

Figure 2. Comparing the I-V characteristics of the simulated and experimental transistors for L_{gate} = 25 nm and V_{ds} = 50 mV

SIMULATION RESULTS AND DISCUSSION

The dependence of the temperature in the channel center on the thickness of gate oxide in FinFET for HfO_2 and Si_3N_4 as gate oxide, and SiO_2, HfO_2, and SiO_2+Si_3N4 as back oxide is simulated. The results of the simulation are shown in Fig. 3. Results show, that the lattice temperature very slowly decreased with increasing the gate oxide thickness for all considered oxide materials, while the contact area between the gate oxide and the channel increased monotonically with increasing the gate oxide thickness (Fig. 4). Increasing the contact area lead to increasing heat dissipation rate, however drain current, and as consequence heat generation rate, practically is not changed with increasing the gate oxide thickness. Obviously, in this case, the heat generation rate has a greater effect than the heat dissipation rate.

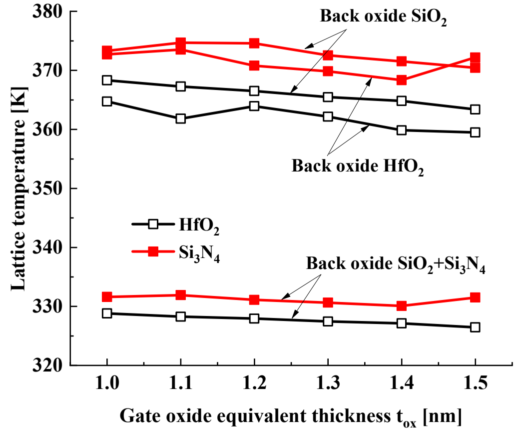

Figure 3. Dependence of the lattice temperature in the channel center on the gate oxide equivalent thickness for different gate oxide and back oxide materials.

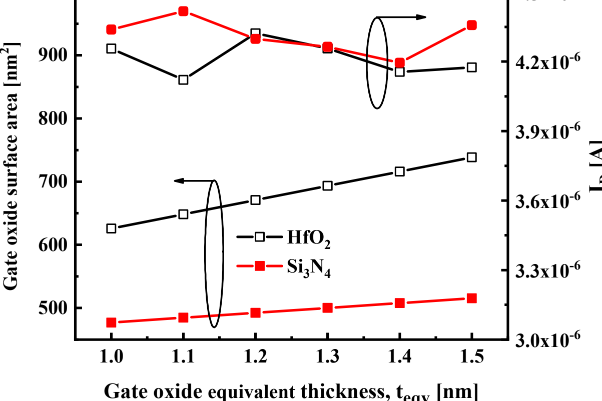

Figure 4. Contact area and drain current dependence on the gate oxide equivalent thickness. BOX is HfO_2

It is seen in Fig. 3 that in the case of using HfO_2 as gate oxide, the lattice temperature is lower than at using Si_3N_4, for all BOX materials. This dependence correlates with drain current dependence on the gate oxide thickness (Fig. 4).

The temperature dependence on the gate oxide thickness is the result of the combined effect of the dielectric constant, thermal conductivity, and the thickness of the gate oxide

Lattice temperature dependence on the BOX thickness T_{box} is monotonous, and the temperature grows with increasing BOX thickness for all considered BOX materials. This dependence is in agreement with [11], [12] and at higher thicknesses is expressed by the formula (1).

$$\Delta T = \frac{(P_t \cdot T_{box})}{K_b \cdot A}, \quad (4)$$

where P_t stands for the heat power generated by the current in the channel, K_b is the heat conductivity of the oxide layer, and A represents the area of the contact surface between the oxide layer and the channel.

Fig 5 shows the dependence of the lattice temperature in the FinFET channel center on the back oxide thickness (TBOX) for different oxide materials. It can be seen that the lattice temperature increases monotonically with increasing TBOX, regardless of the material type. This is explained by the fact that a thicker BOX layer increases the distance between the heat source (channel) and the heat sink (metal contact), thereby reducing the heat dissipation efficiency. Among the considered materials, the combination SiO_2+Si_3N_4 shows the lowest temperature values, which can be attributed to its highest thermal conductivity, as indicated in Table 2.

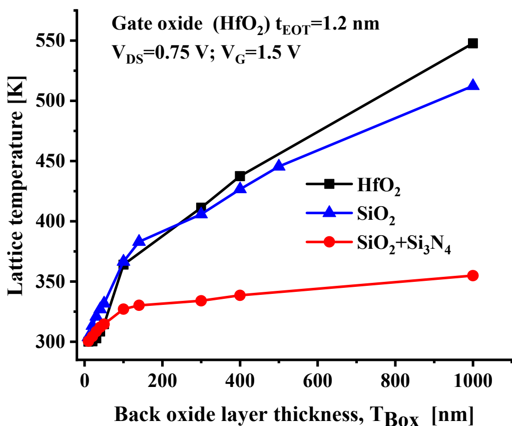

Figure 5. Lattice temperature dependence on the thickness of the BOX for different materials

Table 2. Thermal Conductivity of the oxide materials

Oxide Material	Thermal Conductivity K_b (W m^{-1} K^{-1})
HfO_2	2.3
SiO_2	1.4
Si_3N_4 (SiO_2+Si_3N_4)	18.5

CONCLUSION

Results of the simulation show that the lattice temperature in the center of the FinFET channel depends on the gate oxide as well as the back oxide material. More considerable dependence on the temperature of the materials is seen for back oxide, where the maximal difference in the temperatures lies in the range between 50 and 170 K for BOX thicknesses from 100 to 1000 nm. The maximal temperature difference in using different considered gate oxide materials is approximately 10K in all considered ranges of oxide thicknesses. The material of the oxide layers influences the drain current, but a substantial influence on the temperature is the thermal conductivity of the back oxide material.

The highest immunity against the self-heating effect is achieved using HfO_2 as gate oxide material and SiO_2+Si_3N_4 as back oxide material in the considered range of oxide materials in this work.

ORCID

M.M. Khalilloev, https://orcid.org/0000-0001-5497-6410; **B.O. Jabbarova,** https://orcid.org/0000-0003-1181-5195
A.E. Atamuratov https://orcid.org/0000-0003-2173-3783

REFERENCES

[1] J.P. Colinge, "Multi-gate SOI MOSFETs," Microelectronic Engineering, **84**, 2071-2076 (2007) https://doi.org/10.1016/j.mee.2007.04.038

[2] M. Hemalatha, N.B. Balamurugan, M. Suguna, and D.S. Kumar, "Impact of Variation in Fin Thickness and Self-Heating on the Output Characteristics of Triangular Gate FinFETs," Silicon, **16**, 2253-2266 (2024). https://doi.org/10.1007/s12633-023-02835-3

[3] D. Vasileska, S. M. Goodnick, and K. Raleva, "Self-Consistent Simulation of Heating Effects," in: *Nanoscale Devices in Proceedings of the 13th International Workshop on Computational Electronics*, (Beijing, China, 2009), pp. 1-4. https://doi.org/10.1109/IWCE.2009.5091146

[4] A. Atamuratov, B. Jabbarova, M. Khalilloev, A. Yusupov, and A. Loureriro, "Self-heating effect in nanoscale SOI junctionless FinFET with different geometries," in: *2021 13th Spanish Conference on Electron Devices (CDE)*, pp. 62–65 (IEEE, 2021). https://doi.org/10.1109/CDE52135.2021.9455728

[5] Y. Wang, H. Liang, H. Zhang, D. Li, Y. Lu, M. Yi, and Z. Huang, "A new characterization model of FinFET self-heating effect based on FinFET characteristic parameter," Microelectronic Engineering, **287**, 1112155 (2024). https://doi.org/10.1016/j.mee.2024.112155

[6] B. Smaani, N. Paras, S.B. Rahi, Y.S. Song, R. Yadav, and S. Tayal, "Impact of the Self-Heating Effect on Nanosheet Field Effect Transistor Performance," ECS Journal of Solid-State Science and Technology, **12**(2), 021005 (2023). https://doi.org/10.1149/2162-8777/acb96b
[7] A.E. Atamuratov, B. Jabbarova, M.M. Khalilloev, A. Yusupov, K. Sivasankaran, and J.C. Chedjou, "Impact of the channel shape, back oxide and gate oxide layers on self-heating in nanoscale JL FINFET," Nanosystems: Physics, Chemistry, Mathematics, **13**(2), 148–155 (2022). https://doi.org/10.17586/2220-8054-2022-13-2-148-155
[8] V.S. Basker, T. Standaert, H. Kawasaki, C.C. Yeh, K. Maitra, T. Yamashita, J. Faltermeier, *et al*., in: *Proceedings of the Symposium on VLSI Technology*, (IEEE, 2010), p. 19.
[9] A.E. Atamuratov, B.O. Jabbarova, M.M. Khalilloev, A. Yusupov, "The Self-Heating Effect in Junctionless Fin Field-Effect Transistors Based on Silicon-on-Insulator Structures with Different Channel Shapes," Technical Physics Letters, **47**(7), 542-545 (2021). https://doi.org/10.1134/S1063785021060055
[10] M. Balasubbareddy, K. Sivasankaran, A.E. Atamuratov, and M.M. Khalilloev, "Optimization of vertically stacked nanosheet fet immune to self-heating," Micro and Nanostructures, **182**, 207633 (2023). https://doi.org/10.1016/j.micrna.2023.207633
[11] L.J. McDaid, S. Hall, P.H. Mellor, W. Eccleston, and J.C. Alderman, "Physical origin of negative differential resistance in SOI transistors," Electron. Lett. **25**(13), 827–828 (1989). https://doi.org/10.1049/el:19890557
[12] A.E. Atamuratov, B.O. Jabbarova, M.M. Khalilloev, A. Yusupov, and K. Sivasankaran, "Influence of the Gate Oxide and Back Oxide Material Types on Self-heating Effect in Junctionless FinFET," in: *International Conference of Young Specialists on Micro Nanotechnologies and Electron Devices EDM*, 2024, pp. 2630–2633 https://doi.org/10.1109/EDM61683.2024.10615156

ВПЛИВ МАТЕРІАЛІВ ОКСИДУ ЗАТВОРУ ТА ОКСИДУ ЗВОРОТНОГО ШАРУ НА ЕФЕКТ САМОРОЗІГРІВУ У FinFET

М.М. Халіллоєв[a], Б.О. Джаббарова[a], Ф. Єщанов[b], А.Є. Атамуратов[a]
[a]Ургенчський державний університет, імені Абу Райхана Беруні, Ургенч, Узбекистан
[b]Агентство з оцінки знань та навичок, Хорезмське регіональне відділення, Ургенч, Узбекистан

Досліджено ефект саморозігріву польового транзистора з ребрами (FinFET). Моделюється залежність температури решітки в центрі каналу транзистора від товщини затворного оксиду, а також оксиду зворотного шару. Для затворних та зворотних оксидів розглядаються різні типи найбільш використовуваних оксидних матеріалів (SiO_2, HfO_2 та Si_3N_4) та їх комбінація SiO_2+Si_3N_4. 3D-моделювання виконано за допомогою Sentaurus TCAD. Показано, що температура решітки повільно та монотонно зменшується зі збільшенням товщини затворного оксиду. Однак, температура решітки монотонно зростає зі збільшенням товщини зворотного шару оксиду. Така поведінка температури решітки залежить від співвідношення між швидкістю тепловиділення та розсіювання в каналі транзистора. Отримана поведінка температури решітки пояснюється різницею в теплопровідності оксидних матеріалів. Також залежність температури решітки від товщини затворного оксиду пояснюється збільшенням площі контакту між затворним оксидом та затвором зі збільшенням товщини затворного оксиду. Крім того, враховується, що швидкість джоулевої тепловиділення залежить від струму стоку, який також залежить від оксидних матеріалів.

Ключові слова: *3D-моделювання; FinFET; ефект самонагріву; затворний оксид; зворотний оксид*

East European Journal of Physics. **3**. 357–364 (2025)

DOI: 10.26565/2312-4334-2025-3-36 ISSN 2312-4334

IMPACT OF LOCAL OXIDE TRAPPED CHARGE ON ELECTRICAL AND CAPACITANCE CHARACTERISTICS OF SOI FINFET

Atabek Atamuratov[a], **Ibroximjon Karimov**[b], **Mirzabahrom Foziljonov**[b], **Azamat Abdikarimov**[a], **Odilbek Atamuratov**[c], **Makhkam Khalilloev**[a*]

[a] *Urgench State University, named after Abu Rayhan Biruni, Kh.Olimjan str.,14, Urgench, 220100, Uzbekistan*

[b] *Andijan State University, Universitet str.,129, Andijan, 170100, Uzbekistan*

[c] *Tashkent Institute of Irrigation and Agricultural Mechanization Engineers, National Research University, K. Niyoziy str.39, Tashkent, 100000, Uzbekistan*

[*] *Corresponding Author e-mail: x-mahkam@urdu.uz, x-mahkam@mail.ru*

Received May 7, 2025; revised June 28, 2025; accepted July 19, 2025

In this work, the influence of the local oxide trapped charge on the transfer $I_d - V_g$ characteristics and capacitance of the gate-to-source (drain) connection of the silicon-on-insulator (SOI) structure-based FinFET is simulated. $I_d - V_g$ characteristics are simulated by using the drift-diffusion transport model. Capacitance-Voltage characteristics of the gate-to-source capacitance are simulated by using a small AC signal method. The $I_d - V_g$ characteristics and gate-to-source (gate-drain) capacitance are investigated at different linear sizes and positions of the local oxide trapped charge along the channel. The results of the simulation show that the threshold voltage monotonically decreases with an increase in the linear size of the local charge, and gate-to-source capacitance monotonically increases with an increase in the distance between the source-channel border and the center of the local charge.

Keywords: *FinFET; Lokal charge; Gate-to-source capacitance; p-n junction; C-V dependence*

PACS: 85.30.Tv, 73.40.Qv, 85.30.De

1. INTRODUCTION

One of the main devices of nanoelectronics is field effect transistors, particularly Fin Field Effect Transistors (FinFET), which is continuously scaled over the last several decades. As a result of scaling, the characteristics of the transistors are being degraded due to short channel effects [1], [2], self-heating effect [3], [4], impact of oxide (interface) trapped charge [5], [6]. Among these degradation effects can be noted as appreciable the effects of hot carrier injection [7], [8], bias temperature instability [9]–[11], off-stress [12], and the impact of the radiation-induced charge [13]. These degradation effects are mainly connected with injection or/and generation charges in the oxide layer or at the oxide-semiconductor interface. In nanoscale FETs the random telegraph noise, induced by a single oxide (or interface) trapped charge, can also be considerable [14], [15]. The impact of these effects should be taken into account at designing and using analog as well as digital integrated circuits based on FETs.

The oxide trapped charge can affect MOSFET parameters such as threshold voltage and subthreshold slope of the transfer characteristics. Consequently, it leads to degradation of the transistor characteristics. Therefore, to determine the mechanisms and reasons of the charge trapping it is expediently develop the methods of estimation the position and distribution of the trapped charge along the channel.

Well-known methods for detecting the oxide and interface trapped charge in planar MOSFETs are methods connected with measuring current-voltage and capacitance-voltage dependencies [16]–[18]. Particularly, for this purpose, measurements of subthreshold drain current [16] and gate-to-substrate capacitance-voltage dependence [17], [18] are used. However, these methods should be modified in the case of SOI FinFET, because of specific features of the transistor's structure connected with the presence of the back oxide layer between channel and substrate. Therefore, it is important to consider and study the features of the impact of trapped charges on I-V and C-V dependences in SOI FinFET.

One of the simple and fast methods of diagnostics to detect the charge trapped in the oxide layer or at the interface is based on measurements of the capacitance-voltage characteristics of lateral source (drain)-channel p-n-junctions [19]. Experimental evidence of this method is presented in [13], [20], [21]. It is shown that the non-uniform distribution of the charge in the oxide layer or at the semiconductor-oxide interface is appropriately reflected in source-channel (drain-channel) p-n-junction capacitance [13], [19], [20], [22]. Thus, the distribution along the channel of the trapped charge should also be reflected in other capacitances connected with lateral source-channel (drain-channel) junctions.

In this work, dependencies of the drain current and threshold voltage on linear size and position of the oxide trapped charge, along the channel, are considered for SOI FinFET. The capacitance method mentioned above and first suggested for planar MOSFET [19] is modified for application in SOI FinFET. The modified method will be used to simulate the dependence of the gate-to-source capacitance, C_{gs}, on the position of the local oxide trapped charge.

Cite as: A. Atamuratov, I. Karimov, M Foziljonov, A. Abdikarimov, O. Atamuratov, M. Khalilloev, East Eur. J. Phys. 3, 357 (2025), https://doi.org/10.26565/2312-4334-2025-3-36

© A. Atamuratov, I. Karimov, M Foziljonov, A. Abdikarimov, O. Atamuratov, M. Khalilloev, 2025; CC BY 4.0 license

This paper is organized as follows. In Section 2, we present the description of the considered transistor parameters, simulation conditions, and approaches used. Simulation results with discussions are presented in Section 3. Finally, some concluding remarks are formulated in Section 4.

2. TRANSISTOR PARAMETERS, SIMULATION CONDITIONS, AND APPROACHES

The structure of the simulated SOI FinFET is shown in Figure 1. The geometry and parameters of the simulated FinFET are shown in Table 1.

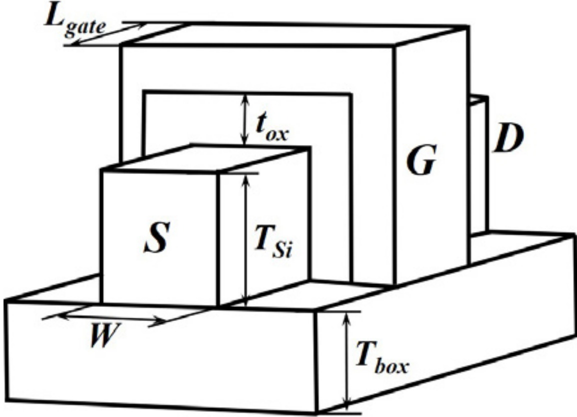

Figure 1. 3D structure of the simulated SOI FinFET

3D simulation were conducted using Advanced TCAD Sentaurus software. Transfer characteristics of the FinFET were simulated by using drift-diffusion as well as thermodynamic transport models to choose an adequate transport model. The results of the simulation are shown in Figure 2. It is shown in the figure that at gate voltages up to $V_g - 1V$, both $I_d - V_g$ curves are the same. And at higher gate voltages drain current is lower at using the thermodynamic transport model, which is connected with increasing the temperature in the channel. In simulation, the range of the gate voltages was limited to 1V; therefore, the use of the drift-diffusion and thermodynamic transport models is equivalent. We used a simple drift-diffusion transport model to save resources (power and time).

Table 1. Here is the caption of your table

Parameter	Designation	Value
Channel doping level (p-Si)	N_a	$1 \cdot 10^{15} cm^{-3}$ (n-type)
Source and drain doping level (n-Si)	N_d	$1 \cdot 10^{20} cm^{-3}$ (n-type)
Gate oxide (HfO_2) thickness	t_{ox}	2.5 nm
Channel thickness	T_{Si}	30 nm
Channel width	W	12 nm
Back oxide layer (SiO_2) thickness	T_{box}	100 nm
Gate length	L_{gate}	25 nm

Density gradient quantum corrections were used to account for quantum effects because transistor sizes are on the nanometer scale. In the mobility model, the doping dependence and velocity saturation at high fields were taken into account. The model used in the simulation was calibrated by comparing $I_d - V_g$ characteristics with experimental results presented in [23] (Figure 3). The experimental $I_d - V_g$ curve presented in [23] was normalised to the width of the channel; therefore, to compare with the simulation results, it was recalculated for the whole transistor width.

In this work, the dependencies of the drain current Id and threshold voltage Vth on the position, L, and width, D, along the channel of the local oxide trapped charge were considered. The dependence of the capacitance C_{gs} of the gate-to-source (drain) connection on the position L was also considered. At considering the dependence on the position L, the width of the local oxide trapped charge D is fixed and equal to 5 nm. At considering the dependence on the width, the local oxide trapped charge is located at the drain end of the gate oxide layer and expands to the center of the oxide layer (Figure 4). The homogeneously charged area models local oxide trapped charge in the oxide layer. Charge density in the charged area is $1 \cdot 10^{12} cm^{-2}$ (or $4 \cdot 10^{18} cm^{-3}$), and it corresponds to the value that can take place in MOSFETs [18].

The choice for consideration of the gate-to-source capacitance C_{gs} is based on the following. The main idea of the capacitance method suggested in [20] to detect the oxide (interface) trapped charge is connected with the impact of

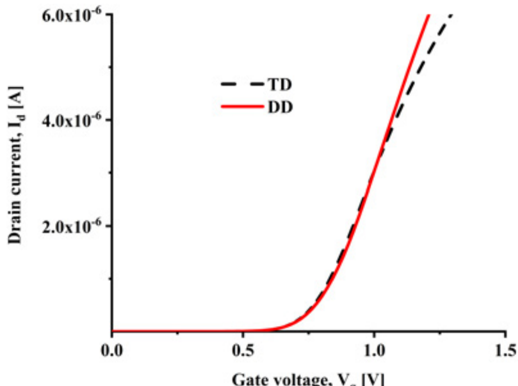

Figure 2. Transfer $I_d - V_g$ characteristics simulated using thermodynamic (TD) and drift-diffusion (DD) transport models.

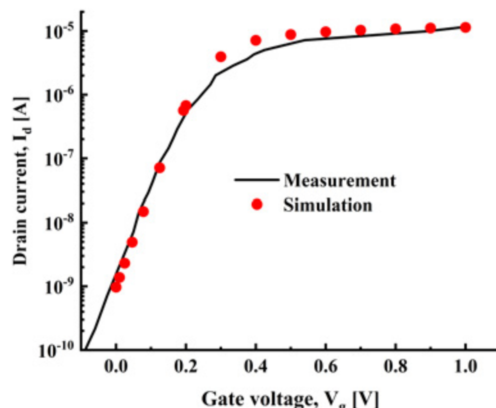

Figure 3. Calibration of the simulation model by comparing simulated and experimental [23] $I_d - V_g$ characteristics of the SOI FinFET transistors with L_{gate} = 25 nm and V_d = 50 mV.

the oxide or/and interface trapped charge on lateral source-channel (drain-channel) p-n-junction capacitance, C_{p-n}, in planar MOSFET. In the case of SOI FinFET, C_{p-n} capacitance can not be measured directly because of the presence BOX layer between the source and substrate. However, this capacitance is included in the capacitance of the gate-to-source (gate-to-drain) connection (Figure 5). Therefore, changes in C_{p-n} capacitance due to oxide trapped charge should be reflected in C_{gs} capacitance.

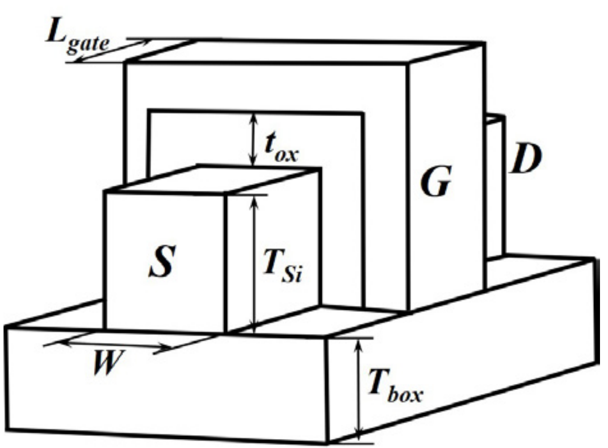

Figure 4. Cross-section of the FinFET showing local oxide trapped charge.

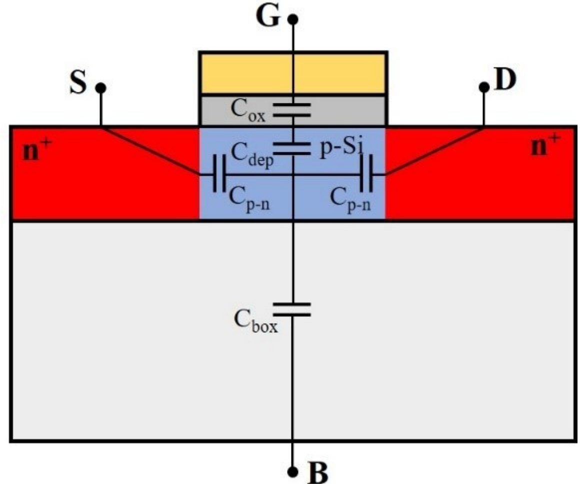

Figure 5. Cross-section of the simulated SOI FinFET with pictured capacitances between contacts.

The gate-to-source connection as well as the gate-to-drain connection contains the following capacitances connected in series: gate oxide capacitance Cox, oxide-semiconductor interface depletion layer capacitance, C_{dep}, source-to-channel p-n-junction capacitance, C_{p-n}. Only in depletion mode, the depletion layer capacitance, C_{dep}, significantly contributes to C_{gs} capacitance. However, in the considered case, a transistor is in accumulation mode, because in the simulation, the p-type source (drain) region is biased by the positive pole of the voltage source relative to the gate. Thus, establishing the accumulation mode at the semiconductor surface, near the oxide-semiconductor interface, results in dismissing the capacitance C_{dep}. Consequently, the resulting capacitance C_{gs} can be expressed by the following formula (1):

$$C_{gs} = \frac{C_{p-n} \cdot C_{ox}}{C_{p-n} + C_{ox}} \tag{1}$$

here, C_{ox} is gate oxide capacitance per unit area, which does not depend on the applied voltage. Estimations show, that C_{p-n} is significantly less than Cox because width of the depletion layer of the source-to-channel (drain-to-channel) p-n-junction is approximately 0.1 µm while gate oxide thickness t_{ox} = 2.5 nm. Thus, in accordance with the formula

(1) C_{gs} is determined mainly by C_{p-n}, which is very sensitive to the distribution of oxide trapped charge [13], [20]. Consequently, in this work, it is simulated the dependence of the C_{gs} on the position of the local oxide trapped charge along the channel.

C-V dependence of the gate-to-source (gate-to-drain) capacitance were simulated with using the small AC signal method. Signal with frequency 1 MHz is used in simulation. The capacitance C_{gs} is simulated at different position of the local oxide trapped charge along the channel.

The local charge with fixed width D=5 nm, in the oxide layer at a distance L from the source-channel border (Figure 4) impacts on the carrier distribution in the channel. Consequently, this impact should be reflected in the source-to-channel junction capacitance and hence in the C-V dependence of the gate-to-source capacitance.

FinFET has symmetry relative the channel center, hence the gate-to-source and gate-to-drain capacitances should be same. Therefore, in the following, mainly the gate-to-source capacitance is considered.

3. SIMULATION RESULTS AND DISCUSSIONS

3.1. Impact of the local charge on electrical characteristics

Figures 6 and 7 illustrate the simulation results regarding the dependence of drain current on the gate voltages at different positions and the width of the local oxide trapped charge. The figures demonstrate that the local oxide trapped charge considerable influence on the transfer $I_d - V_g$ curve, especially in the region above the threshold voltage.

Figure 6b presents the simulation results depicting the dependence of the drain current above threshold voltage on the position L of the local oxide trapped charge. The figure demonstrates that the dependence is nonmonotonic. The drain current is maximal at the position of the local charge near the channel center. However, the dependence of the drain current on the width D is monotonic with saturation at higher D (Figure 7b). The observed behaviors of the drain current can be attributed to the appropriate behavior of the threshold voltage (Figure 8).

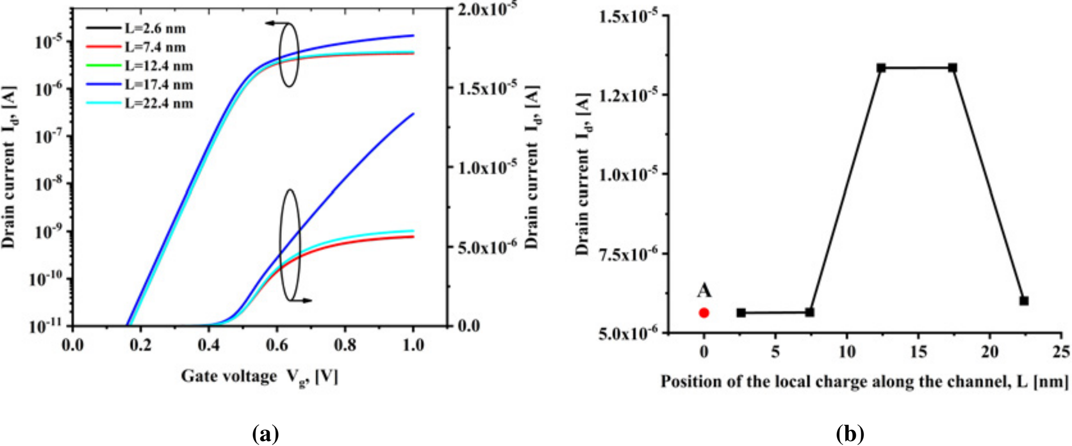

Figure 6. (a) $I_d - V_g$ characteristics at various position, L, of the local oxide trapped charge. (b) Dependence of the drain current, at V_g=1V, V_d=0.75V, on the position, L, of the local oxide trapped charge. Point A corresponds to the case of without oxide trapped charge.

The behavior of the drain current at the change of the position and linear size of the local oxide trapped charge is correlated with the behavior of the threshold voltage. A decrease in the threshold voltage leads to an increase in the drain current and vice versa; an increase in the threshold voltage leads to a decrease in the drain current. The observed changes of threshold voltage with change of the position and width of the local oxide trapped charge can be understood in terms of the change of the distribution of channel surface potential and the corresponding inversion layer carrier concentration along the channel, induced by the field of the local trapped charge.

Originally, in case of absence, the local oxide trapped charge, potential distribution along the channel surface has a bell-shape with a maximum in the middle of the channel and with approximately zero value near the metallurgical border of the source-channel and drain-channel p-n junctions [25]–[27]. Hence, the maximal impact of the local oxide trapped charge on potential distribution and consequently on threshold voltage, can take place at the position of the local charge in the center of the channel. Figure 8a illustrates an appropriate relationship between threshold voltage and position of the local oxide trapped charge.

The threshold voltage shows a monotonic dependence on the linear size of the local charge, D (Figure 8b). This behavior of the threshold voltage is the same as the dependence of threshold voltage on the value of oxide trapped charge in planar long-channel MOSFET [15]. Hence, determining the shift of threshold voltage allows estimating the value of oxide

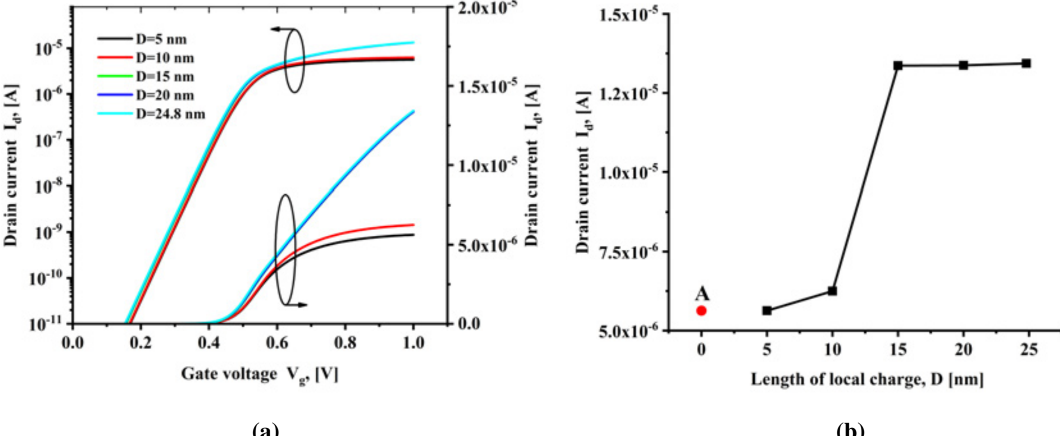

Figure 7. (a) $I_d - V_g$ characteristics at various widths, D, of the local oxide trapped charge. (b) Dependence of the drain current, at V_g=1V, V_d=0.75V, on the width, D, of the local oxide trapped charge. Point A corresponds to the case of absence of the oxide trapped charge.

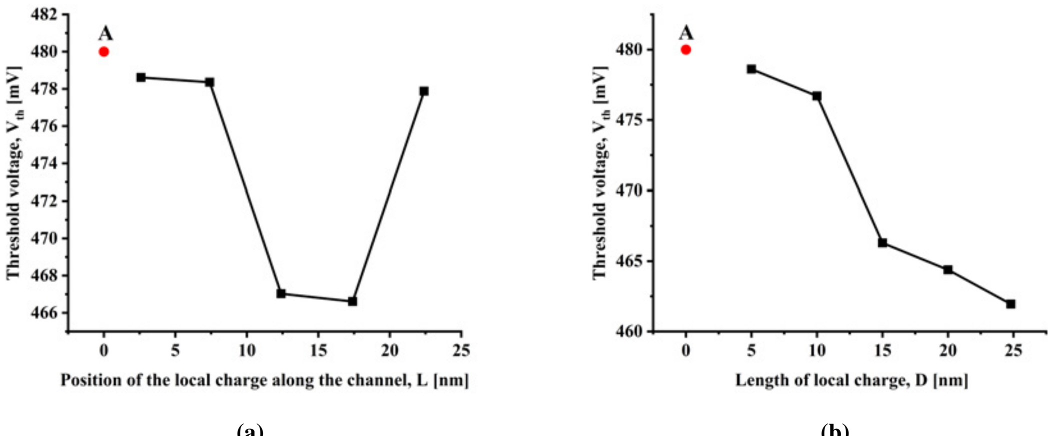

Figure 8. Threshold voltage dependencies on the position, L, (a) and the width, D, (b) of the local oxide trapped charge. Point A corresponds to the case of absence of the oxide trapped charge.

trapped charge in SOI FinFET using the method suggested in [16]. In case of a change in the slope of the subthreshold I-V curve, it also should be accounted for in estimating the change in threshold voltage.

3.2. Impact of the local charge on gate-to-source (gate-to-drain) capacitance

Figure 9 illustrates the simulation results regarding the C-V dependence of the gate-to-source capacitance, C_{gs}, for different position, L, of the local oxide trapped charge. The figure demonstrate that the capacitance C_{gs}, at high applied voltages is significantly and monotonically depends on L (Figure 10). The position corresponding L=2.5 nm (point B in Figure 10) is an exception in this dependence. This is attributed to the fact that in this position the local charged area is in contact with the end of the oxide layer. Consequently, the edge effect is manifested, leading to a considerably high capacitance C_{gs},

The observed increase in the capacitance C_{gs} is linked to the impact of the local trapped charge on carrier concentration within the channel. Indeed, Figure 11 demonstrates that trapping of the charge in the oxide layer leads to an increase in the carrier concentration near the channel surface at all positions of the local charge. In accordance with the definition of capacitance, this results in higher capacitance C_{gs}. In fact, by definition, the capacitance is defined in accordance with formulas (2),

$$C_{gs} = \frac{dQ_V}{dV} \tag{2}$$

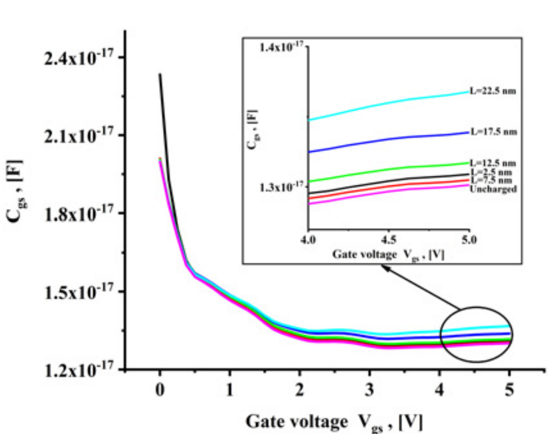

Figure 9. C-V dependence of gate-to-source capacitance C_{gs} at different positions of the local trapped charge.

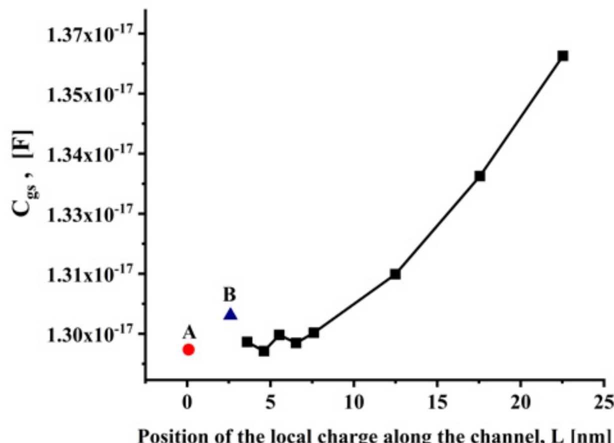

Figure 10. C_{gs} dependence on L at V_{gs}=4.5 V. Point A corresponds to C_{gs} when the local trapped charge is absent, point B corresponds to the position of the local trapped charge at the source end and is in contact with the oxide end (L=2.5 nm).

where dQ_V is a change of the charge in the capacitor C_{gs} at a change in the applied voltage by d_V. Trapping of the local charge into the gate oxide layer leads to adding a charge dQ_{LC} in capacitance C_{gs}, besides dQ_V Therefore, the formula (2) can be rewritten by the following expression (3)

$$C_{gs} = \frac{dQ_V + dQ_{LC}}{dV} \tag{3}$$

It follows from this expression that the capture of local charge leads to an increase in the capacitance C_{gs}

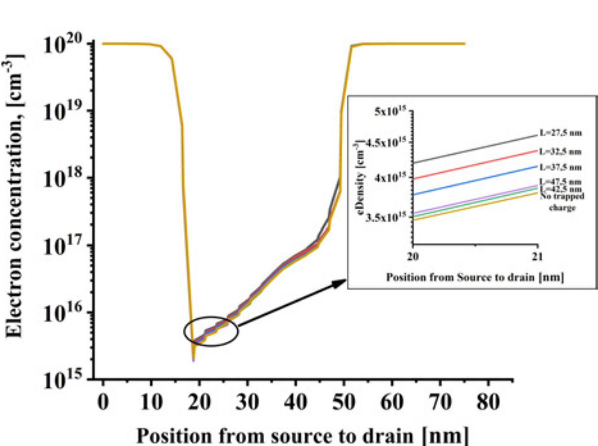

Figure 11. Distribution of electron density along the channel at depth 2nm from the channel surface, at different positions L of the local oxide trapped charge. V_{gs} = 4.5 V

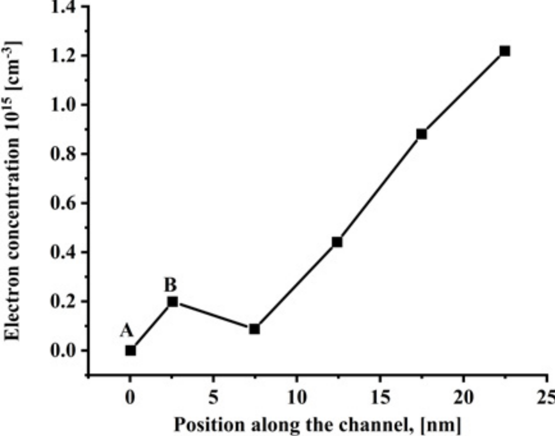

Figure 12. Dependence of the electron density in the channel at a depth of 2 nm from the surface on the position of the local oxide trapped charge. Point A corresponds to the case without oxide trapped charge, and point B corresponds to the position of local charge L=2.5 nm. V_{gs} = 4.5 V

The charges dQ_V and dQ_{LC} are caused by applied voltage and trapped charge, respectively, which are proportional to the change of carrier concentration in the channel. Figure 12 illustrate dependence of the electron density in the channel at a depth 2 nm from the surface on position of the local oxide trapped charge. This dependence correlate with dependence of C_{gs} on the position of local trapped charge shown in Figure 10.

The structure of FinFET has symmetry relative vertical axis passing through the channel center, therefore dependence of gate-to-drain capacitance, C_{gd}, on position L should be the same as the dependence of C_{gs} on position L, but with reversed character. It means that C_{gd} should decrease with increasing L. Indeed, such a character of the dependence is seen in the dependence of C_{gd} on L, carried out from simulation (Figure 13). The relationship between C_{gs} and C_{gd} dependences on the L can be used to estimate the position of the local trapped charge along the channel. For this purpose, the dependence of the ratio C_{gs}/C_{gd} on L can be used (Figure 14).

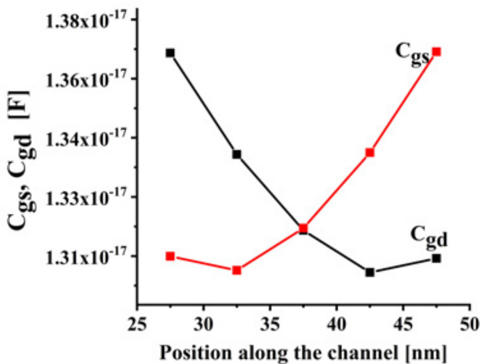

Figure 13. Dependence of C_{gs} and C_{gd} on the position of the local oxide trapped charge, L, along the channel.

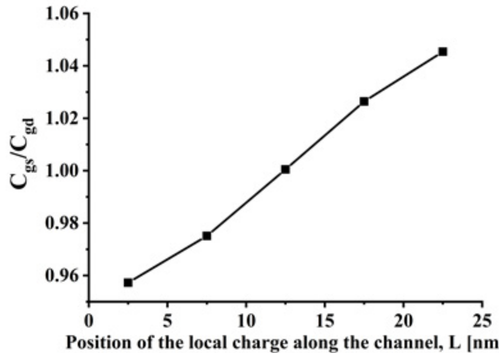

Figure 14. Dependence of the ratio C_{gs}/C_{gd} on the position of the local oxide trapped charge, L, along the channel.

Figure 14 demonstrates that in the case of trapping the local charge at the source side relative to the channel center, the ratio C_{gd}/C_{gs} is less than 1. Value of the ratio C_{gd}/C_{gs} is more than 1 in case of localisation the trapped charge at drain side relative the channel center. In case of localization the trapped charge in the center between source and drain end, the value of the ratio C_{gd}/C_{gs} is equal to 1.

4. CONCLUSIONS

Simulation results show, that the threshold voltage monotonically depends on the linear size, D, along the channel of the charge trapped at drain end of the oxide layer. It allows to estimate integral value of trapped charge in oxide layer in the SOI FinFET as well as in planar MOSFET.

At high applied voltages, gate-to-source capacitance, C_{gs}, monotonically depends on the position of the local oxide trapped charge along channel. C_{gs} monotonically increase with increase distance between source and center of the local charge. Such dependence is explained by the influence of the local charge on the carrier distribution at the surface of the channel. The position of the local charge at the end of the oxide layer is an exception in the mentioned above dependence due to edge effect.

It is shown that the ratio C_{gd}/C_{gs} depends linearly on the position of the local oxide trapped charge along the channel in SOI FinFET. This dependence allows to develop a method to detect the charge in oxide layer and to estimate the distribution of the oxide trapped charge along the channel.

Acknowledgments

The authors are thankful to Prof. R. Aliev from the Andijan State University for participating in discussing the results.

ORCID

Atabek Atamuratov, https://orcid.org/0000-0003-2173-3783; **Ibroximjon Karimov**, https://orcid.org/0009-0002-5714-8658; **Mirzabahrom Foziljonov**, https://orcid.org/0009-0005-0073-1713; **Azamat Abdikarimov**, https://orcid.org/0000-0003-1220-7482; **Odilbek Atamuratov**, https://orcid.org/0000-0002-5010-2692; **Makhkam Khalilloev**, https://orcid.org/0000-0001-5497-6410

REFERENCES

[1] A.E. Atamuratov, M.M. Khalilloev, A. Abdikarimov, Z.A. Atamuratova, M. Kittler, R. Granzner, and F. Schwierz, Nanosystems: Physics, Chemistry, Mathematics, **8**(1), 75 (2017). https://doi.org/10.17586/2220-8054-2017-8-1-75-78

[2] A.E. Atamuratov, A. Abdikarimov, M. Khalilloev, Z.A. Atamuratova, R. Rahmanov, A. Garcia-Loureiro, and A. Yusupov, Nanosystems: physics, chemistry, mathematics, **8**(1), 71 (2017). https://doi.org/10.17586/2220-8054-2017-8-1-71-74

[3] A.E. Atamuratov, B.O. Jabbarova, M.M. Khalilloev, A. Yusupov, and A.G. Loureriro, in: *Proceedings of the 2021 13th Spanish Conference on Electron Devices (CDE)*, (Sevilla, Spain, 2021), pp. 62-64. https://doi.org/10.1109/CDE52135.2021.9455728

[4] R.P. Nelapati, and K. Sivasankaran, Microelectron. J. **76**, 63 (2018). https://doi.org/10.1016/j.mejo.2018.04.015

[5] A.E. Atamuratov, M.M. Khalilloev, A. Yusupov, J. García-Loureiro, J.Ch. Chedjou, and K. Kyandoghere, Appl. Sci. **10**, 5327 (2020). https://doi.org/10.1016/j.cpc.2015.01.024

[6] B. Kaczer, J. Franco, P. Weckx, P.J. Roussel, V. Putcha, E. Bury, M. Simicic, *et al.*, Microelectronics Reliability, **81**, 186 (2018). https://doi.org/10.1016/j.microrel.2017.11.022

[7] J. Martín-Martínez, S. Gerardin, E. Amat, R. Rodríguez, M. Nafría, X. Aymerich, *et al.*, IEEE Transactions on Electron Devices, **56**, 2155 (2009). https://doi.org/10.1109/TED.2009.2026206

[8] A. Jaafar, N. Soin, S.F Wan Muhamad Hatta, S.I. Salim, and Z. Zakaria, Appl. Sci. **11**, 6417 (2021). https://doi.org/10.3390/app11146417

[9] B. Kaczer, T. Grasser, P.J. Roussel, J. Franco, R. Degraeve, and L.A. Ragnarsson, *et al.*, in: *2010 IEEE International Reliability Physics Symposium*, (Anaheim, CA, USA, 2010), pp. 26-32. https://doi.org/10.1109/IRPS.2010.5488856

[10] M.K. Bepary, B.M. Talukder, and M.T. Rahman. Appl. Sci. **12**, 4332 (2022). https://doi.org/10.3390/app12094332

[11] J. Lee, Appl. Sci. **11**, 356 (2021). https://doi.org/10.3390/app11010356

[12] N. Lee, H. Kim, and B. Kang, Appl. Sci. IEEE Electron. Device. Lett. **33**(2), 137 (2012). https://doi.org/10.1109/LED.2011.2174026

[13] A.E. Atamuratov, A. Yusupov, and K. Adinaev, Inorganic Materials, **37**(8), 767 (2001). https://doi.org/10.1023/A:1017918911606

[14] K.S. Ralls, W.J. Skocpol, L.D. Jackel, R.E. Howard, L.A. Fetter, R.W. Epworth, and D.M. Tennant, Physical Review Letters, **52**, 228 (1984). https://doi.org/10.1103/PhysRevLett.52.228

[15] M.M. Khalilloev, B.O. Jabbarova, and A.A. Nasirov, Technical Physics Letters, **45**(12), 1245 (2019). https://doi.org/10.1134/S1063785019120216

[16] P.J. McWhorter, and P.S. Winokur, Applied Physics Letters, **48**(2), 133 (1986). https://doi.org/10.1063/1.96974

[17] E.H. Nicollian, and J.R. Brews, *MOS Physics and Technology*, (Wiley-Interscience, New York, 2003).

[18] L. Boyer, B. Rousset, J. Notingher, S. Agnel, and J.L. Sanchez, in: *Proceedings of the 2010 IEEE Industry Applications Society Annual Meeting*, (Houston, TX, USA, 2010). pp. 1-8. https://doi.org/10.1109/IAS.2010.5614500

[19] A.E. Atamuratov, A. Yusupov, Z.A. Atamuratova, J.C. Chedjou, and K. Kyamakya, Applied Sciences, **10**(21), 7935 (2020). https://doi.org/10.3390/app10217935

[20] A.E. Atamuratov, D.U. Matrasulov, and P.K. Khabibullaev, Doklady Physics, **52**(6), 322 (2007). http://doi.org/10.1134/S1028335807060080

[21] U.I. Erkaboev, S.A. Ruzaliev, R.G. Rakhimov, and N.A. Sayidov, East European Journal of Physics, (3), 270 (2024). https://doi.org/10.26565/2312-4334-2024-3-26

[22] A.E. Atamuratov, M.M. Khalilloev, A. Yusupov, J.C. Chedjou, and K. Kyandoghere, Applied Sciences (Switzerland), **10**(15), 5327 (2020). https://doi.org/10.3390/app10155327

[23] V.S. Basker, T. Standaert, and H. Kawasaki, *et.al.*, in: *Proc. Symp. VLSI Technol*. (Honolulu, HI, USA, 2010), pp. 19–20.

[24] A.S. Starkov, Microelectron. Reliab. **54**, 33 (2014). https://doi.org/10.1016/j.microrel.2013.08.015

[25] A. Asenov, R. Balasubramaniam, A.R. Brown, and J.H. Davies, IEEE Transactions on Electron Devices, **50**(3), 839 (2003). https://doi.org/10.1109/TED.2003.808465

[26] M.G. Dadamirzaev, M.O. Kosimova, S.Boydedayev, and A.S. Makhmudov, East European Journal of Physics, (2), 372 (2024). https://doi.org/10.26565/2312-4334-2024-2-46

[27] J.S. Abdullayev, and I.B. Sapaev, East European Journal of Physics, (3), 344 (2024). https://doi.org/10.26565/2312-4334-2024-3-39

ВПЛИВ ЛОКАЛЬНОГО ЗАРЯДУ, ЗАХОПЛЕНОГО В ОКСИДІ, НА ЕЛЕКТРИЧНІ ТА ЄМНІСНІ ХАРАКТЕРИСТИКИ SOI FinFET

Атабек Атамуратов[a], ** Іброхімжон Карімов**[b], **Мірзабахром Фозілжонов**[b], **Азамат Абдікарімов**[a], **Оділбек Атамуратов**[c], **Махкам Халіллоєв**[a]

[a] *Державний університет Ургенчу імені Абу Райхана Біруні, вул. Х. Алімджана, 14, Ургенч, 220100, Узбекистан*

[b] *Андіжанський державний університет, вул. Університетська, 129, Андіжан, 170100, Узбекистан*

[c] *Ташкентський інститут інженерів іригації та механізації сільського господарства – Національний дослідницький університет, вул. К. Нієзія, 39, Ташкент, 100000, Узбекистан*

У цій роботі моделюється вплив локального заряду, захопленого в оксиді, на передавальні характеристики Id-Vg та ємність між затвором і витоком (стоком) транзистора FinFET на основі структури кремнію на ізоляторі (SOI). Характеристики Id-Vg моделюються з використанням моделі дрейф-дифузійного переносу. Ємнісно-напругові характеристики затвор-виток моделюються за допомогою методу малого змінного сигналу (AC). Досліджено залежність характеристик Id-Vg та ємності затвор-виток (затвор-сток) від різних лінійних розмірів і положень локального заряду в оксиді вздовж каналу. Результати моделювання показують, що порогова напруга монотонно зменшується зі збільшенням лінійного розміру локального заряду, а ємність затвор-виток монотонно зростає зі збільшенням відстані між межею виток-канал і центром локального заряду.

Ключові слова: *FinFET; локальний заряд; ємність затвор-виток; p-n перехід; C-V залежність*

East European Journal of Physics. **3**. 365-374 (2025)
DOI:10.26565/2312-4334-2025-3-37 ISSN 2312-4334

MAGNETIC AND THERMOELECTRIC PROPERTIES OF RbCaYF(Y = C and N) HEUSLER ALLOYS: PROMISING CANDIDATES FOR EMBEDDED SYSTEMS IN TELECOMMUNICATIONS

Kheira Bahnes[a,b], Saliha Rezini[b], Amel Abbad[a,b], Wissam Benstaali[a,b]*, Noureddine Saidi[a,b], Omar Belarbi[a,b]

[a]Laboratory of Technology and Solids Properties, Faculty of Sciences and Technology, Abdelhamid Ibn Badis University, Mostaganem, Algeria

[b]Faculty of Sciences and Technology, BP227, Abdelhamid Ibn Badis University, Mostaganem (27000), Algeria

**Corresponding Author E-mail: ben_wissam@yahoo.fr*

Received March 30, 2025; revised July 31, 2025; accepted August 10, 2025

On the basis of density functional theory, the structural, electronic, magnetic and thermoelectric properties of the d0 new quaternary Heusler alloys RbCaYF (Y= C and N) have been analyzed by means of first-principles calculations. The results predict a stable atomic arrangement in Y-type (III) phase with a ferromagnetic order. The two compounds were found to be half-metallic ferromagnets (HMFs) with an integer magnetic moment of $2\mu_B$ for RbCaCF and $1\mu_B$ for RbCaNF. The ferromagnetism observed is originated from the polarization of the p-Y orbitals with an sp-hybridization. In addition, RbCaCF and RbCaNF display large half metallic (HM) gaps of 0.879, 0.672 eV using Generalized Gradient Approximation (GGA), and 1.730, 1.934 eV with Generalized Gradient Approximation Modified Becke and Johnson (GGA-mBJ) respectively demonstrating stable half metallic features. Besides, thermoelectric properties were computed over a wide range of temperatures. The two Heusler alloys exhibit high values of electric conductivity and figure of merit especially at high temperatures. RbCaCF and RbCaNF d0 Heusler alloys present high spin polarization, robust half-metallicity and high thermoelectric coefficients, which makes them good candidates for spintronic and thermoelectric applications leading to promising enhancements for embedded systems in telecommunications.

Keywords: *Half-metallic; d0 Heusler Alloys; Embedded systems; Thermoelectric Properties; Telecommunications; Wien2k*
PACS: 71.20.Be; 75.50.Cc; 07.07.Df; 73.50.Lw; 42.79.Sz; 71.20.-b

1. INTRODUCTION

Human activities such as automotive exhaust and industrial processes, along with the emission of CO_2, contribute significantly to adverse climate changes. Thermoelectric (TE) materials are crucial in global efforts toward sustainable energy solutions. They are being studied not only for their ability to convert waste thermal energy directly into useful electrical energy but also for their potential to efficiently mitigate environmental pollution.

In recent years, Heusler alloys have emerged as key materials in spintronic devices [1] due to their high Curie temperature and 100% spin polarization at the Fermi level [2-4]. They have shown promising advancement in spintronic applications, offering strong spin transport properties and enabling efficient spin currents manipulation. The greater part of predicted half-metallic ferromagnets (HMFs) [5, 6] are found among Heusler compounds, particularly ternary X2YZ materials that crystallize in the L21 structure [7, 8], where X and Y represent transition metals and Z denotes a main s-p group element. Nevertheless, in some ternary Heusler compounds, disordering effects often compromise their half-metallic nature and impact the magneto-resistance ratio [9, 10]. In response to this challenge, recent research has focused on exploring quaternary Heusler alloys to reduce these limitations. The new alloys can be obtained by replacing one of the X atoms in X2YZ with another atom X′, crystallizing in the LiMgPdSn-type crystal structure [11, 12] withF-43m symmetry [13]. In these compounds, the valence of X' is lower than that of X, and the valence of Y is lower than that of both X and X'.

Over the past few decades, quaternary Heusler alloys have garnered significant attention for their low toxicity and unique properties, including half-metallic ferromagnetism (HMF) and high thermoelectric performance. These characteristics placed them as promising materials for applications in spintronics and thermo-electrics devices. Many scientists have concentrated on confirming the half magnetic characteristics in quaternary Heusler alloys that include magnetic transition-metal elements, such as quaternary Heusler ferromagnets CoFeYGe (Y=Cr and Ti) [14], CoFeScZ (Z=P, As, Sb) [15], CoFeCrZ (Z = Al, Si, Ga and Ge) [16]and VZrReZ (Z= Si, Ge and Sn) [17]. Additionally, Ozdogan et al. theoretically investigated 60 quaternary Heusler alloys, finding that 41 of them exhibited half-metallic properties. In today's spintronic research, there is rising attention in materials with high spin polarization at Fermi energy, promising enhanced magneto-resistance and reduced signal-to-noise ratios in devices. The current trend is to explore new types of half-metallic (HM) compounds, specifically d0 or sp HM compounds, which do not include transition metal elements. Compared with the traditional (HMF) quaternary Heusler materials containing transition metal elements that often exhibit large stray magnetic fields, d0 materials are more practical for real-world applications due to their smaller magnetic moments especially in embedded systems in telecommunication applications. Many d0 quaternary Heusler compounds have been predicted, including those studied by Bouabça et al [19] who examined the structural, electronic, magnetic,

Cite as: K. Bahnes, S. Rezini, A. Abbad, W. Benstaali, N. Saidi, O. Belarbi, East Eur. J. Phys. 3, 365 (2025), https://doi.org/10.26565/2312-4334-2025-3-37
© K. Bahnes, S. Rezini, A. Abbad, W. Benstaali, N. Saidi, O. Belarbi, 2025; CC BY 4.0 license

and thermal properties of the new quaternary Heusler alloys CsSrCZ (with Z = Si, Ge, Sn, P, As, and Sb), Du et al [20, 21] investigated the electronic structures and magnetic properties of quaternary alloys KCaCZ (Z=F and Cl) and KCaNZ (Z = O, S, and Se) where, all the compounds were found to be HM ferromagnetic materials. Rezaei et al [22] studied RbCaNZ (Z = O, S, and Se) quaternary Heusler compounds. These materials exhibit many interesting features, such as a rather large HM gap and a high Curie temperature, and are robust to the change of the lattice parameter. Moreover, d0 Heusler materials have excellent thermoelectric (TE) properties [23, 24], since they convert efficiently waste heat into electricity, offering benefits such as cost-effectiveness, abundance in nature, and environmental friendliness by avoiding toxic elements.

Nevertheless, to the best of our knowledge, up to now, there is no work on RbCaYF (Y= C and N) compounds on the basis of quaternary Heusler structure that has been done and reported. This is why, in this article, quaternary Heusler compounds RbCaYF (Y= C and N) were predicted by means of density functional calculations. We investigated the structural, electronic, magnetic and thermoelectric properties of the two Heusler alloys to verify the possibility of their application in the fabrication of embedded systems for telecommunication engineering. The organization of this work is as follows: Section 1 provides an overview of previous studies on d0 quaternary Heusler alloys. Section 2 offers a brief description of the crystal structure and computational methods used. Section 3 presents the results and their interpretations. Finally, Section 4 summarizes the key findings of the study.

2. COMPUTATIONAL DETAILS

The full potential linearized augmented plane-wave (FP-LAPW) [25, 26] method of density functional theory (DFT), as implemented in WIEN2k code [27] was employed to study the different properties of the new quaternary Heusler alloys RbCaYF (Y = C and N). The exchange and correlation potential were treated using generalized gradient approximation within the parameterization of Perdew–Burke– Ernzerhof (GGA-PBE) [28, 29] and generalized gradient approximation plus Modified Becke and Johnson (GGA-mBJ) [30, 31]. The muffin-tin sphere radii (RMT) were chosen equal to 2 (a.u) for Rb, Ca, Y = (C and N), and F. The plane wave cut-off (K max) was chosen as 8.0/RMT for the expansion of the wave functions in the interstitial region. The choice of this value is due to the fact that it is usually sufficient to converge the total energy to few meV. The Fourier-expanded charge density was truncated at Gmax=12 $(a.u)^{-1}$ to allow a correct convergence of charge density and to keep a reasonable time of calculation. To achieve self-consistency, a k -points in the irreducible wedge of the Brillouin zone generated from a 14 × 14 × 14 mesh which permit to well describe electronic properties. The cut-off energy was limited by -6 Ry value, which defines the separation of valence and core states, this value is the threshold energy below which states are considered core (deep core) and do not participate in chemical bonds. The energy convergence criterion was set to 10^{-6} Ry per formula unit and the criterion for charge convergence was 10^{-4} electrons during self-consistency cycles. These values are used to stop iterations since the system is considered as convergent with great precision.

The thermoelectric properties are calculated with the BoltzTrap code [32], using 120000 k points.

3. RESULTS AND DISCUSSIONS

3.1. Structural properties

The quaternary Heusler compounds are adopted in LiMgPdSn-type crystal structure designated as Y (space group 216). There are three possible different types of atom arrangement in the quaternary Heusler compound XX'YZ: Y-type(I): X (0, 0, 0), X' (0.25, 0.25, 0.25), Y (0.5, 0.5, 0.5), and Z (0.75, 0.75, 0.75); Y-type(II): X (0.25, 0.25, 0.25), X' (0, 0, 0), Y (0.5, 0.5, 0.5), and Z (0.75, 0.75,0.75); Y-type(III): X (0.25, 0.25, 0.25), X' (0.75, 0.75, 0.75), Y (0, 0, 0), and Z (0.5, 0.5, 0.5). The crystal structures are shown in Fig. 01.

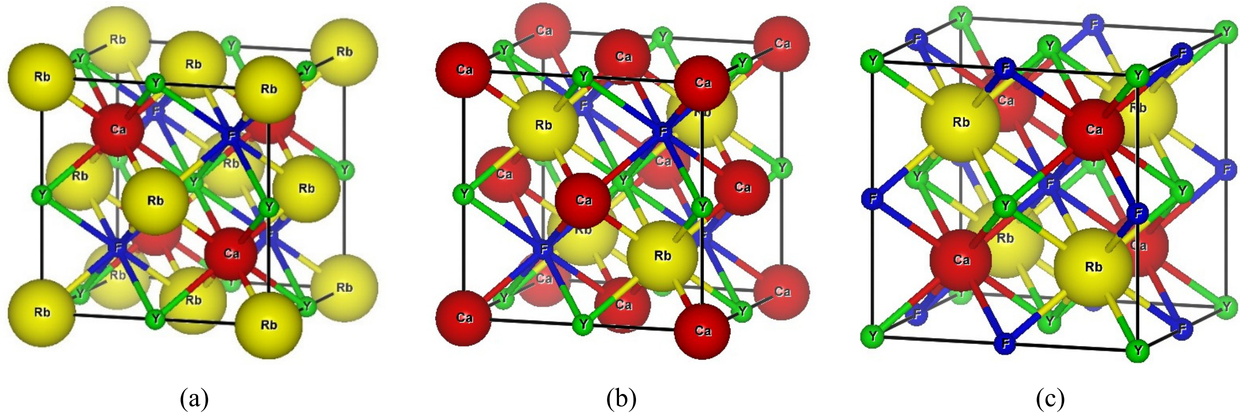

(a) (b) (c)

Figure 1. Visualization of unit cell structure of the RbCaYF (Y = C and N) compounds for (a) Y-type(I) (b) Y-type(II) and (c) Y-type(III) structures using VESTA package

In other to verify the structural and magnetic ground states of the three configurations, the total energies of the non-magnetic (NM) and ferromagnetic (FM) states as a function of the volume were calculated and fitted to the Birch-

Murnaghan's equation of state [33]. The obtained curves are shown in Figures 2 and 3. The results show that Y-type (III) phase is the most favorable structure for both RbCaCF and RbCaNF due to the lowest total energies of equilibrium states. Additionally, the two compounds have the lowest energy in the ferromagnetic state (FM), which indicates that RbCaCF and RbCaNF compounds are most stable in the ferromagnetic state (FM) with the LiMgPdSn-type (III). The energy differences make obvious the significant FM coupling under normal conditions.

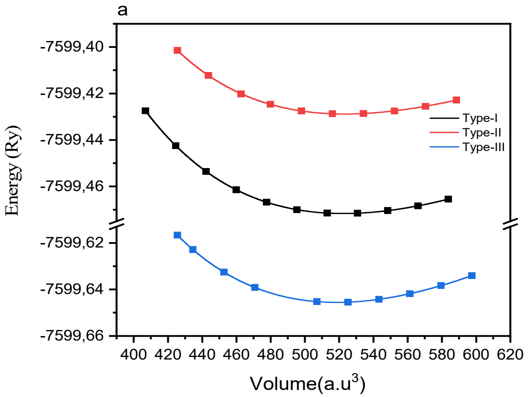

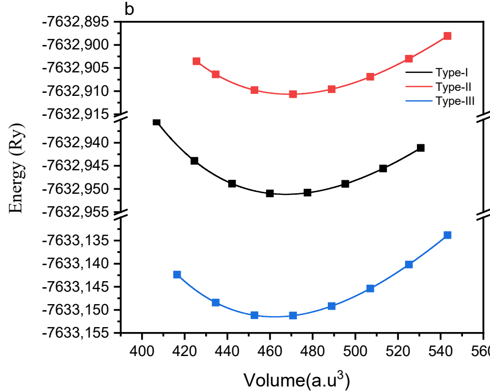

Figure 2. Total energy as a function of unit cell volume for the RbCaCF (a) and RbCaNF (b) compounds in the type-I, type-II, and type-III structures

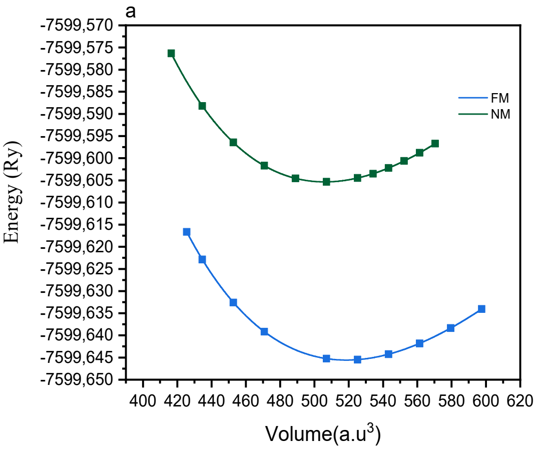

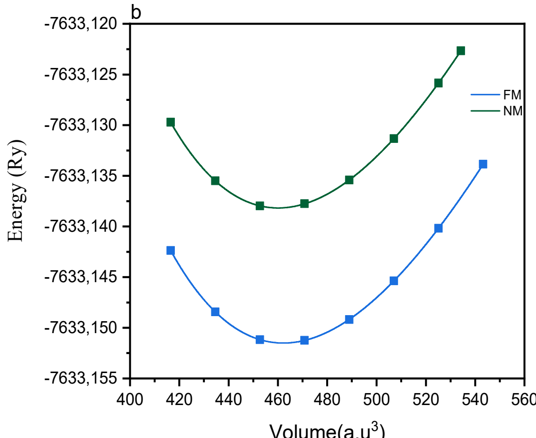

Figure 3. Total energy as a function of unit cell volume in the type-III structures for non-ferromagnetic and ferromagnetic structure for the RbCaCF (a) and RbCaNF (b) compounds

In Table 1, we report our calculated equilibrium lattice constant $a0$, along with bulk modulus B, derivative of bulk modulus B' and the total energies Etot in their different structural and magnetic configurations. As we can see, the obtained equilibrium lattice constant increases with the increase of the atomic radius of anion: 6.49 and 6.74 Å, for RbCaNF and RbCaCF respectively. Moreover, the highest calculated bulk moduli for RbCaYF (Y = C and N) compounds in FM- Y-type (III) configuration confirm the stability of this structure.

Table 1. The calculated bulk parameters, including lattice parameter a_0 (Å), bulk modulus B (GPa), derivative of bulk modulus B', and the total energies Etot (in Ry) per formula unit, of RbCaYF (Y = C and N) compounds in Y-type(I), Y-type(II) and Y-type(III) structures

Alloy	Structure	*Phase*	a_0(Å)	*B*(GPa)	B'	E_{tot}(Ry)
RbCaCF	Y-type(I)	FM	6.76	31.36	4.78	-7599.471666
	Y-type(II)	FM	6.67	28.06	5.49	-7599.428816
	Y-type(III)	FM	6.74	36.09	4.27	-7599.645574
		NM	6.69	38.32	4.23	-7599.605348
RbCaNF	Y-type(I)	FM	6.51	44.53	5.10	-7632.951160
	Y-type(II)	FM	6.52	42.43	4.97	-7632.910680
	Y-type(III)	FM	6.49	49.14	4.52	-7633.151506
		NM	6.48	50.20	4.47	-7633.138173

3.2. Electronic properties

Using GGA and GGA-mBJ approximations, the spin-polarized electronic band structures of RbCaCF and RbCaNF for both spin-up and spin-down with equilibrium lattice parameters considered in the high symmetry directions of the first Brillouin zone are calculated and shown in Fig. 4 and 5, the Fermi level is set to 0 eV. We can see clearly, that the

spin-up electronic bands exhibit a semiconducting behavior with an indirect band gap where the top of the valence bands is at X point and the bottom of conduction bands is at Γ point. The spin down energy bands have an overlap with the Fermi level and show a metallic characteristic. The two approaches give a similar band structure form with a difference in the gap value. The results obtained, illustrate that the two Heusler alloys are d0 half-metallic ferromagnetic materials with 100% spin polarization and the spin-specific carriers should be sufficiently mobile.

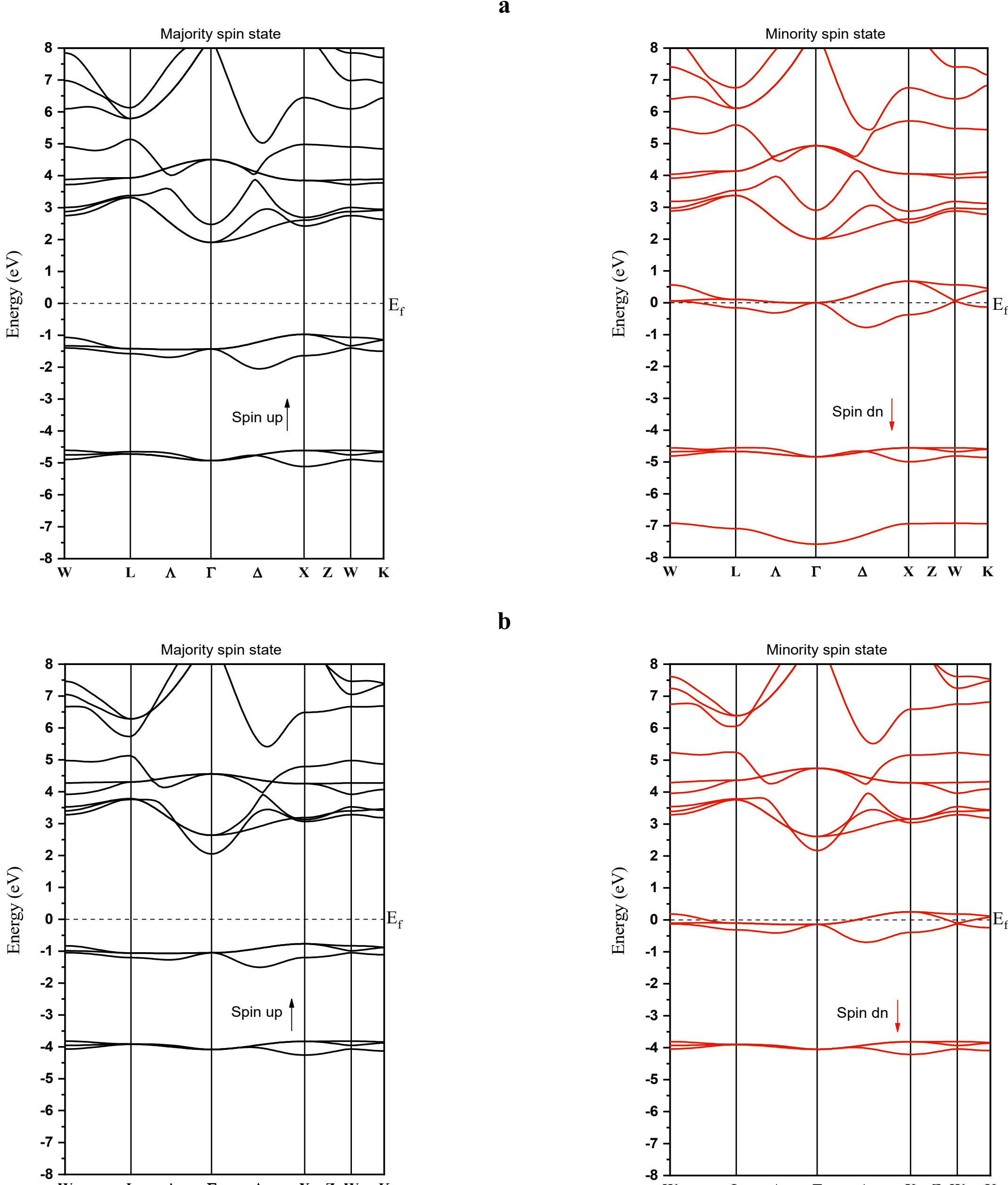

Figure 4. The spin-polarized band structures at the equilibrium lattice parameter of RbCaCF(a) and RbCaNF (b)by using PBE-GGA. Black and red solid lines represent spin-up and spin-down channels, respectively. The dashed line at zero eV indicates the Fermi energy (E_F)

The predicted half-metallic gaps E_{HM} are listed in Table 2. This gap is known to be essential to describe the stability of magnetism of a half-metal [34]. RbCaCF and RbCaNF display large half metallic gaps of 0.879, 0.672 eV using GGA, and 1.730, 1.934 eV with GGA-mBJ respectively illustrating stable half metallic features. Unfortunately, no experimental or theoretical data for the investigated compounds are available for eventual comparison. The calculated density of states (DOS) and partial density of states (PDOS) of RbCaCF and RbCaNF using GGA and GGA-mBJ approximations are shown in Fig. 6 and 7. In order to understand the contribution of each orbital in these atoms we have plotted the angular momentum decomposition of partial density of states. The two compounds have a similar structure. The DOS confirm that majority spin states show semiconducting nature and minority spin states are metallic demonstrating 100% spin polarization at the Fermi level, which is in a good agreement with the band structure calculations. For RbCaCF, and using

GGA the lowest structure extended from -5 eV to -4.5 eV originates mainly from F-p states. The second region from -2eV to 1eV is due to C-p states with a little contribution of Ca-d states.

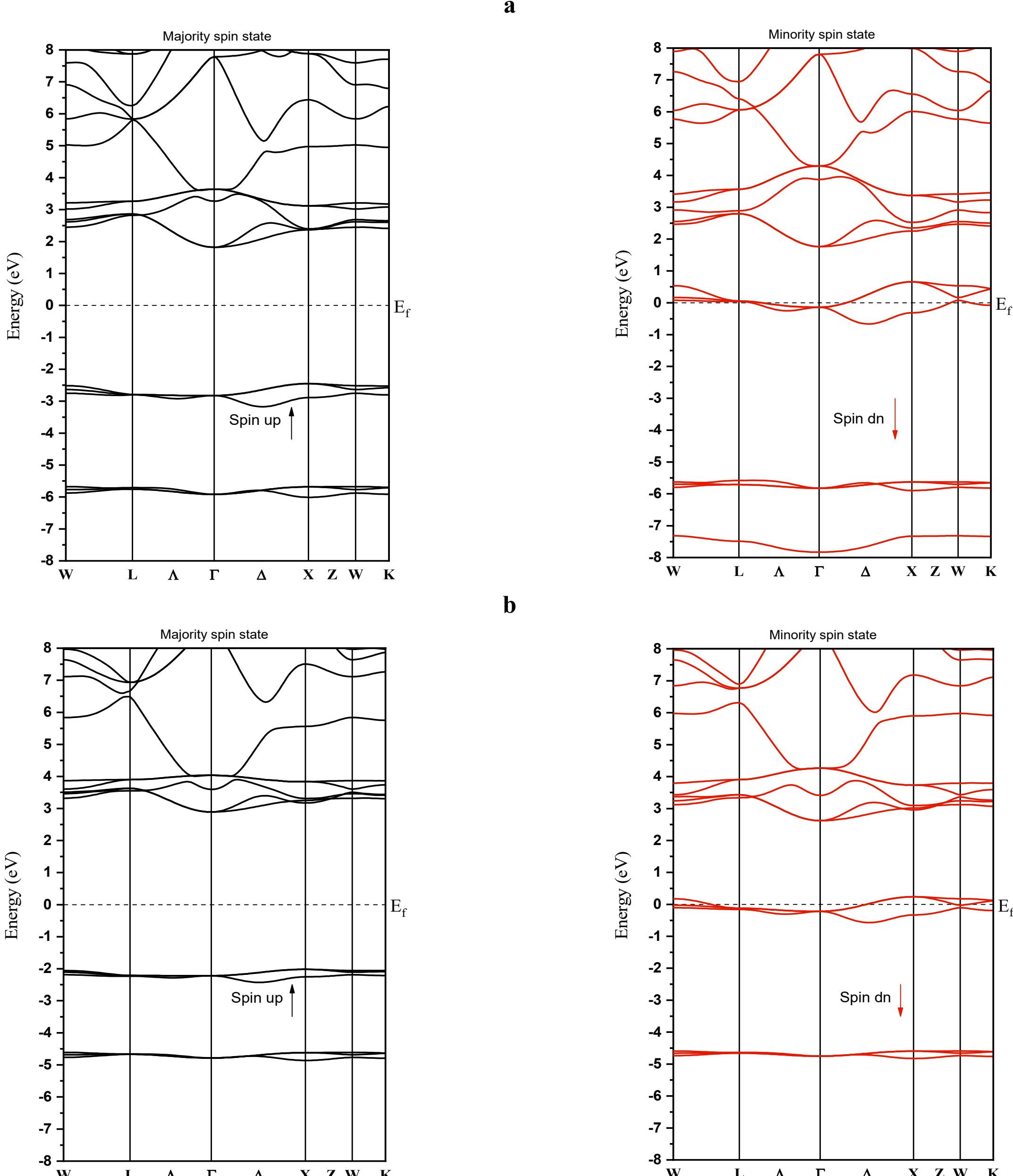

Figure 5. The spin-polarized band structures at the equilibrium lattice parameter of RbCaCF(a) and RbCaNF(b) by using PBE-GGA-mBJ. Black and red solid lines represent spin-up and spin-down channels, respectively. The dashed line at zero eV indicates the Fermi energy (E_F)

Table 2. The virtual semiconducting gap Eg (eV), the half-metallic gap E_{HM} (eV) in quaternary Heusler compounds RbCaYF (Y= C and N)

Alloy	Approximations	VBM	CBM	E_g	E_{HM}
RbCaCF	**GGA**	-0.879	1.814	2.693	0.879
RbCaCF	**GGA-Mbj**	-2.351	1.730	4.081	1.730
RbCaNF	**GGA**	-0.672	1.966	2.639	0.672
RbCaNF	**GGA-Mbj**	-1.934	2.800	4.734	1.934

Hence, the spin polarization is mainly attributed to the contribution of p-d hybridization between C and Ca atoms. The structure from the conduction band minima and above presents a large contribution from Ca-d states. For RbCaNF, the same trend is observed. To realize more realistic electronic density of states, and to overcome the well-known deficiency of DFT regarding energy gap underestimation with GGA functional, and to obtain the exact energy gaps, we

employ the GGA-mBJ as exchange correlation potential and recalculate the spin polarization band structures. The bandgap values computed according to GGA–PBE and GGA–mBJ are listed in Table 02. The major difference observed between GGA–PBE and GGA–mBJ calculations is that the GGA–PBE has underestimated the band gap. By using GGA-mBJ functional corrections, we can see clearly that F-p and C-p states in spin up channels, are shifted downwards Valence Band Maximum (VBM) (from -0.879 eV with GGA to -2.351 eV with GGA–mBJ for RbCaCF and from -0.672 eV with GGA to -1.934 eV with GGA–mBJ for RbCaNF) since GGA–mBJ produces better band splitting. The conduction band still predominantly composed from Rb-d and Ca-d states.

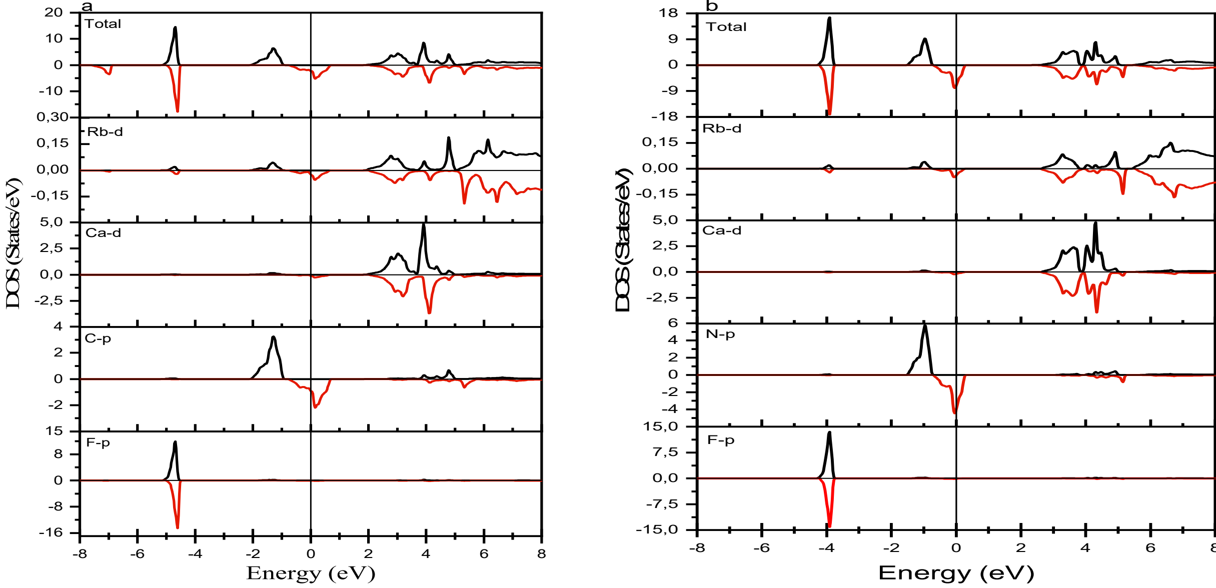

Figure 6. The **t**otal and orbital spin-density of states (DOSs) of ferromagnetic forRbCaCF (a) and RbCaNF (b) compounds by using PBE-GGA. Black and red solid lines represent spin-up and spin-down channels, respectively

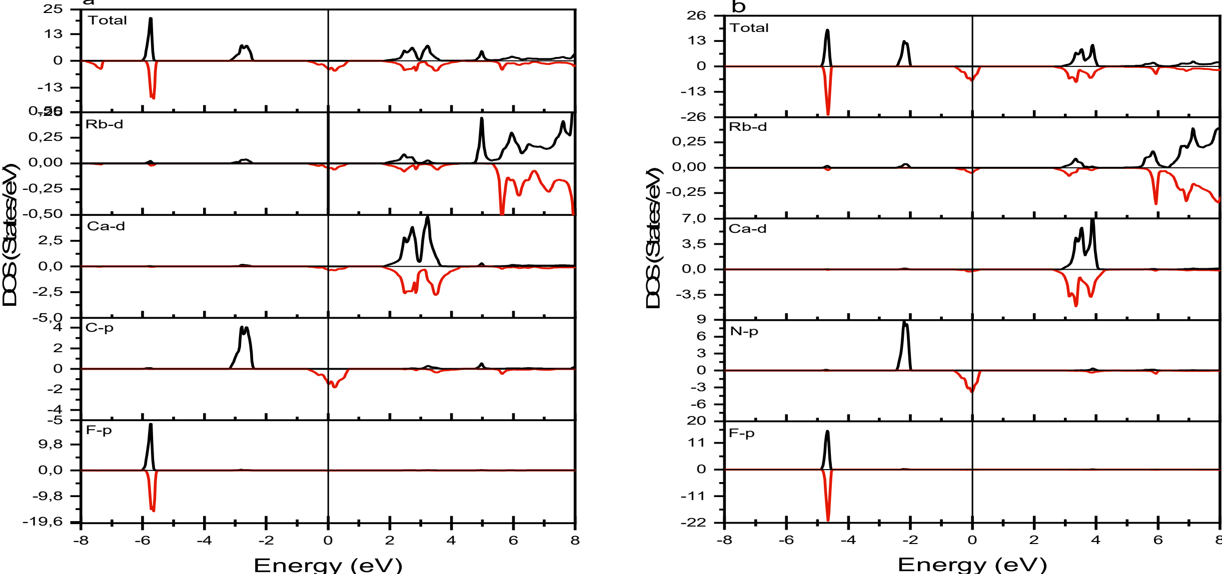

Figure 7. The **t**otal and orbital spin-density of states (DOSs) of ferromagnetic for RbCaCF (a) and RbCaNF (b) compounds by using PBE-GGA-mBJ. Black and red solid lines represent spin-up and spin-down channels, respectively

3.3. Magnetic properties

The calculated magnetic moments of Rb, Ca, Y = (C and N), and F along with total and interstitial magnetic moments are reported in table 3. So, the total magnetic moments μ_{tot} of RbCaCF and RbCaNF compounds are integer with $2\mu_B$ and $1\mu_B$ values respectively. The integer total magnetic moment is a characteristic of (HMFs). We can easily explain these values from the electronic configurations of the two compounds. There are 14 (15) valence electrons in RbCaCF and RbCaNF respectively: (Rb: $5s^1$, Ca: $4s^2$, N: $2s^2$, 2p3, F: $2s^2$, $2p^5$ and C: $2s^2$, $2p^2$) which contribute to the magnetism and bond formation. So, 4 valence electrons occupy the F-2s states in the lowest energy states. 6 of the remaining 10 (11) valence electrons occupy the majority spin p states, which results in the 6 fully filled majority spin bands. The remaining 4 (5) valence electrons partially occupy the 6 lowest minority spin bands. The 2 (1) holes remaining are responsible for

the magnetic moments of $2\mu_B$ and $1\mu_B$, respectively. In addition, the total magnetic moment of RbCaYF (Y = C and N) contains five contributions: Rb atom, Ca atom, F atom, Y atom and the interstitial region. We can see clearly from Table 3, that the magnetic moments of the two compounds originate mainly from the p electrons of C and N atoms. The magnetic moment of the Y atom is parallel to that of Rb atom which confirms the ferromagnetism of the 2 full Heuslers. Since the total magnetic moments are integer, they verify the Slater-Pauling rule which is described by the following formula: $\mu_{Tot} = 12\text{-}Nv$; where μ_{Tot} means the total spin magnetic moment and Nv is the total number of valence electrons per unit-cell. The RbCaYF (Y = C and N) compounds have 10 and 11 valence electrons respectively, so the calculated μ_{tot} for the two compounds satisfy the formula cited above.

Table 3. The calculated atomic magnetic moments M (μ_B) for the RbCaYF(Y=C and N) alloys

Alloy	**M_{tot}**	**M_{Rb}**	**M_{Ca}**	**M_Y**	**M_F**	**M_{int}**
RbCaCF	2.00	0.048	0.047	1.169	0.039	0.699
RbCaNF	1.00	0.016	-0.004	0.794	0.009	0.184

3.4. Thermoelectric properties

Continuing research focuses on finding new Heusler structures and compositions with enhanced thermoelectric performance, by exploring different combinations of X, Y, and Z elements, in addition to examining the effects of several synthesis and processing techniques. Thermoelectric Efficiency is classically measured by the dimensionless figure of merit ZT, which is given by the formula: $ZT=S^2\sigma T/k$ where S is the Seebeck coefficient (thermo-power), σ is the electrical conductivity, T is the absolute temperature, and k is the thermal conductivity. Heusler alloys can exhibit high Seebeck coefficients depending on their composition and the temperature range. A high Seebeck coefficient is attractive for efficient thermoelectric materials as it indicates a large voltage for a given temperature difference. Since quaternary Heusler materials are regarded as the alternate sources of energy because of their aptitude to convert waste heat into electricity and are used for power generation as they are abundant in nature, and principally environmentally friendly, we report in this study and for the first time, Seebeck coefficient: S, electrical conductivity: σ/τ, thermal conductivity: k/τ and figure of merit ZT of the new d0 quaternary Heusler compounds RbCaYF (Y= C and N) using BoltzTrap code. The different parameters are presented on Figures 8 (a), (b), (c) and (d).

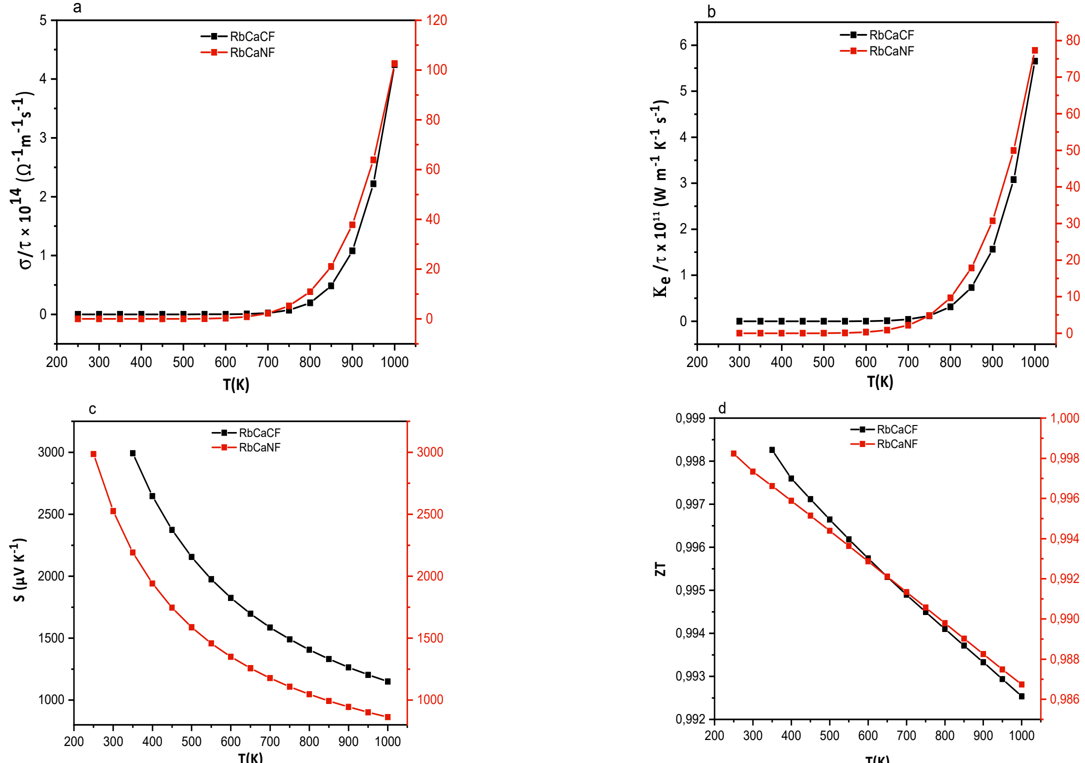

Figure 8. The variation of total electrical conductivity σ/τ (a), total thermal conductivity k/τ (b), total Seebeck coefficient S (c) and figure of merit ZT (d) as a function of temperature for RbCaYF (Y= C and N) compounds

The temperature variation of electrical conductivity σ/τ is reported in Fig. 8 (a). We observe that the electrical conductivity of the two compounds is nearly zero at room temperature but increases exponentially with increasing temperature, at 1000 K it attains 4.24×10^{14} /Ωms and 102.56×10^{14} /Ωms for RbCaCF and RbCaNF, respectively, so RbCaNF shows high electric conductivity comparing to RbCaNF which is consistent with the band structure investigations. In Fig. 8(b), we present the variation of total thermal conductivity k/τ with temperature. It is obvious

that k/τ plots follow a similar trend as those of electrical conductivity σ/τ. The k/τ values show a negligible variation up to 750 k and increases at higher temperatures. It reaches 5.65×10^{10} /WK^{2}ms and 77.31×10^{10} /WK^{2}ms for RbCaCF and RbCaNF, respectively. Figure 8 (c) displays the variation of Seebeck coefficient with the temperature. As we can see, the Seebeck coefficient RbCaYF (Y= C and N) of the two Heusler compounds is positive for the entire temperature range which explains that the holes are dominant charge carriers, therefore RbCaYF are *p*-type materials essential in thermoelectric applications, such as power generation from waste heat and energy-efficient cooling devices. S decreases exponentially with increasing temperature. The values of Seebeck coefficient are 1150 μV/K and 862 μV/K for RbCaCF and RbCaNF at 1000 K respectively. Finally, we calculated the figure of merit ZT which is an essential parameter for assessing the efficiency of thermoelectric materials and devices. High ZT value indicates a more efficient thermoelectric material. A figure of merit ZT equal to 1 signifies that a thermoelectric material has achieved equilibrium between electrical conductivity, Seebeck coefficient, and thermal conductivity [35]. The variation of ZT with temperature for the two Heuslers alloys, is shown on Fig. 8(d), ZT decreases slightly in the large temperature range 200-1000 K, it stills close to the unity for the two compounds. These results suggest the excellent thermoelectric performance of these two d0 Heuslers alloys signifying that they could be promising materials for applications in thermoelectric technologies in particular at high temperatures for example in industrial processes or power plants, so these materials can convert excess heat into electrical power which improves efficiency with reducing energy waste or in space Exploration, they can be very benefit, where they power spacecrafts and rovers.

4. CONCLUSION

To summarize, the structural, electronic magnetic and thermoelectric properties of new d0 quaternary Heuslers compounds RbCaYF (Y = C and N) are predicted using full-potential linearized augmented plane wave (FP-LAPW) method of density functional theory (DFT) within the generalized gradient approximation (GGA) and generalized gradient approximation plus Modified Becke and Johnson (GGA-mBJ). The stable type Y-type (III) configuration structure in the ferromagnetic state (FM) was energetically more favorable due to the lowest total energies of equilibrium states. The two systems are predicted to be HM ferromagnets with a large half metallic gap of 0.879, 0.672 eV using GGA, and 1.730, 1.934 eV with mBJ for RbCaCF and RbCaNF respectively. The use of the modified Becke–Johnson exchange potential approximation (GGA-mBJ) improves the results found by the standard-GGA since it gives an apparent picture of the electronic structure at the Fermi level. The total magnetic moments μ_{tot} of RbCaCF and RbCaNF compounds are integer with $2\mu_B$ and $1\mu_B$ values respectively. The origin of ferromagnetism is the polarization of the p-orbitals of N and C atoms with an sp-hybridization. Additionally, the transport properties of the two compounds predict that the two compounds may perform well particularly at high temperatures. These materials exhibit high values of electric conductivity and figure of merit at 1000K where their application becomes particularly interesting nevertheless, further investigations are required to minimize thermal conductivity and enhance Seebeck coefficient at high temperatures. RbCaCF and RbCaNF d0 Heusler alloys present high spin polarization, robust half-metallicity and high thermoelectric coefficients which makes them good candidates for spintronic and thermoelectric applications. In addition, our Heusler alloys have significant potential for enhancing embedded systems used in telecommunications through their use in spintronics, magnetic sensors, magnetoresistive devices and high-frequency applications. A good number of the investigated properties are reported for the first time and are opened for experimental verification.

Declaration of Funding: No funding was received for this study.

ORCID

Kheira Bahnes, https://orcid.org/0009-0007-3676-1126; **Wissam Benstaali,** https://orcid.org/0000-0003-4634-6210
Noureddine Saidi, https://orcid.org/0009-0004-5343-8572; **Omar Belarbi,** https://orcid.org/0009-0002-6504-359X
Amel Abbad, https://orcid.org/0009-0006-1622-5564; **Saliha Rezini,** https://orcid.org/0000-0002-8080-3051

REFERENCES

[1] R.A. De Groot, F.M. Mueller, P.V. van Engen, and K.H.J. Buschow, (1983). "New class of materials: half-metallic ferromagnets," Physical review letters, **50**(25), 2024-2027 (2024). https://doi.org/10.1103/PhysRevLett.50.2024
[2] P.J. Brown, K.U. Neumann, P.J. Webster, and K.R.A. Ziebeck, "The magnetization distributions in some Heusler alloys proposed as half-metallic ferromagnets," J. Phys.Condens. Matter, **12**, 1827 (2000). https://doi.org/10.1088/0953-8984/12/8/325
[3] T. Graf, C. Felser, and S.S. Parkin, "Simple rules for the understanging of Heusler compounds," Prog. Solid State Ch. **39**, 1-50 (2011). https://doi.org/10.1016/j.progsolidstchem.2011.02.001
[4] C. Felser, I. Wollmann, S. Chadov, G.H. Fecher, and S.S. Parkin, "Basics and perspective of magnetic Heusler compounds," APL Mater. **3**, 041518 (2015). https://doi.org/10.1063/1.4917387
[5] J.M.D. Coey, M. Venkatesan, and M.A. Bari, "Half-Metallic Ferromagnets," in: *High Magnetic Fields. Lecture Notes in Physics*, vol. 595, edited by C. Berthier, L.P. Lévy, and G. Martinez, (Springer-Verlag, NY, 2002), pp. 377–396. https://doi.org/10.1007/3-540-45649-X_15
[6] I. Zutic, J. Fabian, and S.D. Sharma, "Spintronics: Fundamentals and applications," Rev. Mod. Phys. **76**, 323 (2004). https://doi.org/10.1103/RevModPhys.76.323
[7] Galanakis, Ph. Mavropoulos, and P.H. Dederichs, "Electronic structure and Slater–Pauling behaviour in half-metallic Heusler alloys calculated from first principles," J. Phys. D: Appl. Phys. **39**, 765 (2006). https://doi.org/10.1088/0022-3727/39/5/S01

[8] H. Kurt, K. Rode, M. Venkatesan, P. Stamenov, and J.M.D. Coey, "High spin polarization in epitaxial films of ferrimagnetic Mn_3Ga," Phys. Rev. B, **83**, 020405(R) (2011). https://doi.org/10.1103/PhysRevB.83.020405; "$Mn_{3-x}Ga$ ($0 \leq x \leq 1$): Multifunctional thin film materials for spintronics and magnetic recording," Phys. Status Solidi B, **248**, 2338 (2011). https://doi.org/10.1002/pssb.201147122

[9] Y. Miura, K. Nagao, and M. Shirai, "Atomic disorder effects on half-metallicity of the full-Heusler alloys $Co_2(Cr_{1-x}Fe_x)Al$: A first-principles study," Phys. Rev. B, **69**, 144413 (2004). https://doi.org/10.1103/PhysRevB.69.144413

[10] H.C. Kandpal, V. Ksenofontov, M. Wojcik, R. Seshadri, and C. Felser, "Electronic structure, magnetism and disorder in the Heusler compound Co_2TiSn," J. Phys. D: Appl. Phys. **40**, 1587 (2007). https://doi.org/10.1088/0022-3727/40/6/S13

[11] X. Dai, G. Liu, G.H. Fecher, C. Felser, Y. Li, and H. Liu, "New quaternary half metallic material CoFeMnSi," J. Appl. Phys. **105**, 07E901 (2009). https://doi.org/10.1063/1.3062812

[12] G.Z. Xu, E.K. Liu, Y. Du, G.J. Li, G.D. Liu, W.H. Wang, and G.H. Wu, "A new spin gapless semiconductors family: Quaternary Heusler compounds," EPL, **102**, 17007 (2013). https://doi.org/10.1209/0295-5075/102/17007

[13] J. Drews, U. Eberz, and H. Schuster, "Optische Untersuchungen an farbigen Intermetallischen Phasen," J. Less-Common Met. **116**, 271 (1986). https://doi.org/10.1016/0022-5088(86)90235-3

[14] Z. Charifi, T. Ghellab, H. Baaziz, and F. Soyalp, "Characterization of quaternary Heusler alloys CoFeYGe (Y= Ti, Cr) with respect to structural, electronic, magnetic, mechanical, and thermoelectric features," International Journal of Energy Research, **46**(10), 13855-13873 (2022). https://doi.org/10.1002/er.8104

[15] Q. Gao, L. Li, G. Lei, J.B. Deng, and X.R. Hu, "A first-principle study on the properties of a new series of quaternary Heusler alloys CoFeScZ (Z= P, As, Sb)," Journal of Magnetism and Magnetic Materials, **379**, 288-293 (2015). https://doi.org/10.1016/j.jmmm.2014.12.025

[16] M.I. Khan, H. Arshad, M. Rizwan, S.S.A. Gillani, M. Zafar, S. Ahmed, and M. Shakil, "Investigation of structural, electronic, magnetic and mechanical properties of a new series of equiatomic quaternary Heusler alloys CoYCrZ (Z= Si, Ge, Ga, Al): A DFT study," Journal of Alloys and Compounds, **819**, 152964 (2020). https://doi.org/10.1016/j.jallcom.2019.152964

[17] F. Faid, H. Mebarki, K. Mokadem, F.M. Abdalilah, A. Benmakhlouf, M. Khatiri, and T. Helaimia, "Systematic study of structural, elastic, electronic, Magnetism and Half-metallic properties for the quaternary alloys: Heusler type VZrReZ (Z= Si, Ge and Sn)," Journal of Magnetism and Magnetic Materials, 172345 (2024). https://doi.org/10.1016/j.jmmm.2024.172345

[18] K. Özdoğan, E. Şaşıoğlu, and I. Galanakis, "Slater-Pauling behavior in LiMgPdSn-type multifunctional quaternary Heusler materials: Half-metallicity, spin-gapless and magnetic semiconductors," Journal of Applied Physics, **113**(19), 193903 (2013). https://doi.org/10.1063/1.4805063

[19] A. Bouabça, H. Rozale, A. Amar, X.T. Wang, A. Sayade, and A. Chahed, "First-principles study of new series of quaternary Heusler alloys CsSrCZ (Z=Si, Ge, Sn, P, As, and Sb)," J. Magn. Magn. Mater. **419**, 210-217 (2016). https://doi.org/10.1016/j.jmmm.2016.06.018

[20] J. Du, S. Dong, Y.L. Lua, H. Zhao, L.F. Feng, and L.Y. Wang, "Half-metallic ferromagnetic features in d^0 quaternary-Heusler compounds KCaCF and KCaCCl: A first-principles description," J. Magn. Magn. Mater, **428**, 250-254 (2017). https://doi.org/10.1016/j.jmmm.2016.12.038

[21] J. Du, S. Dong, X.T. Wang, H. Rozale, H. Zhao, L.Y. Wang, and L.F. Feng, "Half-metallic ferromagnetism in KCaNX (X = O, S, and Se) quaternary Heusler compounds: A first-principles study," Superlattices Microstruct, **105**, 39-47 (2017). https://doi.org/10.1016/j.spmi.2016.12.055

[22] S. Rezaei, and F. Ahmadian, "First-principles study of half-metallic properties in RbCaNZ (Z = O, S, and Se) quaternary Heusler compounds," J. Magn. Magn. Mater, **456**, 78-86 (2018). https://doi.org/10.1016/j.jmmm.2018.02.006

[23] A. Taleb, A. Chahed, M. Boukli, H. Rozale, B. Amrani, M. Rahmoune, and A. Sayede, "Structural, magneto-electronic and thermophysical properties of the new d0 quaternary heusler compounds KSrCZ (Z= P, As, Sb)," Revista mexicana de fisica, **66**(3), 265-272 (2020). https://doi.org/10.31349/RevMexFis.66.265

[24] S. Gheriballah, B. Bouabdellah, A. Oughilas, M.A. Boukli, M. Rahmoune, and A. Sayede, "Investigating structure, magneto-electronic, and thermoelectric properties of the new d0 quaternary Heusler compounds RbCaCZ (Z= P, As, Sb) from first principle calculations," Indian Journal of Pure & Applied Physics, **58**, 818-824 (2020). https://doi.org/10.56042/ijpap.v58i11.32390

[25] P. Hohenberg, and W.J.P.R. Kohn, "Inhomogeneous Electron Gas," Phys. Rev. B, **136**, B864-B871 (1964). http://dx.doi.org/10.1103/PhysRev.136.B864

[26] J.P. Perdew, J.A. Chevary, S.H. Vosko, K.A. Jackson, M.R. Pederson, D.J. Singh, and C. Fiolhais, "Atoms, molecules, solids, and surfaces: Applications of the generalized gradient approximation for exchange and correlation," Phys. Rev. B, **46**, 6671 (1992). https://doi.org/10.1103/PhysRevB.46.6671

[27] P. Blaha, K. Schwarz, G. K. Madsen, D. Kvasnicka, J. Luitz, *et al.*, "WIEN2k. An augmented plane wave+ local orbitals program for calculating crystal properties," **60**, 155 (2001).

[28] J.P. Perdew, K. Burke, and M. Ernzerhof, "Generalized gradient approximation made simple," Physical review letters, **77**(18), 3865 (1996). https://doi.org/10.1103/PhysRevLett.77.3865

[29] J.P. Perdew, and Y. Wang, "Accurate and simple analytic representation of the electron-gas correlation energy," Phys. Rev. B, **45**, 13244 (1992). https://doi.org/10.1103/PhysRevB.45.13244

[30] F. Tran, P. Blaha, and K. Schwarz, "Band gap calculations with Becke–Johnson exchange potential," Journal of Physics: Condensed Matter, **19**, 196208 (2007). https://doi.org/10.1088/0953-8984/19/19/196208

[31] D. Koller, F. Tran, and P. Blaha, "Improving the modified Becke-Johnson exchange potential," Physical Review B, **85**(15), 155109 (2012). https://doi.org/10.1103/PhysRevB.85.155109

[32] G.K.H. Madsen, and D.J. Singh, "BoltzTraP.A code for calculating band-structure dependent quantities," Computer Physics Communications, **175**(1), 67-71 (2006). https://doi.org/10.1016/j.cpc.2006.03.007

[33] F.D. Murnaghan, "The Compressibility of Media under Extreme Pressures," Proc. Natl. Acad. Sci. USA, **30**, 244-247 (1944). https://doi.org/10.1073/pnas.30.9.244

[34] E. Şaşioglu, L.M. Sandratskii, and P. Bruno, "First-principles study of exchange interactions and Curie temperatures of half-metallic ferrimagnetic full Heusler alloys Mn2V Z (Z = Al, Ge)," J. Phys.: Condens. Matter, **17**, 995 (2005). https://doi.org/10.1088/0953-8984/17/6/017

[35] T. Takeuchi, "Conditions of Electronic Structure to Obtain Large Dimensionless Figure of Merit for Developing Practical Thermoelectric Materials," Mater. Trans. **50**, 2359-2365 (2009). https://doi.org/10.2320/matertrans.M2009143

МАГНІТНІ ТА ТЕРМОЕЛЕКТРИЧНІ ВЛАСТИВОСТІ СПЛАВІВ ГЕЙСЛЕРА RbCaYF(Y = C та N): ПЕРСПЕКТИВНІ КАНДИДАТИ ДЛЯ ВБУДОВАНИХ СИСТЕМ У ТЕЛЕКОМУНІКАЦІЯХ

Хейра Банес[a,b], Саліха Резіні[b], Амель Аббад[a,b], Віссам Бенстаалі[a,b], Нуреддін Саїді[a,b], Омар Беларбі[a,b]
[a]*Лабораторія технологій та властивостей твердих тіл, Факультет наук і технологій, Університет Абдельхаміда Ібн Бадіса, Мостаганем, Алжир*
[b]*Факультет наук і технологій, BP227, Університет Абдельхаміда Ібн Бадіса, Мостаганем (27000), Алжир*

На основі теорії функціоналу густини було проаналізовано структурні, електронні, магнітні та термоелектричні властивості нових четвертинних сплавів Гейслера d0 RbCaYF (Y = C та N) за допомогою розрахунків з перших принципів. Результати передбачають стабільне розташування атомів у фазі Y-типу (III) з феромагнітним порядком. Було виявлено, що дві сполуки є напівметалевими феромагнетиками (HMF) з цілочисельним магнітним моментом 2 μ_B для RbCaCF та 1 μ_B для RbCaNF. Спостережуваний феромагнетизм походить від поляризації p-Y орбіталей з sp2-гібридизацією. Крім того, RbCaCF та RbCaNF демонструють великі напівметалеві (HM) щілини 0,879, 0,672 еВ за допомогою узагальненого градієнтного наближення (GGA) та 1,730, 1,934 еВ відповідно за допомогою узагальненого градієнтного наближення модифікованого методу Бекке-Джонсона (GGA-mBJ), демонструючи стабільні напівметалеві характеристики. Крім того, термоелектричні властивості були розраховані в широкому діапазоні температур. Два сплави Гейслера демонструють високі значення електропровідності та коефіцієнта якості, особливо за високих температур. Сплави Гейслера RbCaCF та RbCaNF d0 мають високу спінову поляризацію, стійку напівметалевість та високі термоелектричні коефіцієнти, що робить їх хорошими кандидатами для спінтроніки та термоелектричних застосувань, що призводить до багатообіцяючих удосконалень вбудованих систем у телекомунікаціях.

Ключові слова: *напівметал; d0 сплави Гейслера; вбудовані системи; термоелектричні властивості; телекомунікації; Wien2k*

EAST EUROPEAN JOURNAL OF PHYSICS. 3. 375-381 (2025)
DOI:10.26565/2312-4334-2025-3-38 ISSN 2312-4334

IMPACT OF RUTHENIUM DIFFUSION ON THE ELECTRICAL PROPERTIES OF THICK FILM RESISTORS

Avazbek T. Dekhkonov[a]*, Gulmurza Abdurakhmanov[a], Mukhriddin E. Tursunov[a], Shokhzod M. Norbekov[b,g], Dilnoza G. Tashmukhamedova[c], Gulbakhor Vokhidova[d], Dibya Prakash Rai[e], Ummat A. Asrorov[f,a]

[a]National University of Uzbekistan named after Mirzo Ulugbek, Tashkent, Uzbekistan
[b]Tashkent Institute of Management and Economics, Tashkent, Uzbekistan
[c]Tashkent State Technical University named after Islom Karimov, Tashkent, Uzbekistan
[d]Alfakom Non-state Training Center, Tashkent, Uzbekistan
[e]Department of Physics, Mizoram University, Aizawl 796004, India
[f]National Pedagogical University of Uzbekistan named after Nizami, Tashkent, Uzbekistan
[g]Almalyk Branch of Tashkent State Technical University, M. Ulug'bek 45, 110100, Almalyk, Tashkent Region, Uzbekistan
**Corresponding Author e-mail: dexqonovavazbek1993@gmail.com*
Received May 8, 2025; revised August 5, 2025; accepted August 5, 2025

The diffusion profile of the RuO_2 into silicate glass and the electrical resistance distribution across diffusion layer have been studied by beveled sample method and energy dispersion spectroscopy. The distribution of content of Ru atoms in the diffusion layer is described by the erfc(x) what means that the diffusion coefficient is independent of the content of Ru atoms. The correlation of the distribution of Ru atom content and the resistance distribution in the diffusion layer showed that it is the diffusion doping of glass that is responsible for the conductivity of thick-film resistors. Thickness of the diffusion layer is more than 100 μm while average distance between RuO_2 particles is about 0.5-2 μm. It means that all volume of the thick-film resistor comes conductive in firing process at 850°C in 10 minutes.
Keywords: *Beveled sample; Diffusion layer; Diffusion coefficient; Resistance distribution; Diffusion profile*
PACS: 72.80.Ng

INTRODUCTION

The conduction mechanism of thick film resistors has been the subject of research for more than 50 years [1-15]. The main efforts of researchers were aimed at explaining the mysterious minimum in the temperature dependence of resistance. Variable range hopping (Mott mechanism), percolation, tunneling through a thin layer of glass between crystalline dopant particles (conducting phase, mainly RuO_2 or ruthenates) and combinations of these mechanisms have been proposed. All these proposals are based on the structure of thick-film resistors observed in an electron microscope and X-ray diffraction patterns, in which crystalline particles of the conducting phase are distributed almost uniformly in a glass matrix. Unfortunately, all these proposals could not explain experimentally observed temperature dependence of resistance, including "metallic" conductivity [13-15].

The maximums of resistance and Seebeck coefficient of thick-film resistors at a temperature of about 1000 K [16] have not attracted researchers.

In [17, 18], based on a set of experimental data, another conductivity mechanism for thick-film resistors was proposed, suggesting 1) the existence of nanocrystals in the glass itself; 2) structural transitions in nanocrystals at high temperatures; 3) diffusion of atoms of the conducting phase into the glass during sintering and the formation of an impurity zone near the top of the valence band of the glass; 4) the conductivity of a thick-film resistor is the sum of activation conductivity along the impurity band and hopping conductivity across nanocrystals. This mechanism made it possible to qualitatively explain the temperature dependence of the conductivity of thick-film resistors in the temperature range from liquid helium to 1100 K.

However, the assumption about the correlation between the diffusion of atoms of the conducting phase into glass and the conductivity of the glass itself has not been confirmed experimentally.

The aim of this article is to experimentally confirm the correlation of the diffusion of atoms into glass and the electrical conductivity of the glass itself.

EXPERIMENTAL METHOD

Sample of glass for experiments has a composition (mass %) SiO_2 – 33; PbO – 67 and was boiled at a temperature 1773 K for 1 hour and cast into a steel mold with dimensions 20×4×4 mm. Cooled glass sample was annealed at 723 K for 3 hours with cooling in a switched off furnace. The opposite wide faces of the sample were grinded parallel to each other and polished to mirror finish. A layer of RuO_2 from an aqueous suspension (1 mass %) was deposited on one of the wide faces of the glass prism for 1 min and dried at 423 K for 1 hour. RuO_2 diffusion into glass was carried out at 923 K for 5

Cite as: A.T. Dekhkonov, G. Abdurakhmanov, M. E. Tursunov, Sh.M. Norbekov, D.G. Tashmukhamedova, G. Vokhidova, D.P. Raie, East Eur. J. Phys. 3, 375 (2025), https://doi.org/10.26565/2312-4334-2025-3-38
© A.T. Dekhkonov, G. Abdurakhmanov, M. E. Tursunov, Sh.M. Norbekov, D.G. Tashmukhamedova, G. Vokhidova, D.P. Raie, 2025; CC BY 4.0 license

hours (Fig. 1a). This low diffusion temperature was chosen to avoid softening the glass and changing the shape of the sample. After diffusion, the sample was polished at an angle of 0.5 degrees to the glass surface (beveled sample, Fig. 1b).

At small polishing angles about 0.5° of a beveled sample, the distance x deep into the diffusion layer is related to the distance l along the surface of the sample as $x = l \operatorname{tg} \varphi \approx l \cdot \varphi = l \cdot \varphi \cdot \pi/180° \approx l \cdot 0.5°/57.3° \approx l/115$, i.e. the diffusion length appears to be increased by approximately 115 times, and a displacement of 0.5 mm along the l axis (Fig. 1*b*) corresponds to a displacement along the x axis of 4.4 µm. This makes it possible to correlate the measured resistance distribution $R(l)$ along the glass surface to the resistance distribution $R(x)$ deep into the diffusion layer and compare the profiles of the distribution of atoms in the diffusion layer with the resistance distribution there.

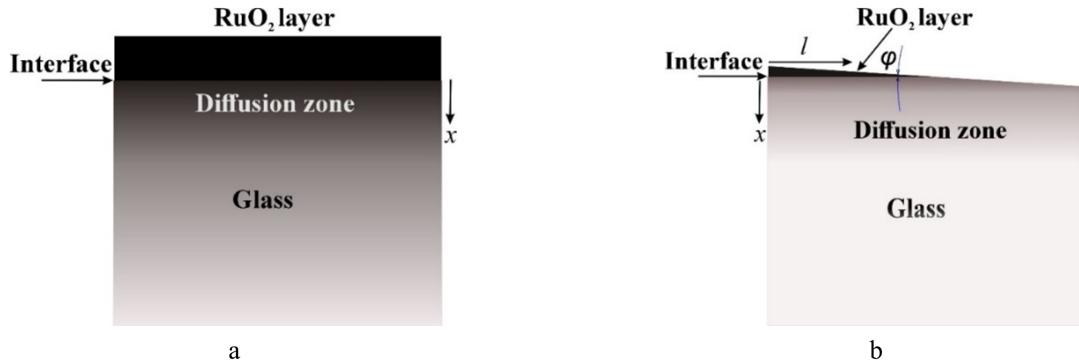

Figure 1. Sample of the glass after diffusion (*a*) and the beveled sample (*b*)

The distribution of Ru atoms along and across the glass surface was measured on a JEOL JSM-IT200 scanning electron microscope with energy dispersive spectrometer (Uzbek-Japanese Innovation Center of Youth, TSTU, Tashkent, Uzbekistan). The resistance R_s distribution along the sample surface (Fig. 2) was measured using a simple-probe (spreading resistance probe – SRP) method [19, 20] with a digital multimeter Rigol DM3058E. The radius a of the tip of the tungsten carbide probe was about 50 µm. The resistivity ρ of the diffusion layer was calculated from the measured resistance R_s as $\rho = 4aR_s$ [19, 20].

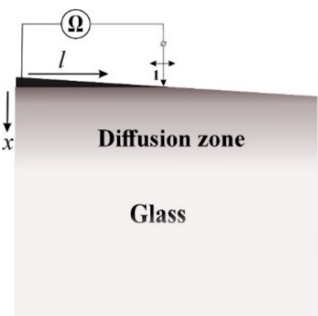

Figure 2. Simple-probe method.
1 – mobile probe, Ω - ohmmeter (multimeter). Noise of the energy dispersive spectra was filtered by Fourier and inverse Fourier transform in Wolfram Mathematica 13 program, which also used to design all graphs

RESULTS AND DISCUSSION

Two types of experiments were carried out to determine the diffusion profile of Ru atoms into glass. In the first experiment, the diffusion profile was measured across the interface between the RuO_2 layer and the glass surface (Fig. 3).

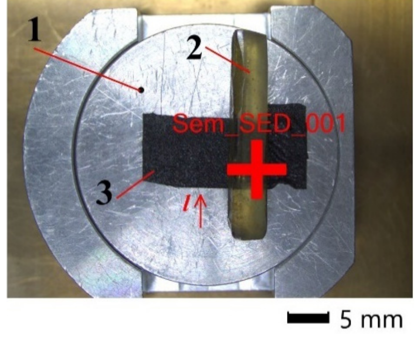

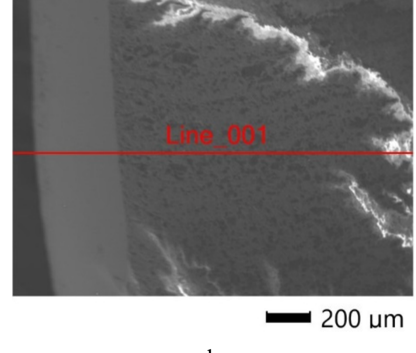

a b

Figure 3. The sample of the glass in the SEM chamber (*a*) and the scanning line (*b*): 1 – sample holder; 2 – glass sample; 3 – two-sided conductive scotch tape. The scanning line in the Fig. 3*b* is perpendicular to the plane of Fig. 3*a* (along the *x*-axes in Fig. 2)

The sample of the glass after diffusion is shown in Fig. 3*a* in the SEM chamber and the scanning line for EDS analysis is in Fig. 3b. This experiment is basic for comparison with the profile, obtained in the second experiment – along the glass surface in beveled sample. Such a comparison is necessary due to the fact that it is impossible to measure the resistance distribution in a diffusion layer with a thickness of units and tens of micrometers, and to obtain this distribution we are forced to use a beveled sample.

The original distribution of the EDS spectra of components in the diffusion layer (across the interface between the RuO_2 layer and the glass surface, line 001 in the Fig. 3b) are shown in the Fig. 4. Note that the number of counts (intensity) in Fig. 4 and below is proportional to the concentration of the corresponding atoms (oxygen, silicon, lead and ruthenium).

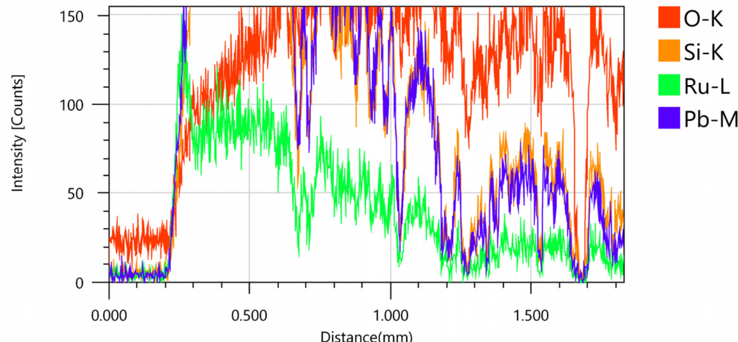

Figure 4. The original EDS spectra of the sample components along the line 001 in the Fig. 3b

The total content of components in the diffusion layer is given in the Table. The content of SiO_2 and PbO oxides, recalculated from these data, corresponds to the initial composition of the glass, while the RuO_2 content is about 4 wt. %. Last fact contradicts to conclusion [21, 22], that solvability of RuO_2 in a silicate glass is less 10^{-4} atomic %, and conforms results of Abdurakhmanov [23], Flachbart et al. [24].

Table. The total content of the sample components from EDS analyses

Element	Line	Mass%	Atom%
O	K	44.38±0.15	82.47±0.28
Si	K	10.05±0.06	10.64±0.06
Ru	L	2.36±0.09	0.69±0.03
Pb	M	43.20±0.21	6.20±0.03
Total		100	100
Line_001_wholespectrum		Fitting ratio 0.2875	

Apparently, the conclusion about the weak solubility of ruthenium dioxide in silicate glass arose from studies of the solubility of metallic ruthenium in various silicate melts, including those used for nuclear waste disposal [25-27]. Indeed, pure metals are poorly soluble in silicate melts, but the solubility of oxides of the same metals can be tens of wt. %. For example, the solubility of metallic lead in a silicate melt is hundredths of a percent, while PbO with SiO_2 forms homogeneous glass with a PbO content of up to 90 wt. %. The glass we study in this article contains 67 wt. % PbO

EDS spectrum of Ru with very intensive noise (Fig. 4) after filtration is shown in Fig. 5. The wide double maximum at 0,25 mm < x < 0,55 mm corresponds to the RuO_2 layer (see Fig. 3*b*). Distribution of the Ru atoms in diffusion layer, described as $I(x) = 10 + 320\,\mathrm{erfc}(1.8\,x)$, indicates that the diffusion coefficient is constant (does not depend on the concentration of ruthenium atoms at the point in question).

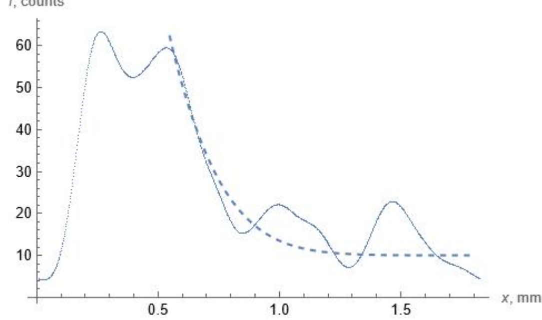

Figure 5. Filtered EDS spectrum of Ru across the diffusion layer (see Fig. 4).
The dotted line is the approximation by the function $10 + 320\,\mathrm{erfc}(1.8\,x)$

It is also seen that the diffusion length in the glass (about 0.335 mm) under diffusion conditions (873 K, 5 h) significantly exceeds the thickness of the glass layer (about 25 μm) and the diameter of the glass powder particles

(0.1-0.2 μm) in thick-film resistors. Standard firing duration of the thick-film resistors at peak temperature is $\tau_s = 10$ min, so diffusion length l_d will be shorter: $l_d = 0.335\sqrt{\tau_s/\tau} = 0.06$ mm. This once again confirms the conclusion of our previous studies [23, 30] that during sintering the entire volume of glass is doped almost uniformly and becomes conductive.

In the second experiment, the distributions of the concentration of ruthenium atoms $I(l)$ and the spreading resistance $R(l)$ along the beveled sample were measured (Fig. 1*b* and Fig. 6). Since the length of the beveled sample is more than 15 mm, and the maximal electronic scanning zone in the SEM is 3 mm, the total EMF was compiled by stitching together 5 separate spectra (Fig. 6). This spectrum has been filtered by Fourier transform as well (Fig. 7).

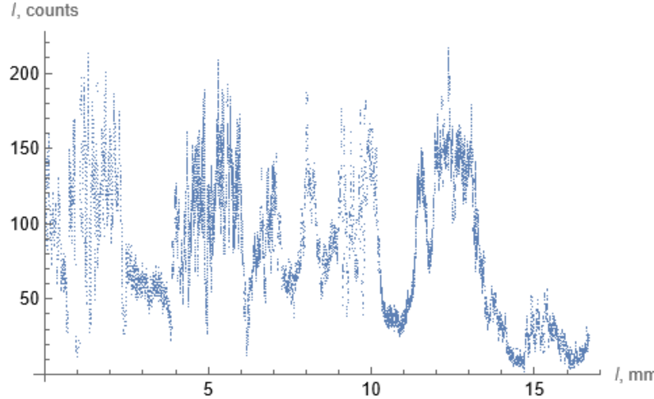

Figure 6. The original EDS spectrum of the Ru along the diffusion layer, stitched from 5 separate scan sections

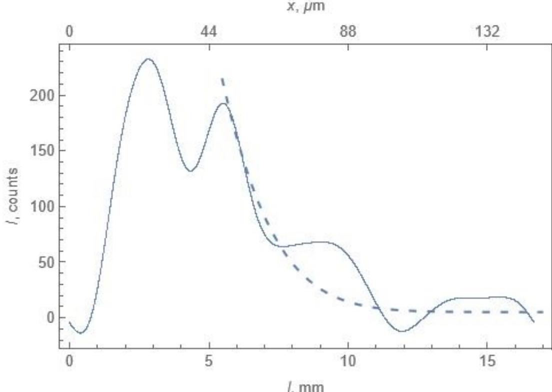

Figure 7. The filtered EDS spectrum of the Ru along the diffusion layer. The dotted line –function 5 + 1600 erfc(0.195 *l*). The meaning of the lower and upper scales, see Fig. 1*b*

One can estimate the diffusion coefficient D(873 K) from the data in Fig. 7, keeping in the mind that erfc(0) = 1 and erfc(1) = 0.1559. The initial intensity of the EDS spectra $I_0 = I(x = 0.53) \approx 55$ counts, therefore the intensity $I_0 \cdot$erfc(1) = 55·0.1559 = 8.57 is achieved at the point x = 1.2 – 0.53 = 0.67 mm. Taking into account the fact that the argument of the function erfc(z) is equal to $z = x/2l_d$, we have $l_d = x/2 \approx 0.335$ mm. Then $D(873\ \mathrm{K}) = l_d^2/\tau \approx (3.35 \cdot 10^{-4})^2/18000 \approx 6.2 \cdot 10^{-12}$ m²/s, which is in good agreement with data on diffusion in oxide glasses [28, 29].

The rescaled distribution of the Ru atoms in Fig. 7, described as 5 + 1600 erfc(0.195 *l*), agrees well with the similar distribution in Fig. 5. The double maximum at 0,25 mm < x < 0,55 mm corresponds to unpolished layer of RuO_2 (see above on Fig. 5). This confirms the possibility of using a beveled sample to establish a correlation between the concentration of ruthenium atoms and the resistivity distribution in the diffusion layer.

Distribution of resistivity in the diffusion layer

Distribution of spread resistance $R_s(l)$ and resistivity $\rho(l)$ along beveled sample is shown in Fig. 8. This distribution consists of two parts: 1) a linear part at x < 5 mm, corresponding to the unpolished RuO_2 layer on the glass; 2) nonlinear part at x > 4 mm, described by the function $R_s(l) = 0.9 + 0.185\, l/((1 - 0.065\, l)\mathrm{erfc}(0.023\, l))$.

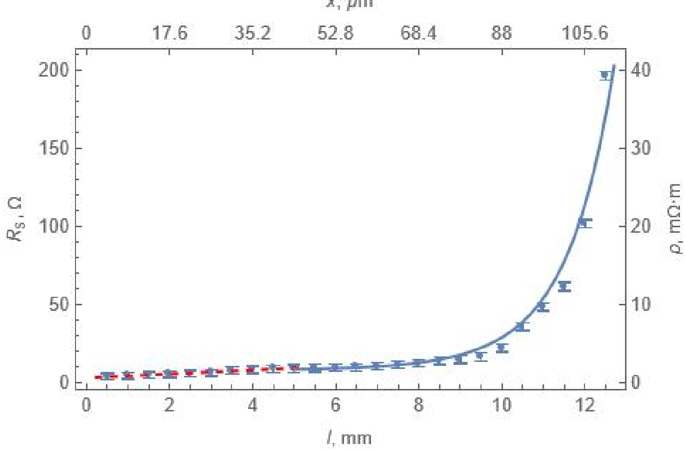

Figure 8. The spread resistance R_s and resistivity ρ distribution along (lower scale) and across (upper scale) the diffusion layer (Fig. 2). The dotted line is the function $R_s(l) = 0.0011 + 0.551\, l$, the solid line is the function $R_s(l) = 0.9 + 0.185\, l/((1 - 0.065\, l)\mathrm{erfc}(0.023\, l))$. See text for explanations of these functions

We are not interested in the linear part of $R(l)$ in the context of this article, and let us consider its second part in more detail. The nonlinear function $R(l)$ above may be expressed as

$$R_s(l) = 0.9 + 0.185l(1 - 0.065l)^{-1}/\mathrm{erfc}\left(l/\sqrt{D\tau}\right), \tag{1}$$

with $1/\sqrt{D\tau} = 0.023\ \mathrm{mm}^{-1}$. Here coefficient 0.185 includes all the constant parameters of the experiment, i. e. radius a of the movable probe for the spread resistance $R_s = \rho/4a$, geometric factors (namely, the constant width of the beveled sample), elementary charge e and the mobility of charge carriers (holes) μ_h, etc. The material resistivity ρ is considered to be inversely proportional to the charge carrier concentration p, which in turn is proportional to the concentration of ruthenium atoms or intensity of EDS spectrum for Ru (Fig. 6). This consideration is expressed by the multiplier $1/\mathrm{erfc}\left(l/\sqrt{D\tau}\right)$.

The factor $l/(1 - 0.065l)$ reflects a change in the geometry of the beveled sample – an increase in the distance between the fixed contact and moving probe (l in the numerator) and a decrease in the cross-section of the sample with distance (1 – 0.065 l in the denominator) in accordance with the definition of the conductor resistance $R = \rho \cdot l/s$ (s is the cross-sectional area of the conductor).

The distribution of ruthenium atoms in the diffusion layer (Fig. 5 and 8) and the distribution of resistivity in the same layer (Fig. 9) are in good agreement with each other. This means that the entire volume of the thick-film resistor is involved in electrical conductivity, but not only conducting chains (endless clusters) formed from dopant (conducting phase) particles.

The fact that the entire volume of a thick-film resistor is electrically conductive is also evidenced by an experiment with laser scribing along current lines [30] and a study of the distribution of piezosensitivity on the nanoscale across the interface glass-RuO_2 layer [31-33].

Totokawa et al. [31-33] have showed that thin film of bismuth-borosilicate glass, doped with ruthenium, 1) contents trivalent as well as tetravalent states of ruthenium; 2) exhibits electrical conductivity, that can be described as variable range hopping; 3) has high strain sensitivity due to the spatial expansion of wave functions of charge carriers (holes) in localized states; 4) ruthenium atoms diffuse into the glass during firing; 5) the diffusion coefficient of Ru into bismuth-borosilicate glass is about $1.4 \cdot 10^{-13}$ m^2/s and the diffusion length is about 100 nm; 6) piezoresistive properties depend on the distance from the interface of layers of glass and RuO_2.

It should be noted based on the results of works [31-33] that the dependence of piezoresistive properties on the distance from the interface between glass and RuO_2 layers indicates a correlation of these properties with the concentration of Ru atoms, but the distribution of resistance depending on this distance has not been studied.

Abe et al. [34, 35] studied the diffusion of atoms from a RuO_2 layer into a glass and vice versa, glass atoms into a ruthenium dioxide layer, using energy dispersive spectrometry. It turned out that ruthenium atoms diffuse into glass to a depth of more than 1 μm, while the diameter of glass particles in pastes for thick-film resistors is less than 1-2 μm, i.e. the entire layer of glass between the dopant particles is doped fairly uniformly. However, the correlation between such glass doping and the electrical conductivity of resistors has not been studied by these authors.

The series of temperature characteristics of resistance for thick film resistors and their analyses from the point of view of possible mechanisms responsible for $R(T)$ are discussed in [13, 36]. The consideration is carried out mainly with an emphasis on the metallic conductivity of RuO_2, as in many other publications [1-15], [37-41] and therefore sufficient correlation with experimental data was not achieved.

The authors hope that the results presented here can help in elucidating the role of glass phase and dopant particles in the mechanism of electrical conductivity of thick film resistors.

In the future, it is necessary to study in more detail the diffusion of transition metal atoms from their oxides into glass for a better understanding of the mechanism of electrical conductivity of thick film resistors.

CONCLUSIONS

The experiment showed that in silicate glass the distribution of the concentration of ruthenium atoms $N(x)$ and the electrical conductivity $\sigma(x) = 1/\rho(x)$ along the depth of the diffusion layer obey the same law erfc(x). This confirms that

1) the diffusion coefficient D of ruthenium atoms in silicate glass is constant and does not depend on their concentration;

2) due to the diffusion of ruthenium atoms, the glass itself becomes electrically conductive;

3) the electrical conductivity of glass is proportional to the concentration of ruthenium atoms. At 873 K over a duration of 5 hours, the diffusion length of Ru atoms in lead-silicate glass was determined to be $l_d = 0.335$ mm based on energy-dispersive spectroscopy data. This value significantly exceeds the diameter of the glass particles typically used in thick-film resistor pastes, indicating that the entire glass volume is uniformly doped. The corresponding diffusion coefficient was estimated to be $D(873\ \mathrm{K}) = 6.2 \times 10^{-12}$ m^2/s, in good agreement with known values for diffusion in oxide glasses.

Acknowledgements

This research was carried out within the framework of grant IL-4821091667 of the Ministry of Higher Education, Science and Innovations of the Republic of Uzbekistan.

Conflict of interests

The authors declare that there are no conflicts of interest.

Authors contribution

A. Dekhkonov: First author, Investigation, Methodology, Calculation of results, formal analysis, Visualization, Validation, Writing-draft, editing draft.
G. Abdurakhmanov: Supervision, Provide Resources, Investigation, Methodology, Calculation of results, formal analysis, Visualization, Validation, editing draft
M. Tursunov: Investigation, Methodology, Calculation of results, formal analysis, Visualization, Validation, editing draft. Sh.Norbekov: Investigation, Methodology, Calculation of results, formal analysis, Visualization, Validation, editing draft.
D. Tashmukhamedova: Investigation, Methodology, Calculation of results, formal analysis, Visualization, Validation, editing draft.
G. Vokhidova: Investigation, Methodology, Calculation of results, formal analysis, Visualization, Validation, editing draft.
D. P. Rai: Investigation, Methodology, Calculation of results, formal analysis, Visualization, Validation, editing draft, Submission.
U. Asrorov: Investigation, Methodology,Visualization, Validation, editing draft.

ORCID

Gulmurza Abdurakhmanov, https://orcid.org/0000-0002-0656-1859
Avazbek T. Dekhkonov, https://orcid.org/0009-0000-8507-2617
Tursunov Mukhriddin, https://orcid.org/0009-0005-6356-7252
Shokhzod M Norbekov, https://orcid.org/0000-0001-8204-6923
Dilnoza G. Tashmukhamedova, https://orcid.org/0000-0001-5813-7518
Dibya Prakash Rai, https://orcid.org/0000-0002-3803-8923
Ummat A. Asrorov https://orcid.org/0009-0009-6800-7392

REFERENCES

[1] R.W. Vest, "Conduction mechanisms in the thick film microcircuits," in: *Final Technical Report*, (Purdue university, US, 1975). https://apps.dtic.mil/sti/pdfs/ADA024825.pdf
[2] G.E. Pike, and C.H. Seager, "Electrical properties and conduction mechanisms of Ru-based thick-film (cermet) resistors," J. Appl. Phys. **48**(12), 5152 (1977). https://doi.org/10.1063/1.323595
[3] D.P.H. Smith, and J.C. Anderson, "Electron conduction in thick film resistors," Thin Solid Films. **71**, 79-89 (1980). https://doi.org/10.1016/0040-6090(80)90186-8
[4] A. Kubovy, "Model of electric conductivity of thick-film resistors. Part III. Temperature Dependence of Sheet Resistivity," Ceramics – Silikaty, **39**(1), l-40 (l995). https://www2.irsm.cas.cz/materialy/cs_content/1995/Kubovy_CS_1995_0000.pdf
[5] F. Forlani, and M. Prudenziati, "Electrical Conduction by Percolation in Thick-Film Resistors," Electrocomponent Science and Technology, **3**, 77-83 (1976). http://dx.doi.org/10.1155/APEC.3.77
[6] B. Morten, M. Prudenziati, M. Sacchi, and F. Sirotti, "Phase transitions in Ru based thick-film (cermet) resistors," J. Appl. Phys. **83**, 2267 (1988). https://doi.org/10.1063/1.341119
[7] C. Grimaldi, T. Maeder, P. Ryser, and S. Strässler, "A model of transport nonuniversality in thick-film resistors," Appl. Phys. Lett. **83**, 189–191 (2003). https://doi.org/10.1063/1.1590733
[8] R. Pflieger, M. Malki, Y. Guari, J. Larionova, and A. Grandjean, "Electrical Conductivity of RuO_2–Borosilicate Glasses: Effect of the Synthesis Route," J. American Ceramic Society, **92**(7), 1560-1566 (2009). https://doi.org/10.1111/j.1551-2916.2009.03088.x
[9] R.M. Hill, "Electrical transport in thick film resistors," Electrocomp. Sci. Technology **6**, 141-145 (1980). http://dx.doi.org/10.1155/APEC.6.141
[10] KSRC. Murthy, "Evolution of conduction mechanism in thick film resistors," Int. J. Adv. Res. **7**(4), 238-256 (2019). https://doi.org/10.21474/IJAR01/8811
[11] M. Prudenziati, and J. Hormadaly, editors, *Printed Films – Materials science and applications in sensors, electronics and photonics*, (Woodhead Publishing, Cambridge, 2012).
[12] K. Flachbart, V. Pavlík, N. Tomašovičová, C.J. Adkins, M. Somora, J. Leib, and G. Eska, "Conduction Mechanism in RuO_2-Based Thick Films," Phys. Stat. Sol. (b), **205**, 399-404 (1998). https://doi.org/10.1002/(SICI)1521-3951(199801)205:1<399::AID-PSSB399>3.0.CO;2-X
[13] K. Bobran, A. Kusy, A. Stadler, and G. Wilczyński, "Conduction in RuO_2-based thick films," Int. J. Electronics, **78** (1), 113-119 (1995). https://doi.org/10.1080/00207219508926143
[14] A. Kusy, A.W. Stadler, K. Mleczko, D. Zak, S. Pawlowski, P. Szałański1, Z. Zawiślak, *et al.*, "Metal-insulator transition in nanocomposites of glass and RuO_2," Ann. Phys. (Leipzig), **8**(5), 507–510 (1999). https://kpe.prz.edu.pl/fcp/HGBUKOQtTKlQhbx08SlkTUgZCUWRuHQwFDBoIVURNWH9UFVZpCFghUHcKVigEQUw/120/public/publikacje_naukowe/akusy_etal_ann_phys.pdf
[15] J.M. Himelick, "Conduction mechanisms in thick film resistors," PhD Thesis, Purdue University, Purdue, 1980), https://docs.lib.purdue.edu/dissertations/AAI8027287/
[16] G. Abdurakhmanov, and N. Abdurakhmanova, "High Temperature Anomalies in Resistivity and Thermoelectric Power of Thick Film Resistors," Phys. Stat. Sol. (a), **202**(9), 1799-1802 (2005). https://doi.org/10.1002/pssa.200420036
[17] G. Abdurakhmanov, "On the Conduction Mechanism of Silicate Glass Doped by Oxide Compounds of Ruthenium (Thick Film Resistors). 3. The minimum of temperature dependence of resistivity," WJCMP. **4**(3), 166-178 (2014). http://dx.doi.org/10.4236/wjcmp.2014.43021
[18] G. Abdurakhmanov, "Peculiarities of the structure and transport properties of alkaline-free lead-silicate glasses doped by metal oxides." D.Sc. thesis, National University of Uzbekistan, Tashkent, Uzbekistan, 2014. https://www.researchgate.net/publication/320465308_Peculiarities_of_the_Structure_and_Transport_Properties_of_Alkaline-Free_Lead-Silicate_Glasses_Doped_by_Metal_Oxides
[19] W.A. Bachmann, and P.A. Hale, USA patent no. US005347226A, "Array spreading resistance probe (ASRP) method for profile extraction from semiconductor chips of cellular construction," (16 November, 1992). https://patents.google.com/patent/US5347226A/en
[20] ASTM F 525 – 00a Standard Test Method for Measuring Resistivity of Silicon Wafers Using a Spreading Resistance Probe https://store.astm.org/f0525-00a.html

[21] P. Palanisamy, D.H.R. Sarma, and R.W. Vest, “Solubility of Ruthenium Dioxide in Lead Borosilicate Glasses,” J. American Ceramic Society, **72**(9), 1755-1756 (1989). https://doi.org/10.1111/j.1151-2916.1989.tb06321.x
[22] A. Prabhu, G.L. Fuller, and R.W. Vest, “Solubility of RuO_2 in a Pb Borosilicate Glass,” J. American Ceramic Society, **57**(9), 408-409 (1974). https://doi.org/10.1111/j.1151-2916.1974.tb11425.x
[23] G. Abdurakhmanov, “On the Conduction Mechanism of Silicate Glass Doped by Oxide Compounds of Ruthenium (Thick Film Resistors). 1. Diffusion and percolation levels,” WJCMP, **1**, 19-23 (2011). http://dx.doi.org/10.4236/wjcmp.2011.12004
[24] K. Flachbart, V. Pavlk, N. Tomašovičová, C.J. Adkins, M. Somora, J. Leib, and G. Eska, “Conduction Mechanism in RuO_2-Based Thick Films, Physica Status Solidi (B), **205**(1), 399-404 (1998). https://doi.org/10.1002/(SICI)1521-3951(199801)205:1<399::AID-PSSB399>3.0.CO;2-X
[25] A. Borisov, and K. Nachtweyh, “Ru solubility in silicate melts: experimental results in oxidizing region,” Lunar and Planetary Science XXIX. www.lpi.usra.edu/meetings/LPSC98/pdf/1320.pdf
[26] U. Backman, M. Lipponen, R. Zilliacus, A. Auvinen, and J. Jokiniemi, “Ruthenium behaviour in severe nuclear accident conditions - progress report,” (2004). http://www.iaea.org/inis/collection/NCLCollectionStore/_Public/36/031/36031958.pdf
[27] V. Laurenz, R.O.C. Fonseca, C. Ballhaus, K.P. Jochum, A. Heuser, and P.J. Sylvester, “The solubility of palladium and ruthenium in picritic melts: 2. The effect of sulfur,” Geochimica et Cosmochimica Acta, **108**, 172–183 (2013). http://dx.doi.org/10.1016/j.gca.2013.01.013
[28] H. Mehrer, *Diffusion in Solids*, Ch. 30. (Springer-Verlag, Berlin, Heidelberg, 2007). http://doi.org:10.1007/978-3-540-71488-0
[29] U.A. Asrorov. Polyacrylamide’s rheological and physicochemical properties: analysis and applications, East European Journal of Physics, 4. 413-418, 2024, ISSN 2312-4334 https://doi.org/10.26565/2312-4334-2024-4-48.
[30] G. Abdurakhmanov, “Electrical conduction in doped silicate glass (thick film resistors),” in: *New Insights into Physical Sciences*, vol. **4**, (Book Publishers International, London-Hooghly, 2020), pp. 47-71. https://doi.org/10.9734/bpi/nips/v4
[31] M. Totokawa, S. Yamashita, K. Morikawa, Y. Mitsuoka, T. Tani, and H. Makino, “Microanalyses on the RuO_2 Particle–Glass Matrix Interface in Thick-Film Resistors with Piezoresistive Effects,” International J. Appl. Ceramic Technology, **6**(2), 195-204 (2009). https://doi.org/10.1111/j.1744-7402.2008.02325.x
[32] M. Totokawa, T. Tani, M. Yoshimura, S. Yamashita, K. Morikawa, Y. Mitsuoka, and T. Nonaka, “Chemical and Piezoresistive Microanalyses at the Interface of RuO_2-Glass Diffusion Pairs,” J. American Ceramic Society, **93**, 481-487 (2010). http://dx.doi.org/10.1111/j.1551-2916.2009.03403.x
[33] M. Totokawa, T. Tani, H. Azuma, A. Takeichi, and R. Asahi, “Transport and Piezoresistive Characteristics of Ruthenium-Doped Bismuth–Borosilicate Glass Thin Films Grown by Pulsed Laser Deposition,” J. Am. Ceram. Soc. **93**(10), 3312–3318 (2010). https://doi.org/10.1111/j.1551-2916.2010.03844.x
[34] O. Abe, and Y. Taketa, “Electrical conduction in thick film resistors,” J. Phys. D: Appl. Phys. **24**(7), 1163-1171 (1991). http://dx.doi.org/10.1088/0022-3727/24/7/022
[35] O. Abe, Y. Taketa, and M. Haradome, “Microstructure and Electrical Conduction in RuO_2 Thick-Film Resistors,” Electrical Engineering in Japan, **110**(1), 21-30 (1990). https://doi.org/10.1541/ieejfms1972.109.111
[36] C. Ferrero, “Proposed theoretical models for thick film transport mechanisms: example of thick film strain gauges on enamelled steels,” 2022. pp. 51. https://www.researchgate.net/publication/358042608
[37] F. Johnson, G.M. Crosbie, and W.T. Donlon, “The effect of processing conditions on resistivity and microstructure of ruthenate-based thick film resistors,” J. Mater. Sci. Materials in Electron. **8**, 29-37 (1997). http://dx.doi.org/10.1023/A:1018596719229
[38] S. Vionnet-Menot, PhD Thesis, “Low firing temperature thick-film piezoresistive composites – properties and conduction mechanism,” Lausanne, EPFL, 2005. https://infoscience.epfl.ch/bitstreams/db5e401d-b3bd-4284-b8c2-9ca034855b10/download
[39] S. Vionnet-Menot, C. Grimaldi, T. Maeder, S. Strässler, and P. Ryser, “Tunneling-percolation origin of nonuniversality: theory and experiments,” Phys. Rev. B, **71**, 064201 (2005). https://doi.org/10.1103/PhysRevB.71.064201
[40] A.N. Lopanov, N.S. Lozinskyy, and Ya. A. Moroz, “Chemical processes accompanying the formation of modified ruthenium resistors and their functional properties,” Russian Chemical Bulletin, International Edition, **69**(9), 1724-1730 (2020). https://link.springer.com/article/10.1007/s11172-020-2955-8
[41] M, Wen, X, Guan, H, Li, and J. Ou, “Temperature characteristics of thick-film resistors and its applications a strain sensor with low temperature-sensitivity,” Sensors and Actuators A, **301**, 111779 (2020). https://doi.org/10.1016/j.sna.2019.111779

ВПЛИВ ДИФУЗІЇ РУТЕНІЮ НА ЕЛЕКТРИЧНІ ВЛАСТИВОСТІ ТОВСТОПЛІВОЧНИХ РЕЗИСТОРІВ

Авазбек Т. Дехконов[a], Гульмурза Абдурахманов[a], Мухріддін Е. Турсунов[a], Шохзод М. Норбеков[b,g], Ділноза Г. Ташмухамедова[c], Гульбахор Вохідова[d], Діб'я Пракаш Рай[e], Уммат А. Асроров[f,a]
[a]*Національний університет Узбекистану імені Мірзо Улугбека, Ташкент, Узбекистан*
[b]*Ташкентський інститут управління та економіки, Ташкент, Узбекистан*
[c]*Ташкентський державний технічний університет імені Іслома Карімова, Ташкент, Узбекистан*
[d]*Недержавний навчальний центр «Альфаком», Ташкент, Узбекистан*
[e]*Кафедра фізики, Університет Мізорам, Айзавл, Індія*
[f]*Національний педагогічний університет Узбекистану імені Нізамі, Ташкент, Узбекистан*
[g]*Алмаликська філія Ташкентського державного технічного університету, Алмалик, Ташкентська область, Узбекистан*

Профіль дифузії RuO_2 у силікатне скло та розподіл електричного опору по дифузійному шару досліджували методом скошеного зразка та енергетично-дисперсійної спектроскопії. Розподіл вмісту атомів Ru в дифузійному шарі описується erfc(x), що означає, що коефіцієнт дифузії не залежить від вмісту атомів Ru. Кореляція розподілу вмісту атомів Ru та розподілу опору в дифузійному шарі показала, що саме дифузійне легування скла відповідає за провідність товстоплівкових резисторів. Товщина дифузійного шару становить понад 100 мкм, а середня відстань між частинками RuO2 становить близько 0,5-2 мкм. Це означає, що весь об'єм товстоплівкового резистора стає провідним в процесі випалу при 850°C протягом 10 хвилин.

Ключові слова: *скошений зразок; дифузійний шар; коефіцієнт дифузії; розподіл опору; дифузійний профіль*

East European Journal of Physics. 3. 382-389 (2025)
DOI:10.26565/2312-4334-2025-3-39 ISSN 2312-4334

SIMULATION OF RADIATION-INDUCED STRUCTURAL AND OPTICAL MODIFICATIONS IN ZnO:S/SI THIN FILM STRUCTURES

Akramjon Y. Boboev[a], Khushroy A. Makhmudov[b], Nuritdin Y. Yunusaliyev[a], Mohlaroyim O. G'ofurjonova[a], Fayzuloh A. Abdulkhaev[a], Gaybullo G. Tojiboyev[a]
[a]*Andijan state university named after Z.M. Babur, Andijan, Uzbekistan*
[b]*Kokand University Andijan branch, Andijan, Uzbekistan*
**Corresponding Author E-mail: aboboevscp@gmail.com*
Received March 3, 2025; revised July 6, 2025; accepted August 12, 2025

The research studied ZnO thin films containing 3 at.% sulphur (S) on silicon (1 μm) through Geant4 simulations for radiation analysis. Analysis of ZnO thin films (400 nm) doped with 3 at.% sulphur (S) on a 1 μm thick silicon substrate through Monte Carlo simulation platform Geant4 considered energy absorption together with particle penetration depth and ionization and secondary electron generation and optical property changes as the study examined different electron radiation energies from 3 keV to 10 keV. The ZnO:S layer absorbed most of the incoming electron energy in the 3-5 keV range which produced increases in defects near the surface while ionization occurred. When electrons used 9-10 keV energies they penetrated the full substrate layer which caused silicon to receive most of the energy absorption. The highest change in parameters occurred at the film-substrate junction when the energy reached 7 keV. All modeling findings demonstrated that the total absorbed energy together with secondary electron production and defect density reaching up to 10^7 increased rapidly with electron energy acceleration. The decrease in optical properties occurs because defects exist at different depths while energy absorption takes place. Electrical and optical characteristics of ZnO:S/Si can be regulated through electron irradiation procedures according to this research. Results from this study will function as fundamentals for creating sensors and optoelectronic devices and protective coatings which operate effectively under high radiation conditions.
Keywords: *Monte Carlo; Energy absorption; Electron energy; Depth; Displacement; Simulation*
PACS: 78.30.Am

INTRODUCTION

The development of modern technology demands improved material resistance against extreme conditions which include high radiation and hadron beam and cosmic particle exposure [1]. The long-lasting operational stability and reliability of materials important for equipment which serves nuclear power applications as well as space exploration and medical radiation therapy. Material surfaces along with atom structures remain the most radiation-sensitive features because exposure produces drastic shifts in electrophysical and optical and mechanical properties [2]. Materials science focuses on developing functional materials operating under radiation conditions while predicting their responses which poses a key challenge for modern research.

Zinc oxide (ZnO) represents a semiconductor material that finds extensive implementation in optoelectronics hardware and sensors as well as catalytic devices [3]. Research data about the radiation stability of ZnO remains insufficient. Research findings indicate that ZnO gains enhanced radiation resistance through appropriate doping with sulfur together with aluminium and nitrogen. The addition of sulphur (S) elements demonstrates both strength in crystal lattice structure while modifying electronic structure which leads to enhanced radiation sensitivity. Researchers have not conducted a comprehensive investigation regarding the response of ZnO thin films containing sulphur (ZnO:S) to electrons across multiple energy levels plus their relationship with the substrate.

The research investigates both theoretical and experimental aspects of the radiation behavior in ZnO:S films with 3 at.% sulfur doped on a 1 μm silicon substrate measuring 400 nm thick. GEANT4 simulated the material response from electrons in the 3 to 10 keV energy range. The research evaluated these parameters extensively at each energy level.

MODEL STRUCTURE AND METHODOLOGY

Material and structure description.

In this study, a heterostructure consisting of a thin film of sulfur-doped zinc oxide (ZnO:S) with a concentration of 3 at.%, 400 nm thick, deposited on a 1 μm thick single-crystal silicon substrate was considered. Due to their high optical transparency and wide band gap, ZnO:S films are considered as a promising material for applications in optoelectronics and sensor technologies. Sulfur doping significantly improves both the electrical and optical properties of ZnO, making this material particularly suitable for use in radiation-sensitive devices [4].

The Geant4 modeling environment.

Geant4 is a widely used Monte Carlo platform for modeling the interaction of particles with matter, successfully used in high-energy physics, astrophysics, and radiation detector design [5]. In this study, the interaction of electrons with energies of 3, 5, 7, 9 and 10 keV with ZnO:S/Si heterostructure was simulated using the Geant4 platform. The simulation

Cite as: A.Y. Boboev, Kh.A. Makhmudov, N.Y. Yunusaliyeva, M.O. G'ofurjonova, F.A. Abdulkhaev, G.G. Tojiboyeva, East Eur. J. Phys. 3, 382 (2025), https://doi.org/10.26565/2312-4334-2025-3-39
© A.Y. Boboev, Kh.A. Makhmudov, N.Y. Yunusaliyeva, M.O. G'ofurjonova, F.A. Abdulkhaev, G.G. Tojiboyeva, 2025; CC BY 4.0 license

addressed key physical processes including energy absorption within the material, electron penetration depth, ionization and excitation probabilities from electron-atom collisions, generation of low-energy secondary electrons arising from primary electron interactions, and formation of radiation-induced defects such as vacancies and interstitial atoms. Additionally, changes in optical parameters such as transmission and absorption coefficients were monitored and analyzed.

Simulation parameters.

During the simulations, 10^6 electrons for each energy level were perpendicularly directed onto the surface of the ZnO:S thin film. The physical properties of the ZnO:S and Si materials were precisely set in the Geant4 environment. The simulation results allowed a detailed analysis of the distribution of absorbed energy, particle penetration depth and ionization probability throughout the structure.

Energy Absorption (Energy Deposition).

Energy absorption (edep) is the process of electron particles transferring kinetic energy to the environment as they interact with matter through ionization, excitation, or other inelastic collisions. The layers of a material in which electron energy absorption occurs has a significant effect on its electromagnetic, thermal, and optical properties. The depth distribution of the absorbed energy makes it possible to determine the most radiation-sensitive regions of the material [6,7].

The absorbed energy profile in the Geant4 simulation is determined based on the calculation of the energy density distributed in each elementary layer of the material:

$$E_{dep}(z) = \frac{dE}{dz} \quad (1)$$

where $E_{dep}(z)$- is the absorbed energy at depth z $(\frac{MeV}{\mu m})$, dz – is the thickness of the elementary layer.

RESULTS AND DISCUSSION

At 3 keV, about 68% of the electron energy is absorbed in the ZnO:S film, and ~32% in the Si substrate. This indicates that 3 keV electrons do not penetrate far into the silicon; the ZnO:S layer absorbs the majority of their energy. At 5 keV, a similar trend is seen (about 62% in ZnO:S vs 38% in Si). By 7 keV, the split is roughly 56% in ZnO:S and 44% in Si, indicating that electrons are now depositing significant energy in the substrate as well. The interface region around the boundary of the film and substrate is receiving a lot of energy at this energy. The total energy absorbed also increases with energy (more energetic electrons have more energy to give), reaching ~125 MeV for 7 keV electrons (per million electrons). A dramatic change occurs at 9 keV: only ~40% of the energy is absorbed in the ZnO:S film, while ~60% is absorbed in Si. At 10 keV, the partition is ~42% in ZnO:S vs 58% in Si. In absolute terms, the silicon substrate at 9-10 keV is absorbing roughly 300 MeV from the million electrons, which is an order of magnitude more energy than it absorbed at 3–5 keV. This means high-energy electrons pass through the thin film and deposit most of their energy deeper in the structure (i.e., in the substrate). These results clearly show that lower-energy electrons primarily damage the ZnO:S thin film, whereas higher-energy electrons primarily damage the silicon substrate. The 7 keV case is intermediate, with substantial energy deposition in both layers, especially near their interface. This has implications for where defects will form (discussed later). The total absorbed energy does not scale linearly with incident energy because not all incident energy is absorbed – some energy may escape as backscattered electrons or X-rays. Interestingly, the total absorbed energy at 10 keV is slightly less than at 9 keV in our simulation (518 MeV vs 530 MeV for 10^6 electrons). This is because a small fraction of 10 keV electrons likely passed completely through the 1.4 μm total thickness without depositing all their energy, or produced bremsstrahlung photons that carried energy away. Thus, 9 keV appears to be the most efficient at depositing energy in this structure (given its size), whereas at 10 keV some energy starts to "leak" out. The depth distribution of the energy deposition reveals more. For 3 keV electrons, the energy is deposited very superficially – within the first few hundred nanometers of the ZnO:S film (as evidenced by 400 nm being the penetration range). For 5 keV, energy deposition extends to the ZnO:S/Si interface. At 7 keV, a significant energy deposition peak occurs at the interface (around 400 nm depth). For 9 and 10 keV, the energy deposition profile peaks inside the silicon substrate (~700–800 nm deep) and then trails off. In essence, as electron energy increases, the zone of energy absorption (and hence potential damage) moves deeper. Practically, if one wanted to protect the substrate from radiation, using lower electron energies would be worse (since the film cannot stop the radiation and the substrate still gets hit at higher energy like 9–10 keV). Conversely, if one wanted to minimize damage to the thin film, very high energy electrons would mostly bypass it and deposit energy in the substrate. This trade-off needs to be considered in design: for example, a thin ZnO film on Si used as a sensor might be badly damaged by a few-keV electrons on its surface, whereas higher-energy electrons would harm the substrate electronics more.

Table 1. Changes in energy distribution under the influence of electron energy in the ZnO:S/Si heterostructure(eal09).

Energy of one electron	Absorbed energy in the ZnO:S layer	Absorbed energy in the Si substrate	Total absorbed energy
3 keV	58.6 MeV (68.1%)	27.4 MeV (31.9%)	86.0 MeV
5 keV	62.8 MeV (62.1%)	38.4 MeV (37.9%)	101.2 MeV
7 keV	~70 MeV	~55 MeV	~125 MeV
9 keV	214.67 MeV	315.22 MeV	529.89 MeV
10 keV	216.52 MeV	301.54 MeV	518.06 MeV

The changes in the distribution of absorbed energy between the ZnO:S layer and the silicon substrate under varying electron energies are summarized in Table 1. As the electron energy increases, a shift in energy absorption from the ZnO:S film to the Si substrate is clearly observed, confirming the dependence of energy deposition on the penetration capability of incident particles.

Penetration Depth.

The electron penetration depth is the maximum distance that particles can penetrate a material before losing all of their energy. This parameter plays an important role in assessing how far the effects of irradiation extend into the structure under investigation. The following relationship is used to estimate the penetration depth:

$$R_p \propto \frac{E_0^n}{\rho} \tag{2}$$

where R_p is the average electron penetration depth, E_0 is the initial energy of the incoming electron (keV), ρ is the density of the material (g/cm³), n≈1.35 is an empirical indicator depending on the nature of the material (for organic substances it is usually in the range of 1.3–1.7) [8]. In cases of strong scattering, electrons can deviate from the rectilinear trajectory, but in most cases the area of maximum energy absorption is located near the maximum penetration depth.

The correlation between incident electron energy and the corresponding penetration depth is detailed in Table 2**.** The data indicate that low-energy electrons are primarily absorbed in the ZnO:S layer, while high-energy electrons penetrate deeper into the silicon substrate.

Table 2. Penetration depth and zone of influence in films depending on electron energy (eal16, eal09, eal03, eal11)

Energy (keV)	Maximum penetration depth (nm)	Depth of interaction region
3 keV	~400–450 nm	Predominantly within the ZnO:S layer
5 keV	~600–700 nm	ZnO:S + interfacial boundary
7 keV	~800 nm	ZnO:S + interface with silicon
9 keV	~900 nm	Predominantly in silicon
10 keV	≥ 900 nm	In the lower regions of the silicon substrate

At energies of 3 keV electrons are completely absorbed within the ZnO:S layer, whereas at energies of 9-10 keV they penetrate entirely into the silicon substrate. In the region around 7 keV, a maximum change of parameters at the boundary between the film and the substrate is possible.

Ionization and Excitation Probability (Ionization and Excitation Probability)

Ionization and excitation probability is the probability that the interaction of particles with matter will result in the knocking out of an electron from an atom or molecule (ionization) or the transfer of an electron to a higher energy level (excitation). These processes are the main mechanisms of energy absorption during electron irradiation.
The probability of ionization can be described using the Bethe formula [9]:

$$\frac{dE}{dx} = 4\pi \frac{Z}{A} \frac{N_A r_e^2 m_e c^2}{\beta^2} \left[ln\left(\frac{2m_e c^2 \beta^2 \gamma^2 T_{max}}{I^2}\right) - 2\beta^2 \right] \tag{3}$$

Where $\frac{dE}{dx}$ – is the energy loss for ionization (stopping power), Z – atomic number of the target, A– atomic mass of the target, $\beta = \frac{v}{c}$, γ– Lorentz factors, T_{max}– maximum energy that can be transferred to an electron during knockout, I – ionization potential of the substance (for ZnO ~103 eV, for Si ~173 eV) [10,11].

The ionization probability depends directly on the energy of the particle and the frequency of its collisions with the atoms of the substance. At higher energy, the ionization probability also increases.

The spatial characteristics of ionization zones at various electron energies are presented in Table 3**.** This table highlights how the location and extent of ionization shift with increasing energy, moving from the film toward the substrate.

Table 3. Depth ranges and peak locations of ionization zones in ZnO:S/Si heterostructure under electron irradiation (LMCG72)

Energy (keV)	Depth of ionization zone	Area with maximum probability
3 keV	200–400 nm (ZnO:S)	~300 nm
5 keV	300–600 nm (ZnO:S–Si)	~400–500 nm
7 keV	400–800 nm (interfeys)	~600 nm
9 keV	500–900 nm (Si)	~750–800 nm
10 keV	600–900+ nm (Si)	~850–900 nm

Simulation results showed that with increasing electron energy, the ionization region shifts to the depth of the structure. At energies of 3-5 keV, the main number of collisions occurs in the ZnO:S film, whereas at energies of 9-10 keV, ionization is observed predominantly in the silicon substrate. In many cases, the ionization probability is considered to be linearly dependent on the absorbed energy:

$$P_{ion}(z) \propto \frac{dE}{dz} \tag{4}$$

i.e., the amount of absorbed energy at a certain depth directly corresponds to the ionization probability in this region. This approach agrees well with the energy distribution plot obtained using simulations in Geant4.

The ionization process leads to the generation of electron-hole pairs, which in turn enhances secondary phenomena: along with ionization, a significant number of secondary electrons are formed. Each act of ionization increases the probability of damage to the crystal lattice.

Generation of Secondary Electrons (Secondary Electrons)

Secondary electrons are low-energy electrons knocked out as a result of interaction of high-energy primary particles (e.g., electrons) with matter. Typically, the energy of such electrons is less than 50 eV and ionization processes or inelastic collisions [12] form them. The following expression can estimate the number of secondary electrons:

$$N_{sec} \approx \frac{E_{dep}}{W} \tag{5}$$

where N_{sec}– number of generated secondary electrons, E_{dep} – absorbed energy (in eV), W – is the average energy required to generate one secondary electron (for ZnO it is about 30-35 eV) [13].

Table 4. Total absorbed energy and estimated secondary electron yield in the ZnO:S/Si structure for different electron energies (per 10^6 incident electrons) (eal16, JA09, SA03)

Electron energy (keV)	Total absorbed energy in the ZnO:S/Si structure (MeV)	Estimated number of secondary electrons
3 keV	~86	≈ 2.9×10^6
5 keV	~101.2	≈ 3.4×10^6
7 keV	~125	≈ 4.1×10^6
9 keV	529.89	≈ 1.76×10^7
10 keV	518.06	≈ 1.73×10^7

The estimated yield of secondary electrons as a function of absorbed energy at each electron energy level is shown in Table 4. As demonstrated, secondary electron production increases significantly with higher primary electron energy.

At 3 keV, the total energy absorbed (~86 MeV) would generate on the order of 2.9 million secondary electrons (if 30 eV generates one SE, 86 Me ≈ 2.9×10^6). This means each 3 keV primary electron produces on average ~3 secondary electrons (since ≈ 2.9×10^6 secondaries for 10^6 primaries). At 5 keV, this rises to about ~3.4 million secondaries, roughly 3–4 per primary. At 7 keV, ~4.1 million secondaries (about 4 per primary). When we go to 9 keV, the number jumps dramatically: ~1.76×10^7 secondary electrons for 10^6 primaries, which is ~17–18 secondary electrons per primary electron. Similarly at 10 keV, ~1.73×10^7 secondaries (also ~17 per primary). The large increase from 7 keV to 9 keV correlates with the large increase in total energy deposited by those higher-energy electrons. This exponential increase is expected because higher-energy electrons undergo more collisions and travel further, thus they have more opportunities to ionize atoms and produce secondary electrons. Additionally, when the electrons penetrate into the higher-density Si, they may produce more secondaries (Si has more electrons per cc to ionize compared to ZnO). The presence of such a high number of secondary electrons has several consequences:

Energy Deposition Cascade: Many of these secondary electrons (which have energies of a few eV to a few tens of eV) will deposit their energy very locally, causing localized heating and further ionization in their immediate vicinity. Surface Charging: A significant fraction of secondary electrons that are created near the surface of the ZnO film can escape the material entirely (especially those generated within ~10 nm of the surface). If many electrons leave the ZnO:S film, the film could become positively charged. Conversely, some secondaries might get trapped in defects, causing negative charging. This is relevant for devices, as charge buildup can alter electrical behavior. Induced Conductivity: Secondary electrons (and the holes left behind) can contribute to a temporary increase in electrical conductivity (as they are essentially free carriers until they recombine or get trapped). At high irradiation flux, this can lead to radiation-induced currents in the material. Imaging and Luminescence: Secondary electrons are the basis for SEM imaging contrast. Also, some of the excited electrons can cause luminescence (cathodoluminescence) if they recombine radiatively. ZnO is known to exhibit cathodoluminescence (often in the green due to oxygen vacancies), so electron irradiation could induce light emission from the ZnO:S film via the creation of secondary electrons and holes. Our simulation qualitatively noted that for 9 keV and 10 keV runs, there was a cloud of low-energy electrons near the surface – these are the secondary electrons being emitted. The yield of secondaries per primary (~17) at 9–10 keV is high but within reason for materials with moderate atomic number. (For reference, materials often have a secondary electron yield peak around a few hundred eV primary energy, but here we are dealing with multiple inelastic collisions from a keV primary leading to many secondaries in total.) In summary, as electron energy increases, not only do we get deeper penetration and more total damage, but we also get a disproportionately larger number of secondary electrons. This secondary electron avalanche effect means higher-energy irradiation can induce a lot more indirect effects (like charging and further local ionization) compared to lower-energy irradiation. [11].

Defect Formation

As a result of particle irradiation, energetic defects are generated within the material. The main types of defects include:

Vacancies (missing atoms from lattice sites), *interstitials* (atoms located in interstitial positions), *Frenkel pairs* (a vacancy paired with an interstitial atom), *displacement damage* (an atom is displaced from its lattice site).

Electron irradiation at keV energy levels typically has a low probability of directly displacing lattice atoms. However, due to high particle flux and the influence of secondary electrons, local energy density can increase, resulting in defect formation [15]. To estimate the number of defects, the classical formula is used:

$$\mathrm{N} = \frac{E_{dep}}{E_d} \tag{6}$$

where N is the number of defects, E_{dep} is the total energy deposited in the film (in eV), E_d is the displacement energy required to displace an atom from its lattice site; for ZnO: $E_d \approx 20 - 30eV$; for Si: $E_d \approx 15eV$ [16].

Table 5. Correlation between electron energy, deposited energy, and estimated defect count in ZnO:S/Si heterostructure (BM60, MC70, NHR85).

Energy (keV)	E_{dep} (MeV)	Estimated number of defects (ZnO:S + Si)
3 keV	~86	≈ 2.9×10^6 (assuming E_d = 30 eV)
5 keV	~101	≈ 3.4×10^6
7 keV	~125	≈ 4.1×10^6
9 keV	529.89	≈ 1.76×10^7
10 keV	518.06	≈ 1.73×10^7

The relationship between electron energy, total deposited energy, and the estimated number of radiation-induced defects is presented in Table 5**.** The results demonstrate a substantial increase in defect formation at energies above 7 keV. High-energy electron radiation dramatically increases the probability of defects in materials. In particular, in the energy range of 9–10 keV, the number of defects can reach several million, which reduces the structural stability of the material and has a direct negative impact on its main properties, such as electrical conductivity and optical properties. The increase in radiation defects occurs mainly as a result of electrons penetrating the material at high energy levels (e.g., above 7 keV). This phenomenon can cause structural distortions (crystal lattice deformations) and functional failures (e.g., reduction of electrical signals, changes in light absorption), especially in ZnO:S/Si-based devices. Also, the sharp increase in the number of defects with increasing energy significantly reduces the reliability and service life of the materials.

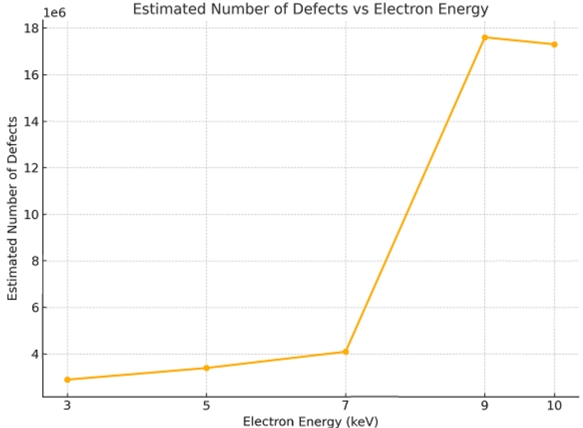

Figure 1. Estimated number of radiation-induced defects in ZnO:S/Si heterostructure as a function of incident electron energy (3–10 keV) (NSJC04, Ste03).

The dependence of the number of radiation-induced defects on the incident electron energy is illustrated in Figure 1**.** The figure reflects an exponential rise in defect count as the energy increases from 3 to 10 keV. The defect count increases rapidly with electron energy, indicating enhanced structural degradation at higher irradiation levels.

Optical Properties: Transmittance and Absorbance

After electron irradiation, the formation of defects, ionization zones, and structural disorders in the material directly affects its optical properties. The main changes observed include:

- Transmittance (T): the ratio of light passing through the material to the total incident light.
- Absorbance (A): the amount of light absorbed by the material.

The following expression describes the relationship between these two parameters:

$$T = \frac{I_t}{I_0}, A = -log_{10}(T) \tag{7}$$

Alternatively, the depth-dependent absorption of light is described by the Lambert–Beer law:

$$I(z) = I_0 \cdot e^{-\alpha z}, \tag{8}$$

where I(z) is the light intensity remaining at depth z, α is the absorption coefficient, z is the material depth (nm or µm) [17]. In the simulation, optical behavior was analyzed based on the depth-wise energy deposition.

The qualitative trends in optical transmittance and absorbance of the ZnO:S/Si structure following irradiation are listed in Table 6**.** It shows a clear degradation of transparency with increasing electron energy due to the growth of radiation-induced defects.

Table 6. Qualitative trends in optical transmittance and absorbance of ZnO:S/Si after electron irradiation (Hub97)

Energy (keV)	Transmittance (trend)	Absorbance (trend)	Note
3 keV	High (>90%)	Very low	Defects mainly near surface; minimal optical impact in bulk ZnO
5 keV	Slightly reduced	Slightly increased	More defects through film; some haze or absorption emerging
7 keV	Moderately reduced	Increased	High defect density at interface; noticeable drop in transparency
9 keV	Low	High	Significant damage to film and substrate; film visibly less transparent
10 keV	Very low (<40%)	Very high	Severe structural damage; film likely visibly opaque/turbid

At 3 keV, since the defects are mostly near the surface of the ZnO film and relatively fewer in number, the film's transparency is mostly retained. We would expect >90% of the original transmittance to remain (for wavelengths above the band edge), and only a very slight increase in absorbance due to perhaps some color centers on the surface. At 5 keV, the ZnO:S film has more defects distributed through its thickness, so there could be a minor reduction in transparency – perhaps the film might show a faint coloration or scattering. The absorbance might increase a bit (maybe a few percent of light is now absorbed/scattered by defect states). By 7 keV, the optical clarity of the film likely degrades more noticeably. The defect density is high, especially near the interface (which might affect how light passes into the substrate or reflects back). The transmittance of the film could drop (for instance, if initially 90% it might drop to something like 70–80%, depending on defect types). Absorbance (or diffuse scattering) in the film increases. This means the film might appear less transparent or "cloudier". At 9 keV, the ZnO:S film is heavily damaged and the substrate is also damaged. The film's transmittance might become quite low – potentially it could become translucent rather than transparent. Additionally, since the substrate (Si) is not transparent in the visible, if one considered the whole structure, obviously it's opaque normally. But considering just the film's optical properties (like using it as a waveguide layer), the introduction of defects would increase optical losses significantly. At 10 keV, the film likely has so many defects (and perhaps microstructural damage) that it could appear visibly darker or opaquer. The term "<40%" in Table 6 is a rough estimate to indicate a large reduction. Absorbance would be very high – many photons would be absorbed by defect states or scattered out of the film. The structural damage at this point (like broken bonds, possibly nano-cracks from intense collision cascades) would drastically impair optical transmission. It is important to note that these are qualitative trends. For a precise assessment, one would perform optical measurements (e.g., measure the transmission spectrum of the film before and after irradiation). However, our simulation results strongly suggest the trend: higher electron energies lead to greater optical degradation. This is consistent with experimental reports on irradiated ZnO, where optical absorption in the visible often increases after high-dose irradiation due to defect creation. One particular optical effect to mention: ZnO often exhibits a characteristic green luminescence when oxygen vacancies are present. If our irradiation creates a lot of oxygen vacancies, the film might show increased green luminescence under UV excitation (or under electron excitation, i.e., cathodoluminescence). So, while transmission decreases, defect-related light emission might increase. The manuscript focuses on transmission/absorption, but this is an interesting side note – radiation can turn ZnO into a more optically active (but less transparent) material by introducing luminescent centers. In summary, the ZnO:S/Si heterostructure's optical transparency is inversely related to the electron irradiation energy: low-energy electrons leave the film mostly transparent, whereas high-energy electrons significantly reduce its transparency. This must be considered for any optical applications of such films in radiation environments. The results imply that by adjusting electron energy (or dose), one could even tune the optical properties (though at the cost of introducing damage). (Figure 2 could illustrate, for example, the penetration depth vs energy, indirectly showing how deeper penetration (higher energy) correlates with more uniform damage through the film and thus more optical loss. However, since it's more directly a penetration figure, it might not explicitly show optical changes.)

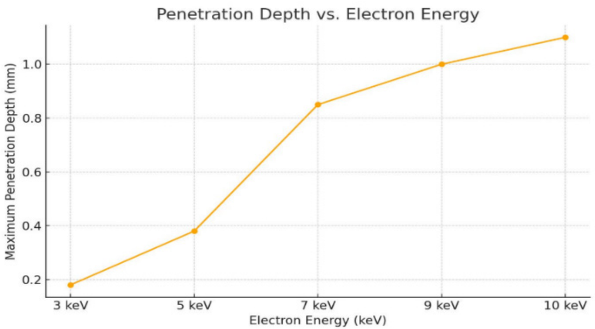

Figure 2. Maximum penetration depth of electrons in ZnO:S/Si heterostructure (MC70, NHR85, BM60)

Figure 2 illustrates the nonlinear dependence of electron penetration depth on incident energy in the 3–10 keV range. As the energy increases, electrons penetrate progressively deeper into the material, with depths exceeding 1 μm at the highest energies. This trend confirms that high-energy electrons induce significant structural modifications within the deeper regions of the silicon substrate.

CONCLUSIONS

The authors use Geant4-based Monte Carlo simulations to deliver comprehensive research findings regarding the structural and optical effects that radiation produces in ZnO:S/Si heterostructures. All parameters examined in this study demonstrate dependence on electron energy levels which control the deposition of energy as well as ionization production and secondary electron generation and defect initiation and optical behavior changes.

The radiation affects the semiconductor primarily at the top layers including the outer surface and the ZnO:S material zone when using electrons with low kinetic energies (3–5 keV). Electrons at higher energies (9–10 keV) manage to pass through the silicon substrate layer where they create extensive energy deposition sites along with a large amount of material defects. Changes in material structure lead directly to reduced transmittance along with higher absorption which badly impacts the optical transparency and device performance.

The study shows that energy-adjusted electrons function as a tool to direct radiation-induced damage distribution throughout ZnO-based components for improving their performance level under irradiated environments. The findings serve as a strong base which enables experimental laboratory testing through the implementation of UV–Vis and AFM and XRD methods of structural and optical analysis.

Future development of radiation-resistant optically tunable thin-film structures becomes viable based on the available data for advanced optoelectronic and sensor applications. Experimental validation of these simulated predictions will unveil better material behavior knowledge under radiation that enables designers to develop stronger electronic and photonic devices.

Conflict of Interests

The authors declare that they have no conflict of interests

Funding

The present research work was financed under the project FZ-292154210 granted by the Ministry of Innovative Development of the Republic of Uzbekistan

ORCID

A.Y. Boboev, https://orcid.org/0000-0002-3963-708X; **N.Y. Yunusaliyev**, https://orcid.org/0000-0003-3766-5420
Kh.A. Makhmudov, https://orcid.org/0009-0004-8845-8741; **F.A. Abdulkhaev**, https://orcid.org/0009-0004-3933-5171
G.G. Tojiboyev, https://orcid.org/0009-0000-5022-8108; **M.O. G‘ufurjonova**, https://orcid.org/0009-0009-8830-9371

REFERENCES

[1] A. Smith and B. Johnson, “Radiation-Resistant Materials for Space Applications: A Review,” Adv. Mater. Interfaces, **9**, 2102345 (2022). https://doi.org/10.1002/admi.202102345
[2] S. Zainabidinov, A. Y. Boboev, and N.Y. Yunusaliyev, “Effect of γ-irradiation on structure and electrophysical properties of S-doped ZnO films,” East Eur. J. Phys. (2), 321 (2024). https://doi.org/10.26565/2312-4334-2024-2-37
[3] S.Z. Zaynabidinov, Sh.U. Yuldashev, A.Y. Boboev and N.Y. Yunusaliyev, “X-ray diffraction and electron microscopic studies of the ZnO<S> metal oxide films obtained by the ultrasonic spray pyrolysis method,” Herald Bauman Moscow State Tech. Univ., Ser. Nat. Sci. **112**(1), 78 (2024). https://doi.org/10.18698/1812-3368-2024-1-78-92
[4] S. Agostinelli, *et al.*, “GEANT4 – A simulation toolkit,” Nucl. Instrum. Methods Phys. Res., Sect. A, **506**(3), 250 (2003). https://doi.org/10.1016/S0168-9002(03)01368-8
[5] S.H. Kim, *et al.*, “Effects of electron irradiation on the properties of ZnO thin films,” Trans. Electr. Electron. Mater. **14**(4), 208 (2013). https://doi.org/10.4313/TEEM.2013.14.4.208
[6] K. Vanheusden, *et al.*, “Mechanisms behind green photoluminescence in ZnO phosphor powders,” J. Appl. Phys. **79**(10), 7983 (1996). https://doi.org/10.1063/1.362349
[7] N.Y. Yunusaliyev, “The Gas-Sensitive Properties of Tin Dioxide Films,” Eur. J. Phys. (4), 439 (2024). https://doi.org/10.26565/2312-4334-2024-4-52
[8] A. Elango, S. Rajendran and R. Sivakumar, “Optical properties of S-doped ZnO films,” J. Phys. D: Appl. Phys. **51**(15), 155102 (2018). https://doi.org/10.1088/1361-6463/aab0ea
[9] H.A. Bethe, “Theory of the Passage of Swift Corpuscular Rays through Matter,” Ann. Phys. **5**, 325 (1930). https://doi.org/10.1002/andp.19303970303
[10] K. Kanaya and S. Okayama, “Penetration and energy-loss theory of electrons in solid targets,” J. Phys. D: Appl. Phys. **5**(1), 43 (1972). https://doi.org/10.1088/0022-3727/5/1/308
[11] R. Chauhan, *et al.*, “Effect of particle energy on penetration depth in ZnO-based thin films,” Radiat. Phys. Chem. **170**, 108665 (2020). https://doi.org/10.1016/j.radphyschem.2019.108665
[12] W.J. Weber, *et al.*, “Radiation effects in crystalline ceramics,” J. Mater. Res. **12**(8), 1946 (1997). https://doi.org/10.1557/JMR.1997.0265
[13] H. Seiler, “Secondary Electron Emission in the Scanning Electron Microscope,” J. Appl. Phys. **54**(11), R1 (1983). https://doi.org/10.1063/1.332840
[14] E.J. Sternglass, “Theory of Secondary Electron Emission,” Phys. Rev. **108**(1), 1 (1957). https://doi.org/10.1103/PhysRev.108.1

[15] K.S. Daliev, *et al*., "Defect Formation in MIS Structures Based on Silicon with an Impurity of Ytterbium," East Eur. J. Phys. (4), 301 (2024). https://doi.org/10.26565/2312-4334-2024-4-33
[16] J.F. Ziegler, M.D. Ziegler and J.P. Biersack, "SRIM – The Stopping and Range of Ions in Matter," Nucl. Instrum. Methods Phys. Res., Sect. B, **268**(11), 1818 (2010). https://doi.org/10.1016/j.nimb.2010.02.091
[17] Y.H. Tak, *et al*., "Characteristics of transparent and conducting ZnO:Al thin films," Thin Solid Films, **411**(1), 12 (2002). https://doi.org/10.1016/S0040-6090(02)00166-1

МОДЕЛЮВАННЯ РАДІАЦІЙНО-ІНДУКОВАНИХ СТРУКТУРНИХ ТА ОПТИЧНИХ МОДИФІКАЦІЙ У ТОНКОПЛІВОЧНИХ СТРУКТУРАХ ZnO:S/Si

Акрамджон Й. Бобоєв[a], Хушрой А. Махмудов[b], Нурітдін Й. Юнусалієв[a], Мохлароїм О. Гофурджонова[a], Файзулох А. Абдулхаєв[a], Гайбулло Г. Тоджибоєв[a]
[a]*Андижанський державний університет імені З.М. Бабура, Андижан, Узбекистан*
[b]*Андижанська філія Кокандського університету, Андижан, Узбекистан*

У дослідженні вивчалися тонкі плівки ZnO, що містять 3 ат.% сірки (S) на кремнії (1 мкм), за допомогою моделювання Geant4 для радіаційного аналізу. Аналіз тонких плівок ZnO (400 нм), легованих 3 ат.% сірки (S), на кремнієвій підкладці товщиною 1 мкм за допомогою платформи моделювання Монте-Карло Geant4 враховував поглинання енергії разом з глибиною проникнення частинок та іонізацією, а також генерацію вторинних електронів та зміни оптичних властивостей, оскільки в дослідженні розглядалися різні енергії електронного випромінювання від 3 кеВ до 10 кеВ. Шар ZnO:S поглинав більшу частину енергії вхідних електронів у діапазоні 3-5 кеВ, що призводило до збільшення дефектів поблизу поверхні під час іонізації. Коли електрони використовували енергії 9-10 кеВ, вони проникали крізь весь шар підкладки, що призводило до отримання кремнієм більшої частини поглинання енергії. Найбільша зміна параметрів відбувалася на стику плівка-підкладка, коли енергія досягала 7 кеВ. Усі результати моделювання показали, що загальна поглинена енергія разом з утворенням вторинних електронів та щільністю дефектів, що досягала 10^7, швидко зростала зі прискоренням енергії електронів. Зниження оптичних властивостей відбувається тому, що дефекти існують на різній глибині під час поглинання енергії. Згідно з цим дослідженням, електричні та оптичні характеристики ZnO:S/Si можна регулювати за допомогою процедур електронного опромінення. Результати цього дослідження слугуватимуть основою для створення сенсорів, оптоелектронних пристроїв і захисних покриттів, які ефективно працюють в умовах високого випромінювання.

Ключові слова: *Монте-Карло; поглинання енергії; енергія електронів; глибина; зміщення; моделювання*

EAST EUROPEAN JOURNAL OF PHYSICS. 3. 390-397 (2025)
DOI:10.26565/2312-4334-2025-3-40 ISSN 2312-4334

IMPACT OF BORON DOPING ON CHARGE DISTRIBUTION AND THERMAL CONDUCTIVITY IN DOUBLE-WALLED CARBON NANOTUBES

Shahnozakhon Muminova[a], Abror Ulukmuradov[b], Xamid Isayev[b], Dildora Mamayeva[b], Utkir Uljayev[a,b]*

[a]*Denov Institute of Entrepreneurship and Pedagogy, 360 Denov City, Surkhandarya Region, 190507, Uzbekistan*
[b]*Tashkent Institute of Textile and Light Industry, Tashkent, 100100, Uzbekistan*
**Corresponding Author E-mail: utkir.uljaev@outlook.com*
Received April 24, 2025; revised August 7, 2025; accepted August 15, 2025

This study investigates the effect of boron (B) doping on the electrical and thermal conductivity properties of single-walled carbon nanotubes (DWNTs) at various temperatures (300 K to 1500 K). The incorporation of boron atoms into DWNTs (5,5)@(10,10) was analyzed to explore how different doping levels (ρ%) influence the partial charge distribution and thermal conductivity. Our findings show that boron doping increases the partial charge within the nanotube structure, with a nonlinear increase in charge as the doping concentration rises from 0% to 10%. This is due to the lower electronegativity of boron, which introduces hole carriers and enhances *p*-type semiconductor behavior. However, at higher doping concentrations (above 5%), defects disrupt the π-electron network, reducing electrical conductivity. Thermal conductivity experiments indicate that the presence of boron leads to a decrease in heat transfer efficiency, especially at higher doping levels (>6%), where defect-induced phonon scattering significantly reduces the thermal conductivity. The results demonstrate that boron doping has a complex impact on the structural, electronic, and thermal properties of DWNTs, with temperature and doping concentration playing critical roles in determining performance.
Keywords: *Double-walled carbon nanotube; Boron doping; Reactive molecular dynamics*
PACS: 61.46.-w, 02.70.Ns

1. INTRODUCTION

Carbon nanotubes (CNTs), a type of carbon-based nanostructure, continue to garner substantial research interest, with the body of literature on the topic growing at an exponential rate [1,2]. The carbon nanotubes (CNT) are tubular-shaped one-dimensional sp^2-hybridized carbon atoms arranged on honeycomb lattices. Since the rediscovery of CNTs by Iijima [3], it is one of the most explored nanomaterials. CNTs are classified as single-, double-, or multi-walled structures, exhibiting either semiconductor (S) or metallic (M) behavior based on their chiral indices. Approximately 60% of all nanotube chiralities are semiconductors, while the remaining 40% are metals [4]. Various types of nanotubes include Carbon Nanotubes (CNTs) [5], Boron Nitride Nanotubes (BNNTs) [6], Silicon Nanotubes (SiNTs) [7], and Hybrid Nanotubes (such as B-CNT and N-CNT, which integrate materials like carbon and boron nitride for multifunctional properties) [8]. These nanotubes, celebrated for their unique properties, have a wide range of applications in microelectronics [8], energy storage [9], sensors [10], and drug delivery [11]. They garner interest across various fields, including physics, chemistry, and materials science [12], showcasing their potential in electronic devices [13], sensors [14], adsorbents [9,15], and numerous other applications.

Various approaches, including functionalization, enable the customization of CNT properties [16]. Functionalization, accomplished through substitution reactions with comparable heteroatoms or functional groups, modifies CNTs' solubility, chemical reactivity, and various other physicochemical characteristics [17]. Notably, functionalization aids in the isolation of nanotube bundles. Consequently, studies have extensively explored CNT interactions with atoms and molecules like boron (B) [18], nitrogen (N) [19], calcium (Ca) [20], palladium (Pd) [21], fluorine (F) [22], bromine [23], and platinum (Pt) [24].

In recent years, boron-doped carbon nanotubes (B-CNTs) have garnered increasing interest due to their exceptional properties and wide-ranging applications [25]. Boron doping introduces alterations to the electronic structure of carbon nanotubes, enhancing their conductivity, catalytic activity, and chemical reactivity [26]. These unique characteristics make B-CNTs highly suitable for applications in energy storage [9], sensing, catalysis and nanotechnology [27]. B-doping of pristine CNTs offers the possibility to transform semiconducting tubes into metallic tubes by lowering the Fermi level into a valance band [28]. It also alters the crystallinity and stiffness of CNTs [29]. Furthermore, the incorporation of boron atoms modifies the band gap of carbon nanotubes, offering tailored properties for specific functional requirements. Therefore, boron (B) remain the preferred elements for substitution reactions [30].

Boron serves as a *p*-type dopant, enhancing nanotube growth by increasing oxidation resistance [31]. The similar atomic sizes of boron and carbon enable their seamless incorporation into the graphite network. Methods used to produce B-CNTs include carbon arc, laser ablation [32], substitution reactions [33], and chemical vapor deposition (CVD) [34]. For instance, Han et al. [35] successfully synthesized B-CNTs via substitution reactions (with a B/C ratio

Cite as: Sh. Muminova, A. Ulukmuradov, X. Isayev, D. Mamayeva, U. Uljayev, East Eur. J. Phys. 3, 390 (2025), https://doi.org/10.26565/2312-4334-2025-3-40
© Sh. Muminova, A. Ulukmuradov, X. Isayev, D. Mamayeva, U. Uljayev, 2025; CC BY 4.0 license

of 4.17), while Chen et al. [36] utilized microwave plasma CVD with trimethyl borate as a doping source. Additionally, Wang et al. [37] fabricated B-CNTs using electron cyclotron resonance chemical vapor deposition (ECR-CVD) on porous silicon substrates. Despite these advancements, precise control over the boron content in CNT structures remains challenging. Boron not only supports nanotube growth [38] but also enhances oxidation resistance [39], making it valuable for adjusting nanotube morphology and properties. The comparable atomic sizes of boron and carbon facilitate their integration into the graphite network. Therefore, B appears to have additional properties in terms of controlling the morphology and properties of nanotubes. CNTs are grown from boron or its compounds using various techniques (e.g., CVD, ALD) [40] and their various properties (i.e., mechanical, optical, electrical) are being studied.

In this study, we investigated molecular dynamics (MD) methods to calculate the electronic and thermal properties of boron-doped double carbon nanotubes (B-DWNT).

2. COMPUTATIONAL DETAILS

We investigate the process of boron (B) doped onto DWNTs (B-DWNTs) through reactive MD simulations employing the LAMMPS package [41]. The ReaxFF potential describes interatomic interactions, accounting for bond breaking and formation [42]. The most commonly used chiral DWNTs in other research studies (5,5)@(10,10) were selected as model system [43,44]. Our model includes pristine metal (5,5)@(10,10) nanotubes, denoted as B-DWNT(5,5)@(10,10) in MD simulations (Fig.1). Selected nanotubes diameters 13.64 Å-13.57 Å for (5,5)@(10,10) fall within experimentally observed ranges (13-16 Å) [45,46]. We apply periodic boundary conditions along the z-axis, allowing simulation of infinitely long B-DWNTs with lengths of 28.12 Å for B-DWNT(5,5)@(10,10) respectively. The (5,5)@(10,10) chiral DWNTs consist of 600 C atoms, respectively, with a B content of 0 to 10% (Fig.1).

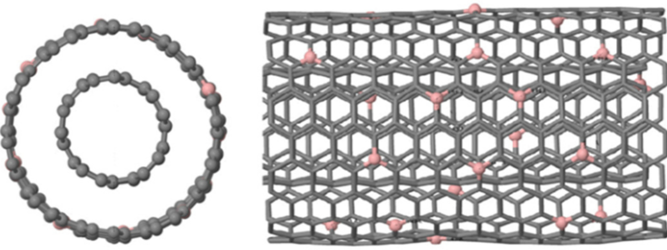

Figure 1. Top and side views of the B-DWNT(5,5)@(10,10) model system. Carbon (C) and Boron (B) atoms are shown in gray and coral, respectively

Initially, we minimize the energy of all model systems using the conjugate gradient method. Subsequently, we equilibrate system temperature and pressure to desired values (300 K, 600 K, 900 K, 1200, 1500 K and 0 Pa) in the NpT ensemble employing a Berendsen thermostat and barostat [47]. Our chosen heating rate (1 K/ps) aligns with previously reported values (0.1–10.0 K/ps) [48] ensuring insignificant deviations in thermodynamic equilibrium during temperature changes. For chemisorption of B atoms on DWNTs, we maintain system temperature at 300-1500 K for 100 ps using a Bussi thermostat [49]. Modeling was performed in the NVE ensemble to determine the heat transfer coefficient in the systems. Since the DWNTs were considered to be infinite in the modeling based on the periodicity conditions, the heat transfer was evaluated not by the number of B atoms, but by the content (%) of B atoms.

Initially, the electrical conductivity (partial charge) of the doped B atoms is calculated according to their amount (*ρ,%*) and temperature (300-1500 K). We estimate the amount (%) of doped B atoms on the surfaces of pure DWNTs at different temperatures (300 K, 600 K, 900 K, 1200 and 1500 K) as follows:

$$\rho = \frac{\text{number of atoms doped } (\mathrm{N}_B)}{\text{total atoms in a pristine DWNT } (\mathrm{N}_C)} * 100\%, \quad (1)$$

where, N_B- number of doping boron (B) and N_C- number of carbon atoms.

In addition, the thermal conductivity coefficient was determined using the Green-Kubo formula [50]:

$$k = \frac{1}{3Vk_BT^2}\int_0^{\infty}\langle J(0)\cdot J(t)\rangle dt, \qquad (1)$$

where V is the system volume, k_B Boltzmann constant, T temperature, The angle brackets $\langle --\rangle$ represent the average value of the heat flux autocorrelation function *J(t)* over all atoms. The heat flux *J(t)* is determined by the following formula:

$$J(t) = \frac{1}{2V}\sum_{i=1}^{N}\sum_{j=1}^{N} r_{ij}\cdot(F_{ij}\cdot v_i), \quad (3)$$

where r_{ij} and F_{ij} represent the distance and force between atoms i and j, and v_i represents the velocity of atom i.

In all cases MD time step is 0.1 fs. The simulations are conducted 10 times for each study case, and the results are obtained by averaging the corresponding physical quantities

RESULTS AND DISCUSSION

Electrical conductivity (partial charge)

When carbon nanotubes (CNTs) are grown with boron (B) at different temperatures, several factors come into play that can affect their structure, properties, and performance. From current literature, boron incorporation into carbon materials requires a high carbonization temperature of about 600-1100 °C (873-1373 K) [51]. The effect of boron on CNTs at low temperatures results in a high density of defects, leading to decreased electrical and thermal properties. Conversely, the addition of boron at high temperatures enhances thermal stability and improves electrical and mechanical properties [52].

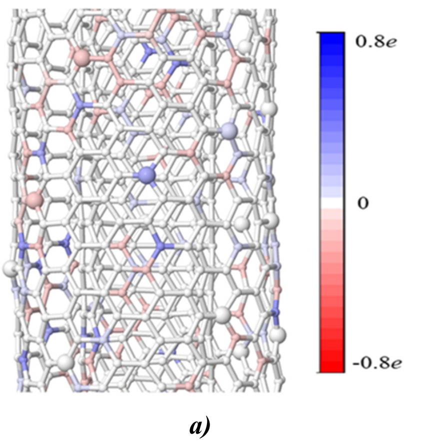

a)

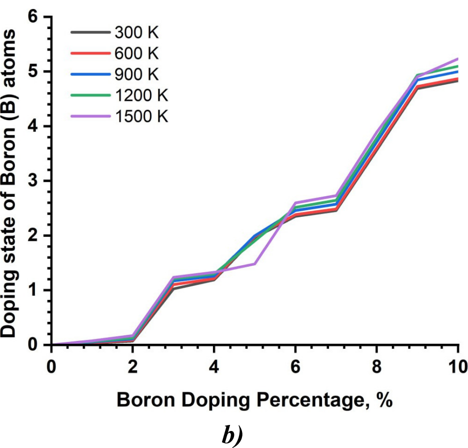

b)

Figure 2. (*a*) B atoms doping onto DWNT(5,5)@(10,10) are introduced, and system atoms exhibit partial charges from -0.8*e* to +0.8*e*, which range from red to blue is depicted by the color spectrum, which shows the transition from electron-rich regions to electron-poor regions, respectively, (*b*) The alteration in the partial charge of adsorbed B atoms in relation to temperature

Therefore, this study investigated the effect of B-DWNTs at selected temperatures of 300 K, 600K, and 900 K, 1200 K, 1500 K. The results indicate variations in the doping of B atoms on the surfaces of DWNT(5,5)@(10,10) at different temperatures (i.e., 300 K, 600 K, 900 K, 1200 K, 1500 K). Various factors influence the chemisorption of B atoms on DWNTs, including the nanotube surface curvature and the arrangement of carbon rings [53,54]. The doped coverage varies with temperature, and depending on their position within the hexagonal cell of the CNT, B atoms may detach from the surface due to temperature effects [55,56]. B atoms doping on the surface of DWNTs are affected by the arrival of other B atoms on the surface. This can result in the formation of molecules through the Langmuir-Hinshelwood recombination mechanism, where two B atoms on the surface covalently bond to form a B molecule. The temperature range (300-1500 K) employed in this study alters the quantity of B atoms doped on the surface [57,58].

Atoms in the system are color-coded to represent positive charges in blue and negative charges in red, while uncharged atoms are depicted in white (Fig. 2*a*). In this study, the charge distribution in the system changes with temperatures corresponding to ρ % of B atoms added in DWNT. In particular, the change in the partial charge in the system with an increase in ρ % in the temperature range from 300 K to 1500 K is shown in Figure 2*b*. It can be seen from the results that the partial charge in the system also increases nonlinearly with an increase in ρ %. One of the reasons for the non-linear increase may be related to the gravitational force used to calculate the interactions between the partial atoms [43]. The difference in electronegativity results in a variation in partial charges of carbon nanotube (CNT) and B atoms. Specifically, with increasing ρ % (i.e., from 300 K to 1500 K), the partial charging in DWNT increases due to the lower electronegativity of B (2.04) compared to carbon (2.55), causing it to lose electrons and generate a positive partial charge. That is, as the doping concentration (ρ %) increases, the number of boron atoms increases, leading to more changes in the electron distribution within the DWNT structure. This enhances the interaction with neighboring carbon atoms and other boron atoms, resulting in an increase in partial charge. The partial charge of B atoms in B-DWNT(5,5@10,10) increased from approximately 1%) to approximately 5.833e (10%) in the doped state (at temperatures between 300 and 1500 K) for 300 K, while in the case B-DWNT(5,5@10,10) nanotubes, the values increased from ~0.041*e* (1%) to ~5.868*e* (10%), respectively, at a temperature of 600K. At 900K, the values increased from ~0.065*e* (1%) to ~6.096*e* (10%). At 1200K, the increase was from ~0.065*e* (1%) to ~5.096*e* (10%). Finally, at 1500K, the change was from ~0.0674*e* (1%) to ~5.233*e* (10%) (Table 1).

Table 1. Partial charge variation with boron (B) atom doping at different temperatures for B-DWNT(5,5@10,10)

Boron doping (%)	**Partial charge, *e***				
	(5,5@10,10)				
	300 K	**600 K**	**900 K**	**1200 K**	**1500 K**
1	0.032	0.041	0.053	0.065	0.074
7	2.457	2.484	2.572	2.646	2.728
10	4.830	4.867	4.996	5.096	5.233

This indicates that an increase in the concentration of B leads to an increase in positive partial charges of the DWNT. This validates the outcomes achieved in earlier investigations [40]. B-DWNTs (DWNT(5,5)@(10,10) doped with B atoms and subjected to different temperatures, then the changes in their partial charges (*e*) are compared (*Supplementary information*).

The results indicate that at low boron doping (<1%), the increase in partial charge is not very significant (Fig. 2*b*). This is because low boron atoms create defects in the carbon lattice, which limits the free movement of π-electrons. As a result, electrical conductivity decreases due to increased scattering of charge carriers. As the doping of B atoms increases (1-5%), a slight increase in the partial charge in the B-DWNT system was observed (at 300-900 K). Since boron has a lower electronegativity than carbon, it introduces hole carriers into the structure, enhancing the *p*-type semiconductor properties of the B-DWNT. Under these conditions, electrical conductivity can increase. At high boron doping (>5%), a sharp decrease in the partial charge was observed. At very high boron concentrations (>8%), the π-electron network of the carbon nanotube is disrupted, and the excess defects lead to scattering of charge carriers. In this study, the average lengths of C-C and B-C bonds were found to be 1.426 and 1.514 Å, respectively, thus supporting the conclusion mentioned earlier [26].

Generally, the low electronegativity of boron introduces hole carriers, resulting in positive partial charges and *p*-type behavior in DWNTs.

Variation in thermal conductivity (*k*)

Figure 3 shows the thermal conductivity coefficient for (5,5@10,10) doped with different amounts (*ρ*%) of boron (B) as a function of temperature (300-1500 K).

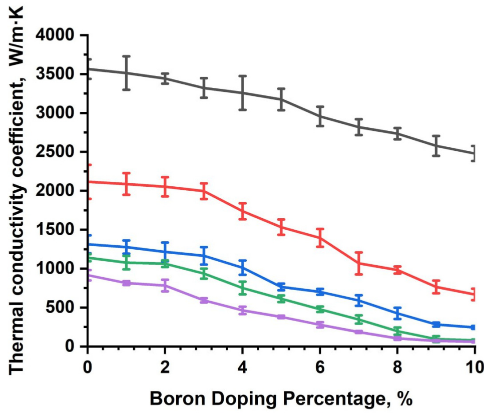

Figure 3. The variation of the thermal conductivity coefficient with doping amount and temperature

When analyzing the thermal conductivity (*k*) as a function of B doping concentration in B-DWNTs, at 300 K, *k* decreased noticeably by a factor of 1.012 at 1% (1%) B doping compared to the undoped case. At 600 K, the reduction was even greater, with k decreasing by a factor of 1.013. At higher temperatures 900 K, 1200 K, and 1500 K the thermal conductivity dropped by factors of 1.028, 1.058, and 1.124, respectively (Table 2). As the doping concentration *ρ*% of B atoms increases, thermal conductivity *k* also varies with temperature (*see Supplementary Information*).

Table 2. Thermal conductivity variation with boron (B) atom doping at different temperatures for B-DWNT(5,5@10,10)

Boron doping (%)	Thermal conductivity coefficient (W/m·K)				
	5,5@10,10				
	300 K	600 K	900 K	1200 K	1500 K
0	3564	2115	1313	1140	916
1	3512	2087	1277	1077	815
3	3321	1995	1165	936	593
5	3173	1533	764	613	379
8	2734	982	425	197	103
10	2479	668	245	78	61

Specifically, for B-DWNT(5.5@10.10), at temperatures of 300 K and 900 K, the thermal conductivity *k* at 1% doping is 3512 W/m•K and 1277 W/m•K, respectively. Likewise, at 1200 K and 1500 K, the difference increases, with k being 1.14 times and 1.30 times greater, respectively.

Overall, as the concentration of doped B atoms increases, the thermal conductivity of the two nanotubes begins to diverge. This behavior is primarily due to the weak phonon-electron interaction of boron. At 300 K, an initial increase in boron concentration (*ρ*%) in the DWNT structure results in a slight rise in thermal conductivity (by more than 3%), followed by a gradual decline (exceeding 4%). When B doping reaches 4–5%, the thermal conductivity drops significantly.

One contributing factor is the increased presence of structural defects, which sharply enhances phonon scattering-phonons being the primary heat carriers in carbon nanotubes. As the B doping concentration (ρ%) rises, so does the number of defects, leading to greater phonon scattering and reduced heat transfer.

When B doping falls within the 6%-10% range, structural disorder becomes more pronounced, resulting in a significant drop in thermal conductivity. At 10% boron doping, particularly in B-DWNT(5.5@10.10), thermal conductivity nearly reaches its minimum due to maximum phonon scattering and a sharp decline in transport efficiency. Notably, across nearly all temperature ranges (300-1500 K), the decline in thermal conductivity typically begins around 7%–8% doping.

Overall, at moderate temperatures (300–400 K), increased phonon interactions amplify the influence of boron doping on thermal conductivity, resulting in a slight decrease in thermal conductivity as boron content rises. For instance, B-DWNTs doped with 1% boron exhibit higher thermal conductivity compared to those with 2% or 3% doping. At elevated temperatures (T > 500 K), phonon-phonon scattering becomes the dominant mechanism, leading to a reduction in thermal conductivity regardless of the doping level. However, in heavily doped B-DWNTs (>6%), thermal conductivity is significantly lower due to the inability of lattice vibrations to propagate effectively amid excessive structural defects. As a result, the system's thermal conductivity varies with changes in external temperature. Boron doping creates defects and disrupts the phonon transport network in DWNTs, leading to increased phonon scattering and a reduction in thermal conductivity, particularly at high doping concentrations.

CONCLUSION

The results demonstrate that the intentional introduction of boron atoms into DWNTs leads to changes in both electrical and thermal conductivity, specifically an increase in electrical conductivity (partial charge) and a decrease in thermal conductivity (k). The average partial charge (e) in the B-DWNT system increased from 0.032e to 4.830e at 300 K for B-DWNT(5.5@10.10) as the B content (ρ%) rose. Between 600 K and 1500 K, the increase in ρ% was 2.31 and 2.56 times greater (at 1% and the 1500 K/300 K ratio), respectively, while the increase in partial charge was 1.11 and 1.15 times greater (at 7% and the 1500 K/300 K ratio). At the maximum B doping level (10%), the partial charge increased by 1.08 and 1.09 times, respectively. Therefore, the increase in partial charge with rising ρ% in B-DWNTs can be attributed to a combination of electronic distribution, thermal effects, structural changes, and ionic effects.

At room temperature (300 K), the thermal conductivity of 1% doped B-DWNTs is approximately 3564 W/mK for (5.5@10.10) and 3651 W/mK. As the boron content (ρ%) increases, the thermal conductivity of (5.5@10.10) chiral B-DWNTs decreases more than that of. Specifically, when 7% boron is added to (5.5@10.10) chiral B-DWNTs and 6.75% boron is, their thermal conductivity decreases by 1.26 times, respectively, compared to the 0% case. These results demonstrate the potential for modifying the electrical and thermal conductivity of DWNTs through boron doping, enhancing their suitability for use in thermal interface materials (TIMs).

Acknowledgment

This research was carried out within the framework by the fundamental research program of the Academy Sciences of Uzbekistan.

ORCID

Abror Ulukmuradov, https://orcid.org/0000-0002-7135-9673; **Utkir Uljayev,** https://orcid.org/0009-0002-2564-5270

REFERENCES

[1] S. Iijima, "Carbon nanotubes: past, present, and future," Phys. B: Condens. Matter **323**, 1-5 (2002). https://doi.org/10.1016/S0921-4526(02)00869-4

[2] S. Rathinavel, K. Priyadharshini, and D. Panda, "A review on carbon nanotube: An overview of synthesis, properties, functionalization, characterization, and the application," Mater. Sci. Eng. B **268**, 115095 (2021). https://doi.org/10.1016/j.mseb.2021.115095

[3] S. Iijima, "Helical microtubules of graphitic carbon," Nature **354**, 56-58 (1991). https://doi.org/10.1038/354056a0

[4] K.E. Moore, D.D. Tune, and B.S. Flavel, "Double-Walled Carbon Nanotube Processing," Adv. Mater. **27**, 3105 (2015). https://doi.org/10.1002/adma.201405686

[5] N. Anzar, R. Hasan, M. Tyagi, N. Yadav, and J. Narang, "Carbon nanotube - A review on Synthesis, Properties and plethora of applications in the field of biomedical science," Sens. Int. **1**, 100003 (2020). https://doi.org/10.1016/j.sintl.2020.100003

[6] J.H. Kim, T.V. Pham, J.H. Hwang, C.S. Kim, and M.J. Kim, "Boron nitride nanotubes: synthesis and applications, Nano Converg. **5**, 17 (2018). https://doi.org/10.1186/s40580-018-0149-y

[7] P. Castrucci, M. Scarselli, M. De Crescenzi, M. Diociaiuti, Prajakta S. Chaudhari, C. Balasubramanian, *et al.*, "Silicon nanotubes: Synthesis and characterization," Thin Solid Films, **508**(1-2), 226-230 (2006), https://doi.org/10.1016/j.tsf.2005.07.348

[8] S.V. Sawant, A.W. Patwardhan, J.B. Joshi, and K. Dasgupta, "Boron doped carbon nanotubes: Synthesis, characterization and emerging applications – A review," Chem. Eng. J. **427**, 131616 (2022). https://doi.org/10.1016/j.cej.2021.131616

[9] U. Khalilov, U. Uljayev, K. Mehmonov, P. Nematollahi, M. Yusupov, and E. Neyts, "Can endohedral transition metals enhance hydrogen storage in carbon nanotubes?" Int. J. Hydrog. Energy, **55**, 604-610 (2024). https://doi.org/10.1016/j.ijhydene.2023.11.195

[10] U.B. Uljaev, S.A. Muminova, and I.D. Yadgarov, "Nitrogen Adsorption on Double-Walled Carbon Nanotube at Different Temperatures: Mechanistic Insights from Molecular Dynamics Simulations," East Eur. J. Phys. (1), 361-365 (2024). https://doi.org/10.26565/2312-4334-2024-1-34

[11] M.F. Naief, S.N. Mohammed, H.J. Mayouf, and A.M. Mohammed, "A review of the role of carbon nanotubes for cancer treatment based on photothermal and photodynamic therapy techniques," J. Organomet. Chem. **999**, 122819 (2023). https://doi.org/10.1016/j.jorganchem.2023.122819
[12] A. Ali, S.S. Rahimian Koloor, A.H. Alshehri, and A. Arockiarajan, "Carbon nanotube characteristics and enhancement effects on the mechanical features of polymer-based materials and structures – A review," J. Mater. Res. Technol. **24**, 6495-6521 (2023). https://doi.org/10.1016/j.jmrt.2023.04.072
[13] M. Soto, T.A. Boyer, S. Biradar, L. Ge, R. Vajtai, A. Elías-Zúñiga, P.M. Ajayan, and E.V. Barrera, "Effect of interwall interaction on the electronic structure of double-walled carbon nanotubes," Nanotechnology, **26**, 165201 (2015). https://doi.org/10.1088/0957-4484/26/16/165201
[14] Y. Yao, R. Shen, J. Xu, and Z. Feng, "Progress in electrochemical sensing of epinephrine using carbon nanomaterials: A review," Int. J. Electrochem. Sci. **19**, 100750 (2024). https://doi.org/10.1016/j.ijoes.2024.100750
[15] M. Sajid, M. Asif, N. Baig, M. Kabeer, I. Ihsanullah, and A.W. Mohammad, "Carbon nanotubes-based adsorbents: Properties, functionalization, interaction mechanisms, and applications in water purification," J. Water Process Eng. **47**, 102815 (2022). https://doi.org/10.1016/j.jwpe.2022.102815
[16] D. Liu, L. Shi, Q. Dai, X. Lin, R. Mehmood, Z. Gu, and L. Dai, "Functionalization of carbon nanotubes for multifunctional applications," Trends Chem. **6**, 186-210 (2024). https://doi.org/10.1016/j.trechm.2024.02.002
[17] M. Adamska, and U. Narkiewicz, "Fluorination of Carbon Nanotubes − A Review," J. Fluor. Chem. **200**, 179-189 (2017). https://doi.org/10.1016/j.jfluchem.2017.06.018
[18] D. Silambarasan, V.J. Surya, V. Vasu, and K. Iyakutti, "Experimental investigation of hydrogen storage in single walled carbon nanotubes functionalized with borane," Int. J. Hydrog. Energy, **36**, 3574-3579 (2011). https://doi.org/10.1016/j.ijhydene.2010.12.028
[19] Y. Tison, *et al.*, "Identification of Nitrogen Dopants in Single-Walled Carbon Nanotubes by Scanning Tunneling Microscopy," ACS Nano, **7**, 7219-7226 (2013). https://doi.org/10.1021/nn4026146
[20] S.H. De Paoli Lacerda, J. Semberova, K. Holada, O. Simakova, S. D. Hudson, and J. Simak, "Carbon Nanotubes Activate Store-Operated Calcium Entry in Human Blood Platelets," ACS Nano, **5**, 5808-5813 (2011). https://doi.org/10.1021/nn2015369
[21] H. Wu, D. Wexler, and H. Liu, "Effects of different palladium content loading on the hydrogen storage capacity of double-walled carbon nanotubes," Int. J. Hydrog. Energy **37**, 5690 (2012). https://doi.org/10.1016/j.ijhydene.2011.12.120
[22] L.G. Bulusheva, Y.V. Fedoseeva, E. Flahaut, J. Rio, C.P. Ewels, V.O. Koroteev, G. Van Lier, *et al.*, "Effect of the fluorination technique on the surface-fluorination patterning of double-walled carbon nanotubes," Beilstein J. Nanotechnol. **8**, 1688-1698 (2017). https://doi.org/10.3762/bjnano.8.169
[23] L.G. Bulusheva, A.V. Okotrub, E. Flahaut, I.P. Asanov, P.N. Gevko, V.O. Koroteev, Yu.V. Fedoseeva, *et al.*, "Bromination of Double-Walled Carbon Nanotubes," Chem. Mater. **24**, 2708-2715 (2012). https://doi.org/10.1021/cm3006309
[24] D. Xia, Y. Luo, Q. Li, Q. Xue, X. Zhang, C. Liang, and M. Dong, "Extracting the inner wall from nested double-walled carbon nanotube by platinum nanowire: molecular dynamics simulations," RSC Adv. **7**, 39480 (2017). https://doi.org/10.1039/C7RA07066G
[25] U. Uljayev, S. Muminova, K. Mehmonov, I. Yadgarov, and A. Ulukmuradov, "Boron interaction with double-walled carbon nanotubes across temperature ranges," Mod. Electron. Mater. **10**, 3 (2024). https://doi.org/10.3897/j.moem.10.3.131526
[26] S.V. Boroznin, "Carbon nanostructures containing boron impurity atoms: synthesis, physicochemical properties and potential applications," Mod. Electron. Mater. **8**, 23-42 (2022). https://doi.org/10.3897/j.moem.8.1.84317
[27] M. Sireesha, V.J. Babu, A.S. Kiran, and S. Ramakrishna, "A review on carbon nanotubes in biosensor devices and their applications in medicine," Nanocomposites **4**, 36 (2018). https://doi.org/10.1080/20550324.2018.1478765
[28] L. Wirtz, and A. Rubio, "Band structure of boron doped carbon nanotubes," **685**, 402-405 (2003). https://doi.org/10.1063/1.1628059
[29] J. Saloni, W. Kolodziejczyk, S. Roszak, D. Majumdar, G. Hill, Jr., J. Leszczynski, "Local and Global Electronic Effects in Single and Double Boron-Doped Carbon Nanotubes," J. Phys. Chem. C, **114**(3), 1528–1533 (2010). https://doi.org/10.1021/jp910625w
[30] D. Jana, C.-L. Sun, L.-C. Chen, and K.-H. Chen, "Effect of chemical doping of boron and nitrogen on the electronic, optical, and electrochemical properties of carbon nanotubes," Prog. Mater. Sci. **58**, 565-635 (2013). https://doi.org/10.1016/j.pmatsci.2013.01.003
[31] T.-J. Li, *et al.*, "Boron-doped carbon nanotubes with uniform boron doping and tunable dopant functionalities as an efficient electrocatalyst for dopamine oxidation reaction," Sens. Actuators B: Chem. **248**, 288-297 (2017). https://doi.org/10.1016/j.snb.2017.03.118
[32] P. Ayala, J. Reppert, M. Grobosch, M. Knupfer, T. Pichler, and A. Rao, "Evidence for substitutional boron in doped single-walled carbon nanotubes," Appl. Phys. Lett. **96**, 183110 (2010). https://doi.org/10.1063/1.3427432
[33] S. Parham, *Heteroatom-Doped Carbon Allotropes in Solar Cells Application*, in *Heteroatom-Doped Carbon Allotropes: Progress in Synthesis, Characterization, and Applications*, vol. 1491, (American Chemical Society, 2024), pp. 127–149.
[34] S.V. Sawant, S. Banerjee, A.W. Patwardhan, J.B. Joshi, and K. Dasgupta, "Effect of in-situ boron doping on hydrogen adsorption properties of carbon nanotubes," Int. J. Hydrog. Energy **44**, 18193-18204 (2019). https://doi.org/10.1016/j.ijhydene.2019.05.029
[35] W. Han, Y. Bando, K. Kurashima, and T. Sato, "Synthesis of boron nitride nanotubes from carbon nanotubes by a substitution reaction," Appl. Phys. Lett. **73**, 3085-3087 (1998). https://doi.org/10.1063/1.122680
[36] C.F. Chen, C.L. Tsai, and C.L. Lin, "The characterization of boron-doped carbon nanotube arrays," Diam. Relat. Mater. **12**, 1500-1504 (2003). https://doi.org/10.1016/S0925-9635(03)00181-X
[37] Z. Wang, C.H. Yu, D. Ba, and J. Liang, "Influence of the gas composition on the synthesis of boron-doped carbon nanotubes by ECR-CVD," Vacuum, **81**, 579-582 (2007). https://doi.org/10.1016/j.vacuum.2006.05.012
[38] X. Blase, J.-C. Charlier, A. De Vita, R. Car, Ph. Redlich, M. Terrones, W. K. Hsu, *et al.*, "Boron-Mediated Growth of Long Helicity-Selected Carbon Nanotubes," Phys. Rev. Lett. **83**, 5078 (1999). https://doi.org/10.1103/PhysRevLett.83.5078

[39] L.E. Jones, and P.A. Thrower, "Influence of boron on carbon fiber microstructure, physical properties, and oxidation behavior," Carbon, **29**, 251-269 (1991). https://doi.org/10.1016/0008-6223(91)90076-U
[40] M. Terrones, A. Jorio, M. Endo, A.M. Rao, Y.A. Kim, T. Hayashi, H. Terrones, *et al*., New direction in nanotube science, Mater. Today **7**, 30 (2004). https://doi.org/10.1016/S1369-7021(04)00447-X
[41] A.P. Thompson, *et al.*, "LAMMPS - a flexible simulation tool for particle-based materials modeling at the atomic, meso, and continuum scales," Comput. Phys. Commun. **271**, 108171 (2022). https://doi.org/10.1016/j.cpc.2021.108171
[42] J.E. Mueller, A.C.T. van Duin, and W.A.I. Goddard, "Development and Validation of ReaxFF Reactive Force Field for Hydrocarbon Chemistry Catalyzed by Nickel," J. Phys. Chem. C **114**, 4939-4949 (2010). https://doi.org/10.1021/jp9035056
[43] J.R. Lukes, and H. Zhong, "Thermal Conductivity of Individual Single-Wall Carbon Nanotubes," J. Heat Transf. **129**, 705-716 (2007). https://doi.org/10.1115/1.2717242
[44] A.T. Zahra, A. Shahzad, A. Manzoor, J. Razzokov, Q.U.A. Asif, K. Luo, and G. Ren, "Structural and thermal analyses in semiconducting and metallic zigzag single-walled carbon nanotubes using molecular dynamics simulations," PLOS ONE **19**, e0296916 (2024). https://doi.org/10.1371/journal.pone.0296916
[45] G. Chen, S. Bandow, E.R. Margine, C. Nisoli, A.N. Kolmogorov, V.H. Crespi, R. Gupta, G.U. Sumanasekera, *et al.*, "Chemically Doped Double-Walled Carbon Nanotubes: Cylindrical Molecular Capacitors," Phys. Rev. Lett. **90**, 257403 (2003). https://doi.org/10.1103/PhysRevLett.90.257403
[46] K. Mehmonov, A. Ergasheva, M. Yusupov, and U. Khalilov, "The role of carbon monoxide in the catalytic synthesis of endohedral carbyne," J. Appl. Phys. **134**, 144303 (2023). https://doi.org/10.1063/5.0160892
[47] H.J.C. Berendsen, J.P.M. Postma, W.F. Van Gunsteren, A. DiNola, and J.R. Haak, "Molecular dynamics with coupling to an external bath," J. Chem. Phys. **81**, 3684-3690 (1984). https://doi.org/10.1063/1.448118
[48] J. Sun, P. Liu, M. Wang, and J. Liu, "Molecular Dynamics Simulations of Melting Iron Nanoparticles with/without Defects Using a Reaxff Reactive Force Field," Sci. Rep. **10**, 3408 (2020). https://doi.org/10.1038/s41598-020-60416-5
[49] G. Bussi, D. Donadio, and M. Parrinello, "Canonical sampling through velocity rescaling," J. Chem. Phys. **126**, 014101 (2007). https://doi.org/10.1063/1.2408420
[50] Y.-K. Kwon, and P. Kim, *Unusually High Thermal Conductivity in Carbon Nanotubes*, in *High Thermal Conductivity Materials*, edited by S.L. Shindé, and J.S. Goela (Springer, New York, NY, 2006), pp. 227–265.
[51] A. Sharma, A. Patwardhan, K. Dasgupta, and J.B. Joshi, "Kinetic study of boron doped carbon nanotubes synthesized using chemical vapour deposition," Chem. Eng. Sci. **207**, 1341-1352 (2019). https://doi.org/10.1016/j.ces.2019.06.030
[52] M.M.S. Fakhrabadi, A. Allahverdizadeh, V. Norouzifard, and B. Dadashzadeh, "Effects of boron doping on mechanical properties and thermal conductivities of carbon nanotubes," Solid State Commun. **152**, 1973-1979 (2012). https://doi.org/10.1016/j.ssc.2012.08.003
[53] P. Ayala, *et al.*, "Tailoring N-Doped Single and Double Wall Carbon Nanotubes from a Nondiluted Carbon/Nitrogen Feedstock," J. Phys. Chem. C **111**, 2879-2884 (2007). https://doi.org/10.1021/jp0658288
[54] W. Su, X. Li, L. Li, D. Yang, F. Wang, X. Wei, W. Zhou, *et al.*, "Chirality-dependent electrical transport properties of carbon nanotubes obtained by experimental measurement," Nat. Commun. **14**, 1672 (2023). https://doi.org/10.1038/s41467-023-37443-7
[55] U. Khalilov, A. Bogaerts, B. Xu, T. Kato, T. Kaneko, and E. C. Neyts, "How the alignment of adsorbed ortho H pairs determines the onset of selective carbon nanotube etching," Nanoscale, **9**, 1653-1616 (2017). https://doi.org/10.1039/C6NR08005G
[56] N.R. Abdullah, H.O. Rashid, M.T. Kareem, C.-S. Tang, A. Manolescu, and V. Gudmundsson, "Effects of bonded and non-bonded B/N codoping of graphene on its stability, interaction energy, electronic structure, and power factor," Phys. Lett. A **384**, 126350 (2020). https://doi.org/10.1016/j.physleta.2020.126350
[57] X. Sha, B. Jackson, and D. Lemoine, "Quantum studies of Eley–Rideal reactions between H atoms on a graphite surface," J. Chem. Phys. **116**, 7158-7169 (2002). https://doi.org/10.1063/1.1463399
[58] T. Zecho, A. Güttler, X. Sha, D. Lemoine, B. Jackson, and J. Küppers, "Abstraction of D chemisorbed on graphite (0001) with gaseous H atoms," Chem. Phys. Lett. **366**, 188-195 (2002). https://doi.org/10.1016/S0009-2614(02)01573-7

APPENDIX
Supplementary information

Table 1. Partial charge variation with boron (B) atom doping at different temperatures for B-DWNT(5.5@10.10)

Boron doping (%)	Partial charge 300 K	Partial charge 600 K	Partial charge 900 K	Partial charge 1200 K	Partial charge 1500 K
0%	0.00	0.00	0.00	0.00	0.00
1%	~0.032	~0.041	~0.053	~0.065	~0.074
2%	~0.072	~0.088	~0.108	~0.128	~0.168
3%	~1.025	~1.102	~1.172	~1.207	~1.236
4%	~1.188	~1.212	~1.258	~1.298	~1.327
5%	~1.963	~1.984	~1.997	~1.901	~1.478
6%	~2.351	~2.382	~2.456	~2.516	~2.597
7%	~2.457	~2.484	~2.572	~2.646	~2.728
8%	~3.563	~3.602	~3.711	~3.782	~3.891
9%	~4.690	~4.727	~4.843	~4.933	~4.904
10%	~4.830	~4.867	~4.996	~5.096	~5.233

Table 2. Thermal conductivity variation with boron (B) atom doping at different temperatures for B-DWNT(5.5@10.10)

Boron Doping (%)	**Thermal conductivity coefficient (W/m·K)**				
	300 K	**600 K**	**900 K**	**1200 K**	**1500 K**
0%	3564	2115	1313	1140	916
1%	3512	2087	1277	1077	815
2%	3442	2052	1214	1064	783
3%	3321	1995	1165	936	593
4%	3257	1737	1012	751	464
5%	3173	1533	764	613	379
6%	2956	1395	702	478	278
7%	2818	1067	590	346	186
8%	2734	982	425	197	103
9%	2577	765	282	94	73
10%	2479	668	245	78	61

ПРОВІДНІСТЬ У ДВОСТІННИХ ВУГЛЕЦЕВИХ НАНОТРУБКАХ

Шахнозахон Мумінова[a], Аброр Улукмурадов[b], Хамід Ісаєв[b], Ділдора Мамаєва[b], Уткір Ульджаєв[a,b]
[a]*Денауський інститут підприємництва та педагогіки, м. Денау, 360, Сурхандар'їнська область, 190507, Узбекистан*
[b]*Ташкентський інститут текстильної та легкої промисловості, Ташкент, 100100, Узбекистан*

У цьому дослідженні вивчається вплив легування бором (B) на електро- та теплопровідні властивості одностінних вуглецевих нанотрубок (DWNT) за різних температур (від 300 K до 1500 K). Було проаналізовано включення атомів бору в DWNT (5,5)@(10,10), щоб дослідити, як різні рівні легування (ρ%) впливають на розподіл часткового заряду та теплопровідність. Наші результати показують, що легування бором збільшує частковий заряд у структурі нанотрубки, з нелінійним збільшенням заряду зі збільшенням концентрації легування від 0% до 10%. Це пов'язано з нижчою електронегативністю бору, який вводить носіїв дірок та посилює поведінку напівпровідника p-типу. Однак, при вищих концентраціях легування (вище 5%), дефекти порушують π-електронну мережу, зменшуючи електропровідність. Експерименти з теплопровідності показують, що присутність бору призводить до зниження ефективності теплопередачі, особливо при вищих рівнях легування (>6%), де індуковане дефектами розсіювання фононів значно знижує теплопровідність. Результати демонструють, що легування бором має складний вплив на структурні, електронні та теплові властивості DWNT, причому температура та концентрація легування відіграють вирішальну роль у визначенні характеристик.

Ключові слова: *двостінна вуглецева нанотрубка; легування бором; реактивна молекулярна динаміка*

EAST EUROPEAN JOURNAL OF PHYSICS. 3. 398-407 (2025)
DOI:10.26565/2312-4334-2025-3-41 ISSN 2312-4334

SPIN-POLARIZED PROPERTIES OF Ni-DOPED ZnSe: FIRST-PRINCIPLES SIMULATION AND MODELLING

V.N. Jafarova[a,b]*, A.N. Jafarova[a], A.J. Ahmadova[c]

[a]*Azerbaijan State Oil and Industry University, 20 Azalig Ave., AZ-1010, Baku, Azerbaijan*
[b]*Khazar University, 41 Mehseti Str., AZ1096, Baku, Azerbaijan*
[c]*Nakhchivan State University, AZ-7012, Nakhchivan, Azerbaijan*
**Corresponding Author E-mail: vusala.cafarova@asoiu.edu.az*

Received June 1, 2025; revised August 8, 2925; accepted August 19, 2025

This work delivers an in-depth *ab initio* investigation into the electronic and magnetic characteristics of ZnSe systems doped with nickel, evaluated at three distinct impurity levels: 3.125%, 6.25% and 12.5%. The analysis is grounded in density functional theory (DFT), employing the local spin density approximation (LSDA) framework, further refined with Hubbard U corrections to effectively capture the pronounced electron correlation effects typical of transition metal d-electrons. The incorporation of Ni into the ZnSe matrix significantly modifies the electronic structure, leading to half-metallic behavior and pronounced spin polarization. Total magnetic moments of 4.0 μ_B per supercell were observed. Furthermore, energy comparisons between ferromagnetic and antiferromagnetic configurations confirmed that the ferromagnetic phase is more energetically stable. These results highlight the potential of Ni-doped ZnSe in spintronic applications where controlled magnetic and electronic properties are crucial.

Keywords: *ZnSe:Ni; Ferromagnetic; Half-metal; Magnetic moment; First-principles simulation; Density Functional Theory*
PACS: 61.72.-y; 75.50.Pp; 68.55.Ln

1. INTRODUCTION

Diluted Magnetic Semiconductor materials (DMSMs) have significantly advanced systems science by facilitating the development of multifunctional compounds that exhibit a combination of magnetic behavior and semiconducting capabilities. These hybrid functionalities make DMSs particularly attractive for next-generation applications in engineering, environmental monitoring, optoelectronics, and especially in the rapidly developing field of spintronics, where control over electron spin is essential.

Compared to other potential diluted magnetic semiconductor (DMS) hosts, ZnSe offers several key advantages that make it a particularly promising candidate for spintronic applications. For instance, ZnO, despite being widely studied, suffers from the formation of intrinsic defects such as oxygen vacancies and zinc interstitials, which lead to unintentional n-type conductivity and hinder the achievement of stable p-type behavior [1]. CdTe and ZnTe, while possessing favorable electronic characteristics, exhibit stronger spin-orbit coupling and involve cadmium-a toxic element that raises serious environmental and safety concerns [2]. ZnS, moreover, demonstrates limited solubility for transition metal (TM) dopants and lacks consistent experimental confirmation of room temperature ferromagnetism [3].

In contrast, ZnSe presents a well-balanced and advantageous profile. It combines a favorable wide direct band gap (Exp.: ~2.7 eV [4]; 2.763 eV [5]) with relatively low spin-orbit coupling enhancing spin coherence and facilitating spin transport in devices [6], [7] along with excellent chemical and thermal stability. Its structural compatibility with standard thin-film growth techniques further enables efficient dopant incorporation and device fabrication [3]. These combined characteristics make ZnSe an attractive host matrix for TM-doped DMS systems aimed at spin-based applications.

Studying the electronic and magnetic properties of ZnSe doped with transition metals such as Ni is essential for evaluating its potential as a functional DMS. The material's electronic structure dictates critical device-relevant properties, optical response, electrical conductivity, and carrier mobility, while TM-induced magnetic behavior is key to achieving room-temperature ferromagnetism vital for spintronic operations. Of particular interest is half-metallicity, where one spin channel is metallic and the other semiconducting, enabling fully spin-polarized currents at the Fermi level. Such characteristics are fundamental to devices like spin valves, magnetic tunnel junctions, and spin field-effect transistors.

This focus aligns with established theoretical and experimental advancements in DMS physics. Dietl et al. [8] developed a seminal mean-field model of hole-mediated ferromagnetism in tetrahedrally coordinated semiconductors, which underpins much of DMS theory development. Tanaka and Higo demonstrated large tunneling magnetoresistance in GaMnAs/AlAs/GaMnAs junctions, highlighting the functionality of ferromagnetic semiconductors in device contexts [9]. Foundational also are visionary perspectives on spintronics and DMSs provided by Wolf et al. [10] and Awschalom & Flatté [11], as well as first-principles formulations by Sato et al., which collectively guide and justify material selection and device design strategies [12].

Moreover, the role of intrinsic defects is critical in DMS performance. Defects such as vacancies and interstitials can dramatically influence magnetic coupling including mechanisms like bound magnetic polaron formation and may either stabilize or inhibit ferromagnetic ordering. Importantly, defect-dopant interactions can be harnessed to tailor band

Cite as: V.N. Jafarova, A.N. Jafarova, A.J. Ahmadova, East Eur. J. Phys. 3, 398 (2025), https://doi.org/10.26565/2312-4334-2025-3-41
© V.N. Jafarova, A.N. Jafarova, A.J. Ahmadova, 2025; CC BY 4.0 license

gaps, control charge carrier density, and enhance magneto-optical effects. Understanding this interplay is therefore essential for optimizing ZnSe-based DMS materials.

This work aims to provide a comprehensive first-principles investigation into the electronic structure, magnetic behavior, and defect effects in Ni-doped ZnSe supercells. By comparing undoped and doped configurations and analyzing spin-resolved band structures and densities of states, we identify the origins of half-metallicity and spin polarization in $Zn_{1-x}Ni_xSe$. These results contribute to the fundamental understanding of II–VI DMS systems and support the future design of spin-based optoelectronic devices.

Zinc selenide (ZnSe), a II-VI compound semiconductor, is inherently non-magnetic and possesses a direct band gap of approximately 2.70 eV [4], which makes it highly suitable for various optoelectronic devices. Its applications span from laser diodes, lasers, and light-emitting diodes to solar cells, microwave and terahertz emitters, and mid-infrared (IR) tunable lasers [11-13]. However, by introducing transition metal (TM) dopants such as Co or Ni into the ZnSe lattice, its properties can be significantly tailored to exhibit spin polarization and ferromagnetic behavior - transforming the material into a DMS.

Numerous studies have focused on TM-doped $Zn_{1-x}TM_xSe$ compounds, recognizing their potential as functional materials for spin-based electronic and magnetic devices [14-21]. For example, Sato et al. [12, 22] predicted high Curie temperatures in Cr- and V-doped ZnSe using first-principles simulations based on a zinc-blende structure. Similarly, theoretical investigations by Benstaali et al. [15] on Co-doped ZnSe, Mahmood et al. [23] on Ti-doped ZnSe, and Arif et al. [24] on Co-doped CdSe revealed half-metallic ferromagnetic phases, confirming the viability of these materials for spintronic technologies.

Our earlier work [25] demonstrated that the introduction of a Zn vacancy in Mn-doped ZnSe leads to half-metallic ferromagnetism, supporting the idea that defects and dopants together play a critical role in tuning the magnetic characteristics of such systems. In the present study, we extend this line of investigation to Ni-doped ZnSe with one and two doping concentrations: 3.125 %, 6.25% and 12.5%. Using first-principles DFT simulations, we analyze the electronic structure, spin polarization, and magnetic ordering (ferromagnetic vs. antiferromagnetic) of the doped systems. Our findings reveal that the incorporation of Ni ions induces robust ferromagnetic ordering and high spin polarization, transforming ZnSe into a ferromagnetic semiconductor. This highlights its potential application in spintronic devices where efficient spin injection and manipulation are required.

The primary novelty of this work lies in the systematic first-principles study of the electronic and magnetic properties of Ni-doped ZnSe, specifically at doping concentrations of 3.125 %, 6.25% and 12.5%. By applying spin-polarized density functional theory (DFT), we analyze the impact of nickel doping on the electronic structure, magnetic ordering, and half-metallicity of ZnSe. This work offers new insights into the fundamental behavior of diluted magnetic semiconductors (DMS), particularly in how transition metal doping can tune the material's properties to make them suitable for spintronic applications.

The purpose of this study is to explore how Ni doping influences the magnetic and electronic properties of ZnSe, focusing on the emergence of half-metallic ferromagnetism and spin-polarization in the material. In doing so, we investigate the role of nickel in modifying the band structure and inducing a spin asymmetry, which is critical for future spintronic devices such as spin valves and magnetic tunnel junctions.

The motivation behind this work is rooted in the growing demand for materials that can simultaneously exhibit semiconducting and magnetic properties, crucial for advancing spin-based technologies. While previous studies have investigated other DMS systems, our work emphasizes ZnSe as an ideal candidate due to its favorable electronic characteristics and minimal spin-orbit coupling. Our findings contribute to expanding the understanding of Ni-doped ZnSe, offering a pathway for designing new materials for applications in spintronics, where controlling electron spin is essential for efficient device operation.

In light of these considerations, this manuscript presents an in-depth study with a clearly defined objective, ensuring that the research not only contributes to the scientific community but also addresses the challenges in developing high-performance DMS materials for next-generation technologies.

2. CALCULATION METHOD

In this research, *ab initio* simulations were carried out within the framework of DFT, coupled with the pseudopotential method [26] for analyzing the electronic and magnetic characteristics of semiconductors, half-metals, and nanoscale materials. The computational framework was implemented using the Atomistix ToolKit (ATK, http://quantumwise.com/) integrated within the Virtual NanoLab (VNL) simulation environment. The ATK was chosen for DFT calculations due to its integrated real-space basis and efficient treatment of spin-polarized systems in large supercells. ATK has been widely used in semiconductor studies for over a decade. Its reliability is supported by strong agreement with both experimental data and results obtained from other well-established DFT packages, confirming its suitability for modeling TM-doped ZnSe systems. Moreover, the calculations were completed within a relatively short PC time, demonstrating the software's computational efficiency for large-scale supercell models.

In our study, we also continuously explored various DFT-based methods, including LDA, GGA, MGGA, and hybrid functionals, to investigate the electronic and magnetic properties of the materials. Our experience showed that LDA and GGA, when combined with Hubbard U corrections, were successfully applied in the calculations. For most of

our calculations, we successfully used LDA and LSDA methods to model the electronic and magnetic properties. It should be noted that we also tested hybrid functionals for various compositions, but due to the considerably longer computational time required for these calculations, we decided to discontinue their use for the current study. The many-body interactions between electrons and atomic nuclei were treated within the Kohn-Sham formalism [27], which transforms the complex many-electron problem into a set of self-consistent one-electron equations. To solve these equations, we applied the linear combination of atomic orbitals method. The exchange-correlation effects were treated within the local spin density approximation, supplemented by Hubbard U corrections [28] to better account for the on-site Coulomb interactions, particularly for the localized d-electrons of the transition metals as reported in Refs. [29, 30]. In this study, the magnetism of diluted magnetic semiconductor systems $Zn_{1-x}TM_xSe$ was investigated under conditions similar to those used in previous works [25, 29, 30]. Supercell models were developed by replacing one or two Zn atoms with Ni^{2+} ions to simulate doping concentrations. Hubbard U corrections were applied to improve the accuracy of band gap predictions and to account for strong electron correlation effects associated with Ni 3d orbitals. In our calculations, the Hubbard U parameters were set as follows: Zn (3d) = 4.5 eV and Se (4p) = 3.8 eV.

To investigate the magnetic properties of Ni-doped ZnSe, supercell models consisting of 32 and 64 atoms were constructed based on the wurtzite ZnSe structure with initial lattice parameters a = 3.98 Å and c = 6.53 Å, as reported in Refs. [31, 32]. Nickel doping was simulated by substituting one or two Zn atoms with Ni^{2+} ions, corresponding to doping concentrations of 3.125 %, 6.25% and 12.5%, respectively. Ni atoms were substituted at Zn sites in the ZnSe lattice, as the substitution is energetically favorable and commonly reported in the literature for DMS studies. Although Ni has a slightly smaller atomic radius (~1.24 Å) than Zn (~1.34 Å) [33], structural relaxation during DFT optimization showed no significant lattice distortion or clustering at the doping levels considered.

The crystal structure of ZnSe was assumed to be hexagonal, belonging to the $P6_3mc$ space group [29]. The electronic structure and spin-resolved properties were computed using norm-conserving pseudopotentials from the Fritz-Haber-Institute (FHI), along with a double-zeta polarized (DZP) basis set. The Brillouin zone integration was carried out using a 5×5×5 Monkhorst-Pack k-point grid The plane-wave energy cutoff was set to 100 Ry to ensure convergence of total energy and magnetic properties. In the Ni-doped ZnSe systems, the separation between Ni atoms depends on the size of the supercell. For the 32-atom supercell, the optimized Ni-Ni distance is 7.96 Å, while in the 64-atom supercell, it increases to 9.50 Å. This distance corresponds to the spatial separation between the two Ni dopant atoms along the [001] crystallographic direction (i.e., parallel to the c-axis of the supercell).

To illustrate this configuration, a representative figure is included below, showing the dopant positions and the direction along which the measurement was performed. During geometry optimization, both atomic positions and lattice vectors were fully relaxed. Structural relaxation was performed until the forces on each atom were below 0.001 eV/Å and the total stress was less than 0.001 eV/Å^3. These settings ensure that the calculated Ni-Ni distances accurately reflect the relaxed equilibrium geometry in the ferromagnetic (FM) state of the system.

To analyze the distribution of magnetic moments, Mulliken population analysis was used. The calculations allowed for a detailed investigation of the magnetic ordering, spin polarization, and stability of different magnetic phases. Both ferromagnetic (FM) and antiferromagnetic (AFM) configurations were considered by appropriately arranging the spins of the Ni atoms (Ni↑Ni↑ and Ni↑Ni↓ configurations).

This computational approach provides a reliable basis for predicting the spin-polarized behavior of Ni-doped ZnSe:Ni at various doping levels and for assessing its potential use in spintronics.

3. RESULTS AND DISCUSSION

Electronic properties of ZnSe and ZnSe:Ni

Initially, the electronic band structures and density of states (DOS) for undoped ZnSe were calculated using supercells containing 32 and 64 atoms. In order to accurately determine the band gap and the dispersion relations of the bands, first-principles calculations were performed within the local spin density approximation (LSDA) framework, incorporating Hubbard U corrections for the Zn *d*- (4.5 eV) and O *p*-electrons (3.8 eV). To observe the changes induced in the electronic band structure upon Ni doping and for comparison purposes, the band structure of undoped ZnSe with a 32-atom supercell is presented in Figure 1.

It is worth noting that the band structure and band gap of the 64-atom ZnSe supercell are analogous. The calculated band gap of 2.70 eV for undoped ZnSe in this study is in good agreement with previous experimental results. For instance, wavelength-modulated spectroscopy reported a band gap of 2.70 eV [4], while other experimental studies have investigated the optical band gap properties of ZnSe and yielded a slightly higher value of 2.763 eV [5]. Additionally, optically-pumped lasing has been demonstrated in doped ZnSe epitaxial layers grown by metal-organic vapour-phase epitaxy [5].

Figure 2 illustrates the total density of states (TDOS) for undoped ZnSe using the 32-atom supercell. Based on the results of the band structure and DOS calculations for ZnSe, the valence band can be primarily divided into three distinct groups. The first group, located at the top of the valence band, mainly originates from the *p*-states of Se atoms. The second group of valence states is predominantly contributed by the *d*-orbitals of Zn atoms. The lowest-lying states (third group) are primarily derived from the *s*-states of Se atoms. As seen in Figures 1 and 2, the zones corresponding to spin-up and spin-down states in the band structure completely overlap, and the DOS curves are perfectly symmetric.

These results obtained for the electronic properties (electronic structure and DOS) indicate that the undoped ZnSe compound is a nonmagnetic material.

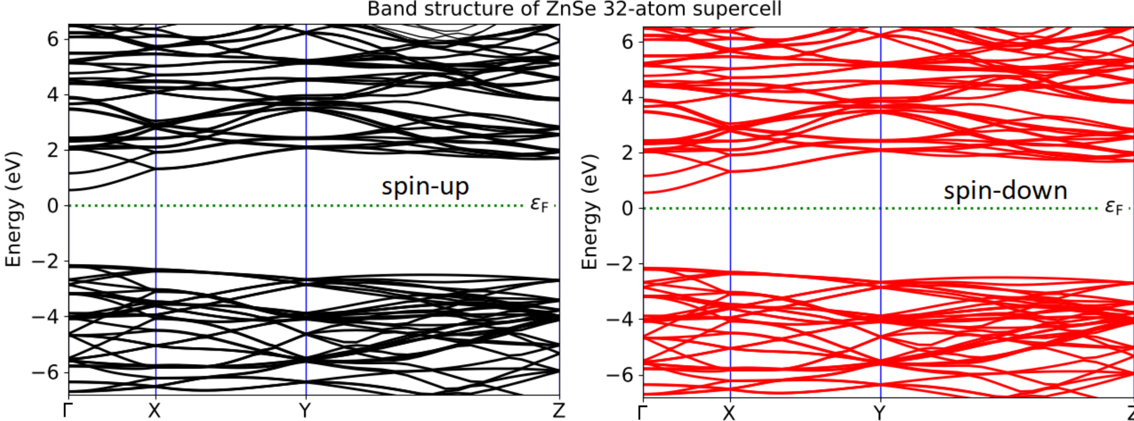

Figure 1. Spin-polarized band structure of undoped ZnSe supercell containing 32 atoms, calculated using first-principles methods

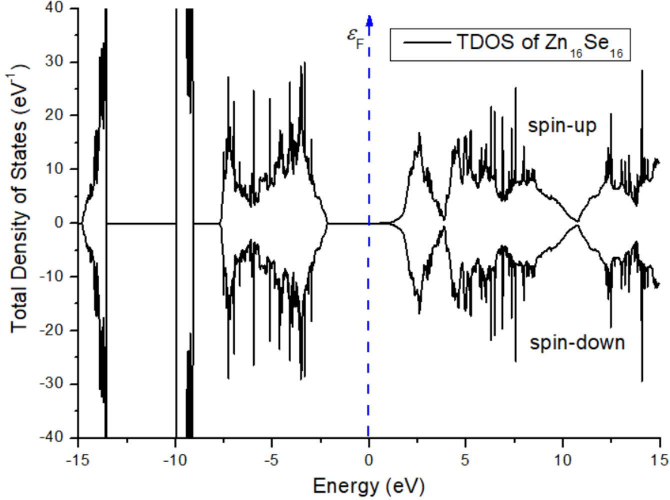

Figure 2. Spin-polarized TDOS diagram for undoped ZnSe supercell containing 32 atoms

The band structure interpretation of ZnSe:Ni supercells reveals that the incorporation of Ni atoms substantially modifies the band structure of the host semiconductor. Specifically, impurity-induced states emerge near the Fermi level, with some of these states crossing the Fermi energy. This behavior is a clear indicator of the onset of magnetic ordering in the system, driven by the interaction between the localized d-electrons of Ni and the host lattice. The calculated spin-polarized band structures for majority- and minority-spin channels, along with Figures 3 and 4 illustrate the total density of states (TDOS), while Figure 5 presents the partial density of states (PDOS) for Se and Ni atoms in the 32-atom Ni-doped ZnSe supercell.

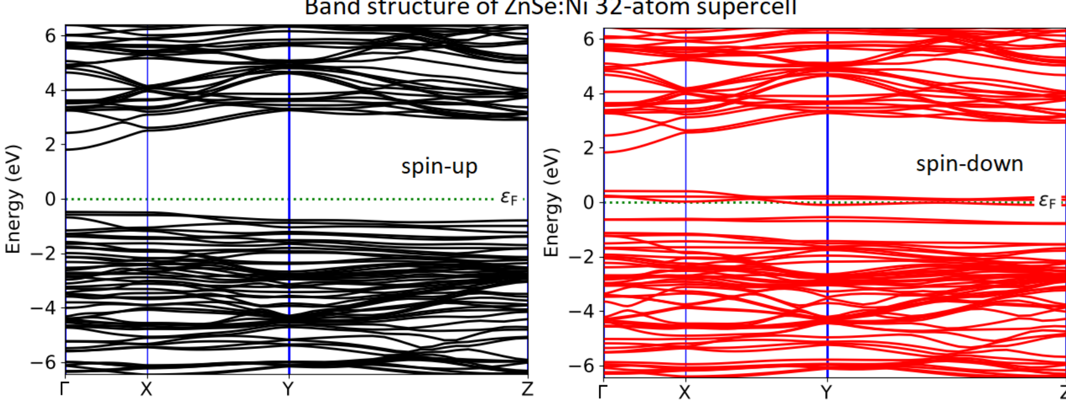

Figure 3. Spin-polarized band structure of Ni-doped ZnSe supercell containing 32 atoms, calculated using first-principles methods

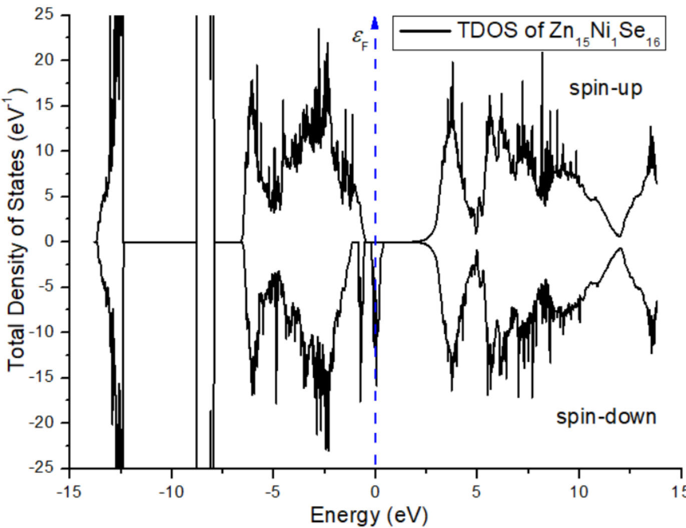

Figure 4. Spin-polarized TDOS diagram for a Ni-ZnSe supercell containing 32 atoms

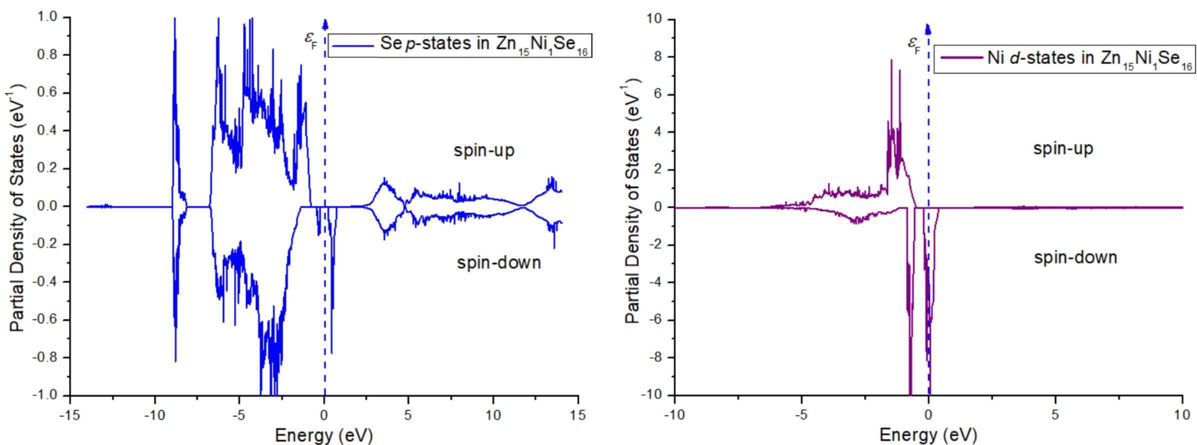

Figure 5. Spin-polarized PDOS diagram for Ni and Se atoms in Ni-ZnSe 32-atom supercell.

Additionally, from first-principles calculations, we have studied the electronic properties of a ZnSe 64-atom supercell doped with a Ni atom. The obtained band structures (minority and majority spin) and DOS curves are shown in Figures 6-8. The PDOS plot shows that Ni 3d orbitals contribute significantly to the DOS vicinity of Fermi energy. A significant hybridization occurs between the Ni 3d orbitals and the Se 4p states, most prominently in the spin-down state. This orbital mixing alters the band structure by introducing spin-dependent energy levels, which manifest as a distinct spin asymmetry in the DOS. The spin-up states exhibit a clear band gap, characteristic of semiconducting behavior, whereas the spin-down states retain metallic states at the Fermi level. Such properties are of particular interest for spintronic applications, where the control of spin currents is essential for device performance. The magnetic moment primarily originates from Ni 3d orbitals, while Se atoms also contribute slightly through p-d hybridization.

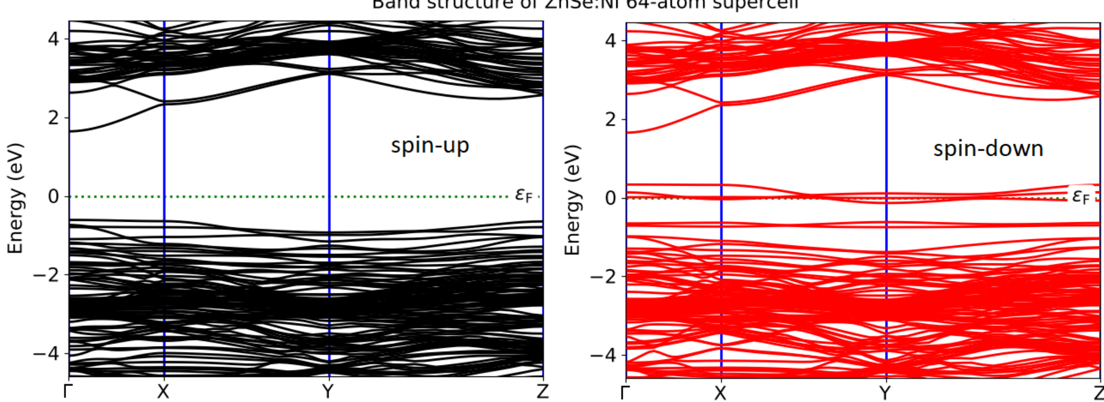

Figure 6. Spin-polarized band structure of Ni-doped ZnSe supercell containing 64 atoms, calculated using first-principles methods.

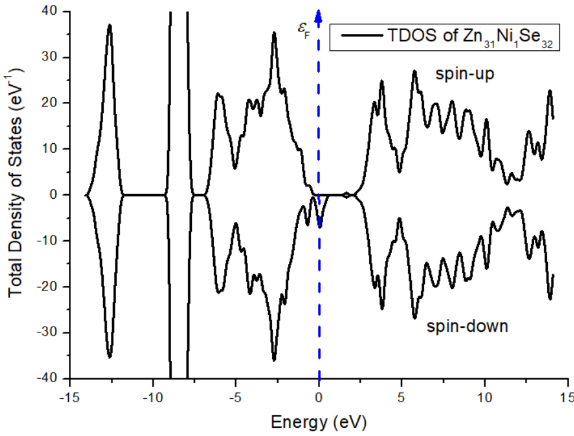

Figure 7. Spin-polarized TDOS diagram for a Ni-ZnSe supercell containing 64 atoms.

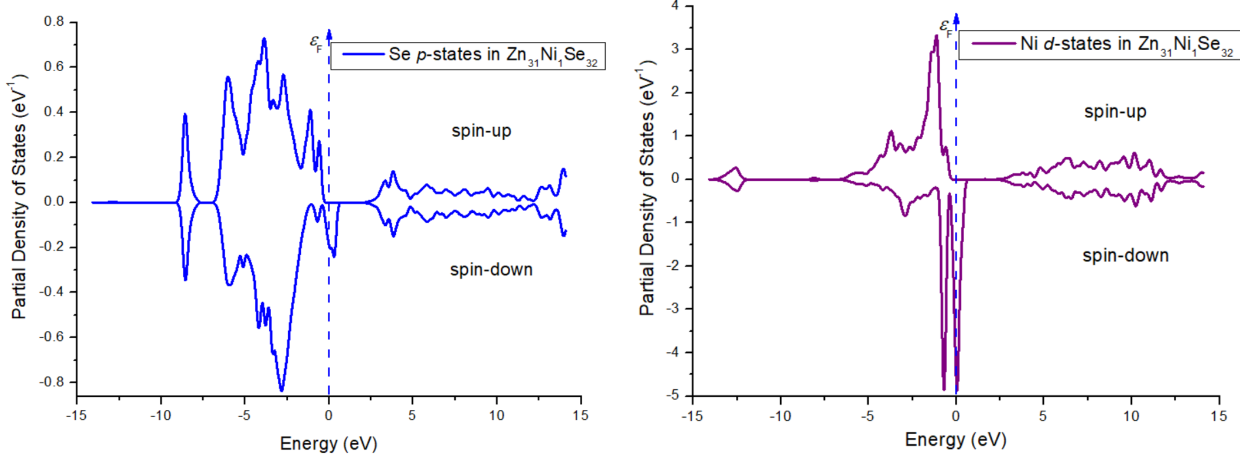

Figure 8. Spin-polarized PDOS diagram for Ni and Se atoms in Ni-ZnSe 64-atom supercell.

These findings emphasize the role of transition metal dopants and host atom interactions in tailoring the spintronic properties of ZnSe-based diluted magnetic semiconductors. A pronounced imbalance between the spin-up and spin-down electronic states is observed, providing clear evidence of spin polarization in the Ni-ZnSe system. This asymmetry indicates that the electronic structure favors one spin orientation over the other, a critical feature for materials considered in spintronic device design, where spin-selective transport plays a key role. The PDOS diagrams, shown in Figures 5 and 8, highlights strong hybridization between the Ni 3d orbitals and the Se 4p orbitals, which plays a crucial role in mediating the magnetic interactions. The replacement of Zn atoms with Ni introduces significant changes to the electronic structure, most notably causing a reduction in the band gap of the spin-up channel and inducing metallic behavior in the spin-down channel.

Table 1 presents the calculated band gap energies for both undoped and Ni-doped ZnSe supercells. For the undoped systems ($Zn_{16}Se_{16}$ and $Zn_{32}Se_{32}$), the band gaps are identical for both spin-up and spin-down channels (2.70 eV), indicating a symmetric electronic structure and confirming the non-magnetic nature of pure ZnSe. Upon Ni doping, significant spin polarization emerges. In the $Zn_{15}Ni_1Se_{16}$ supercell (6.25% Ni), the spin-up band gap decreases to 2.48 eV, while the spin-down band gap closes completely (0.00 eV), indicating the onset of half-metallic behavior. A similar trend is observed in the $Zn_{31}Ni_1Se_{32}$ supercell (3.125% Ni), where the spin-up gap further reduces to 2.24 eV, with the spin-down channel remaining metallic (0.00 eV). This spin-selective behavior, semiconducting in the spin-up channel and metallic in the spin-down, is a defining feature of half-metallic ferromagnetism. It is observed in both 32- and 64-atom ZnSe supercells doped with Ni, confirming that Ni incorporation introduces strong spin asymmetry and transforms the electronic structure of ZnSe.

Table 1. Band gap results for undoped and doped ZnSe

Supercells	*x*, %	Spin-up, eV	Spin-down, eV
$Zn_{16}Se_{16}$	0.0	2.70	2.70
$Zn_{32}Se_{32}$	0.0	2.70	2.70
$Zn_{15}Ni_1Se_{16}$	6.25	2.48	0.00
$Zn_{31}Ni_1Se_{32}$	3.125	2.24	0.00

Such half-metallic properties, characterized by a fully spin-polarized density of states at the Fermi level, are highly desirable for spintronic applications, as they enable efficient spin injection and control in advanced electronic and optoelectronic devices. These findings establish $Zn_{1-x}Ni_xSe$ as a promising candidate for next-generation spin-based technologies.

Ferromagnetic properties of ZnSe:Ni

The magnetic properties of $Zn_{1-x}Ni_xSe$ systems were analyzed using the Mulliken population method. Both the total and local magnetic moments were calculated for Ni-doped ZnSe systems, including the Ni^{2+} ions and their neighboring atoms. While pure ZnSe exhibits no magnetic behavior, doping with Ni ions induces magnetic properties in the system. The majority of the magnetization arises from the hybridization between the p-electronic states of the host selenium atoms and the d states of the Ni impurity ions.

Figure 9 presents the spin-polarization structure of the $Zn_{15}Ni_1Se_{16}$ supercell from first-principles simulations. The black arrows indicate the magnetic moments of atoms: the lengths of these arrows are scaled according to the values of the corresponding magnetic moments.

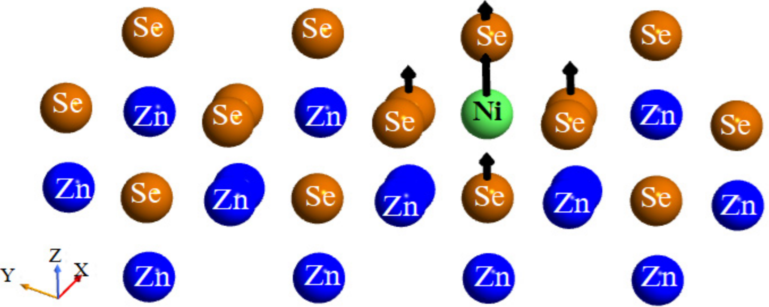

Figure 9. Spin-polarization map of the Ni-doped ZnSe 32-atom supercell.

For the Ni-ZnSe systems, the computed total magnetic moment within the examined supercell configurations is around 4 μ_B per Ni dopant atom. Additionally, the local magnetic moment, primarily originating from the Ni site, contributes significantly to the overall magnetic behavior of the system, which localized specifically on each Ni ion is estimated to be about 1.2 μ_B. The dominant contribution to the overall magnetization primarily arises from the nickel ion's 3d electronic states, which provide nearly 1.2 μ_B of magnetic moment. In contrast, the surrounding zinc atoms contribute only a negligible amount to the total magnetic moment, indicating that their role in the magnetic behavior of the system is minimal. Interestingly, a significant positive contribution to the magnetic moment also comes from four selenium atoms that are chemically bonded directly to the nickel dopant. These selenium atoms collectively contribute approximately 0.85 μ_B, highlighting the strong p-d hybridization between Se p orbitals and Ni d orbitals plays a crucial role in mediating and amplifying the magnetic characteristics of the ZnSe:Ni system. This orbital interaction not only facilitates magnetic exchange coupling but also significantly contributes to the stabilization of the observed ferromagnetic ground state in the material.

Figure 10 represents the spin-polarized density of states (DOS) for the four selenium (Se) atoms chemically bonded to a nickel (Ni) atom in the ZnSe:Ni supercell. The asymmetry between the spin-up and spin-down states near the Fermi level (εF) indicates a significant spin polarization, suggesting a contribution of these Se atoms to the overall magnetic behavior of the system.

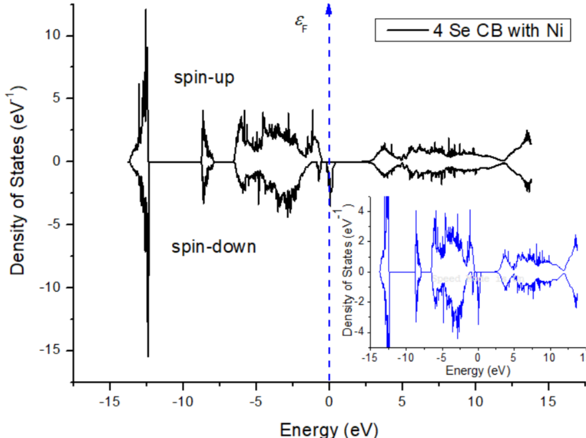

Figure 10. Spin-polarized DOS diagrams of the four selenium atoms chemically bonded to Ni in the ZnSe:Ni supercell structure, illustrating their contribution to the magnetic behavior.

Table 2. Bond lengths between two nickel dopants and total energy differences for Ni-doped ZnSe at 12.5% and 6.25% concentrations

Supercells	Number of atoms	Bond length (Ni-Ni), Å	Δ*E* [eV]
$Zn_{14}Ni_2Se_{16}$ (2 Ni(Zn)-doped in ZnSe)	32	7.96	0.12004
$Zn_{30}Ni_2Se_{32}$ (2 Ni(Zn)-doped in ZnSe)	64	9.50	0.02328

The theoretically calculated bond distances between two impurity atoms and the energy differences ($\Delta E = E_{AFM} - E_{FM}$) for ZnSe:Ni compounds at 12.5 and 6.25 % concentrations are represented in the following Table 2. The total energy difference between the antiferromagnetic (AFM) and ferromagnetic (FM) configurations serves as a critical parameter for evaluating the magnetic stability of Ni-doped ZnSe systems. A positive value of ΔE indicates that the ferromagnetic phase is energetically preferred over the antiferromagnetic one, suggesting a stable ferromagnetic ground state. In our results, the smaller supercell (32 atoms) with a bond length of 7.96 Å shows a larger ΔE (0.12004 eV), indicating stronger ferromagnetic coupling and greater magnetic stability at this doping concentration. Meanwhile, the larger supercell (64 atoms) with a longer bond length of 9.50 Å exhibits a smaller ΔE (0.02328 eV), suggesting weaker ferromagnetic interactions and relatively reduced stability. These findings imply that the magnetic properties and stability of Ni-doped ZnSe are strongly dependent on dopant concentration and spatial arrangement, which is crucial for designing spintronic devices with optimized performance.

Figure 11 describes the variation of total energy difference (ΔE) and bond length (Å) for the different Ni-ZnSe supercell structures containing 32- and 64-atoms. We obtained that increasing the size of the supercell from 32 to 64 atoms results in a noticeable increase in the bond length between two Ni dopants, from 7.96 Å to 9.50 Å. At the same time, the total energy difference decreases from 0.12004 to 0.02328 eV indicates the FM state becomes energetically more favorable in larger supercells, reflecting enhanced magnetic stability with reduced Ni-Ni interaction strength due to increased spatial separation. These results support the idea that dilute Ni doping in ZnSe maintains ferromagnetic stability, particularly at lower concentrations where dopants are more isolated.

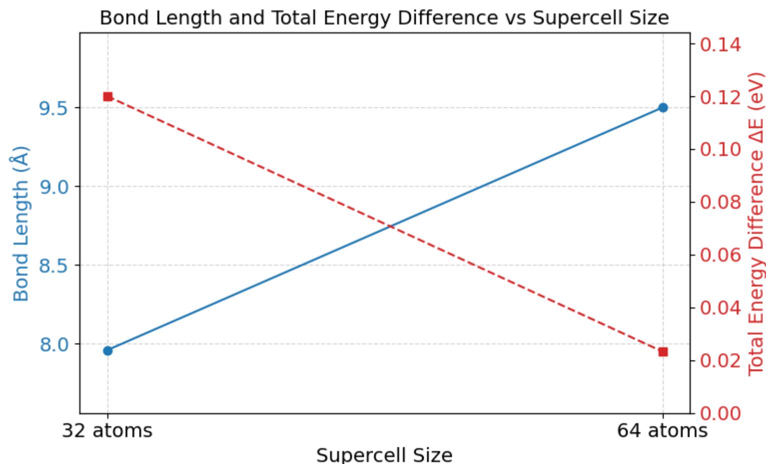

Figure 11. The variation of total energy difference (ΔE) and bond length (Å) for Ni-ZnSe systems.

Our first-principles results (see Table 2) demonstrate that the FM phase is more stable than the AFM phase in Ni-ZnSe compounds. The spin-polarized band structures and electronic DOS results reveal that nickel doping induces a high-spin state with half-metallic characteristics in the ZnSe supercells. These characteristics underscore the significant promise of Ni-ZnSe as a functional material for advanced technologies, especially in the realm of spintronics, where high spin polarization and robust magnetic stability are critical for device performance.

4. CONCLUSION

In this work, spin-polarized first-principles simulations based on DFT were conducted to explore the magnetic and electronic properties of ZnSe doped by Ni at doping concentrations of 12.5% and 6.25%. The *ab initio* results suggest that the incorporation of nickel substantially modifies the host material's electronic and magnetic structure, giving rise to a half-metallic ferromagnetic state, a feature highly desirable for spintronic applications.The obtained value of magnetic moment of the doped supercells is approximately 4.0 μ_B, where the dominant contribution arises from the localized 3d states of the Ni^{2+} ions, with additional hybridization from the p-states of neighboring Se atoms.

The spin-resolved band structure and DOS analyses confirm the presence of spin polarization near the Fermi energy, indicating potential applicability in spintronic technologies. Furthermore, Mulliken population analysis and spin-density visualizations reveal strong magnetic ordering primarily around Ni sites.

We also evaluated the total energy differences between ferromagnetic (FM) and antiferromagnetic (AFM) configurations. The results consistently show that the FM phase is energetically more favorable, especially at lower

doping concentrations, signifying magnetic stability in diluted Ni configurations. Increasing the size of the supercell results in reduced magnetic interaction between Ni dopants, as reflected by the increased bond length and decreased ΔE values.

Overall, the findings indicate that Ni-ZnSe systems exhibit the key characteristics of a promising DMS materials with half-metallic behavior, positioning it as a strong contender for future applications in spintronic technologies, optoelectronic systems, and magneto-electronic devices.

ORCID

V.N. Jafarova, https://orcid.org/0000-0002-0643-1464; **A.N. Jafarova**, https://orcid.org/0000-0001-8150-1787
A.J. Ahmadova, https://orcid.org/0009-0004-9657-5649

REFERENCES

[1] L. Liu, *et al.*: "Oxygen vacancies: the origin of n-type conductivity in ZnO," Physical Review B, **93**, 235305 (2016). https://doi.org/10.1103/PhysRevB.93.235305
[2] E. A. Zhukov, *et al.*: "Spin coherence of electrons and holes in ZnSe-based quantum wells studied by pump–probe Kerr rotation," Physica Status Solidi B, **251**(9), 1872-1880 (2014). https://doi.org/10.1002/pssb.201350233
[3] L. Ławniczak-Jabłońska, *et al.*: "Correlation between XANES of the transition metals in ZnS and ZnSe and their limit of solubility," Physica B: Condensed Matter, **208**, 497-502 (1995). https://doi.org/10.1016/0921-4526(94)00732-B
[4] D. Theis, "Electronic structure of ZnSe," Physica Status Solidi (b), **79**, 125 (1977). https://doi.org/10.1002/pssb.2220790112
[5] G. P. Yablonskii, *et al.*: "Optically-Pumped Lasing of Doped ZnSe Epitaxial Layers Grown by Metal-Organic Vapour-Phase Epitaxy," Physica Status Solidi (a) **159**, 543-557 (1997). https://doi.org/10.1002/1521-396X(199702)159:2%3C543::AID-PSSA543%3E3.0.CO;2-S
[6] W. Y. Liang and A. D. Yoffe: "Electronic structure of II–VI compounds," Proceedings of the Royal Society of London. Series A, Mathematical and Physical Sciences, **300**, 326 (1967).
[7] B. Pejova, "The higher excited electronic states and spin–orbit splitting of the valence band in three-dimensional assemblies of close-packed ZnSe and CdSe quantum dots in thin film form," Journal of Solid State Chemistry, **181**(8), 2041-2048 (2008). https://doi.org/10.1016/j.jssc.2008.03.038
[8] T. Dietl, H. Ohno, and F. Matsukura, "Hole-mediated ferromagnetism in tetrahedrally coordinated semiconductors," Physical Review B, **63**, 195205 (2001). https://doi.org/10.1103/PhysRevB.63.195205
[9] M. Tanaka and Y. Higo, "Large tunneling magnetoresistance in GaMnAs/AlAs/GaMnAs ferromagnetic semiconductor tunnel junctions," Physical Review Letters, **87**(2), 026602 (2001). https://doi.org/10.1103/PhysRevLett.87.026602
[10] S. A. Wolf, *et al.*: "Spintronics: A spin-based electronics vision for the future," Science, **294**(5546), 1488-1495 (2001). https://doi.org/10.1126/science.1065389
[11] D. D. Awschalom and M. E. Flatté, "Challenges for semiconductor spintronics," Nature Physics, **3**(3), 153-159 (2007). https://doi.org/10.1038/nphys551
[12] K. Sato, *et al.*: "First-principles theory of dilute magnetic semiconductors," Reviews of Modern Physics, **82**(2), 1633-1690 (2010). https://doi.org/10.1103/RevModPhys.82.1633
[13] F. Goumrhar, *et al.*: "Ab-initio calculations for the magnetic properties of TM(Ti,V)-doped zinc-blende ZnO," International Journal of Modern Physics B, **32**, 1850025 (2018). https://doi.org/10.1142/S021797921850025X
[14] B. Xiao, *et al.*: "Optical and electrical properties of vanadium-doped ZnTe crystals grown by the temperature gradient solution method," Optical Materials Express, **8**, 431-439 (2018). https://doi.org/10.1364/OME.8.000431
[15] W. Benstaali, *et al.*: "Ab-initio study of magnetic, electronic and optical properties of ZnSe doped-transition metals," Materials Science in Semiconductor Processing, **16**, 231 (2013). http://dx.doi.org/10.1016/j.mssp.2012.10.001
[16] C. Kim, *et al.*: "Middle-infrared random lasing of Cr^{2+} doped ZnSe, ZnS, CdSe powders, powders imbedded in polymer liquid solutions, and polymer films," Optics Communications, **282**, 2049-2052 (2009). https://doi.org/10.1016/j.optcom.2009.02.023
[17] J.E. Williams, *et al.*: "Mid-IR laser oscillation in Cr2+:ZnSe planar waveguide," Optics Express, **18**, 25999-26006 (2010). https://doi.org/10.1364/OE.18.025999
[18] N. Myoung, *et al.*: "Energy scaling of 4.3 μm room temperature Fe: ZnSe laser," Optics Letters **36**, 94-96 (2011). https://doi.org/10.1364/OL.36.000094
[19] I.S. Moskalev, V.V. Fedorov, S.B. Mirov, "10-Watt, pure continuous-wave, polycrystalline Cr^{2+}:ZnS laser," Optics Express, 17, 2048-2056 (2009). https://doi.org/10.1364/oe.17.002048
[20] V.I. Kozlovsky, *et al.*: "Room-temperature tunable mid-infrared lasers on transition-metal doped II–VI compound crystals grown from vapor phase," Physica Status Solidi B, **247**, 1553-1556 (2010). http://dx.doi.org/10.1002/pssb.200983165
[21] S.ZH. Karazanov, *et al.*: "Electronic structure and optical properties of ZnX (X=O, S, Se, Te): A density functional study," Physical Review B, **75**, 155104 (2007). http://dx.doi.org/10.1103/PhysRevB.75.155104
[22] K. Sato, and H. Katayama-Yoshida, "Ab initio Study on the Magnetism in ZnO-, ZnS-, ZnSe and ZnTe-Based Diluted Magnetic Semiconductors," Physica Status Solidi (b), **229**, 673-680 (2002). https://doi.org/10.1002/1521-3951(200201)229:2%3C673::AID-PSSB673%3E3.0.CO;2-7
[23] Q. Mahmood, *et al.*: "The study of electronic, elastic, magnetic and optical response of $Zn_{1-x}Ti_xY$ (Y = S, Se) through mBJ potential," Current Applied Physics, **16**, 549-561 (2016). https://doi.org/10.1016/j.cap.2016.03.002
[24] S. Arif, *et al.*: "Investigation of half metallicity in Fe doped CdSe and Co doped CdSe materials," Current Applied Physics, **12**, 184-187 (2012). https://doi.org/10.1016/j.cap.2011.05.034
[25] V.N. Jafarova, "Study the electronic and magnetic properties of Mn-doped wurtzite ZnSe using first-principle calculations," Indian Journal of Physics, **97**, 2639-2647 (2023). http://dx.doi.org/10.1007/s12648-023-02598-y
[26] P. Hohenberg, and W. Khon, "İnhomogeneous electron gas," Physical Review B, **136**, 864-871 (1964). https://doi.org/10.1103/PhysRev.136.B864

[27] D.M. Ceperley, and B.J. Alder, "Ground state of the electron gas by a stochastic method," Physical Review Letters, **45**, 566-569 (1980). https://doi.org/10.1103/PhysRevLett.45.566
[28] M. Cococcioni, and S. De Gironcoli, "Linear response approach to the calculation of the effective interaction parameters in the LDA+U method," Physical Review B, **71**, 035105 (2005). https://doi.org/10.1103/PhysRevB.71.035105
[29] V.N. Jafarova, "Ab-initio calculation of structural and electronic properties of ZnO and ZnSe compounds with wurtzite structure," International Journal of Modern Physics B, **36**, 2250156 (2022). https://doi.org/10.1142/S0217979222501569
[30] V.N. Jafarova, and M.A. Musaev, "First-principles study of structural and electronic properties of ZnSe with wurtzite structure," Technium: Romanian Journal of Applied Sciences and Technology, **6**, 42-46 (2023).
[31] R.W.G. Wyckoff, *Crystal Structures*, Second Edition, (Interscience Publishers, New York, 1963). https://search.worldcat.org/search?q=au=%22Wyckoff%2C%20R.%20W.%20G.%22
[32] V.N. Jafarova, and H.S. Orudzhev, "Structural and electronic properties of ZnO: A first-principles density-functional theory study within LDA(GGA) and LDA(GGA)+ U methods," Solid State Communnications, **325**, 114166 (2021). https://doi.org/10.1016/j.ssc.2020.114166
[33] R. D. Shannon, "Revised effective ionic radii and systematic studies of interatomic distances in halides and chalcogenides," Acta Crystallographica Section A, **32**(5), 751-767 (1976). https://doi.org/10.1107/S0567739476001551

СПІН-ПОЛЯРИЗОВАНІ ВЛАСТИВОСТІ ZnSe, ЛЕГОВАНОГО Ni: МОДЕЛЮВАННЯ ТА СИМУЛЯЦІЇ НА ОСНОВІ ПЕРШИХ ПРИНЦИПІВ

В.Н. Джафарова[a,b], А.Н. Джафарова[a], А.Дж. Ахмадова[c]
[a]*Азербайджанський державний університет нафти та промисловості, 20 Azalig Ave., AZ-1010, Баку, Азербайджан*
[b]*Хазарський університет, 41 Mehseti Str., AZ1096, Баку, Азербайджан*
[c]*Державний університет Нахчівана, AZ 7012 Нахчіван, Азербайджан*

У цьому дослідженні проведено всебічний *ab initio* аналіз електронних та магнітних властивостей систем ZnSe, легованих нікелем, досліджених при трьох концентраціях домішок – 3.125 %, 6,25% та 12,5%. Аналіз виконано за допомогою теорії функціонала густини (DFT) у рамках локального наближення спінової густини (LSDA), доповненого корекціями Габбарда U для точного врахування сильних ефектів електронної кореляції, характерних для d-орбіталей перехідних металів. Введення атомів Ni в решітку ZnSe суттєво змінює електронну структуру, викликаючи напівметалічну поведінку та виражену спінову поляризацію. Загальний магнітний момент становить приблизно 4,0 μ_B на суперкомірку. Крім того, порівняння енергій ферромагнітного та антиреферромагнітного станів показало, що ферромагнітна фаза є більш стабільною з енергетичної точки зору. Ці результати підкреслюють потенціал ZnSe, легованого Ni, для застосування у спінтроніці, де критично важливим є точний контроль магнітних та електронних властивостей.

Ключові слова: *ZnSe:Ni; феромагнетик; напівметал; магнітний момент; моделювання на основі першопринципів; теорія функціонала густини*

EAST EUROPEAN JOURNAL OF PHYSICS. 3. 408-412 (2025)
DOI:10.26565/2312-4334-2025-3-42 ISSN 2312-4334

EFFECT OF TEMPERATURE ON THE CURRENT-VOLTAGE CHARACTERISTICS OF n-GaAs-p-$(ZnSe)_{1-x-y}(Ge_2)_x(GaAs_{1-\delta}Bi_\delta)_y$ HETEROSTRUCTURES

Akramjon Y. Boboev[a], Iqboljon M. Soliev[b], Nuritdin Y. Yunusaliyev[a], Murodiljon M. Xotamov[a]
[a]*Andijan State University named after Z.M. Babur, Andijan, Uzbekistan*
[b]*Andijan State pedagogical institute, Andijan, Uzbekistan*
**Corresponding Author E-mail: aboboevscp@gmail.com*
Received March 29, 2025; revised July 14, 2025; accepted July 24, 2025

This paper investigates the electrophysical properties of *n*-GaAs-*p*-$(ZnSe)_{1-x-y}(Ge_2)_x(GaAs_{1-\delta}Bi_\delta)_y$ heterostructures at different temperatures. The epitaxial *n*-GaAs-*p*-$(ZnSe)_{1-x-y}(Ge_2)_x(GaAs_{1-\delta}Bi_\delta)_y$ grown on GaAs substrates showed p-type conductivity, their resistivity (5 Ω·cm), charge carrier concentration ($\rho = 1.5\cdot10^{16}$ cm^{-3}) and carrier mobility (μ = 300 cm²/V·s) were determined by Hall method. Experimental values of the mobility of the main charge carriers allowed us to determine the mobility of the non-main charge carriers, which amounted to ($\mu = 1890$ cm²/V·s) by means of theoretical calculations. In the current-voltage (I–V) characteristics of the *n*-GaAs-*p*-$(ZnSe)_{1-x-y}(Ge_2)_x(GaAs_{1-\delta}Bi_\delta)_y$ heterostructure, a quadratic dependence of $J \sim V^2$ was revealed, and this dependence does not change with increasing temperature in the transition to regions with a sharp increase in current. Analysis of these regions of the volt-ampere characteristic showed that the mechanism of current flow is determined by the direct drift of charge carriers. It was proposed to use *n*-GaAs-*p*-$(ZnSe)_{1-x-y}(Ge_2)_x(GaAs_{1-\delta}Bi_\delta)_y$ heterostructures in voltage amplifiers, constant voltage converters, as well as in electronic and thermoelectronic devices.
Keywords: *Heterostructure; Epitaxy; Current-voltage characteristic; Temperature; Donor doping; Charge carriers; Mobility*
PACS: 78.30.Am

INTRODUCTION

A3B5 wide bandgap semiconductor compounds are considered as potential materials for the production of optoelectronic devices operating in the mid- and far-infrared (IR) spectral regions. Currently, extensive research is being conducted to develop and study various electronic device structures based on InSb, InAs, GaSb, GaAs and their solid-state alloys [1-3]. Among these materials, GaAs compounds and their complex solid alloys $(GaAs)_{1-x-y}(Ge_2)_x(ZnSe)_y$ are of particular interest, in particular due to the high mobility of electrons and holes [4-6]. These characteristics make such materials suitable for the fabrication of high-speed optoelectronic devices. Additionally, the $(GaAs)_{1-x-y}(Ge_2)_x(ZnSe)_y$ solid solutions allow for the spectral range of device structures to be extended from 1.1 eV to 2.65 eV due to the wide tunability of *x* and *y* composition parameters [7]. However, the widespread practical application of devices fabricated from GaAs-based compounds and their solid solutions is limited by the insufficient understanding of the electro-physical properties of these materials and the structures based on them. Therefore, the present study aims to investigate the electro-physical properties of *n*-GaAs-*p*-$(ZnSe)_{1-x-y}(Ge_2)_x(GaAs_{1-\delta}Bi_\delta)_y$ heterostructures at various temperatures.

MATERIALS AND METHODS

$(ZnSe)_{1-x-y}(Ge_2)_x(GaAs_{1-\delta}Bi_\delta)_y$ solid solutions were grown on (100)-oriented, 400 µm thick GaAs substrates with electron-type conductivity using the liquid-phase epitaxy (LPE) method under forced cooling conditions from a Bi-containing multicomponent melt solution. The composition of the melt and the crystallization onset temperature were selected based on preliminary experimental results and the phase diagram of the GaAs–Ge–ZnSe–Bi multicomponent system. The resulting epitaxial films exhibited *p*-type conductivity, a specific resistivity of 5 Ω·cm, a charge carrier concentration of $1.5\cdot10^{16}$ cm^{-3}, carrier mobility μ = 300 cm²/V·s and a thickness of 8 µm. To investigate the current-voltage characteristics (I-V curve) of the structures fabricated on the basis of $(ZnSe)_{1-x-y}(Ge_2)_x(GaAs_{1-\delta}Bi_\delta)_y$ solid solutions, ohmic contacts were formed by vacuum sputtering. Silver contacts were deposited on the back side of the sample (entire surface) and on the solid-solution side as square-shaped contacts with a surface area of 6 mm². Additionally, the temperature dependence of the current-voltage (I–V) characteristics of the *n*-GaAs-*p*-$(GaAs_{1-\delta}Bi_\delta)_{1-x-y}(Ge_2)_x(ZnSe)_y$ heterostructures was studied in both forward and reverse bias modes. The experimental data were processed using the OriginPro 2022 software package.

RESULTS AND DISCUSSION

Figure 1 presents current-voltage characteristics (I-V) of multicomponent *n*-GaAs-*p*-$(ZnSe)_{1-x-y}(Ge_2)_x(GaAs_{1-\delta}Bi_\delta)_y$ heterostructures in logarithmic scale at different (1 – 30 °C, 2 – 50 °C, 3 – 70 °C, 4 – 90 °C, 5 – 110 °C, 6 – 130 °C, 7 – 150 °C) temperatures.

Cite as: A.Y. Boboev, I.M. Soliev, N.Y. Yunusaliyev, M.M. Xotamov, East Eur. J. Phys. 3, 408 (2025), https://doi.org/10.26565/2312-4334-2025-3-42
© A.Y. Boboev, I.M. Soliev, N.Y. Yunusaliyev, M.M. Xotamov, 2025; CC BY 4.0 license

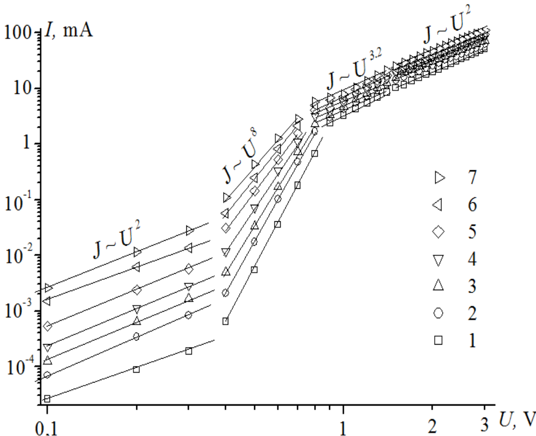

Figure 1. Current-voltage characteristics of *n*-GaAs-*p*-$(ZnSe)_{1-x-y}(Ge_2)_x(GaAs_{1-\delta}Bi_\delta)_y$ heterostructures in logarithmic scale at different temperatures: 1 – 30 °C, 2 – 50 °C, 3 – 70 °C, 4 – 90 °C, 5 – 110 °C, 6 – 130 °C, 7 – 150 °C

Analysis of the obtained results in logarithmic scale showed that in the forward bias region, at all measured temperatures, the current demonstrates a linear dependence on the applied voltage according to the expression: $J = A\cdot V^\alpha$, where α is a power-law exponent that varies depending on the voltage range [8].

In the initial region of the current-voltage characteristic, from 0.1 V to 0.3 V, a "jump" or transition region is observed, where the current follows a quadratic dependence: $J \sim V^\alpha$ ($\alpha \approx 2$). This behavior suggests that the charge transport in this voltage range obeys the following relation [9].

$$V = M(J)B_0\sqrt{\frac{J}{2}}. \tag{1}$$

Here, the quantity $M(J)$ is expressed by the following formula:

$$M(J) \approx 1 + 3m\left[2 + C\left(\alpha\tau_i/c_p\right)\sqrt{J}\right]^2, \tag{2}$$

here, $m = 2\tau_i N_d V_p^*/8b(b+1)n_p d$; and $C = [bn_p/qV_p^*(b+1)]$. In these ratios, V_p^* - represents the imperfection value of the injection contact [10].

Thus, this particular region of the current-voltage characteristic (I-V) manifests when the denominator in the recombination rate expression reaches extremely small values. This behavior is typically observed in cases where the recombination process dominates the carrier transport mechanism, and the contact imperfection contributes significantly to the overall voltage drop across the structure [11].

$$u_r = N_r \frac{c_n c_p (pn - n_i^2)}{c_n(n+n_1) + c_p(p+p_1) + \alpha\tau_i pn}. \tag{3}$$

Here, the terms are defined as follows: N_r – concentration of recombination centers (complexes), n, p – concentrations of electrons and holes, respectively, n_i – intrinsic carrier concentration in the semiconductor, c_n, c_p – capture coefficients for electrons and holes, n_1, p_1 – equilibrium concentrations of electrons and holes corresponding to the impurity energy level aligned with the Fermi level (known as Shockley–Read static factors), τ_i – time constant associated with electron exchange processes within the recombination complex, α – coefficient dependent on the type of defect complex.

This type of recombination mechanism may arise not only under the above-mentioned conditions but also in the presence of metastable recombination complexes, such as negatively charged acceptor–positively charged impurity ion pairs, or positively charged donors paired with negatively charged vacancies, which can form in various configurations within semiconductors.

At low excitation levels, i.e., when the final term in the denominator of expression (3) becomes negligible, the recombination rate can be described by the Shockley–Read statistics. In such a case, the current transport mechanism across the heterojunction based on the current-voltage characteristics (I-V) assumes a conventional form corresponding to the ohmic relaxation of the volumetric space charge under drift conditions. This behavior is described as follows [12]:

$$V = \sqrt{\frac{8d^3 J}{9q\mu_p\mu_n\tau_p N_d}} = B_0\sqrt{J}. \tag{4}$$

Firstly, the value of B_0 is determined from the slope of the experimentally obtained straight line corresponding to the relation $J=V^\alpha$, using the following expression:

$$B_0 = \sqrt{\frac{8d^3}{9q\mu_p\mu_n\tau_pN_d}}. \quad (5)$$

In our case, the value of B_0 at room temperature is found to be: B_0=0.001 V·A$^{-1/2}$ Considering the film thickness d = 5 µm and using experimental data, it is also possible to estimate the concentration of shallow-level donor impurity centers. For our structure at room temperature, this concentration is: N_d=1.2·10^{15} cm^{-3}. According to the Hall effect measurements, the mobility of the majority charge carriers (holes) is: μ_r=300 cm^2/V·s. Based on theoretical calculations, the mobility of minority carriers (electrons) can be determined using the relationship: μ_n=b·μ_r=1890 cm^2/V·s, where b is the ratio of minority to majority carrier mobilities, and in our case, at room temperature, b = 6.3 [13].

As the temperature increases, the B_0 value rises from 0.001 V·A$^{-1/2}$ to 0.369 V·A$^{-1/2}$, while the mobilities of both majority (μ_n) and minority charge carriers and their lifetimes (τ_r), as well as the concentration of shallow donor levels (N_d), decrease. This behavior indicates that in the investigated solid solutions, the diffusion of charge carriers into deeper impurity regions plays a significant role in the current transport mechanism of the heterostructures [14]. Moreover, starting from an applied voltage of V = 0.4, a sharp increase in current is observed in the current-voltage characteristics (I-V), which follows a power-law relationship of the form: J = V$^\alpha$ = 8. This region is known as the pre-breakdown region (see Figure 1). In this regime, the last term in the denominator of expression (3) begins to play a significant role in the recombination rate. Consequently, the recombination rate deviates from the Shockley–Read statistics and takes on a fundamentally different form [15].

$$u_r = \frac{N_r}{\tau_i}\left(1 - \frac{2}{\tau_i c_p p}\right). \quad (6)$$

The dependence of the current on the applied voltage in this regime takes the following form:

$$J = \frac{q^2(b+1)^2N_rd^3}{\varepsilon\tau_i^2c_p(V_0-V)}. \quad (7)$$

Here: ε – the dielectric permittivity (dielectric constant) of the grown epitaxial films. This parameter characterizes the film's ability to polarize in response to an electric field and plays a crucial role in determining the electric field distribution, capacitance, and overall electrostatic behavior of the heterostructure. It directly influences charge carrier dynamics, recombination rates, and space-charge region properties in semiconductor devices. $V_0 = \sqrt{\frac{q(b+1)N_rd^4}{2\varepsilon\tau_i\mu_p}} = const.$

From equation (7), it follows that the current increases as the denominator decreases with increasing applied voltage-that is, the current rises rapidly. This behavior indicates the onset of a highly nonlinear transport mechanism. In particular, within the voltage range V = 0.4-0.8 V, a sharp increase in current is observed, marking the transition from ohmic or quadratic behavior to a pre-breakdown or injection-enhanced regime.

This phenomenon has been thoroughly discussed in the study by [16]. In that work, the authors analyze the mechanisms responsible for such nonlinear current growth, including enhanced injection, formation of space-charge regions, and recombination through complex defect states. In the studied heterostructures, this sharp rise in current in the V = (0.4–0.8) V range is indicative of the increasing role of injected charge carriers and their recombination via complex deep-level centers. This behavior also signals the transition into a regime where classical drift-diffusion models are no longer sufficient, and recombination-limited or space-charge-limited current mechanisms begin to dominate. When the applied voltage to the studied samples is increased from 0.9 V to 1.5 V, the current-voltage relationship assumes the form: $J = A\cdot V^{3.2}$ (as shown in Figure 1). According to the theoretical analysis provided by [17], this region of the current-voltage characteristic may arise due to electron exchange through complex recombination centers during the recombination of nonequilibrium charge carriers. In this case, the final term in the denominator of equation (3) satisfies the following condition:

$$c_n(n+n_1) + c_p(p+p_1) < \alpha\tau_i pn. \quad (8)$$

The I-V curve also takes the following analytical expression:

$$V = \frac{(b+1)d^2N_r}{N_d\mu_p\tau_i} + \frac{d}{q\mu_p(b+1)C}\sqrt{J} - \frac{2(b+1)N_rd^2c_p}{N_d\mu_p\alpha\tau_iC}\frac{1}{\sqrt{J}} = A + B\sqrt{J} - \frac{D}{\sqrt{J}}. \quad (9)$$

where A, V, and D are quantities that depend on the concentration of ionized atoms in deep pores, the ratio of electron and hole mobilities, and the thickness of the interlayer junction base, and can be determined based on the results of experimental studies. To determine the quantity A, two experimental points V_1, J_1 and V_2, J_2 are selected from the dependence of current on voltage in the form J ~ V$^{3.2}$. The results obtained by calculation are presented in Table 1. It can also be seen from the table that the value of A does not change much with increasing temperature, which in turn indicates that the N_r/τ_i ratio does not change. In addition, it is possible to determine the values of B and D by selecting three experimental points V_1, J_1), (V_2, J_2), (V_3, J_3) in the region of a sharp increase in current flow. According to the data

presented in Table 1 and the calculation results, it was found that the value of D increases with increasing temperature and the value of B decreases. This, in turn, indicates that the n-GaAs substrate and *p*-$(ZnSe)_{1-x-y}(Ge_2)_x(GaAs_{1-\delta}Bi_\delta)_y$ epitaxial film increase the value of "c" in the relationship (3) at the boundary of the separation and that the concentration of hole-holding centers is related to c_p. The results obtained and the results obtained using calculations show that expression (9) can be used to characterize the slope of the volt-ampere characteristic in the form $J \sim V^\alpha$.

Table 1. The values of the quantities A, B and D given in relation (9) are calculated from the experimental results of I-V curve at different temperatures

t, ºC	30	50	70	90	110	130	150
A. V	0.69	0.7	0.705	0.711	0.717	0.723	0.73
D. V·mA$^{-1/2}$	1.38	2.12	2.44	2.94	4.16	5.58	7
B. V·A$^{1/2}$.	0.0174	0.0156	0.0146	0.0134	0.0131	0.013	0.0128

After a sharp increase in the applied voltage of the current to the samples, a repeating quadratic field with $J \sim V^\alpha$, where α = 2, was observed (Fig. 2). In this case, the last part in the denominator of relation (3) begins to play a decisive role and the recombination rate u_r $u_r=N_r/\tau_i$ is completely saturated [18]:

$$V = \frac{(b+1)d^2N_r}{2N_d\mu_p\tau_i} + \frac{d}{q\mu_p(b+1)C}\sqrt{J}, \quad (10)$$

The determination of the value of Nr/τi for this region is carried out in the same way as for the region of sharp increase in the dependence of the current strength on the applied voltage. First, a straight line equation is constructed for two selected experimental points, from which the values of various quantities corresponding to the value of the first part of expression (10) are determined:

$$\frac{A}{2} = \frac{(b+1)d^2N_r}{2N_d\mu_p\tau_i}, \quad (11)$$

Using several mathematical substitutions, based on the quantities d, b, and N_d in the relation (11), $N_r/\tau_i = 5.2\cdot10^{18}$ cm$^{-3}\cdot$s^{-1} was obtained.

CONCLUSION

Thus, in the *n*-GaAs-*p*-$(ZnSe)_{1-x-y}(Ge_2)_x(GaAs_{1-\delta}Bi_\delta)_y$ heterostructure, the forward-biased current-voltage characteristics exhibit a transition from a quadratic relationship ($J \sim V^2$) to regions of steep current increase. It was found and theoretically supported that this behavior does not change significantly with increasing temperature.

Beyond the pre-breakdown region, the dependence of current on voltage reveals two distinct characteristic regions. The analysis of these regions in the I-V characteristics of *n*-GaAs-*p*-$(ZnSe)_{1-x-y}(Ge_2)_x(GaAs_{1-\delta}Bi_\delta)_y$ heterostructures confirms the dominance of the direct drift-based charge transport mechanism. Based on these findings, the investigated heterostructures are promising for use in voltage-multiplying devices, constant-voltage converters where high-frequency or time-domain response is not critical, and in various electronic and thermoelectronic applications.

Conflict of Interests

The authors declare that they have no conflict of interests

Funding

The present research work was financed under the project FZ-292154210 granted by the Ministry of Innovative Development of the Republic of Uzbekistan.

ORCID

A.Y. Boboev, https://orcid.org/0000-0002-3963-708X; **N.Y. Yunusaliyev**, https://orcid.org/0000-0003-3766-5420
I.M. Soliev, https://orcid.org/0009-0003-6623-2218

REFERENCES

[1] T. Danilova, B. Zhurtanov, A. Imenkov and Y. Yakovlev, Semiconductors, **39**, 1235 (2005). https://doi.org/10.1134/1.2128447
[2] A. Krier, X.L. Huang and V.V. Sherstnev, in: Mid-infrared Semiconductor Optoelectronics. Springer Series in Optical Sciences, edited by A. Krier, vol 118, (Springer, London 2006), pp. 359–394. https://doi.org/10.1007/1-84628-209-8_11
[3] T. Li, P. Wang, H. Fu, *et al*., Physical Review Letters, **115**(13), 136804 (2015). https://doi.org/10.1103/PhysRevLett.115.136804
[4] S. Zainabidinov, A. Saidov, M. Kalanov and A. Boboev, Applied Solar Energy, **55**, 291 (2019). https://doi.org/10.3103/S0003701X1905013X
[5] A.S. Saidov, S.Z. Zainabidinov, M.U. Kalanov, A.Y. Boboev and B.R. Kutlimurotov, Applied Solar Energy, **51**(3), 206 (2015). https://doi.org/10.3103/S0003701X15030111
[6] S. Suprun, V. Sherstyakova and E. Fedosenko, Semiconductors, **43**(11), 1526 (2009). https://doi.org/10.1134/S1063782609110220
[7] A.Y. Boboev. East European Journal of Physics. **3**, 216 (2024). https://doi.org/10.26565/2312-4334-2024-3-31
[8] S. Saidov, A.Yu. Leiderman, Sh.N. Usmonova and U.P. Asatova, Technical Physics Letters. **46**(11), 1124 (2020). https://doi.org/10.1134/S1063785020110279

[9] S. Zainabidinov, A.Y. Boboev and N.Y. Yunusaliyev, East Eur. J. Phys. (2), 321 (2024). https://doi.org/10.26565/2312-4334-2024-2-37
[10] S. Zainabidinov, A. Saidov, A. Boboev and D. Abdurahimov. Herald of the Bauman Moscow State Technical University, Series Natural Sciences. **100**(1), 72 (2022). https://doi.org/10.18698/1812-3368-2022-1-72-87
[11] C. Wang, R.C.I. MacKenzie, U. Würfel, D. Neher, T. Kirchartz, C. Deibel and M. Saladina, Advanced Energy Materials, **240**, 5889 (2025). https://doi.org/10.1002/aenm.202405889
[12] S. Kumar and R. Singh, IEEE Transactions on Electron Devices, **68(**4), 1892 (2021). https://doi.org/10.1109/TED.2021.3062803
[13] A.Y. Boboev, B.M. Ergashev, N.Y. Yunusaliyev, J.S. Madaminjonov, East Eur. J. Phys. (2), 431 (2025), https://doi.org/10.26565/2312-4334-2025-2-53
[14] Sh.A. Mirsagatov, A.Yu. Leiderman and O.K. Ataboev, Phys. Solid State, **55**, 1635 (2013). https://doi.org/10.1134/S1063783413080192
[15] Z. Chen and Y. Zhao, Physical Review B, **101**(19), 195305 (2020). https://doi.org/10.1103/PhysRevB.101.195305
[16] S.Z. Zainabidinov and Kh.M. Madaminov, Bulletin of Bauman Moscow State Technical University, Natural Sciences Series, **4**, 58 (2020).
[17] J. Wang, *et al*., Microelectronics Reliability, **144**, 114967 (2023). https://doi.org/10.1016/j.microrel.2023.114967
[18] Y. Zhang, *et al*., Applied Physics Letters, **119**, 052102 (2021). https://doi.org/10.1063/5.0059687

ВПЛИВ ТЕМПЕРАТУРИ НА ВОЛЬТ-АМПЕРНІ ХАРАКТЕРИСТИКИ ГЕТЕРОСТРУКТУР n-GaAs-p-$(ZnSe)_{1-x-y}(Ge_2)_x(GaAs_{1-\delta}Bi_\delta)_y$

Акрамжон Ю. Бобоєв[a], Ікболжон М. Солієв[b], Нурітдін Ю. Юнусалієв[a], Муродилжон М. Хотамов[a]
[a]*Андижанський державний університет імені З.М. Бабур, Андижан, Узбекистан*
[b]*Андижанський державний педагогічний інститут, Андижан, Узбекистан*

У цій статті досліджуються електрофізичні властивості гетероструктур n-GaAs-p-$(ZnSe)_{1-x-y}(Ge_2)_x(GaAs_{1-\delta}Bi_\delta)_y$ за різних температур. Епітаксійні n-GaAs-p-$(ZnSe)_{1-x-y}(Ge_2)_x(GaAs_{1-\delta}Bi_\delta)_y$, вирощені на підкладках GaAs, показали p-тип провідності, їх питомий опір (5 Ом·см), концентрація носіїв заряду ($\rho = 1{,}5\cdot10^{16}$ см⁻³) та рухливість носіїв ($\mu = 300$ см²/В·с) були визначені методом Холла. Експериментальні значення рухливості основних носіїв заряду дозволили нам визначити рухливість неосновних носіїв заряду, яка становила ($\mu = 1890$ см²/В·с) за допомогою теоретичних розрахунків. У вольт-амперних (ВАХ) характеристиках гетероструктури n-GaAs-p-$(ZnSe)_{1-x-y}(Ge_2)_x(GaAs_{1-\delta}Bi_\delta)_y$ виявлено квадратичну залежність $J \sim V^2$, і ця залежність не змінюється зі збільшенням температури при переході до областей з різким збільшенням струму. Аналіз цих областей вольт-амперної характеристики показав, що механізм протікання струму визначається прямим дрейфом носіїв заряду. Було запропоновано використовувати гетероструктури n-GaAs-p-$(ZnSe)_{1-x-y}(Ge_2)_x(GaAs_{1-\delta}Bi_\delta)_y$ в підсилювачах напруги, перетворювачах постійної напруги, а також в електронних та термоелектронних пристроях.
Ключові слова: *гетероструктура; епітаксія; вольт-амперна характеристика; температура; донорне легування; носії заряду; рухливість*